NASA CR-72542
Rocketdyne R-6636-3

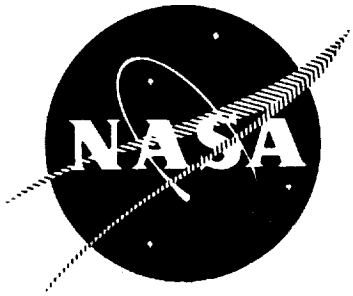

FINAL REPORT
FLUORINE-HYDROGEN PERFORMANCE EVALUATION
PHASE II: SPACE STORABLE PROPELLANT
PERFORMANCE DEMONSTRATION

By

B. J. Waldman

prepared for
NATIONAL AERONAUTICS AND SPACE ADMINISTRATION

Contract NASw-1229

ROCKETDYNE
North American Rockwell Corporation
6633 Canoga Avenue, Canoga Park, California

NOTICE

This report was prepared as an account of Government sponsored work. Neither the United States, nor the National Aeronautics and Space Administration (NASA), nor any person acting on behalf of NASA:

A.) Makes any warranty or representation, expressed or implied, with respect to the accuracy, completeness, or usefulness of the information contained in this report, or that the use of any information, apparatus, method, or process disclosed in this report may not infringe privately owned rights; or

B.) Assumes any liabilities with respect to the use of, or for damages resulting from the use of any information, apparatus, method or process disclosed in this report.

As used above, "person acting on behalf of NASA" includes any employee or contractor of NASA, or employee of such contractor, to the extent that such employee or contractor of NASA or employee of such contractor prepares, disseminates, or provides access to, any information pursuant to his employment or contractor with NASA, or his employment with such contractor.

Requests for copies of this report should be referred to

National Aeronautics and Space Administration
Office of Scientific and Technical Information
Attention: AFSS-A
Washington, D. C. 20546

NASA CR-72542
Rocketdyne R-6636-3

FINAL REPORT
FLUORINE-HYDROGEN PERFORMANCE EVALUATION
PHASE II-SPACE STORABLE PROPELLANT
PERFORMANCE DEMONSTRATION

By

B. J. Waldman
Advanced Systems

Technically Reviewed and Approved By:

S. F. Iacobellis
Manager
Advanced Systems

J. Friedman
Program Manager
Small Engine Division

April 1969

FOREWORD

This report presents the final theoretical and experimental results of a 47-month study titled Fluorine/Hydrogen Performance Evaluation Program. The Contract, NASw-1229, was conducted by Rocketdyne, a Division of North American Rockwell Corporation and was directed for the National Aeronautics and Space Administration by F. Stephenson (NASA-OART) and P. Herr (NASA-LeRC).

The report is submitted in three volumes:

Phase I, Part I	Analysis, Design and Demonstration of High-Performance Injectors for the Liquid Fluorine-Gaseous Hydrogen Propellant Combination
Phase I, Part II	Nozzle Performance Analysis and Demonstration
Phase II	Space Storable Propellant Performance Demonstration

ABSTRACT

This report covers work performed under Phase II of the Fluorine/Hydrogen Performance Evaluation Program, a research effort conducted under NASA Contract NASw-1229. During this phase of the program, the propellants F_2-O_2/CH_4, OF_2/CH_4, F_2-O_2/B_2H_6 and OF_2/B_2H_6 were tested in an altitude-simulation facility using two high-area-ratio nozzles and one low-area-ratio nozzle. Performance and heat transfer data were recorded, analyzed and compared with analytical predictions.

ACKNOWLEDGEMENT

Major contributions to the success of this program were made by the following people:

S. A. Evans..... Analysis, data interpretation and report preparation.

A. W. Huebner..... Test program coordination, facility and hardware design, and data processing.

T. L. Nielsen..... Facility design and test stand operation.

CONTENTS

ILLUSTRATIONS

TABLES

INTRODUCTION

The potential payload and operational gains possible for future spacecraft using space storable propellants have long been recognized. The two propellant combinations most often considered for this role are fluorine-oxygen/methane (F_2-O_2/CH_4) and oxygen difluoride/diborane (OF_2/B_2H_6). However, some uncertainties existed both in the theoretical and experimental performance of these propellants due to the scarcity of precision high area ratio test data and a recent major revision in the heat of formation of OF_2 by the National Bureau of Standards. Therefore, a performance investigation program was undertaken to establish the true performance levels of these propellants in a high precision test program. This program is the second phase of a larger project of propellant performance characterization which also included a performance demonstration for fluorine/hydrogen (F_2/H_2).

The fluorine/hydrogen phase, Phase I, beginning 27 May 1965, was concerned primarily with detailing the performance characteristics of this combination and establishing an accurate analytical performance model. The results of Phase I were presented in the first two volumes of the final report. During that phase the injector, combustion chamber and nozzle configurations were selected, designed and built. The same hardware has been carried over into Phase II.

Phase II of the program which is described in this volume of the final report began 27 July 1967. To achieve the Phase II objectives, a series of highly instrumented, precise performance tests were conducted with the propellants of interest. The tests included variations in nozzle contour, nozzle area ratio, mixture ratio, and chamber pressure.

SUMMARY

The primary objective of Phase II of the Fluorine-Hydrogen Performance Evaluation Program has been the determination of the deliverable performance of the oxidizers F_2-O_2 and OF_2 with the fuels CH_4 and B_2H_6. To achieve this objective a total of 134 tests were conducted including high area ratio performance tests, injector verification tests, and facility verification tests. The primary performance results are summarized in Fig. 1. Other major results are verification of a revised performance potential for OF_2, and successful operation of a thrust chamber using gaseous diborane injection.

A summary of the tests conducted during the program is shown in Table 1. This table also lists pages in the text where specific detailed test information can be found. The test matrix was designed to produce direct comparisons between OF_2 and F_2-O_2(70-30) performance with both fuels. This was done to determine whether the heat of formation for OF_2 recommended by the National Bureau of Standards, 1.95 kcal/mole at the normal boiling point (5.84 kcal/mole at standard conditions), Ref. 1 gives a more accurate indication of the performance of OF_2 relative to F_2-O_2(70-30) than does the previously accepted value of -7.4 kcal/mole.

Tests were conducted with five propellant combinations: F_2-O_2(82.5-17.5)/CH_4, F_2-O_2(70-30)/CH_4, OF_2/CH_4, OF_2/B_2H_6, F_2-O_2(70-30)/B_2H_6. Nozzle geometries included a 60:1 area ratio 70-percent bell, a 60:1 area ratio 15-degree cone, and a 4:1 area ratio 15-degree cone. Mixture ratio was varied over the range of interest for each propellant. Chamber pressure was 100 psia, except for one F_2-O_2(70-30)/B_2H_6 series at 55 psia. The nominal thrust level at 100 psia was 2500 lbf.

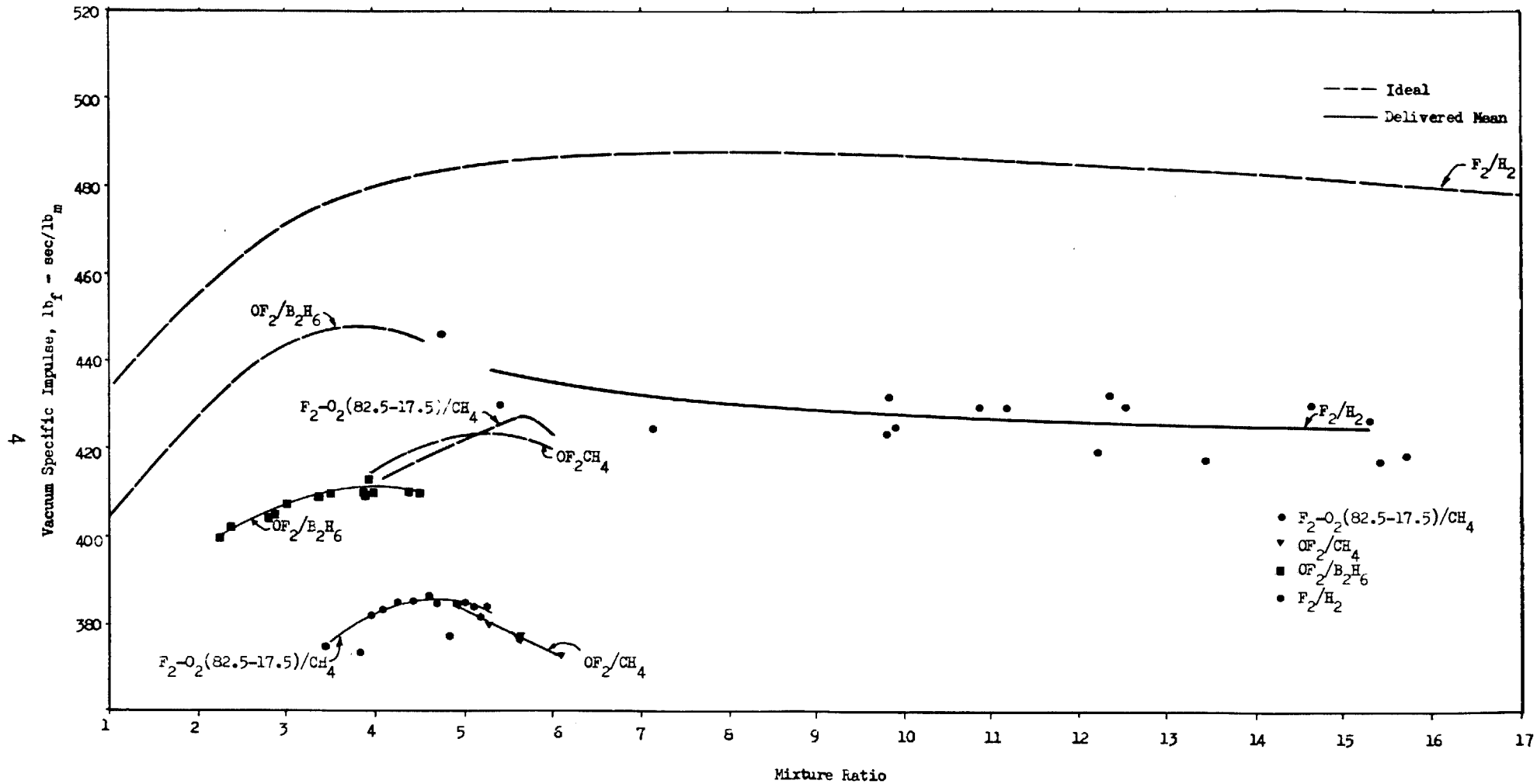

Figure 1. Propellant Performance Comparison at a Chamber Pressure of 100 psia

TABLE 1 TECHNICAL INFORMATION INDEX

Fuel	Oxidizer	Nozzle	Test Numbers	Maximum Specific Impulse lb_f-sec/lbm	Specific Impulse Page:	Injector Performance Page:	Thrust Chamber Performance Page:	Heat Transfer Results Page:
CH_4	F_2-O_2 (82.5-17.5)	Low Area Ratio	033-042	---	---	18, 19	---	28
		Cone	043-054	386	13, 22	18	22, 61	28, 29
		Bell	055-060	384	13, 23	18	23, 62	28, 30
	F_2-O_2 (70-30)	Cone	073-078	376	14, 24	20	24, 70	28, 29
	OF_2	Cone	122-130	383	17, 25	20	25, 70	28, 29
		Bell	109-121	---	---	---	71	28, 30
B_2H_6	F_2-O_2 (70-30)	Low Area Ratio	087-092	---	---	38	---	44
		Cone	061-072 074-086	---	35, 36, 43	37	43, 79	44, 46, 48
		Bell	093-100	407	34, 42	37	42, 78	44, 47
	OF_2	Cone	001-006 (1969	412	32, 40	37	40, 77	44, 46, 48
		Bell	101-108	411	32, 41	37	41, 78	44, 47

Direct performance comparisons were obtained between two different F_2-O_2 mixtures with methane fuel and between the two different nozzle contours for both OF_2/B_2H_6 and F_2-O_2(82.5-17.5)/CH_4. Low area ratio tests were conducted to compare injector efficiencies derived from chamber pressure and from thrust. The test program for Phase II was conducted at the Rocketdyne Nevada Field Laboratory altitude simulation facility B-3 test stand. Because this was a new facility, a series of F_2/H_2 tests was conducted to verify that data from the new test stand were consistent with the Phase I results.

The program consisted exclusively of short duration performance determination tests using heat sink hardware. The propellant feed systems provided the oxidizers as liquids and the fuels as gases. In the case of diborane this was significant because it was the first time diborane has been used in gaseous form in a rocket engine. All tests were highly instrumented and included measurements of combustor and nozzle wall pressure profiles, and combustor and nozzle heat flux profiles as well as thrust and flowrate. Instrumentation was designed for precise specific impulse performance determination. All critical measurements were redundant and frequently calibrated.

The specific impulse test results have consistently been able to resolve performance effects of 1-percent magnitude. The difference between OF_2 and F_2-O_2(70-30), a 6 lbf-sec/lbm effect, has been clearly evident in the test results. The relative performance of the bell and conical nozzles, different by only about 2 lbf-sec/lbm, was reproducibly indicated.

Since the primary objective of the program was to produce experimental data which can be used directly, the test results have been presented in two distinctly different ways. The actual observed test data are shown first without manipulation or adjustment. These data describe the behavior of an important class of advanced propellants and constitute the key results of this program. The interpreted performance data, in

the form of thrust chamber efficiencies are shown in a separate section. These data, when compared to the theoretical models, indicate important trends and show the present state-of-the-art in performance prediction. In the remaining sections, the method of obtaining meaningful data from test measurements and the performance model for data correlation are presented, and the facility, instrumentation and hardware are described.

CONCLUSIONS

This program has established the following facts based directly on test results:

1. A specific impulse of 386 lbf-sec/lbm was produced with F_2-O_2(82.5-17.5)/CH_4 at a chamber pressure of 100 psia and an area ratio of 60. This performance level was relatively insensitive to nozzle contour.

2. The heat flux measured for F_2-O_2(82.5-17.5)/CH_4 was essentially identical to that measured for F_2/H_2 and no heat transfer inhibiting deposit was observed in these short duration tests.

3. A specific impulse of 412 lbf-sec/lbm was produced with OF_2/B_2H_6 at a chamber pressure of 100 psia and an area ratio of 60. This performance level was relatively insensitive to nozzle contour.

4. The heat flux measured for OF_2/B_2H_6 was significantly higher than that for F_2-O_2/CH_4 or F_2/H_2, approximately 20-percent higher in the combustion chamber and 100-percent higher in the nozzle.

5. The OF_2/B_2H_6 injector remained free of deposits after many tests and an accumulated duration of 30 seconds. A coating of B_2O_3 was observed on the combustion chamber wall and nozzle to an area ratio of 3.

6. For both CH_4 and B_2H_6, the specific impulse produced with OF_2 was higher than that for F_2-O_2(70-30) by an amount that is in agreement with the newly adopted NBS heat of formation.

SECTION I

METHANE TEST RESULTS

The methane test program was designed to establish both the deliverable performance of F_2-O_2/CH_4 and the sensitivity of this performance to variations in nozzle contour and in oxidizer composition and energy content. A total of 39 individual test data points was obtained and each of the objectives was met. Summarized in this section are the specific impulse results, injector performance, nozzle performance, heat transfer and hardware condition. Detailed discussion of the performance trends and comparison with predictions are presented in Section IV.

The deliverable performance of F_2-O_2(82.5-17.5)/CH_4 was measured for the 60:1 area ratio 15-degree cone in eleven tests and for the 70-percent bell in six tests. The injector performance for this propellant combination was verified in six tests using a 4:1 area ratio conical nozzle. The results of these tests were a maximum specific impulse of 386 lbf-sec/lbm and injector efficiencies consistently above 97-percent.

The deliverable performance of F_2-O_2(70-30)/CH_4 and OF_2/CH_4 were examined in twelve tests. The maximum measured specific impulse was 383 lbf-sec/lbm for OF_2 and 376 lbf-sec/lbm for F_2-O_2(70-30) with injector efficiencies above 97-percent. These results confirm the energy content difference expected between OF_2 and F_2-O_2. A secondary result of the F_2-O_2(70-30) testing was an indication of the performance trend with F_2 to O_2 ratio.

Heat transfer levels were measured for the three oxidizers and were generally similar to those for F_2/H_2. A slight sooty residue was evident with F_2-O_2(82.5-17.5) but did not appear to affect the heat transfer. By contrast, the hardware remained clean when the same tests were repeated with F_2-O_2(70-30) and OF_2.

HIGH AREA RATIO MEASURED SPECIFIC IMPULSE

The experimental specific impulse results for F_2-O_2(82.5-17.5)/CH_4 with both the bell and conical nozzles are shown in Fig. 2. The theoretical one-dimensional isentropic chemical equilibrium performance is provided as a reference on the same figure. The two nozzles generated nearly identical performance with the bell specific impulse only 1 to 2 lbf-sec/lbm below that of the 15-degree cone. The peak performance is 386 lbf-sec/lbm and occurs at a mixture ratio of approximately 4.7. The theoretical peaks at 5.7. The difference is partly caused by the injector efficiency trend with mixture ratio and partly by nozzle performance effects discussed later in this section.

A performance test series was conducted with an oxidizer composition of 70-percent fluorine (F_2-O_2(70-30)) using the conical nozzle. The results are shown in Fig. 3 compared with the results for F_2-O_2(82.5-17.5). The peak value is 376 lbf-sec/lbm, approximately 10 lbf-sec/lbm lower than the theoretical optimum F_2-O_2 ratio. This sensitivity to oxidizer composition is substantially larger than anticipated; Fig. 4. Although the phenomenon is not presently understood and a detailed analysis to determine the physical basis was outside the scope of this program, some possible explanations are discussed in Section IV.

To verify the heat of formation for OF_2, a test series was conducted under the same conditions used for F_2-O_2(70-30), its compositional equivalent.

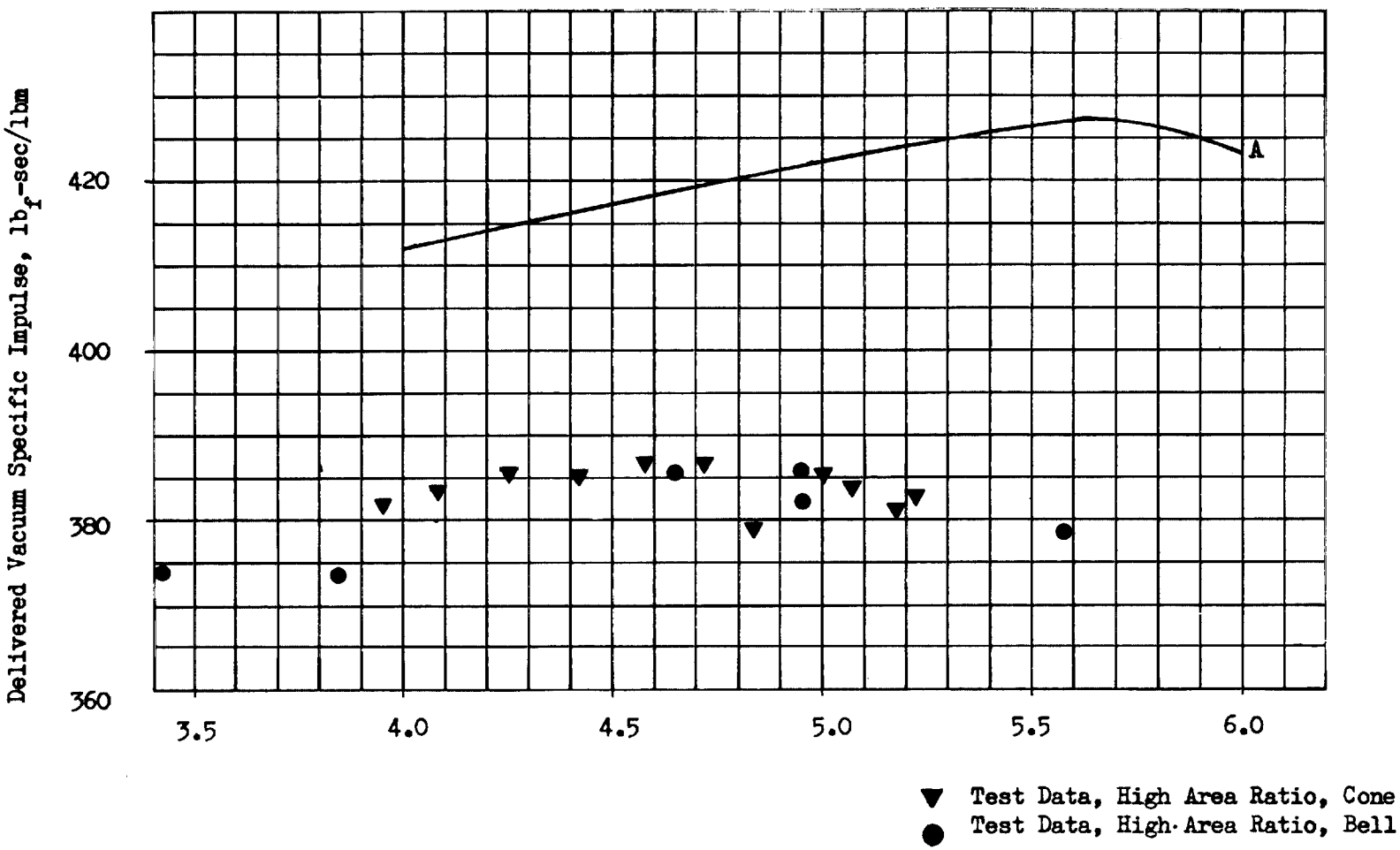

A. One-Dimensional Isentropic Chemical Equilibrium Expansion Performance.

Figure 2. Delivered Vacuum Specific Impulse for F_2-O_2(82.5-17.5)/CH_4 at a Chamber Pressure of 100 psia for the 15-degree Cone and the 70-percent Bell.

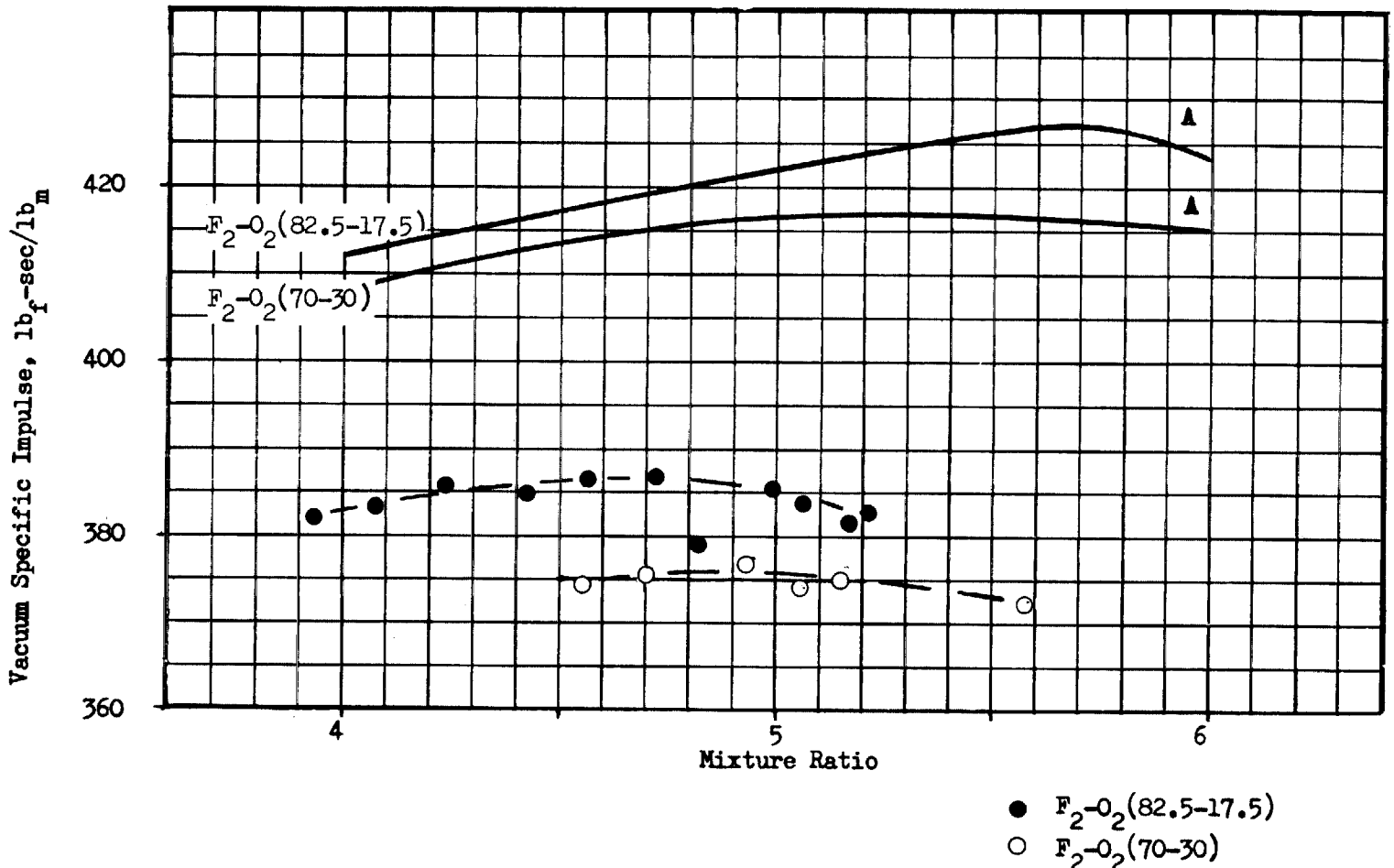

A. One-Dimensional Isentropic Chemical Equilibrium Composition Expansion Performance

Figure 3. Delivered Vacuum Specific Impulse for CH_4 with F_2-O_2(70-30) and F_2-O_2(82.5-17.5) at a chamber pressure of 100 psia for the 15-degree Cone.

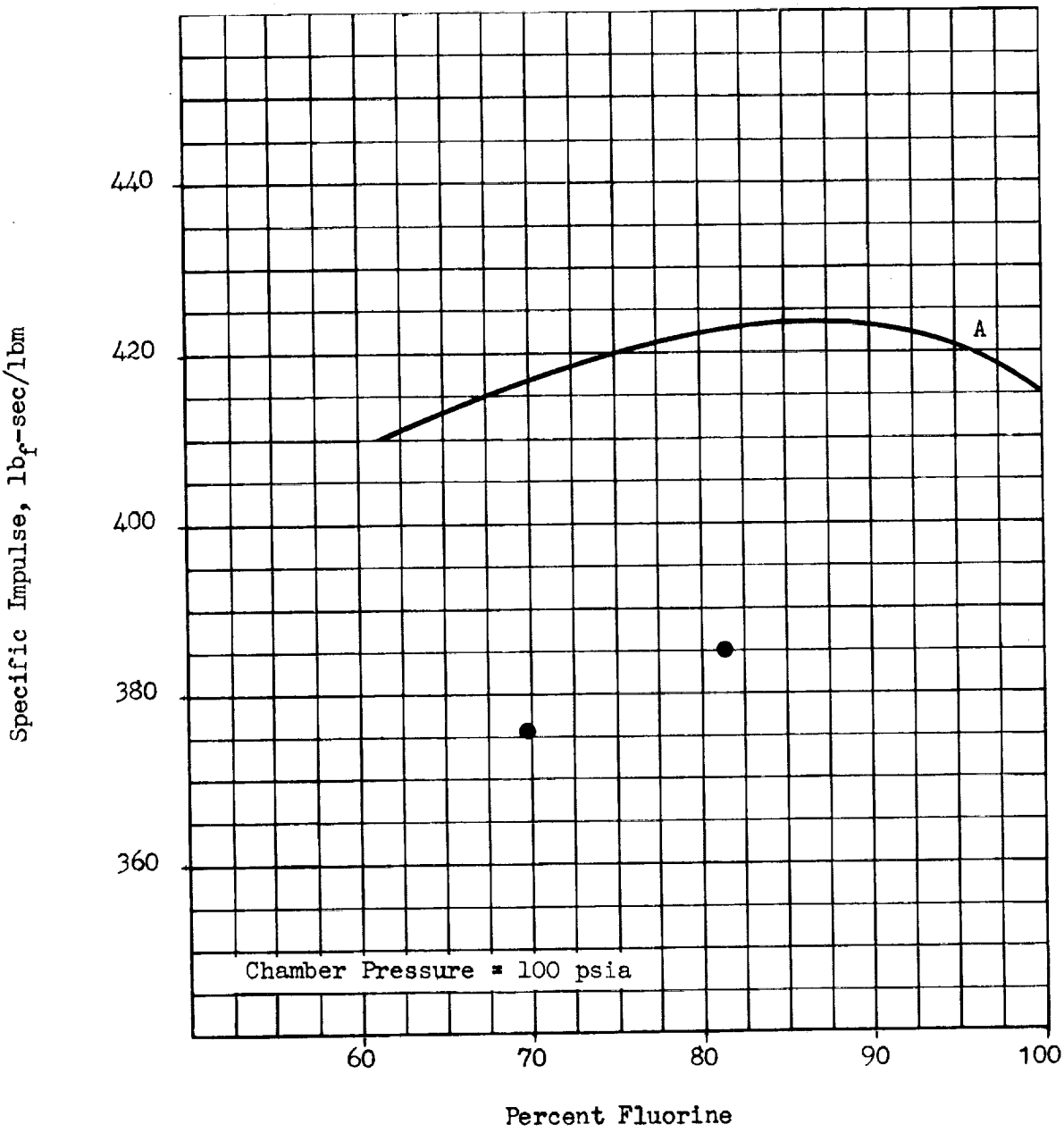

Figure 4. Specific Impulse as a Function of Fluorine Concentration for F_2-O_2/CH_4 at a Mixture Ratio of 5 for the 15-degree Cone.

The results are shown in Fig. 5. The performance difference, approximately 7 lbf-sec/lbm, was in agreement with the value predicted using the Ref. 1 heat of formation. The difference decreased with increasing mixture ratio, as expected.

INJECTOR PERFORMANCE

The injector efficiencies (defined in Section V) measured in the F_2-O_2 (82.5-17.5)/CH_4 tests are shown in Fig. 6. The results were reproducible between the test series and the efficiency was consistently above 97 percent. A comparison between the injector efficiency calculated from a static pressure measurement corrected to stagnation and the injector efficiency implied from low area ratio specific impulse is shown in Fig. 7. These tests were conducted at altitude to match exactly the high area ratio conditions and to give an accurate thrust measurement. The agreement between the two methods was excellent, giving added confidence to the division of efficiencies between injector and nozzle computed for the high area ratio tests. The fact that the data follow a 45-degree line indicates that the injector and thrust chamber losses can be treated independently. The injector efficiencies for F_2-O_2(70-30)/CH_4 and OF_2/CH_4 are shown in Fig. 8 and are generally above 99 percent, considerably higher than observed with F_2-O_2(82.5-17.5). This difference in efficiency is discussed in more detail in Section IV.

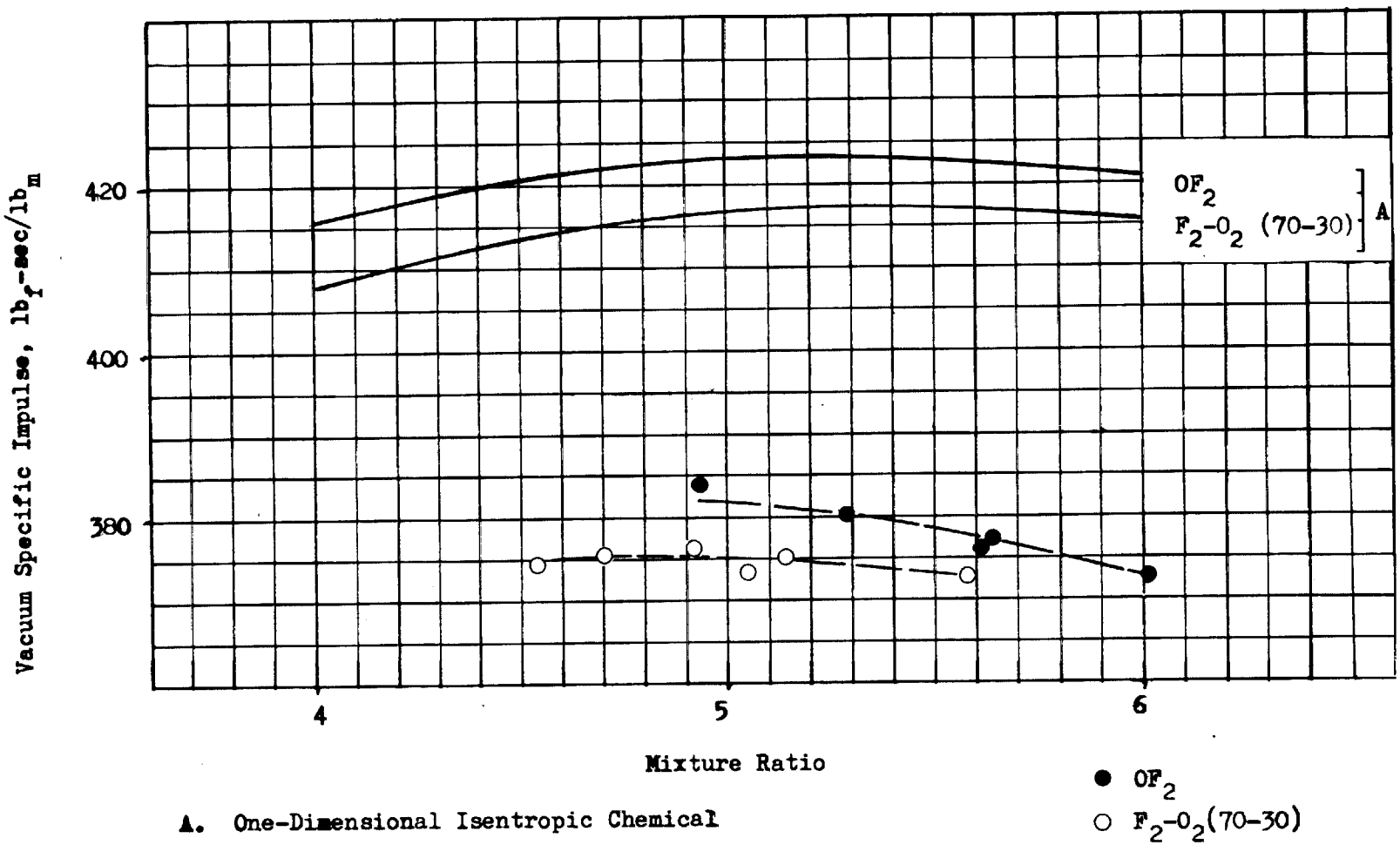

A. One-Dimensional Isentropic Chemical Equilibrium Expansion Performance.

Figure 5. Delivered Vacuum Specific Impulse for CH_4 with OF_2 and F_2-O_2(70-30) at a Chamber Pressure of 100 psia for the 15-degree Cone.

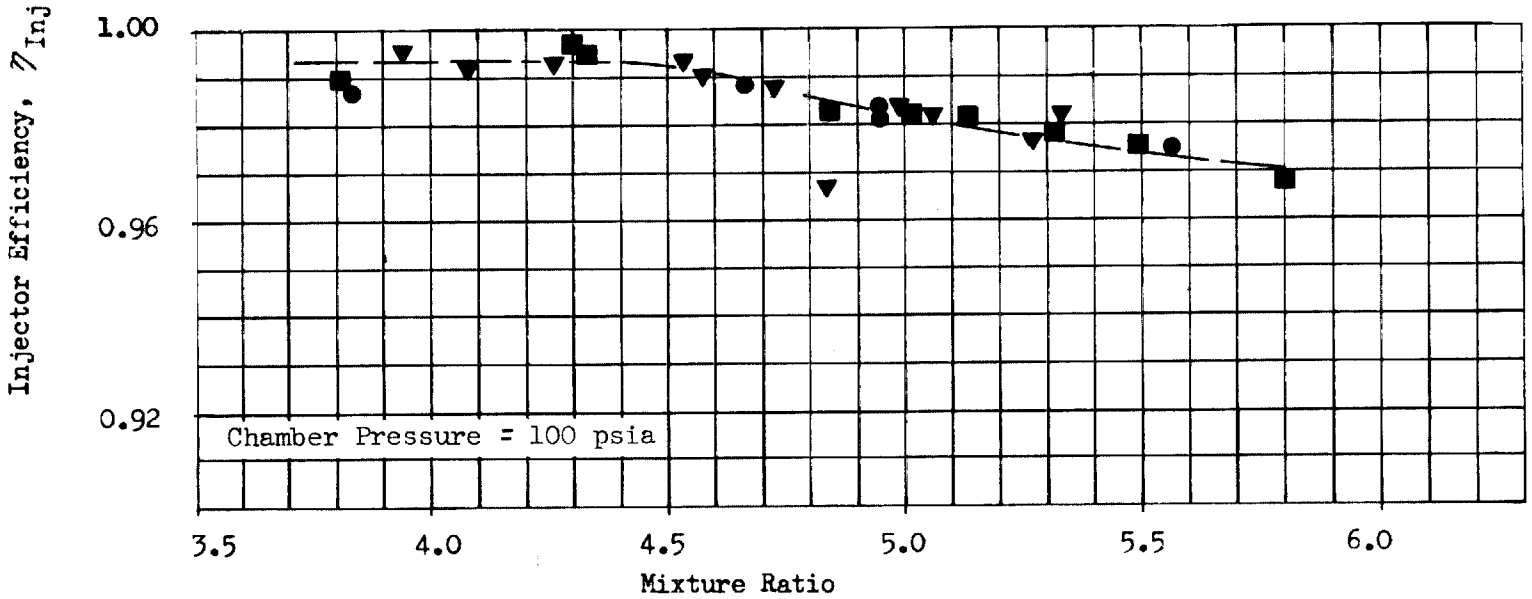

Figure 6. Injector Efficiency as a Function of Mixture Ratio for F_2-O_2(82.5-17.5)/CH_4

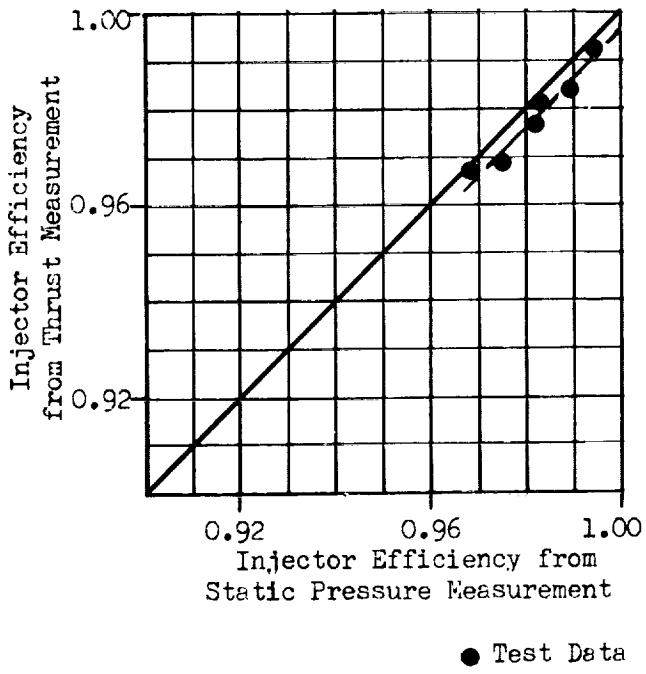

Fig. 7. Comparison of Injector Efficiency Calculated from Static Pressure with Injector Efficiency Calculated from Thrust for F_2-O_2 (82.5-17.5)/CH_4

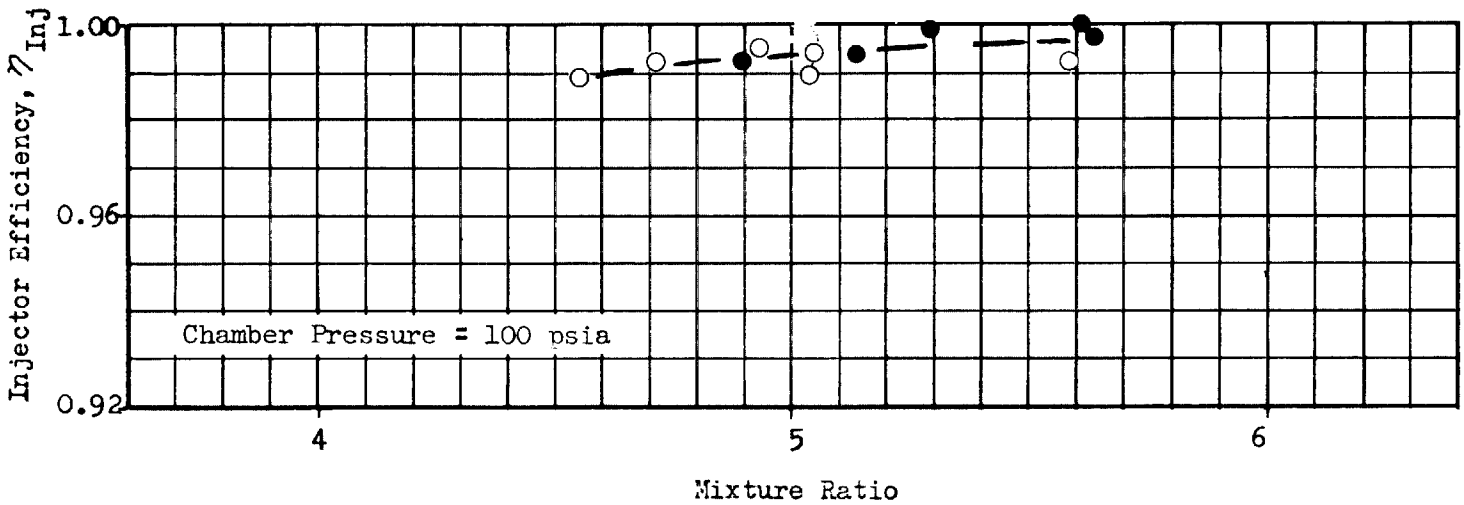

Figure 8 . Injector Efficiency as a Function of Mixture Ratio for OF_2/CH_4 & F_2-O_2(70-30)/CH_4

THRUST CHAMBER PERFORMANCE

Because of the wide range of propellants, chamber pressures and mixture ratios tested during the course of the program the injector could not be optimum for all conditions. However, by the use of gaseous fuel injection and a combustion chamber L* of 30, the injector efficiency for all the propellants was quite high. However, some of the trends of measured specific impulse are masked by the variation in injector efficiency that would probably not be present for point optimized injectors.

To determine the trends in performance caused by the thrust chamber, the specific impulse was normalized to one value of injector efficiency, 98-percent, which seemed to be a realistically achievable minimum efficiency for an optimized injector with uniform mixture ratio.

The normalized specific impulse for F_2-O_2(82.5-17.5)/CH_4 is shown in Fig. 9 and 10 as a function of mixture ratio for the 15-degree cone and the 70-percent bell. The predicted performance was calculated using the methods described in Section V. The difference between predicted and measured performance is discussed in Section IV. On a normalized basis, the specific impulse peaks between 5 and 5.2 mixture ratios. The peak specific impulse was 385 lbf-sec/lbm for the cone and 384 lbf-sec/lbm for the bell.

The normalized specific impulse for F_2-O_2(70-30)/CH_4 and OF_2/CH_4 is presented in Fig. 11 and 12 for the 15-degree cone. The difference in performance between OF_2 and F_2-O_2(70-30) was again consistent with the new NBS heat of formation. Also of interest is the variation of normalized specific impulse with F_2 concentration. On a normalized basis the difference between F_2-O_2(82.5-17.5) and F_2-O_2(70-30) was 14 lbf-sec/lbm, Fig. 13.

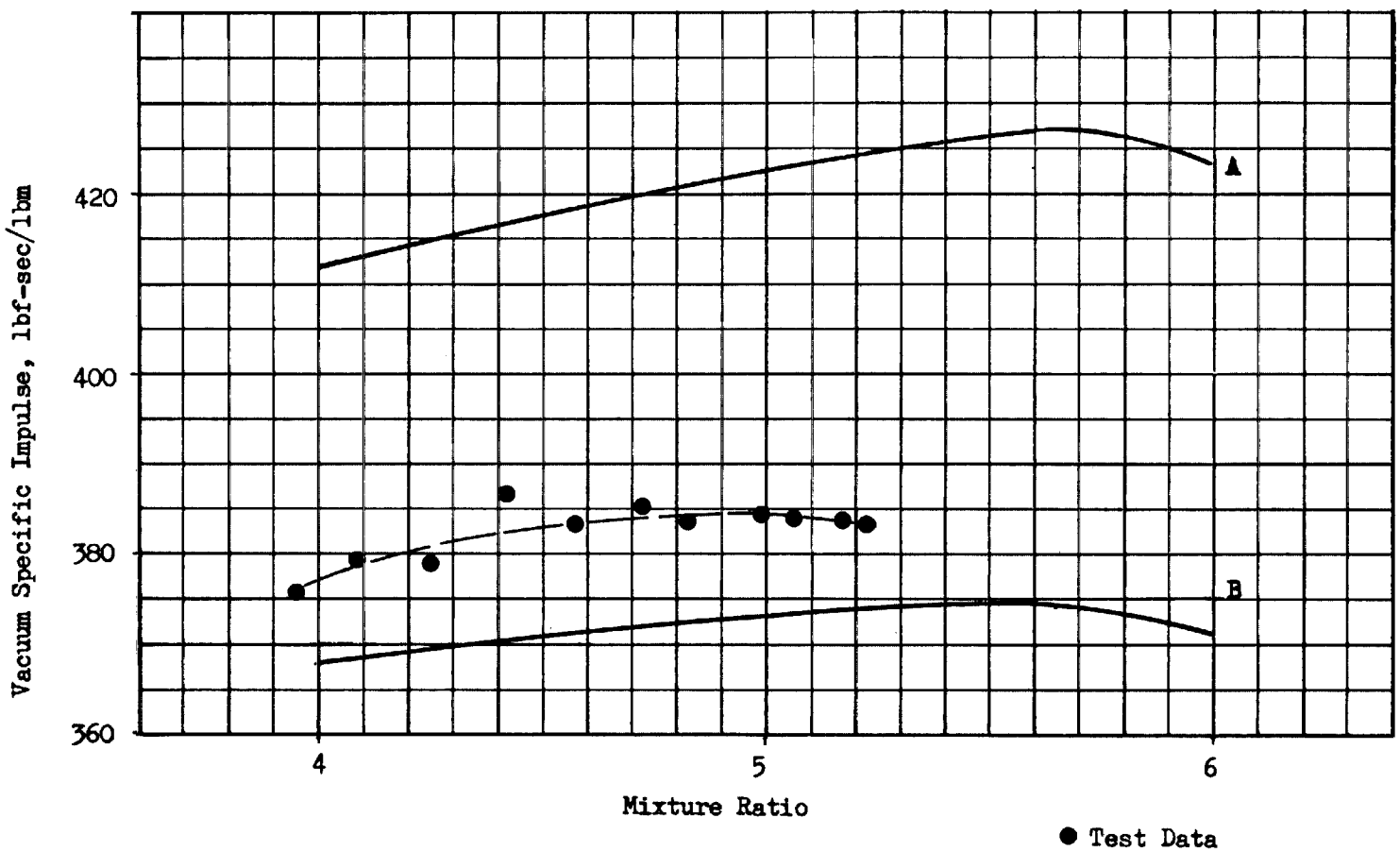

A. One-Dimensional Isentropic Chemical Equilibrium Expansion Performance.

B. Predicted Performance ($\eta_{Inj} = 0.98$)

Note: All Test Data Adjusted to 98-percent Injector Efficiency.

Figure 9. Adjusted Vacuum Specific Impulse for F_2-O_2(82.5-17.5)/CH_4 at a Chamber Pressure of 100 psia for the 15-degree Cone

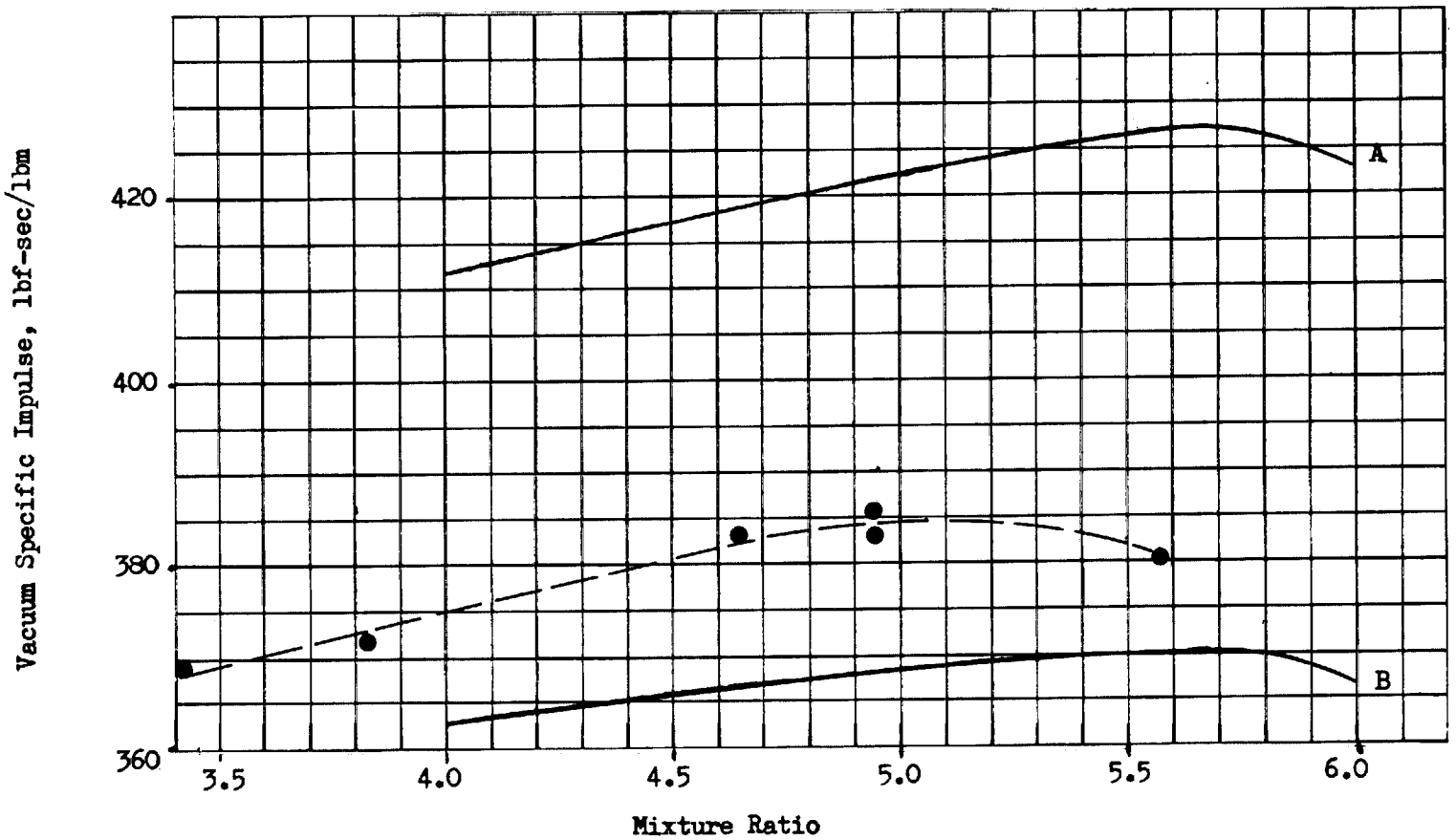

A. One-Dimensional Isentropic Chemical Equilibrium Expansion Performance.

B. Predicted Performance ($\eta_{Inj} = 0.98$).

Note: All Data Ajusted to 98-percent Injector Efficiency.

Figure 10. Adjusted Vacuum Specific Impulse for F_2-O_2(82.5-17.5)/CH_4 at a Chamber Pressure of 100 psia for the 70-percent Bell.

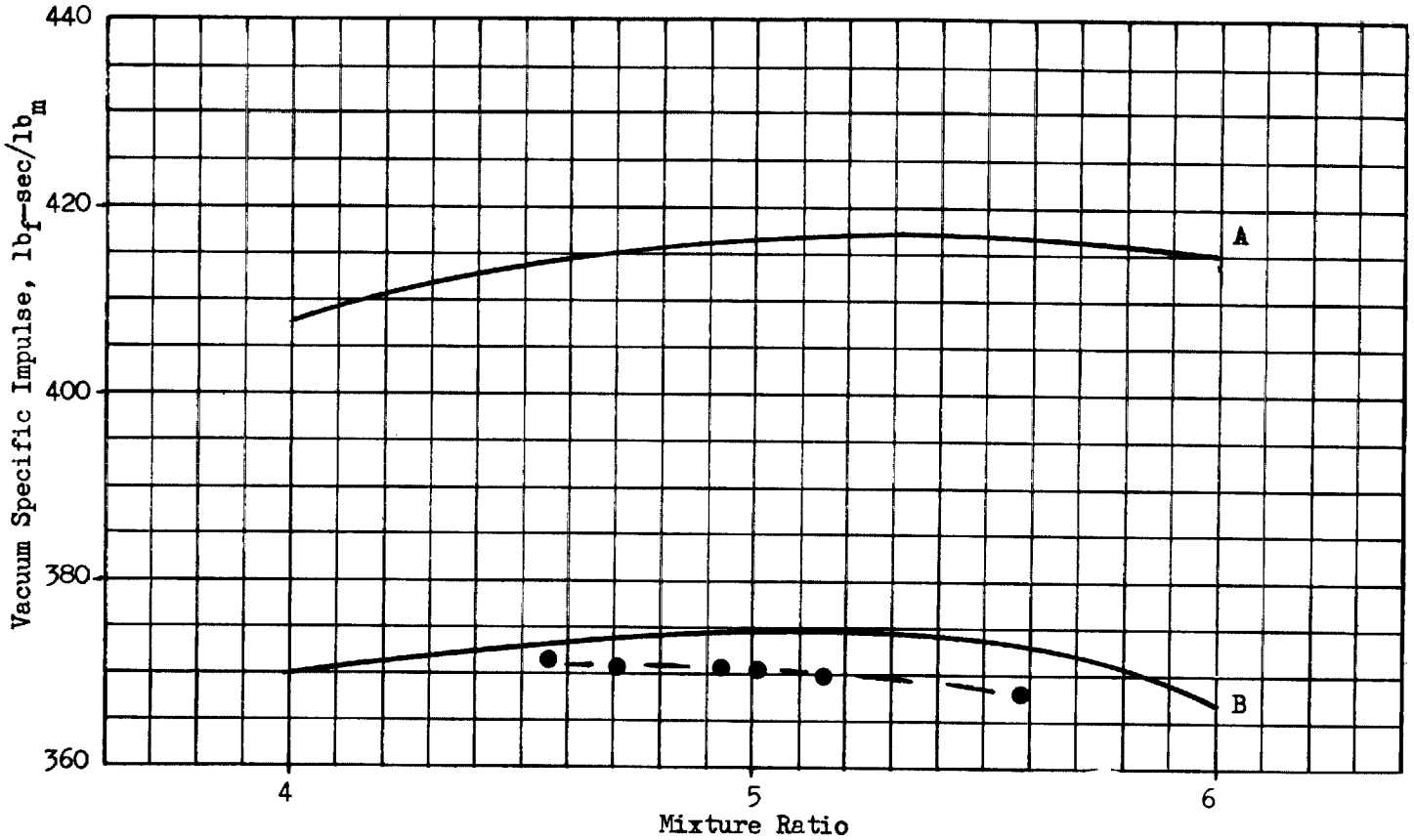

A. One-dimensional isentripic chemical equilibrium composition expansion performance.
B. Predicted performance ($\eta_{inj.} = 0.98$)

● Test Data

NOTE: All data adjusted to 98 percent injector efficiency

Fig. 11. Adjusted Vacuum Specific Impulse for F_2-O_2(70-30)/CH_4(Gas) at a Chamber Pressure of 100 psia for the 15-degree Cone

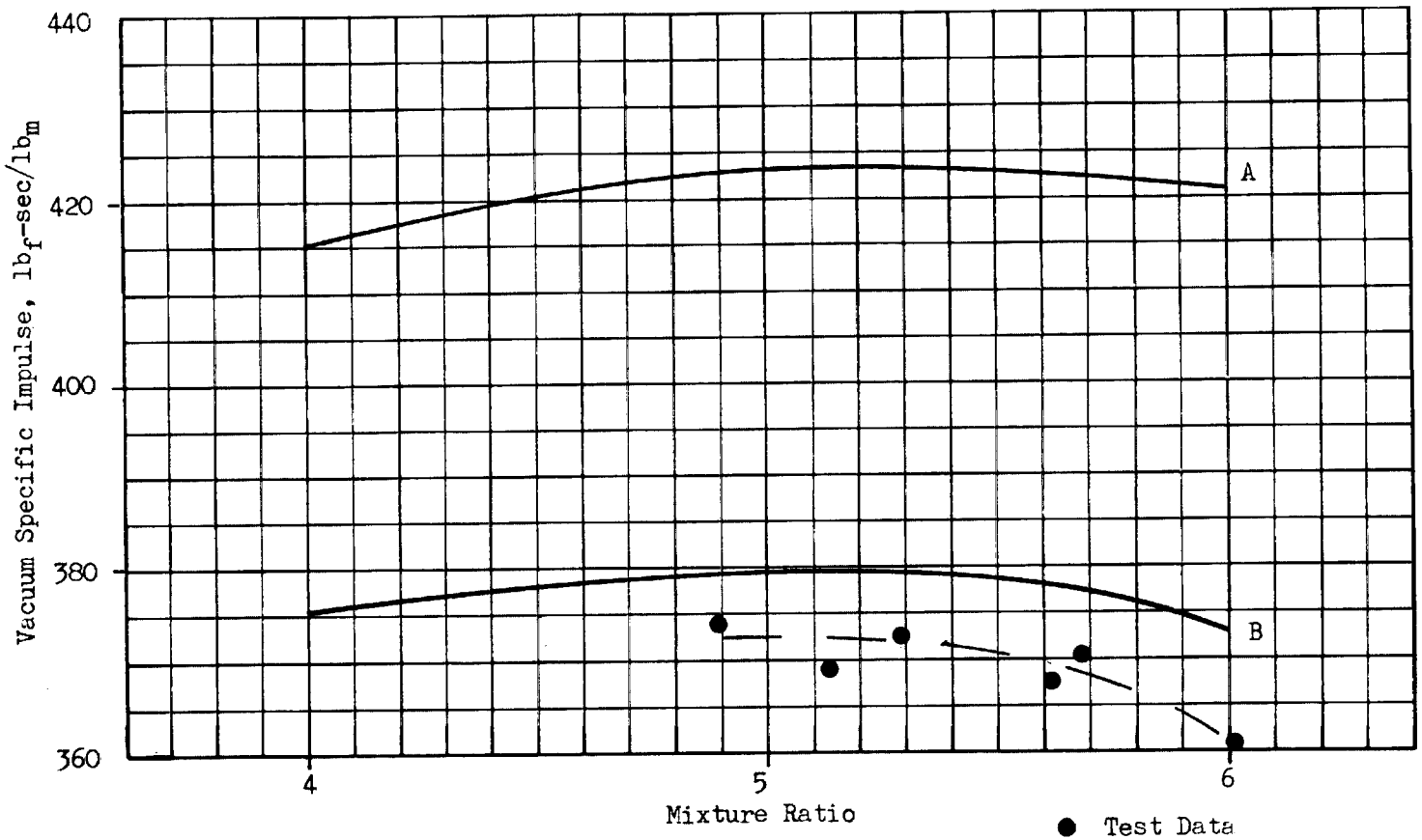

A. One-dimensional isentropic chemical equilibrium composition expansion performance
B. Predicted performance ($\eta_{inj.} = 0.98$)

Note: All data adjusted to 98-percent injector efficiency

Fig. 12. Adjusted Vacuum Specific Impulse for OF_2/CH_4 (Gas at a Chamber Pressure of 100 psia for the 15-degree Cone.

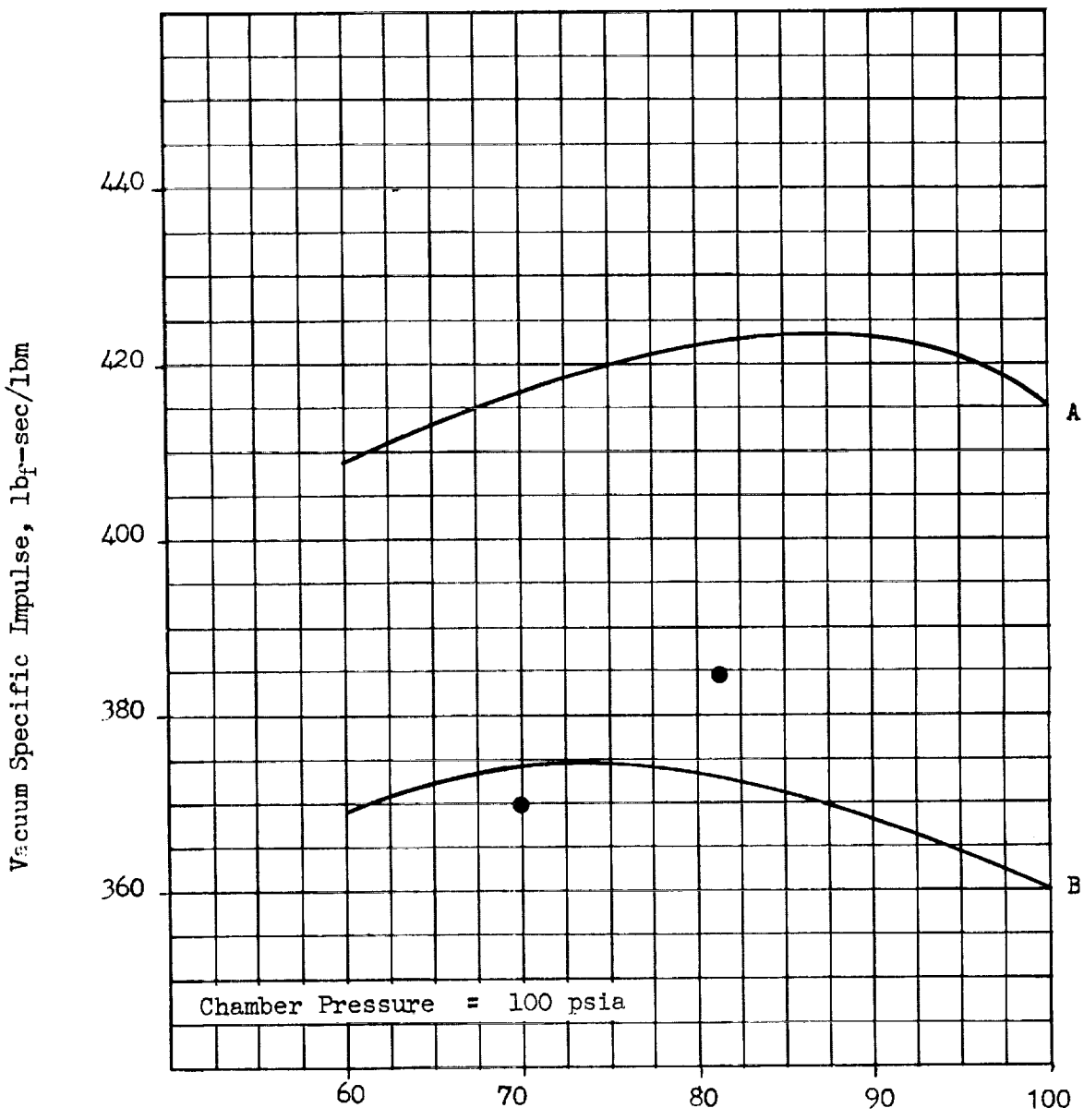

A. One-dimensional Isentropic Chemical Equilibrium Expansion Performance.
B. Predicted Performance. ($\eta_{Inj} = 0.98$)

Figure 13. Effect of Fluorine Concentration on F_2-O_2/CH_4 Specific Impulse at a Mixture Ratio of 5 with Injector Efficiency Normalized to 98-percent.

compared to 10 lbf-sec/lbm for the measured values, indicating that the change in nozzle performance with F_2 concentration was very rapid.

HEAT TRANSFER

In the combustion chamber, the heat transfer rates were comparable to those for F_2/H_2. These chamber heat transfer coefficients (Fig. 14) were considerably higher than predicted by any standard boundary layer theory. The most likely explanation is that the turbulence in the chamber near the walls is so high that a continuous boundary layer did not form. The diborane tests also tend to support this explanation.

In the expansion nozzle, the heat flux values for F_2-O_2/CH_4 were again similar to those for F_2/H_2 and can be predicted using a boundary layer starting in the contraction region (Fig. 15 and 16).

HARDWARE CONDITION

Following the F_2-O_2(82.5-17.5)/CH_4 tests, the hardware had a sooty residue. The injector orifices were clear but the rest of the injector had a definite film. Following the F_2/O_2(70-30)/CH_4 tests, the hardware was clean.

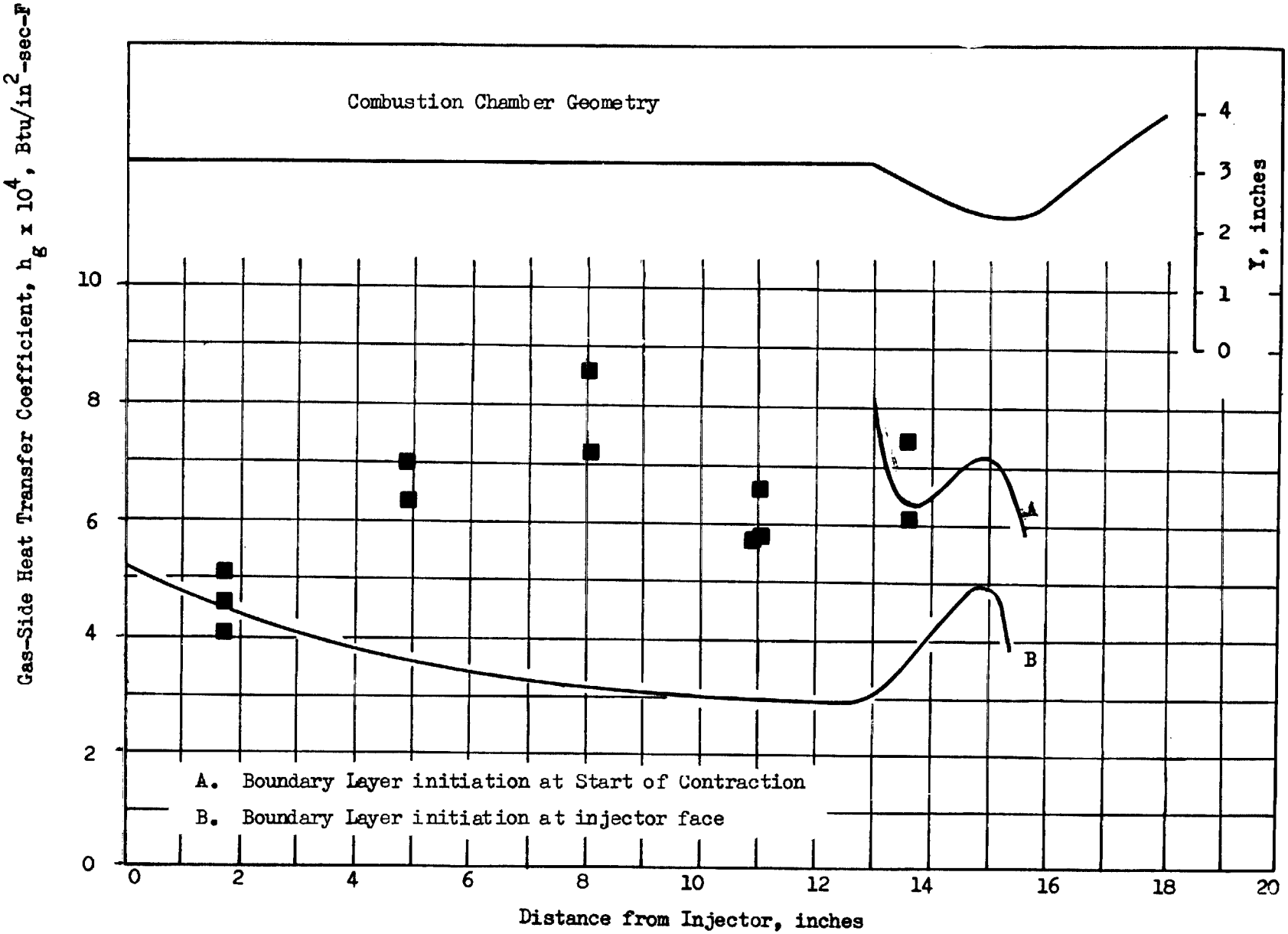

Figure 14. Combustion Chamber Heat Transfer Coefficients for F_2-O_2/CH_4 at a Chamber Pressure of 100 psia

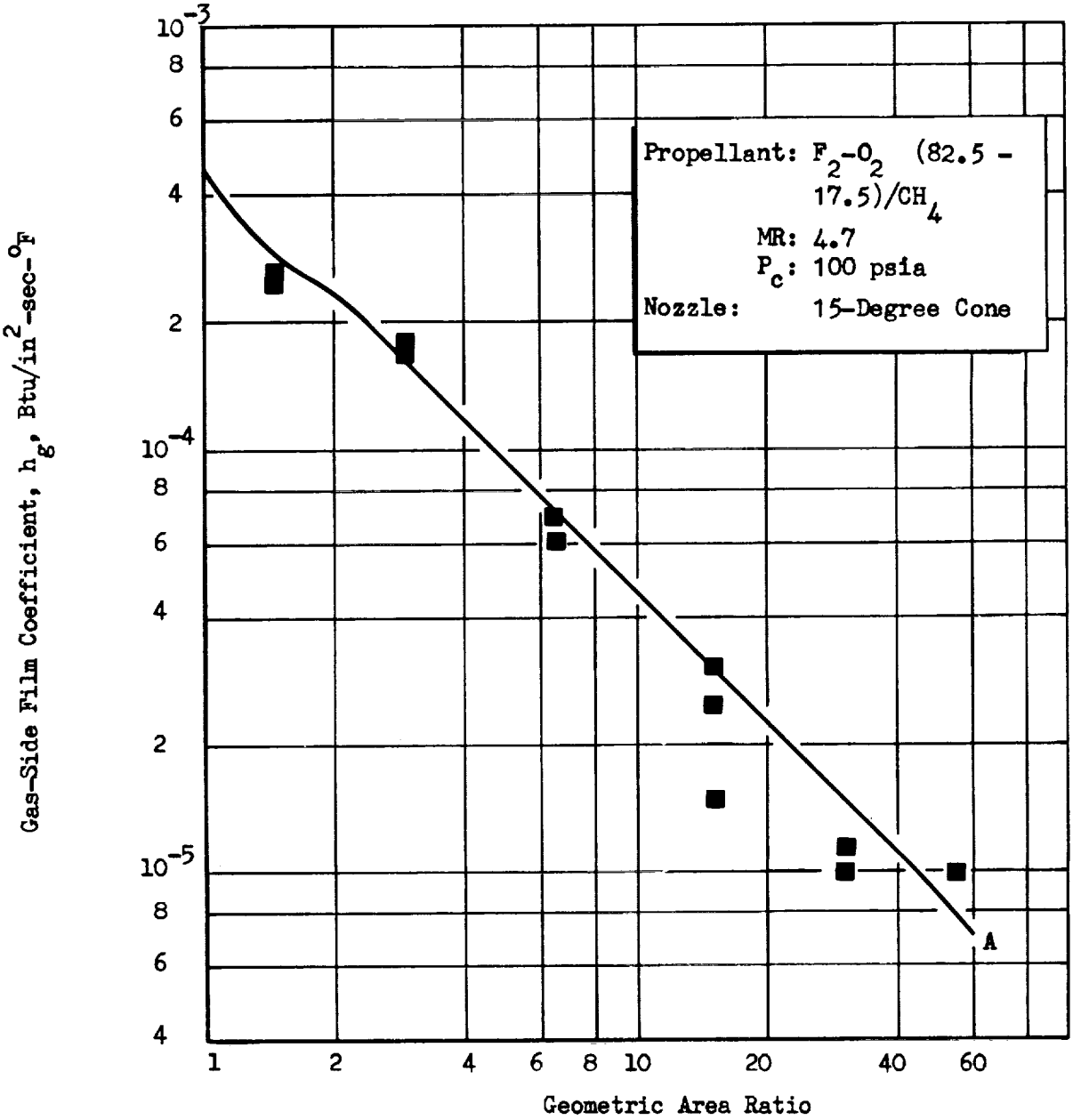

A. Predicted Value ■ Test Data

Figure 15. Nozzle Heat Transfer Coefficients for the 15-degree Cone with F_2-O_2(82.5-17.5)/CH_4 at a Chamber Pressure of 100 psia.

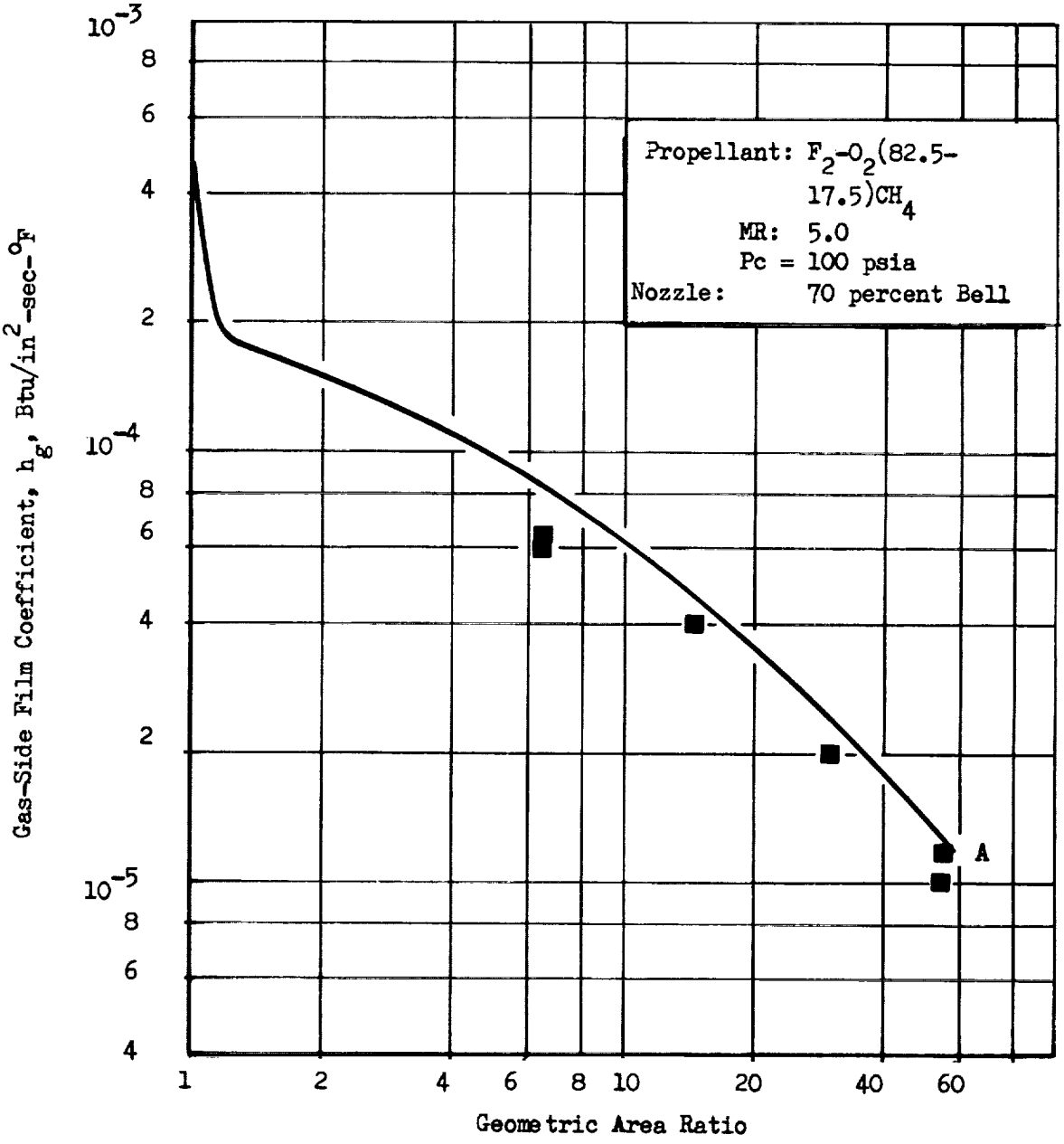

A. Predicted Value ■ Test Data

Figure 16. Nozzle Heat Transfer Coefficients for the 70 Percent Bell Nozzle with F_2-O_2(82.5-17.5)/CH_4 at a Chamber Pressure of 100 psia.

SECTION II

DIBORANE TEST RESULTS

The diborane test program was designed to determine the deliverable performance of the OF_2/B_2H_6 propellant combination and to give additional verification of the relative performance of OF_2 and F_2-O_2(70-30). A total of 48 diborane tests including six injector verification tests was conducted to achieve the desired results. The high area ratio tests included OF_2/B_2H_6 with both nozzles, F_2-O_2(70-30)/B_2H_6 with the bell nozzle at 100 psia and with the cone at 55 psia. Summarized in this section are the delivered specific impulse measurements, injector performance, heat transfer and hardware condition.

The maximum performance levels obtained with diborane were 412 lbf-sec/lbm for OF_2 and 407 lbf-sec/lbm for F_2-O_2(70-30). The injector efficiency was above 97 percent at all mixture ratios. The measured difference between OF_2 and F_2-O_2(70-30) provided added confirmation of the difference between the OF_2 and F_2-O_2(70-30) heats of formation.

The measured heat transfer levels were significantly higher than those for F_2-O_2/CH_4 or F_2/H_2. A thin flaky deposit was left on the thrust chamber walls but the injector remained clean.

HIGH AREA RATIO MEASURED SPECIFIC IMPULSE

The specific impulse measured for the bell and cone with OF_2/B_2H_6 is shown in Fig. 17. The relative insensitivity to nozzle contour was similar to the F_2-O_2/CH_4 results. The peak performance of 412 lbf-sec/lbm occurred at a mixture ratio of 4 but was nearly constant over the range from 3.5 to 4.5

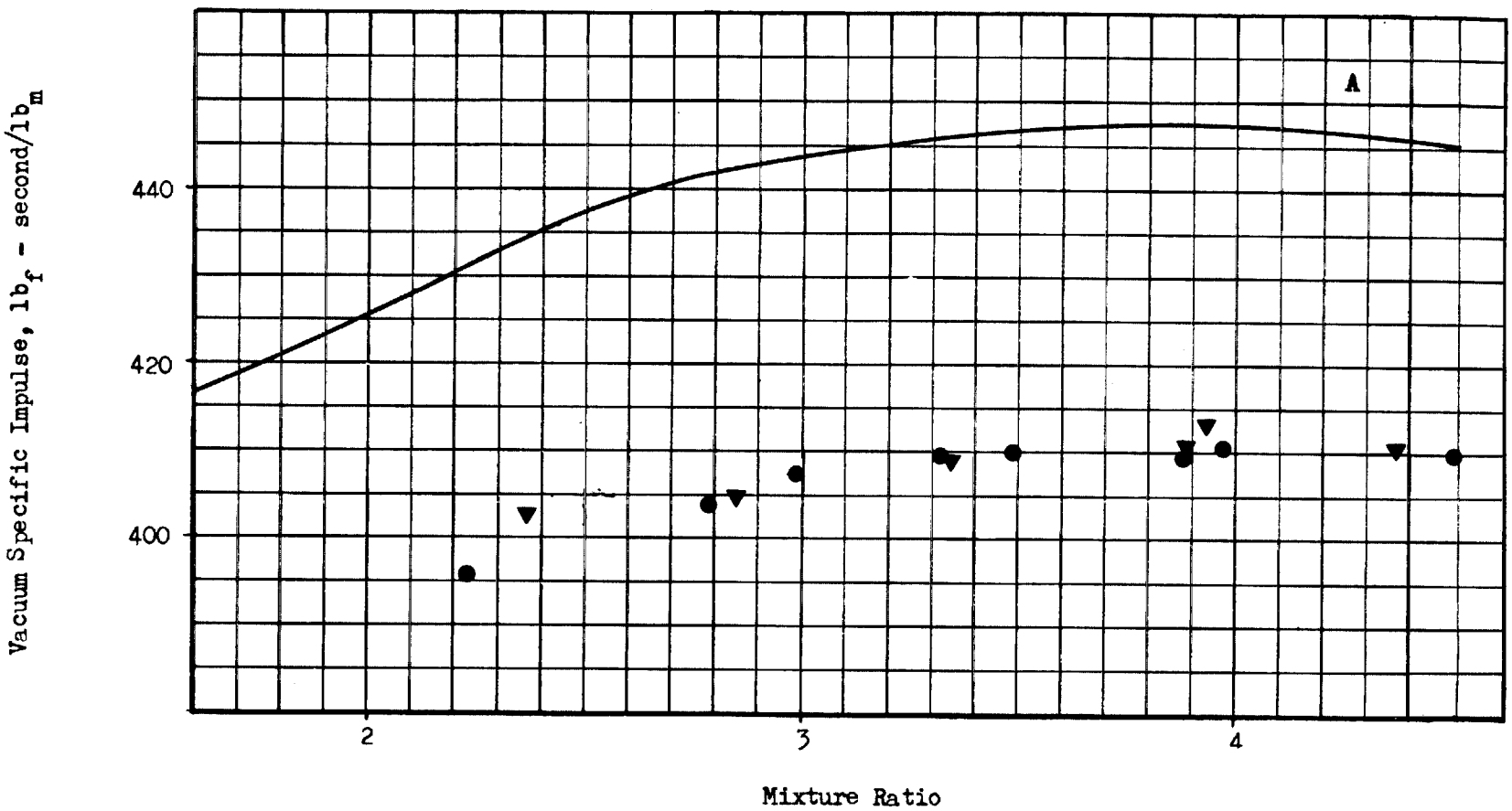

A. One Dimensional Isentropic Chemical Equilibrium Composition Expansion Performance.

Figure 17. Delivered Vacuum Specific Impulse for OF_2/B_2H_6 for the 15-degree Cone and the 70-percent Bell at a Chamber Pressure of 100 psia.

For the bell nozzle, the performance of OF_2 is compared with F_2-O_2(70-30) in Fig. 18. A comparison of the experimental difference with the theoretical difference is also shown. It is clear that the test data support the revised heat of formation for OF_2.

The test results for F_2-O_2(70-30)/B_2H_6 in the conical nozzle are shown in Fig. 19. On these tests there was an indication of a 1-percent anomaly in the thrust measurement. Comparison of the data with the other B_2H_6 results supports this contention. Although these data are not precise enough to use for the more subtle comparisons that depend on data accurate within less than one percent, their quality is still good enough to provide further confirmation of the deliverable performance for this propellant.

One test series was conducted for F_2-O_2(70-30)/B_2H_6 with the conical nozzle at a chamber pressure of 55 psia. The specific impulse results are shown in Fig. 20 indicating a peak value of 396 lbf-sec/lbm.

INJECTOR PERFORMANCE

The injector efficiencies measured for diborane with OF_2 and with F_2-O_2(70-30) are shown in Fig. 21. The efficiencies for the two oxidizers were virtually identical as would be expected and the efficiency level was above 97 percent.

The correlation between injector efficiency calculated using static pressure and throat area and injector efficiency implied from low area ratio specific impulse is shown in Fig. 22. The flowrate measurements on this test series appear to have been about 1-percent high, reducing both types of efficiencies by the same amount but not affecting the correlation.

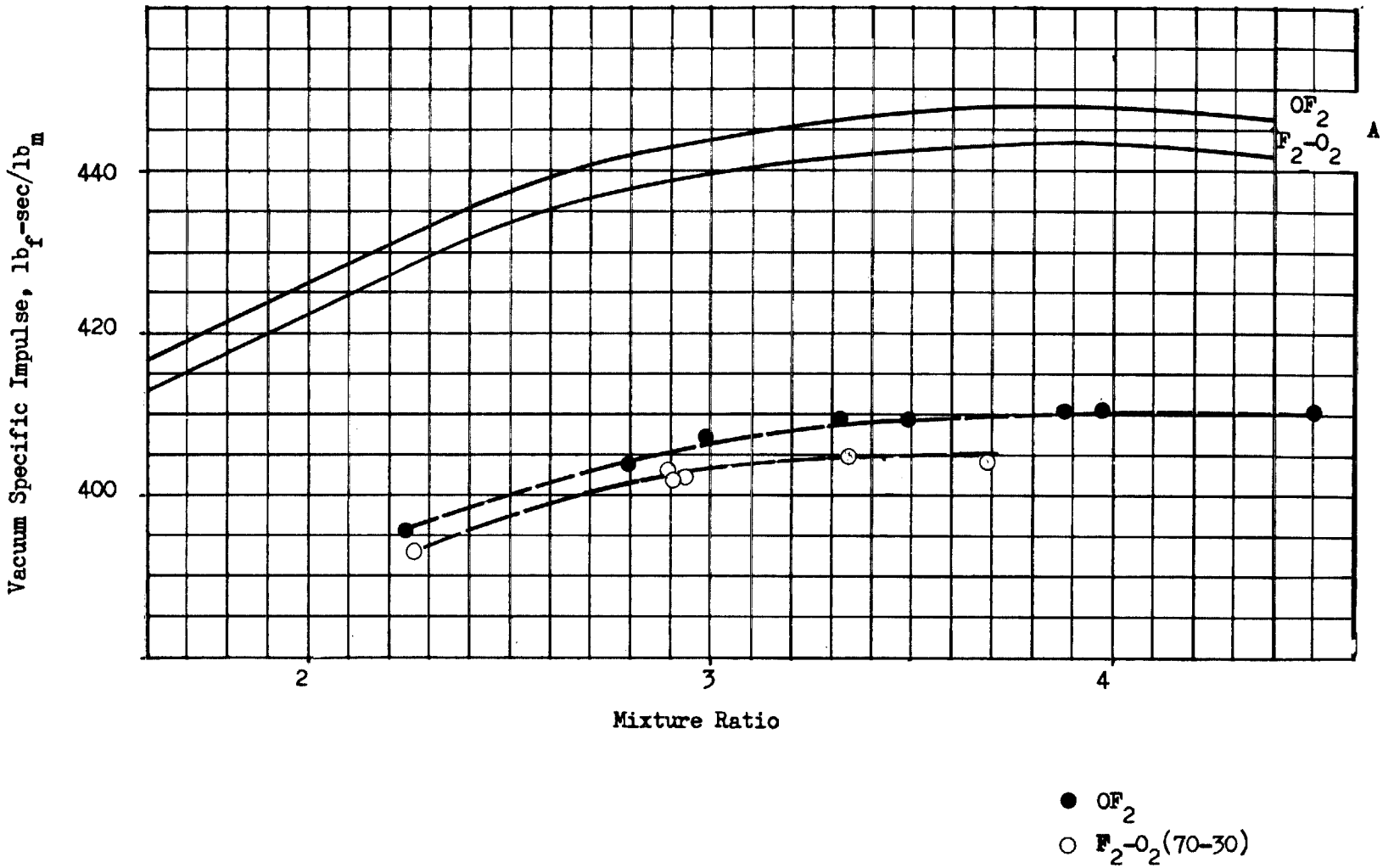

A. One-Dimensional Isentropic Chemical Equilibrium Expansion Performance.

Figure 18. Delivered Vacuum Specific Impulse for B_2H_6 with OF_2 and F_2-O_2(70-30) at a Chamber Pressure of 100 psia for the 70-percent Bell Nozzle.

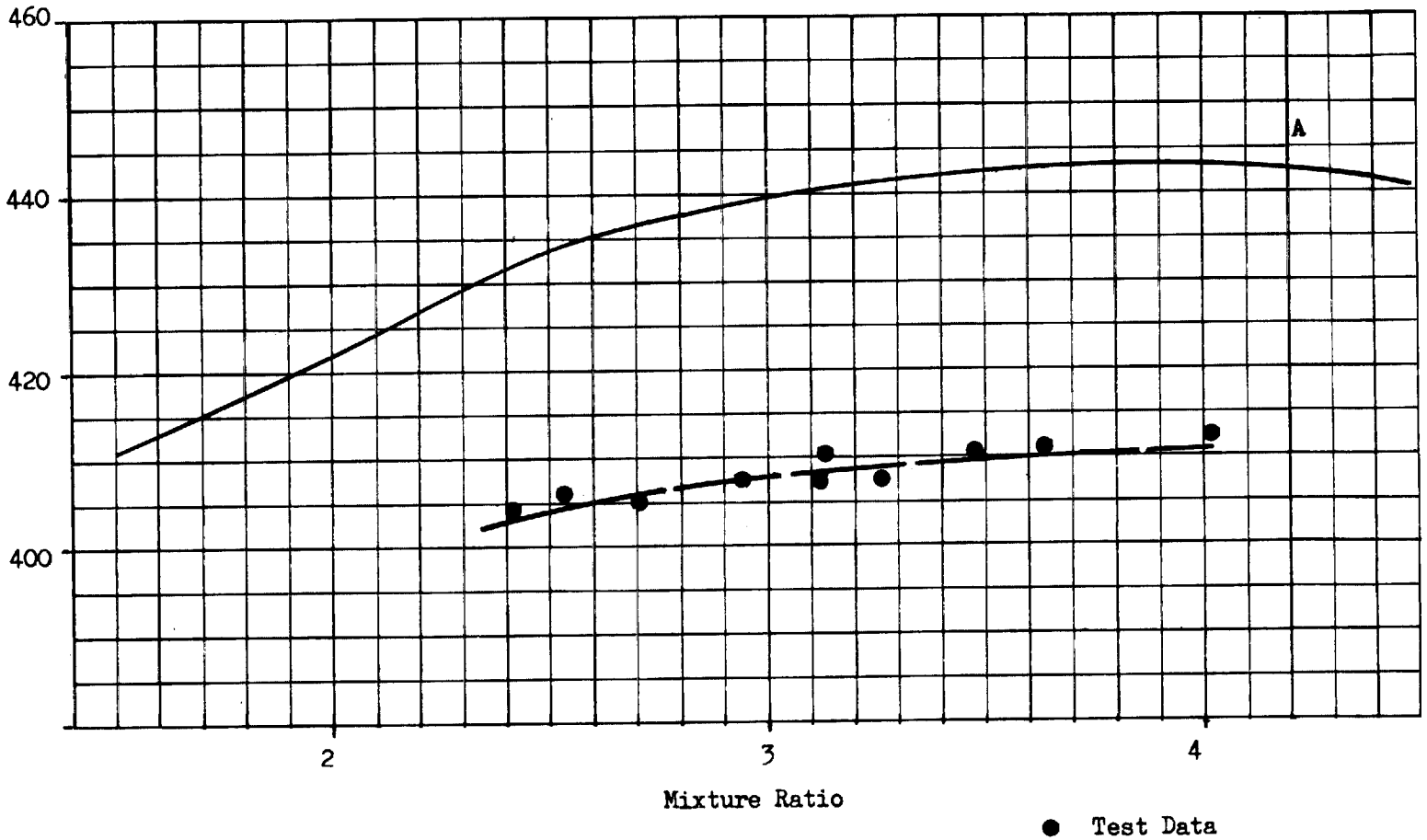

A. One-dimensional isentropic chemical equilibrium composition expansion performance.
Note: A 1-percent anomaly exists in the thrust for this data.

Figure 19. Delivered Vacuum Specific Impulse for F_2-O_2(70-30)/B_2H_6 at a Chamber Pressure of 100 psia for the 15-degree Cone.

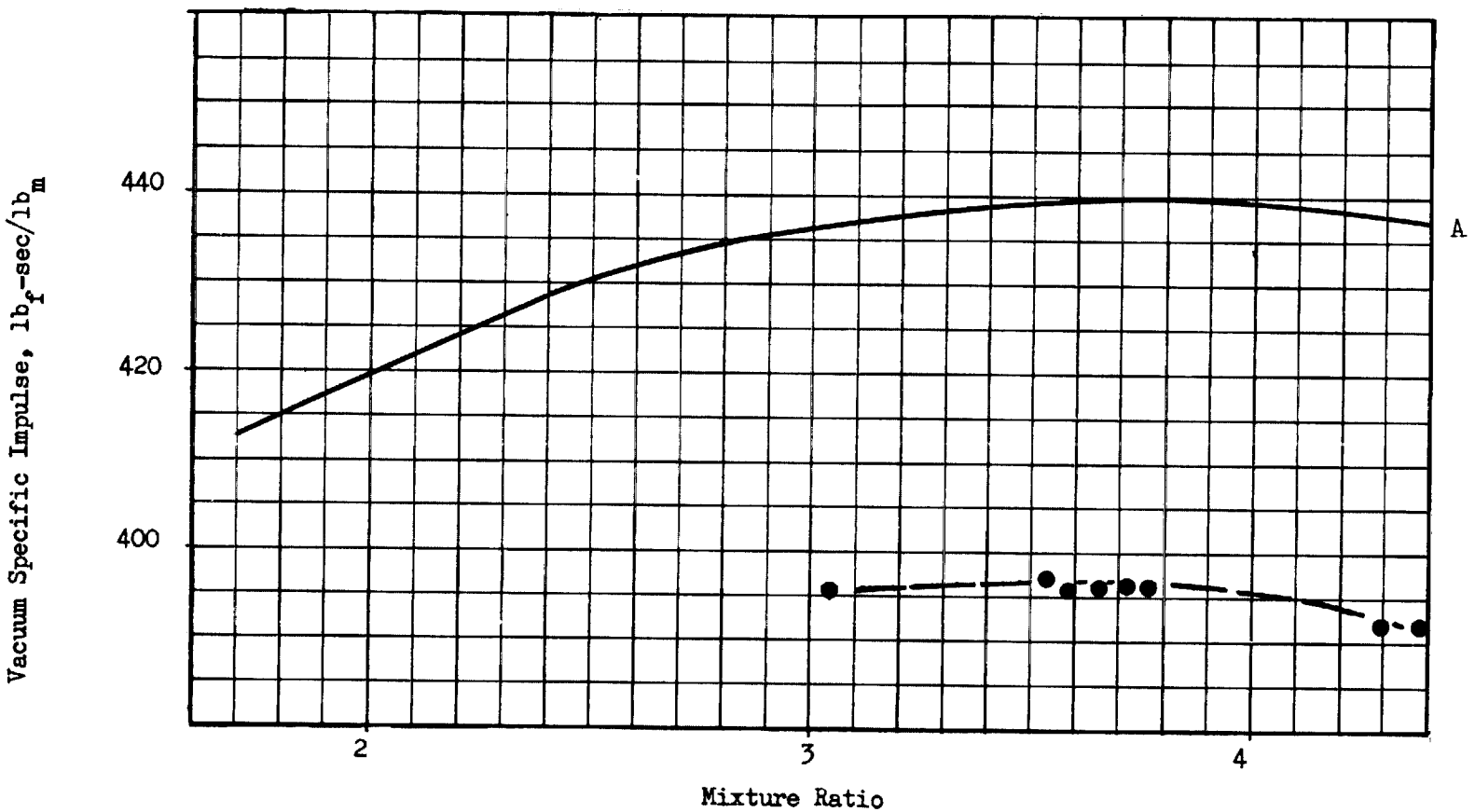

A. One Dimensional Isentropic Chemical Equilibrium Composition Expansion Performance

Figure 20. Delivered Vacuum Specific Impulse for F_2-O_2 (70-30)/B_2H_6 at a Chamber Pressure of 55 psia for the 15-degree Cone[2]

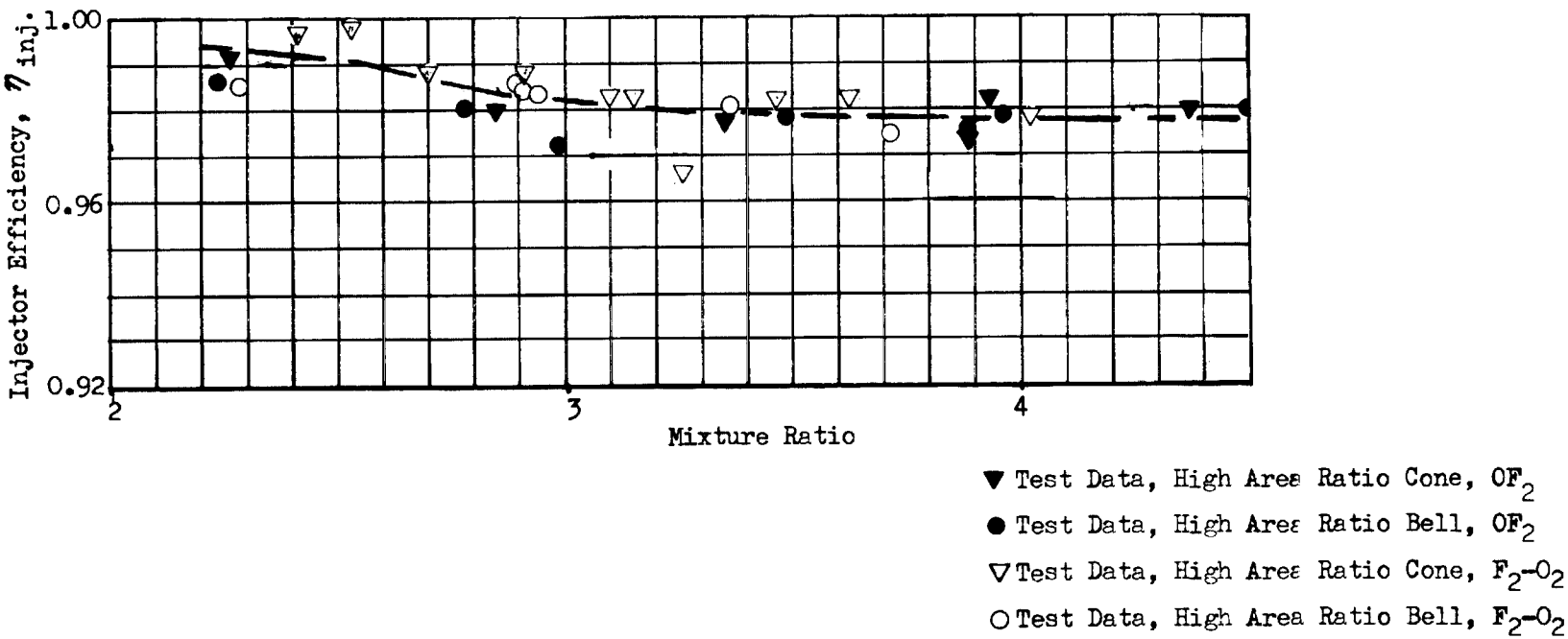

Fig. 21. Injector Efficiency as a Function of Mixture Ratio for F_2-O_2(70-30)/B_2H_6 and OF_2/B_2H_6

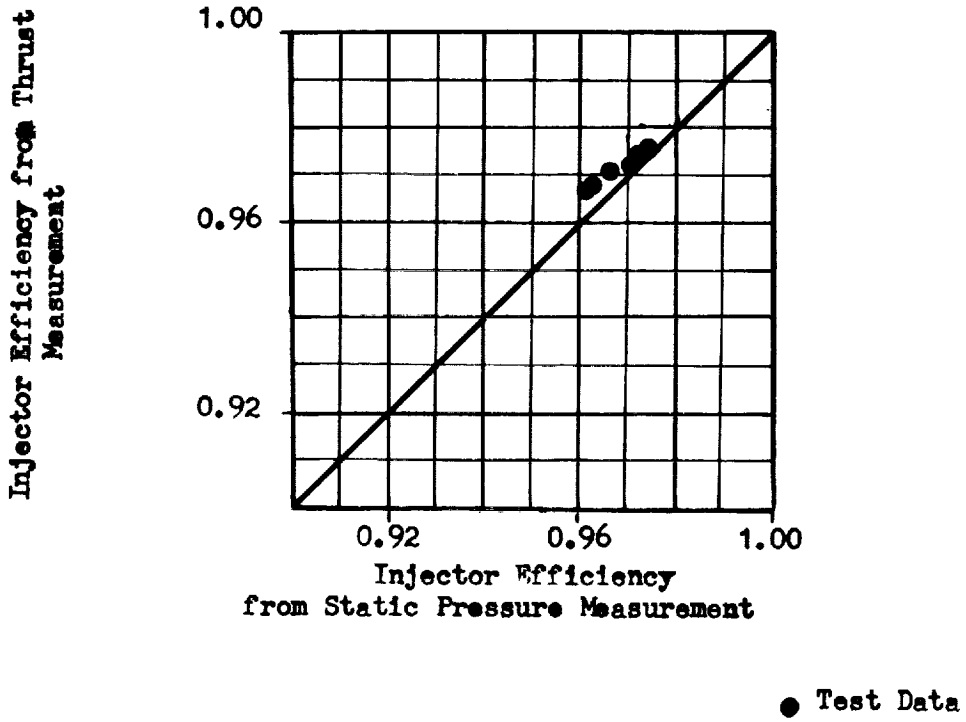

Figure 22. Comparison of Injector Efficiency Calculated from Static Pressure with Injector Efficiency Calculated from Thrust

The agreement between the two methods is good but the trend is somewhat different than for methane. Whereas the methane results showed the value determined from thrust to be slightly lower than the value from pressure, the diborane showed it higher. No explanation of this effect is available at this time.

THRUST CHAMBER PERFORMANCE

The diborane thrust chamber performance trends can most easily be examined by normalizing the performance to one value of injector efficiency. (This is the same procedure used for the methane data.) The value of 98 percent was again chosen as being a realistic injector efficiency considering the results of the tests.

The normalized specific impulse for OF_2/B_2H_6 is shown in Fig. 23 and 24 as a function of mixture ratio for the 15-degree cone and the 70-percent bell. The predicted performance was calculated using the methods described in Section V. The discrepancy between predicted and measured performance is discussed in Section IV. On a normalized basis, the specific impulse maximized near mixture ratio 4 with a maximum value of 413 lbf-sec/lbm for the cone and 412 lbf-sec/lbm for the bell.

The normalized specific impulse for F_2-O_2(70-30)/B_2H_6 is shown in Fig. 25 for the 70-percent bell nozzle. The difference between OF_2 and F_2-O_2(70-30) on a normalized basis, 7 lbf-sec/lbm, is again consistent with the new NBS heat of formation. Also of interest is the variation of performance with chamber pressure. The normalized specific impulse for the 55 psia test series is shown in Fig. 26. The data scatter is somewhat larger than for the 100 psia tests because the instruments were not operating in their optimum range. However, the scatter is still well within ± 1-percent.

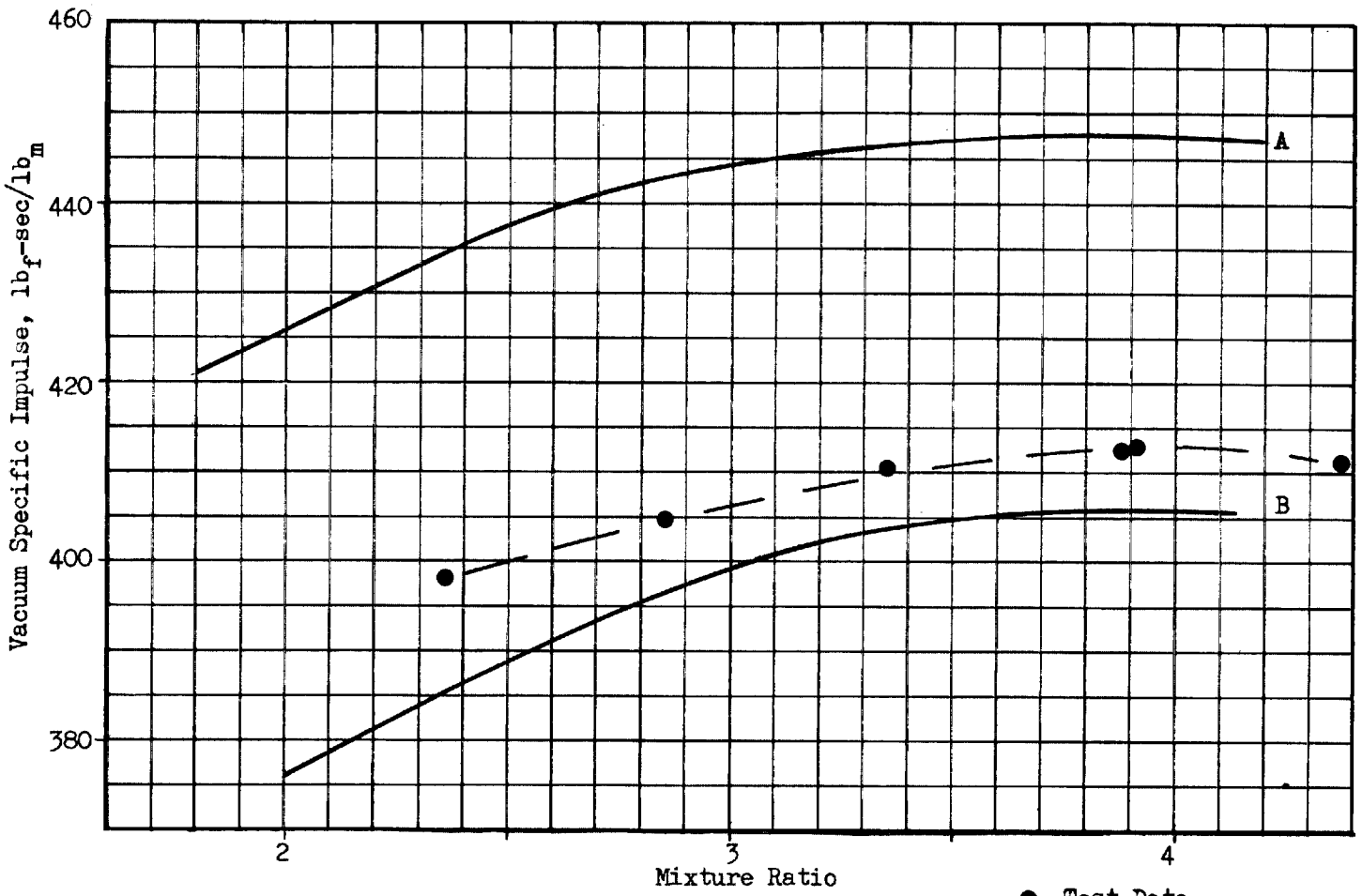

Fig. 23. Adjusted Vacuum Specific Impulse for OF_2/B_2H_6 at a Chamber Pressure of 100 psia for the 15-degree Cone.

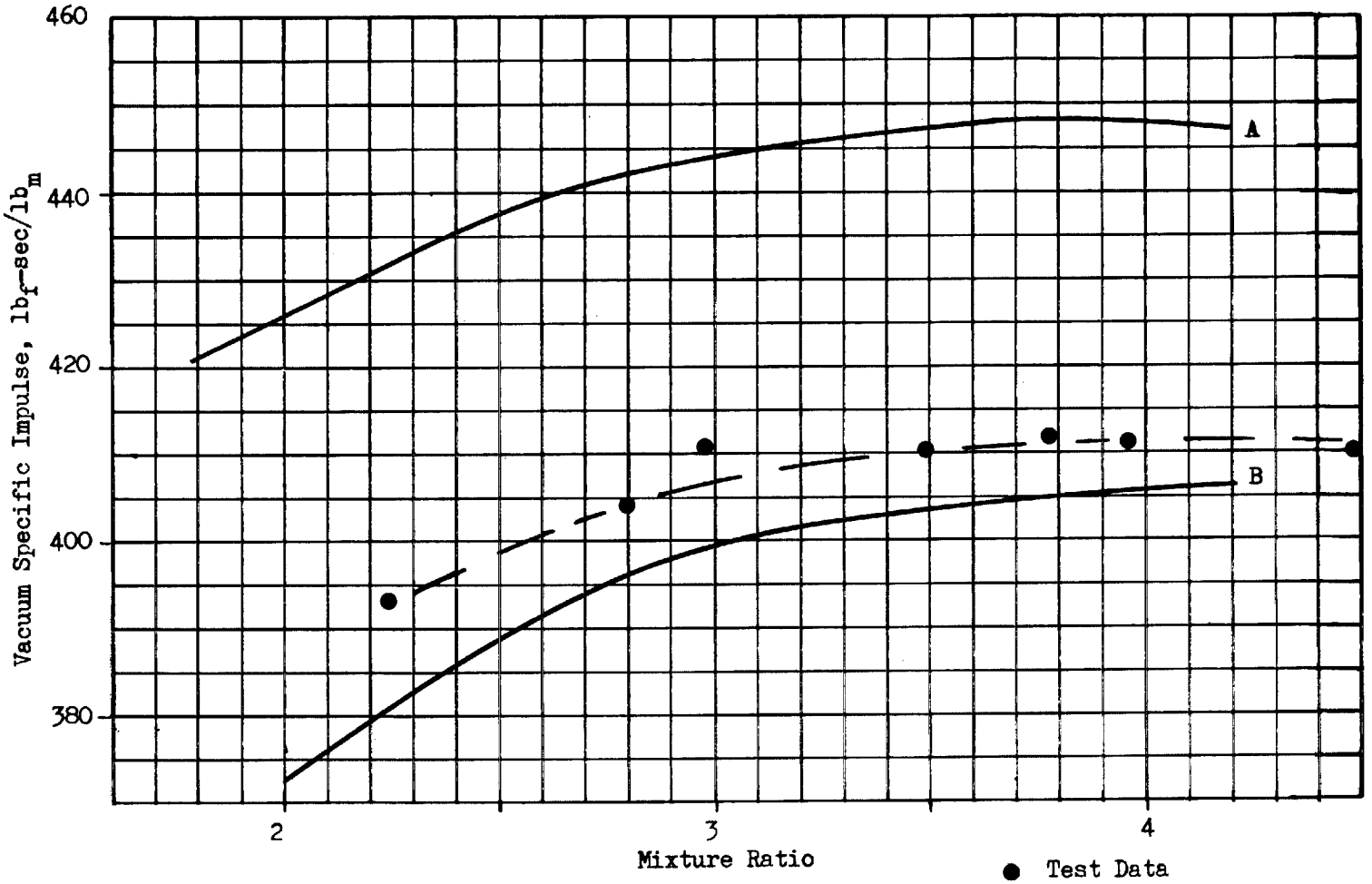

A. One-dimensional isentropic chemical equilibrium composition performance
B. Predicted performance ($\eta_{inj.} = 0.98$)

Fig. 24. Adjusted Vacuum Specific Impulse for OF_2/B_2H_6 at a Chamber Pressure of 100 psia for the 70-percent Bell

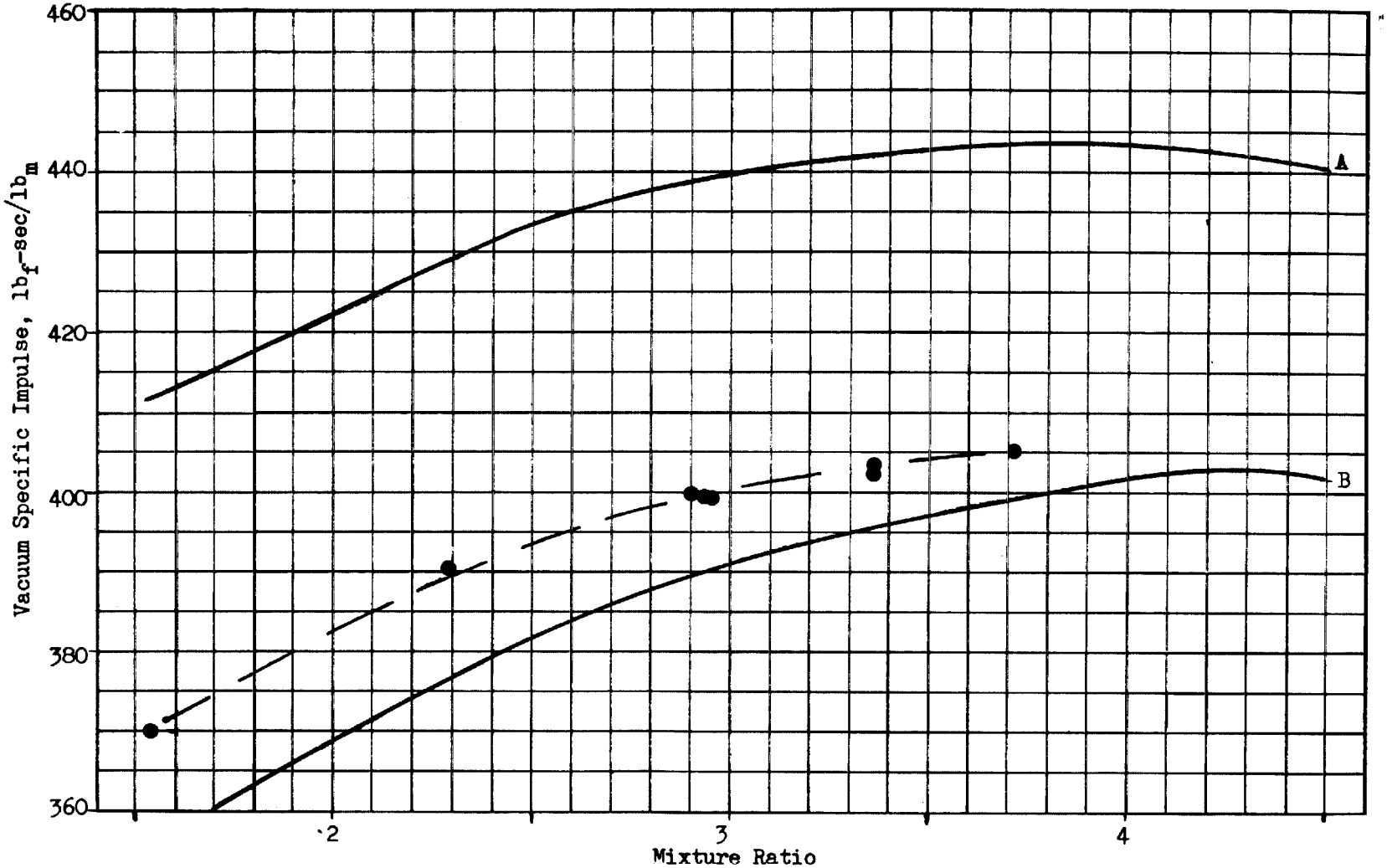

A. One-dimensional isentropic chemical equilibrium expansion performance
B. Predicted performance ($\eta_{inj.} = 0.98$)

● Test Data

NOTE: All data adjusted to 98-percent injector efficiency

Fig. 25. Adjusted Vacuum Specific Impulse Comparison Between Theory and Experiment for F_2-O_2(70-30)/B_2H_6 at a Chamber Pressure of 100 psia for the 70-percent Bell Nozzle.

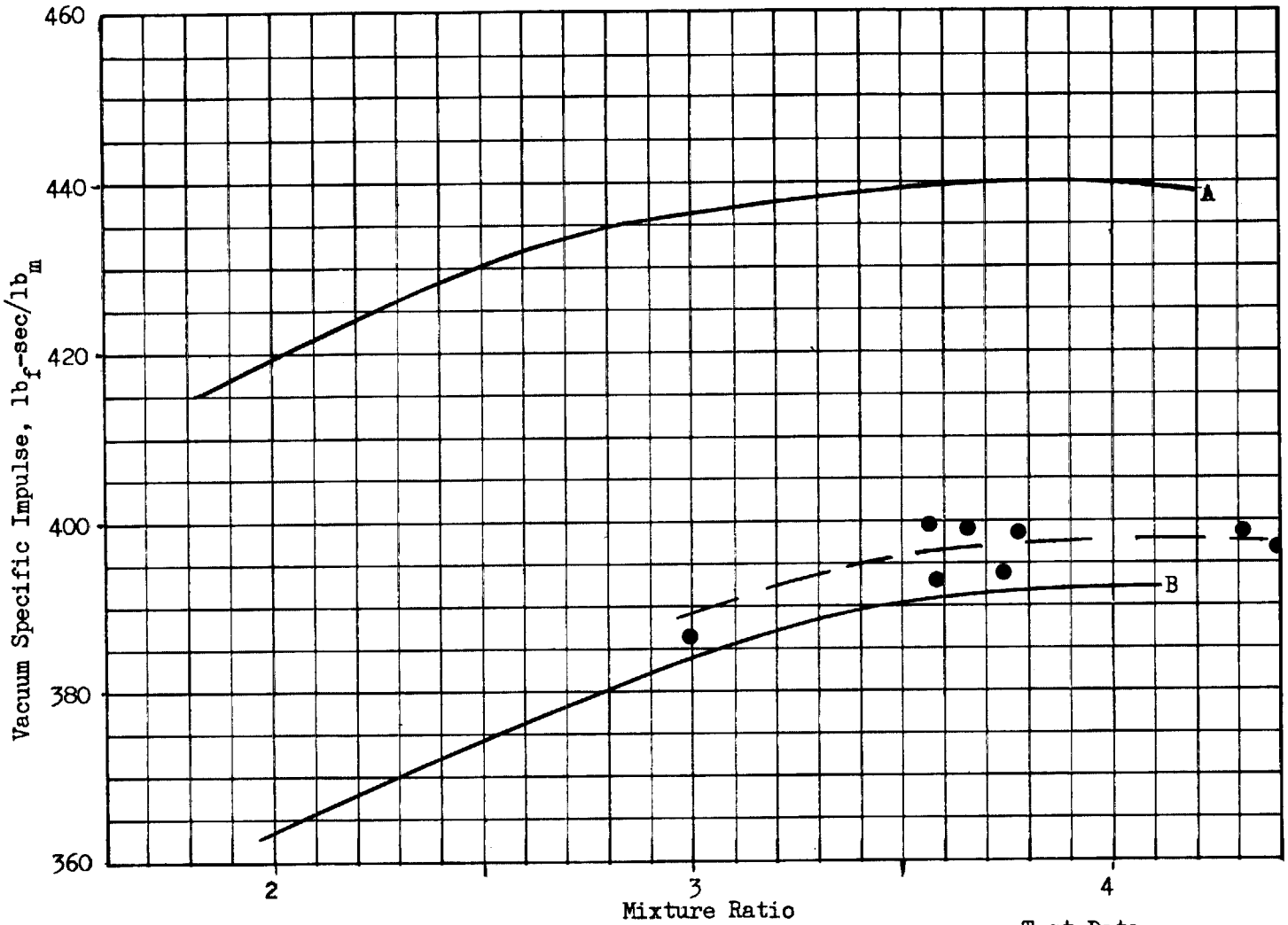

Fig. 26. Adjusted Vacuum Specific Impulse for F_2-O_2(70-30)/B_2H_6 at a Chamber Pressure of 55 psia for the 15-degree Cone

HEAT TRANSFER

The heat transfer rates for diborane were considerably higher than those observed for the other propellants. In the combustion chamber, the heat transfer rates were about 20 percent higher than those for F_2-O_2/CH_4, Fig. 27. In the nozzle (Fig. 28 and 29) the rates were about 100 percent higher than those measured for F_2-O_2/CH_4. Variations with mixture ratio (Fig. 29) and pressure (Fig. 30) were also investigated. No detectable difference was observed between OF_2 and F_2-O_2 (70-30).

HARDWARE CONDITION

Following the diborane tests there was a flaky deposit on part of the internal surface of the thrust chamber. However, the deposit was light and did not appear on the injector.

The major constituent of the exhaust of OF_2/B_2H_6 is the unstable compound BOF. When this compound comes in contact with a cool surface (< 1000 F) it decomposes to solid B_2O_3 and gaseous BF_3. The B_2O_3 is left behind as a deposit. In other test programs this deposit has been observed on both the injector and combustion chamber walls and has sometimes been so severe as to cause major problems, e.g. Ref. 2. However, in this program, the deposit was found only on the chamber walls and appears to be flaky in nature as shown in Fig. 31. There was nearly a total absence of deposit on the injector face. This may have been due to the gas injection. This injector pattern produces very little spray back to the injector face since droplets are entrained in the high velocity gas stream. Whatever the reason, tests have been conducted with both oxidizer-and fuel-rich cutoffs and in no case was deposition observed.

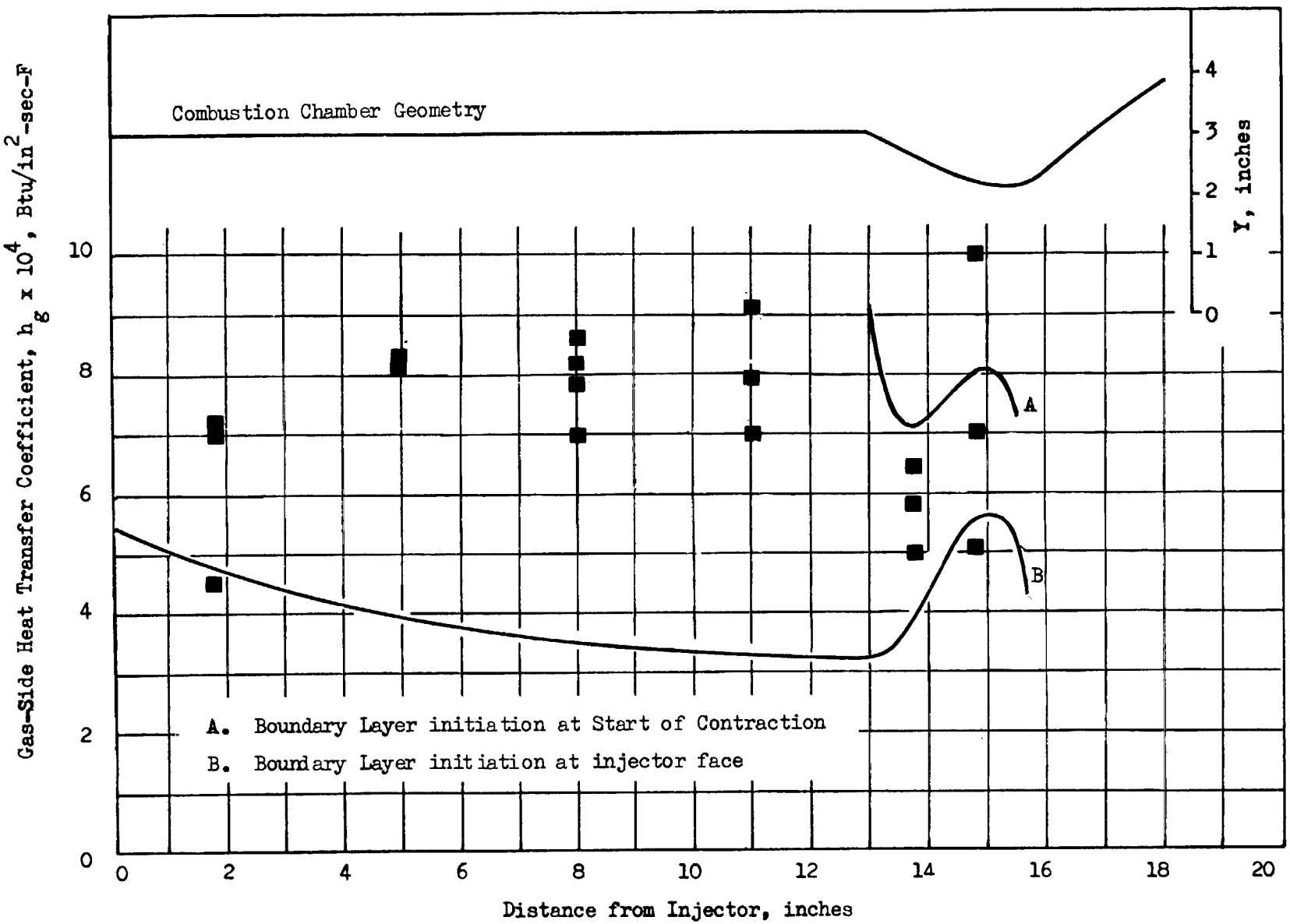

Figure 27. Combustion Chamber Heat Transfer Coefficients for OF_2/B_2H_6 and F_2-O_2/B_2H_6 at a Chamber Pressure of 100 psia.

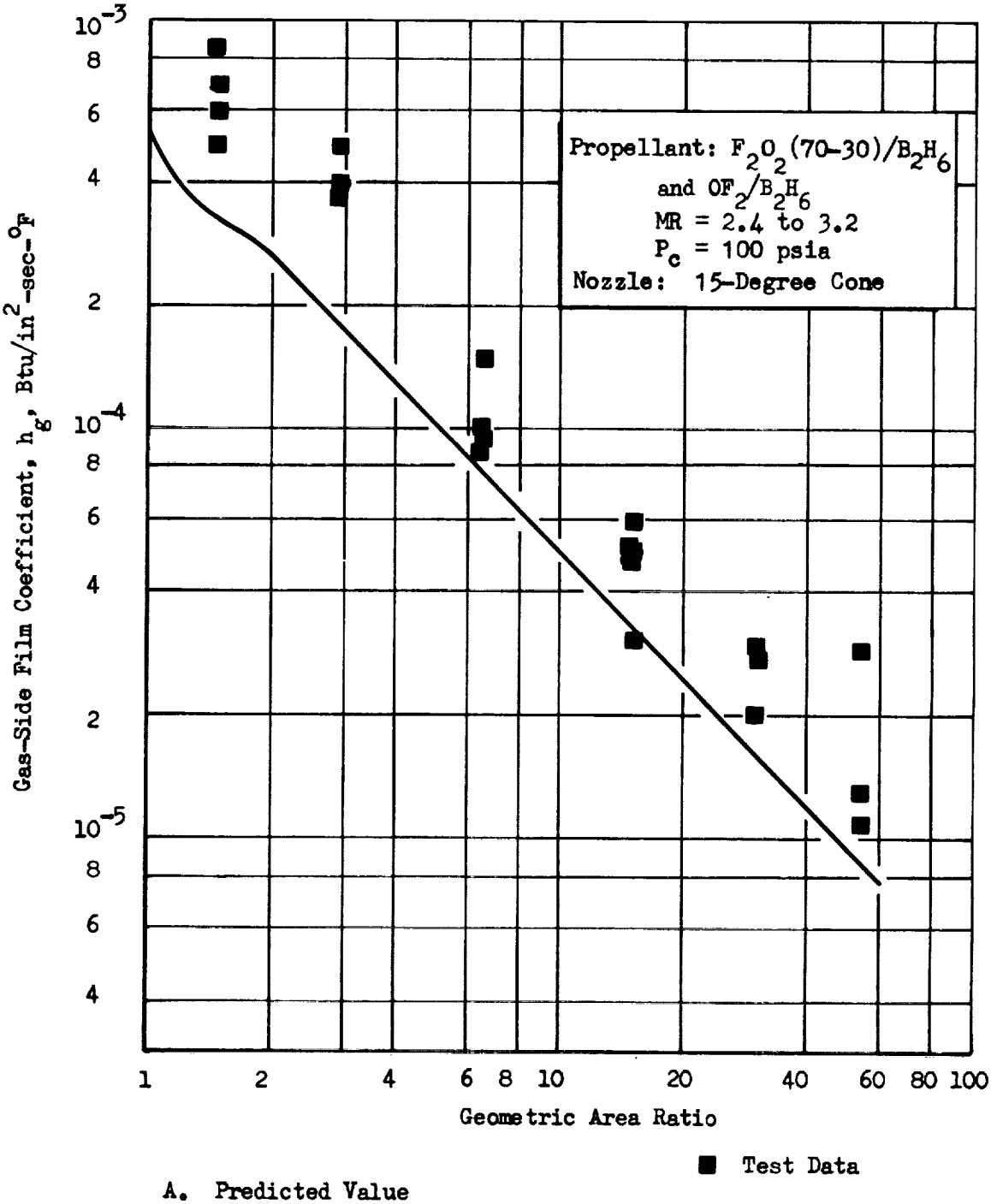

A. Predicted Value

Figure 28. Nozzle Heat Transfer Coefficient for the 15-Degree Cone with OF_2/B_2H_6 and F_2-O_2(70-30)/B_2H_6 at a Chamber Pressure of 100 psia.

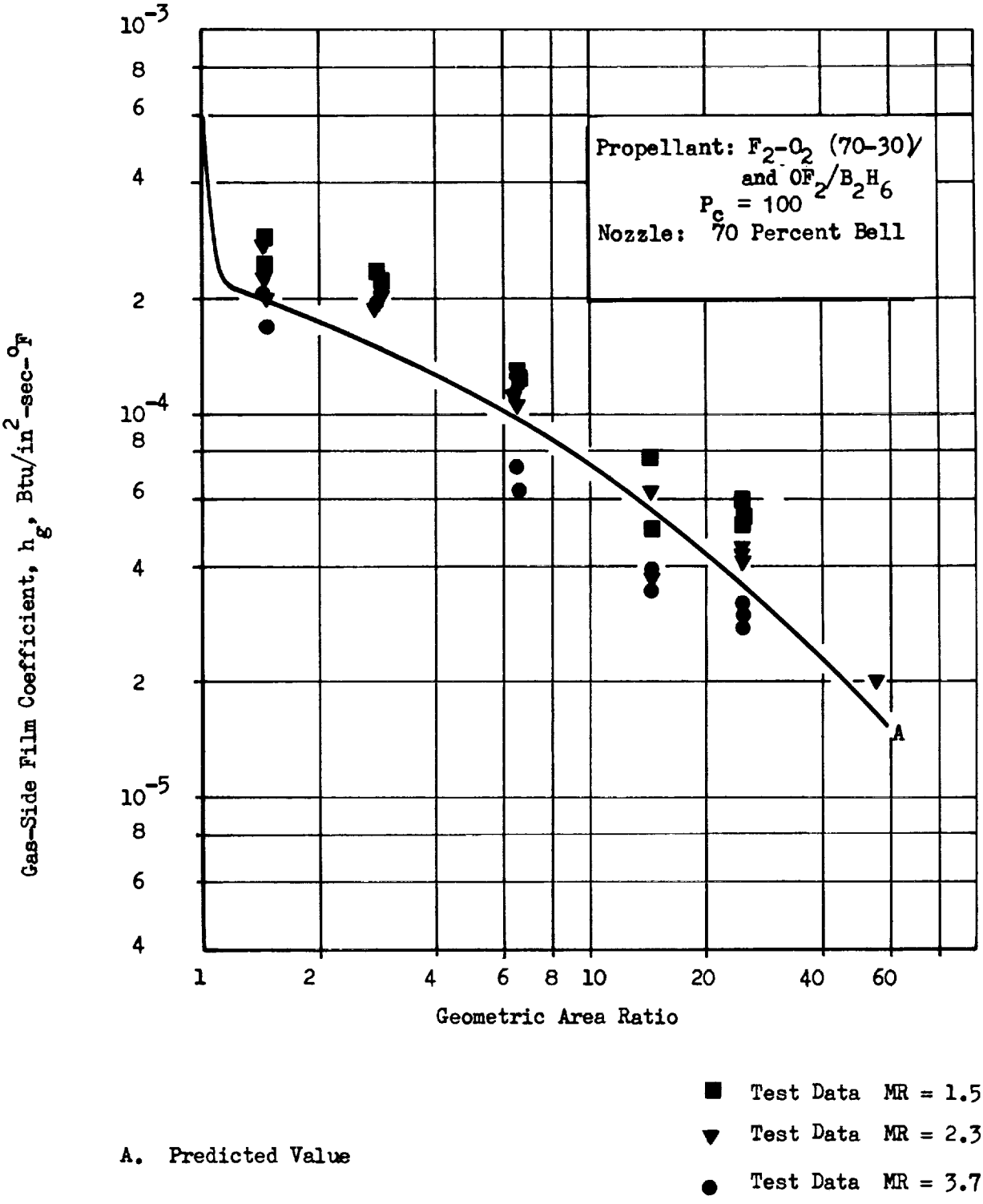

Figure 29. Nozzle Heat Transfer Coefficient for the 70 Percent Bell Nozzle with OF_2/B_2H_6 and F_2-O_2(70-30)/B_2H_6 at at a Chamber Pressure of 100 psia

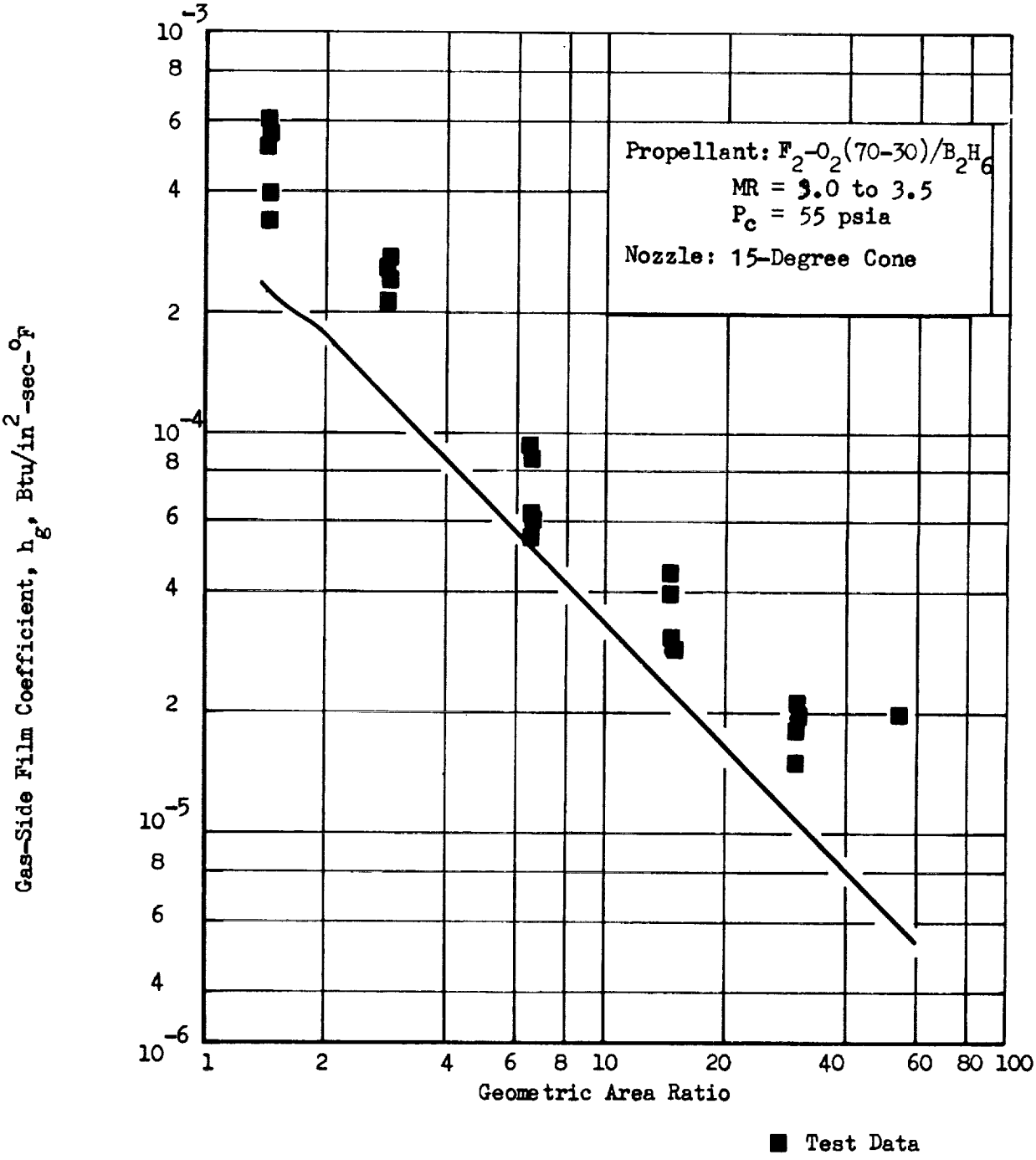

A. Predicted Value

Figure 30. Nozzle Heat Transfer Coefficients for the 15-degree Cone for F_2-O_2(70-30)/B_2H_6 at a Chamber Pressure of 55 psia.

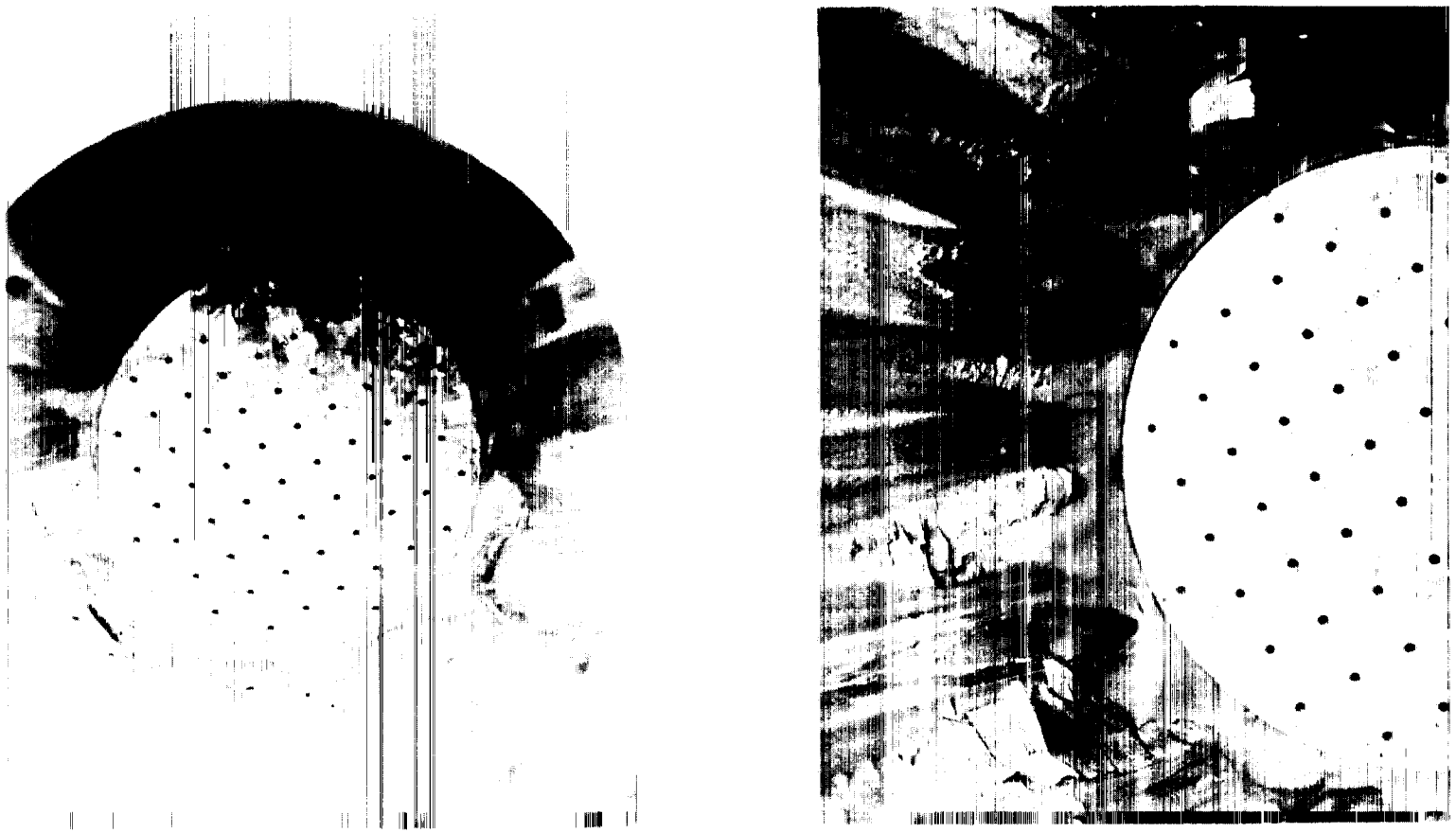

Figure 31. Injector and Combustion Chamber after F_2-O_2(70-30)/B_2H_6 Test Number 377-072

The deposit in the throat area appears more persistent, as seen in Fig. 32. In the nozzle, the deposition gradually reduced until, at about an area ratio of 3, it disappeared. The remainder of the nozzle, to an area ratio of 60 was totally free of deposits.

Figure 32. Nozzle Region Deposition for F_2-O_2(70-30)/B_2H_6

SECTION III

INTERPRETATION OF PHASE I TEST DATA FOR FLUORINE-HYDROGEN

In Phase I of this program an extensive test program was conducted with fluorine/hydrogen. Nozzle performance was examined for a wide variety of nozzle contours, area ratios, chamber pressures and mixture ratios. The results are documented in Refs. 3, 4 and 5. As a result of the continued studies and experimentation in Phase II, some changes in the interpretation of the original data are recommended.

For Phase II, the test program was moved to a new test position designed expressly for this project and a significantly improved oxidizer flow measurement capability was introduced. A series of F_2/H_2 tests was conducted to assure consistency between the results for the two test stands. Thrust chamber efficiency of the same engine hardware tested on the two stands was compared and seen to be in agreement (Section IV). The improved oxidizer flow measurement gave a small difference in flowrate. This caused a difference in the determined specific impulse and characteristic velocity values.

Because the new flow measurements are superior it is recommended that the original F_2/H_2 data now be interpreted for specific impulse by combining the thrust chamber efficiencies obtained in Phase I with the injector efficiencies obtained from the F_2/H_2 tests on the new test stand in Phase II. The recommended injector efficiency curve is shown in Fig. 33 of this volume. The Phase I thrust chamber efficiencies are included in Section IV.

For comparison with the normalized F_2-O_2/CH_4 and OF_2/B_2H_6 results shown in Sections I and II of this report, Figs. 34 and 35 display F_2/H_2 specific impulse data at 100 psia with the two nozzles used in Phase II. These figures were obtained by combining the thrust chamber efficiency results for the cone and bell in Figs. 61 and 64 with an injector efficiency value of 98-percent.

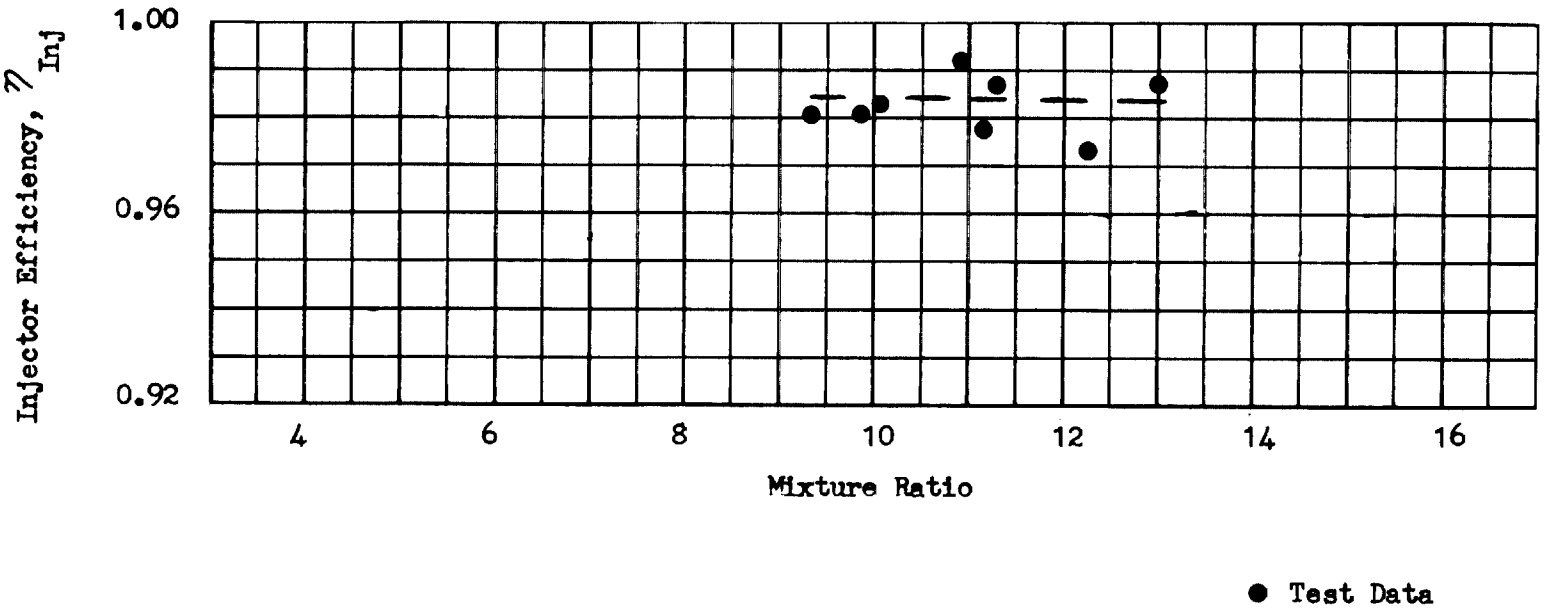

Figure 33 . Injector Efficiency for F_2/H_2 at a Chamber Pressure of 100 psia.

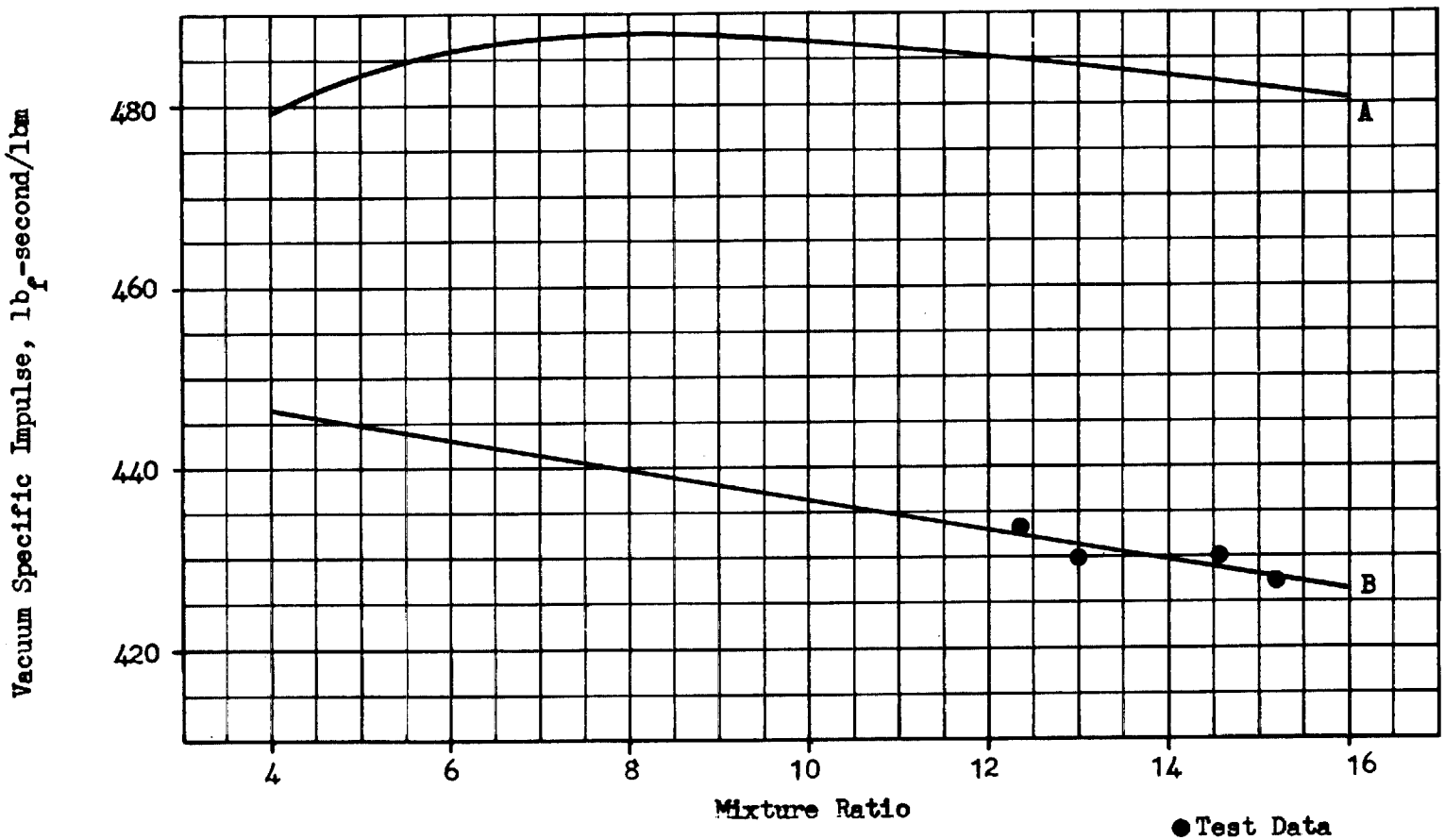

A. One-Dimensional Isentropic Chemical Equilibrium Expansion Performance

B. Predicted Performance ($\eta_{Inj} = 0.98$)

Note: All Data Adjusted to 98-percent Injector Efficiency

Figure 34. Adjusted Specific Impulse for F_2/H_2 at a Chamber Pressure of 100 psia for the 15-degree Cone.

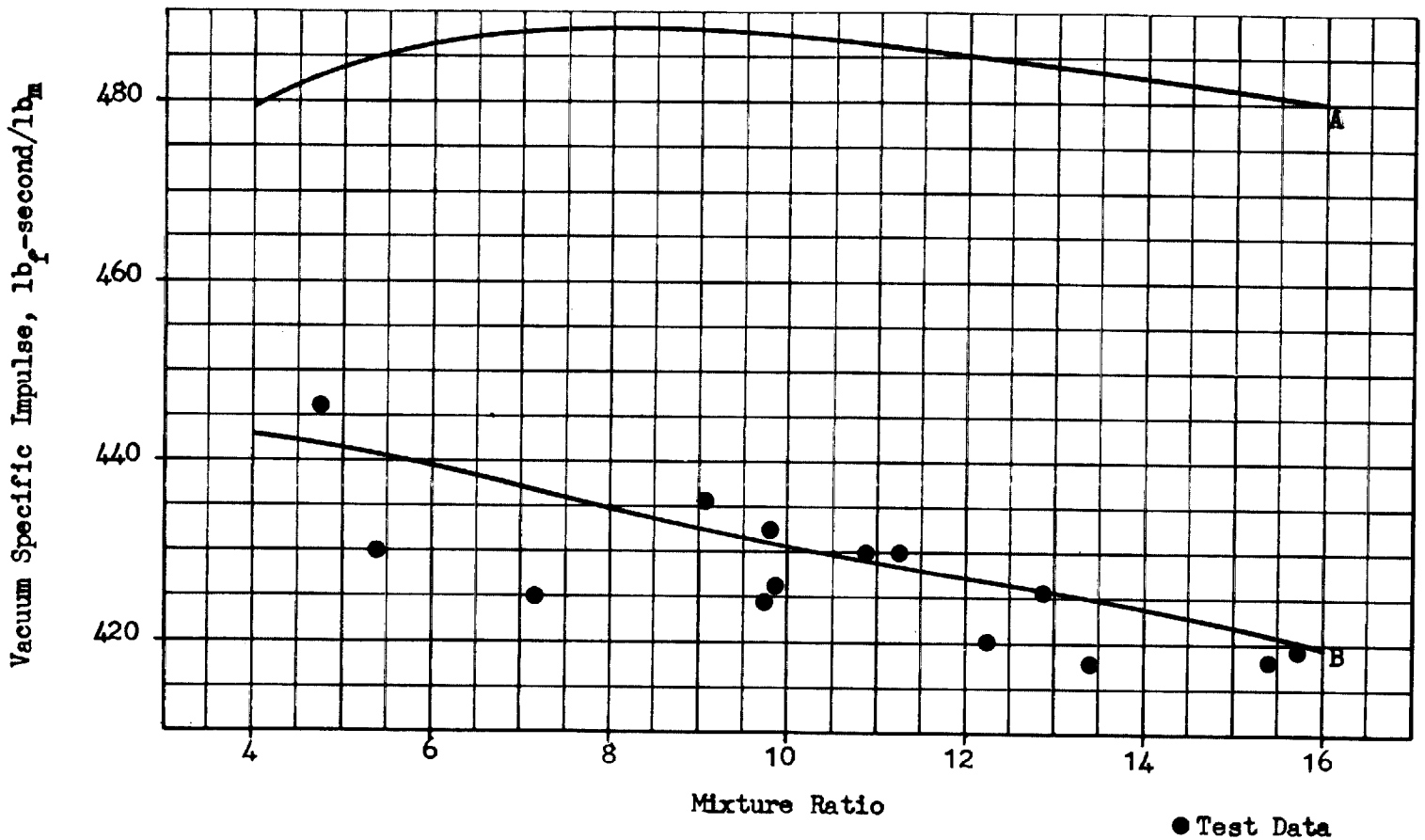

A. One-Dimensional Isentropic Chemical Equilibrium Composition Expansion Performance.

B. Predicted Performance (η_{Inj} = 0.98)

Note: All Data Adjusted to 98-percent Injector Efficiency

Figure 35. Adjusted Specific Impulse for F_2/H_2 at a Chamber Pressure of 100 psia for the 70-percent Bell.

SECTION IV

DATA INTERPRETATION

In the preceding sections the test results have been described as they were obtained. In this section the performance data are described in relation to all other data measurements and to the theoretical predictions. The primary objectives of these comparisons are to ensure the accuracy and consistency of the test data and to indicate areas in which the analytical models need improvement. Since this program involved a relatively limited number of tests such comparisons help to eliminate random errors and prevent the possibility of systematic errors. This careful scrutiny of the data is made possible by the wide variety of measurements taken. In addition to the basic measurements of thrust and flowrate, a complete wall pressure profile is taken from the injector to the nozzle exit. Heat transfer is measured over the same range. At times, even injector pressure drops have been used to substantiate flowrates. These various data are essentially independent and can thus be used to provide substantiation of the basic measurements. To aid in the interpretation of the data, the specific impulse losses are separated into the loss related to the injector and that related to the thrust chamber as described in Section V.

F_2-O_2/CH_4 AND OF_2/CH_4

The great variety of tests conducted with CH_4 and the three oxidizers F_2-O_2(82.5-17.5), F_2-O_2(70-30), and OF_2 makes possible an extensive comparison of theoretical and experimental performance results. The primary objective of this comparison is the assurance of high quality data.

Injector Efficiency

Data of several types tend to support the validity of the injector efficiency determinations for all three oxidizers. The low area ratio injector verification tests produced good agreement between the two methods of determining injector efficiency, Fig. 7. The thrust based method, which is virtually independent of errors in either chamber pressure or throat area, correlated the method based upon chamber pressure and throat area. Further, the corrections from combustion chamber wall pressure to chamber stagnation pressure were carefully checked by the independent method of full scale cold flow tests, Page 107. The data were repeatable from test to test and showed consistent mixture ratio trends. All values were below 100-percent, assymptotic to 100-percent at low mixture ratio for F_2-O_2(82.5-17.5) and between 99 and 100-percent for F_2-O_2(70-30) and OF_2.

For both F_2-O_2(70-30) and OF_2 the injector efficiency was 1 to 2 percent higher than for F_2-O_2(82.5-17.5) at high mixture ratios. This difference is qualitatively supported by comparison of the combustion chamber pressure profiles for the different oxidizers, Fig. 36. It is seen that for OF_2 and F_2-O_2(70-30), which have the same chemical composition, the initial pressure decay is more rapid, indicating a more rapid energy release. The fact that the pressure rise near the contraction zone from the cold flow tests was nearly the same as the rise observed for all three oxidizers (Fig. 74) makes it unlikely that significant combustion was continuing in this region.

Although it is not evident why the difference in oxidizer composition should have an effect on injector performance efficiency, the data are consistent and the possibility of a real effect should not be neglected.

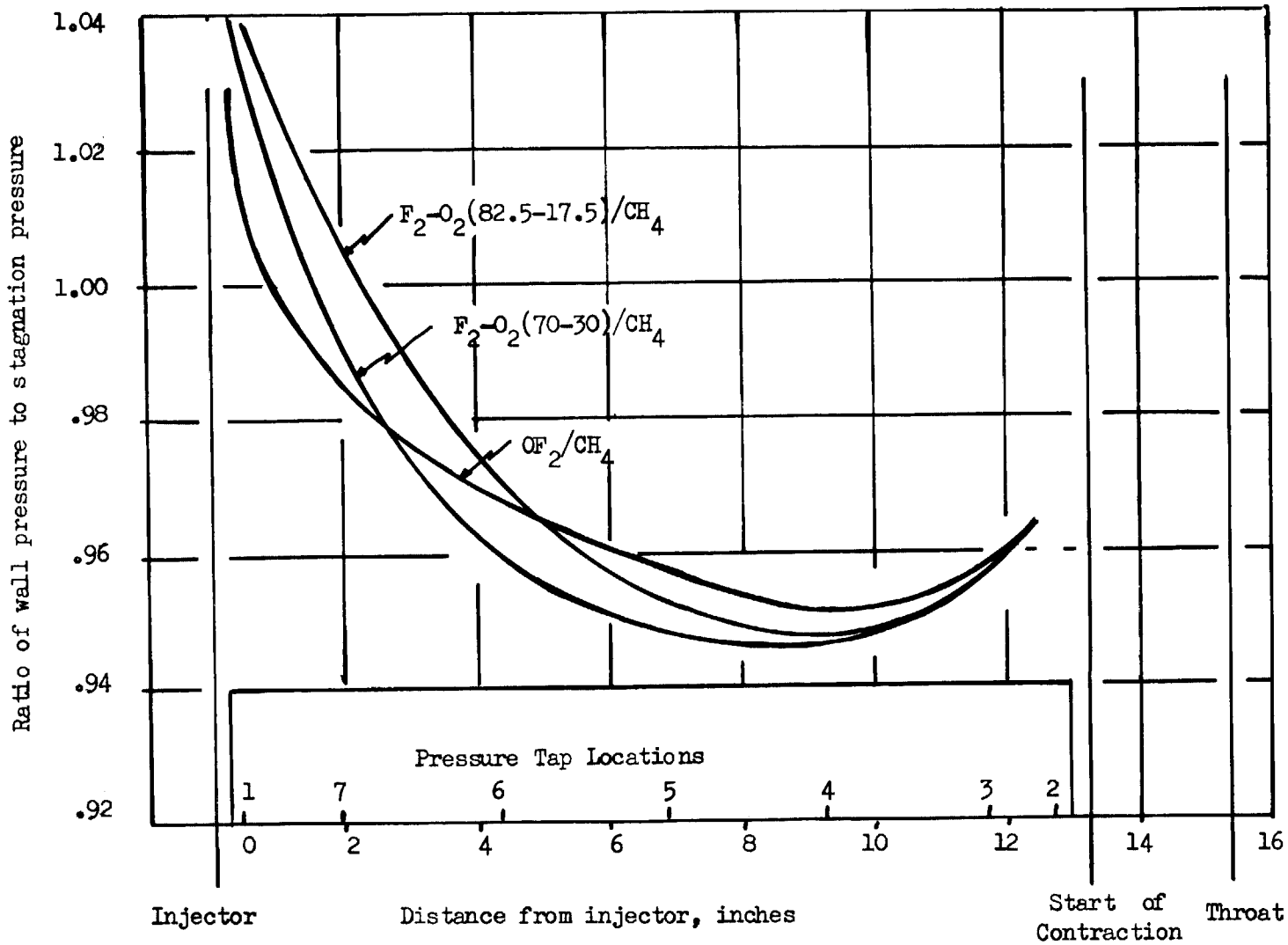

Figure 36. Comparison of Combustion Chamber Wall Pressure Profiles

Some potential causes might be the atomization and vaporization efficiency of the injector, the shape of the theoretical C* vs mixture ratio curve (Appendix B), or a chemical kinetic effect caused by the higher oxygen (or lower fluorine) concentration. An explanation based on atomization or vaporization is unlikely. The OF_2 is more dense and the F_2-O_2(70-30) less dense than F_2-O_2(82.5-17.5) making velocity an improbable cause. Further, the difference in critical parameters of OF_2 and F_2-O_2(70-30) is large and, on that basis, F_2-O_2(70-30) would be expected to resemble F_2-O_2(82.5-17.5) more than it does OF_2. The other two explanations are plausible, but insufficient information is available to make a judgment.

Thrust Chamber Efficiency

The two significant trends observed in thrust chamber efficiency for methane are that the values for F_2-O_2(82.5-17.5) (Fig. 37 and 38) are substantially higher than predicted and that the dependence on F_2-O_2 concentration is much larger than predicted.

Substantiating the high values of thrust for F_2-O_2(82.5-17.5) are the nozzle wall pressure measurements shown in Figs. 39 through 42 These pressures were consistently higher than predicted in the high area ratio region but near the predicted values in the throat region. (The latter supports the good correlation of injector efficiencies shown in Fig. 7) The cause of the unexpectedly high performance is not clear. The good injector efficiency correlation makes it most likely the cause is either a wall effect or a core effect occurring in the nozzle.

Examining the wall effects, the heat transfer data (Figs. 14 through 16) were predicted by the boundary layer theory with some accuracy and the magnitude of the boundary layer loss is neither large enough nor sensitive enough to nozzle contour, mixture ratio or fluorine concentration for an

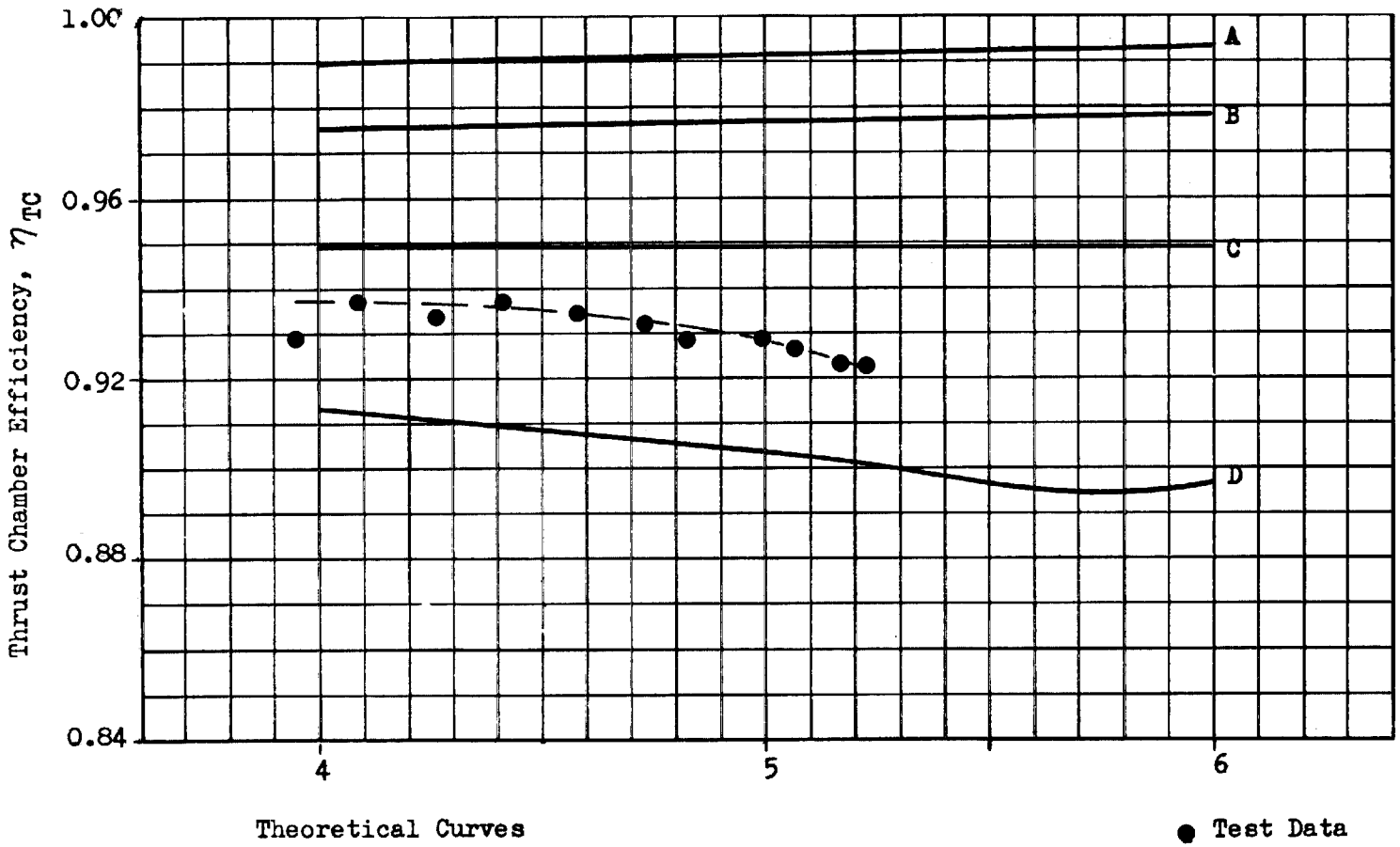

Theoretical Curves

A. Heat Loss
B. Heat Loss and Divergence
C. Heat Loss, Divergence and Boundary Layer
D. Heat Loss, Divergence, Boundary Layer and Kinetics

● Test Data

Figure 37. Thrust Chamber Efficiency for F_2-O_2(82.5-17.5)/CH_4 at a Chamber Pressure of 100 psia for the 15-degree Cone.

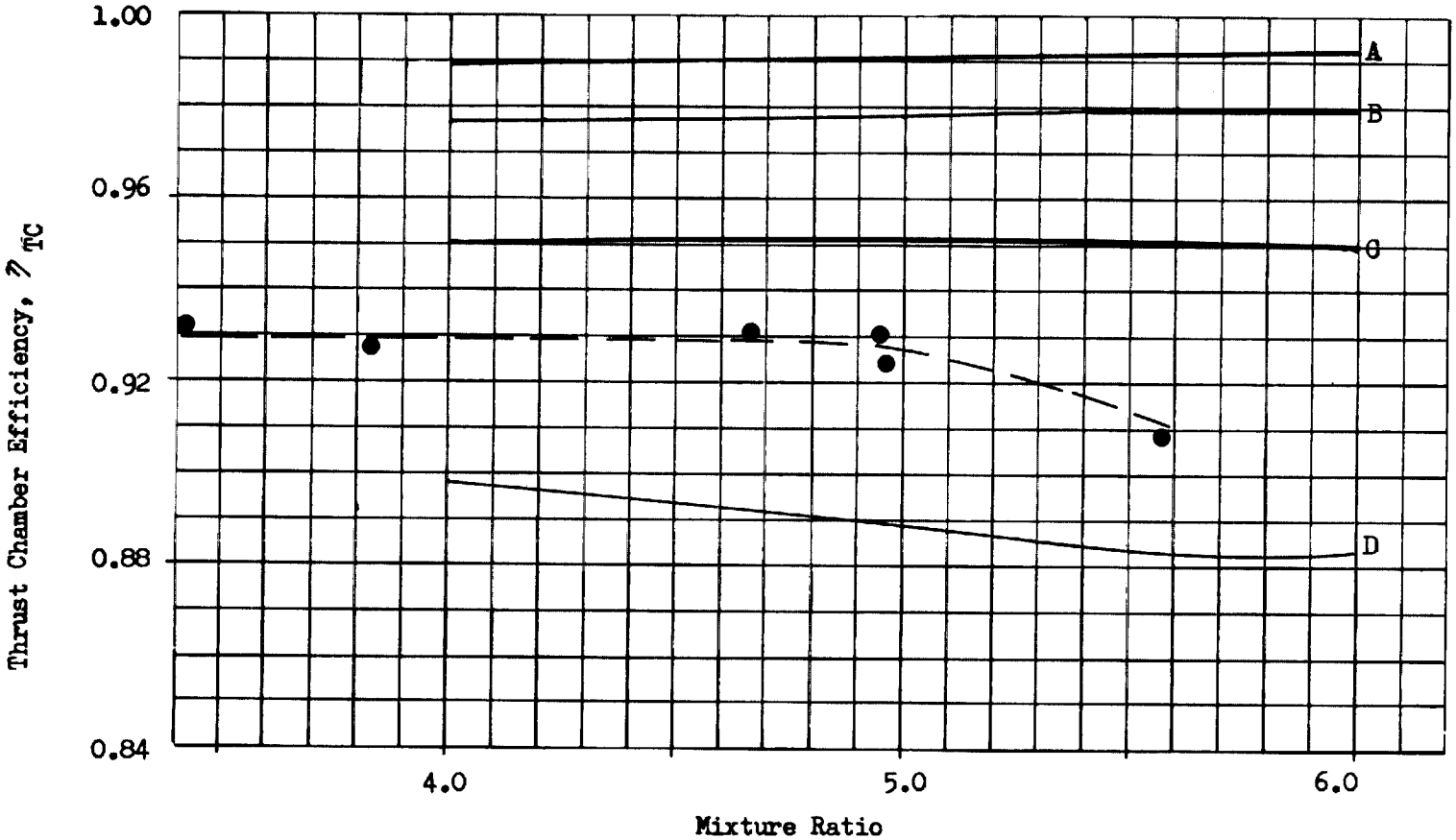

Figure 38. Thrust Chamber Efficiency for F_2-O_2(82.5-17.5)/CH_4 at a Chamber Pressure of 100 psia for the 70-percent Bell

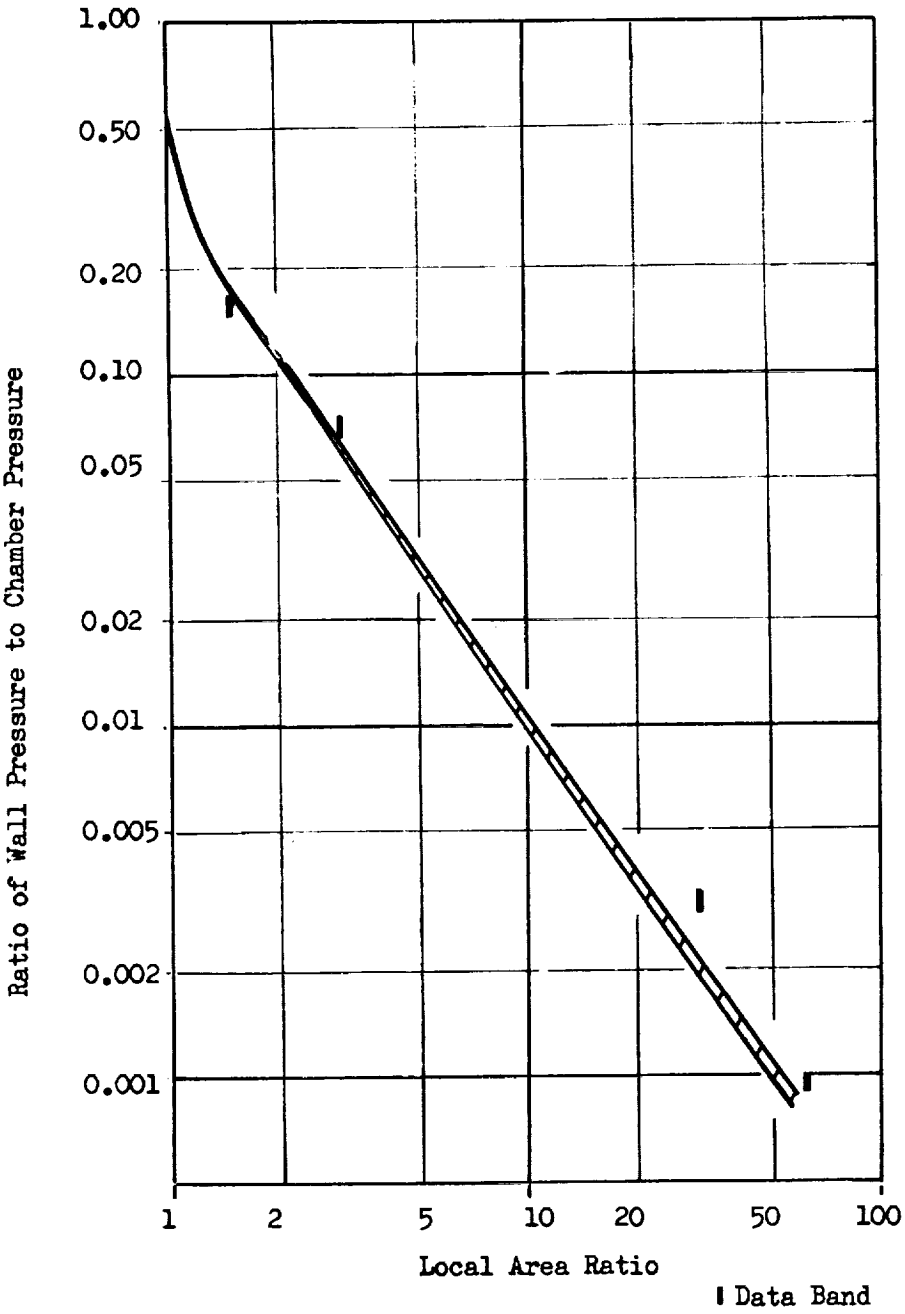

Figure 39. Area Ratio Effect on Nozzle Wall Pressure Correlation for F_2-O_2(82.5-17.5)/CH_4 for 15-degree Cone at 100 psia Chamber Pressure.

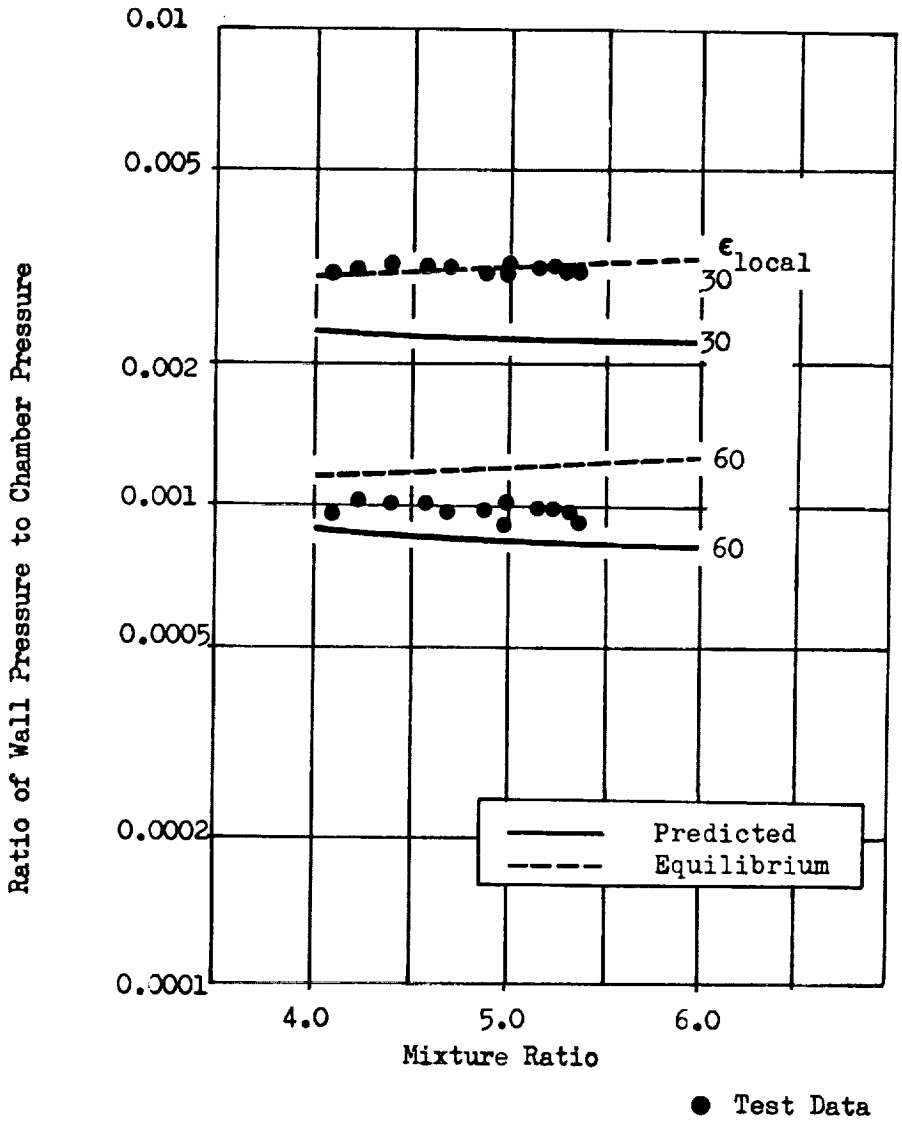

Figure 40. Mixture Ratio Effect on Nozzle Wall Pressure Correlation for F_2-O_2(82.5-17.5)/CH_4 for 15-degree Long Throat Cone at 100 psia Chamber Pressure

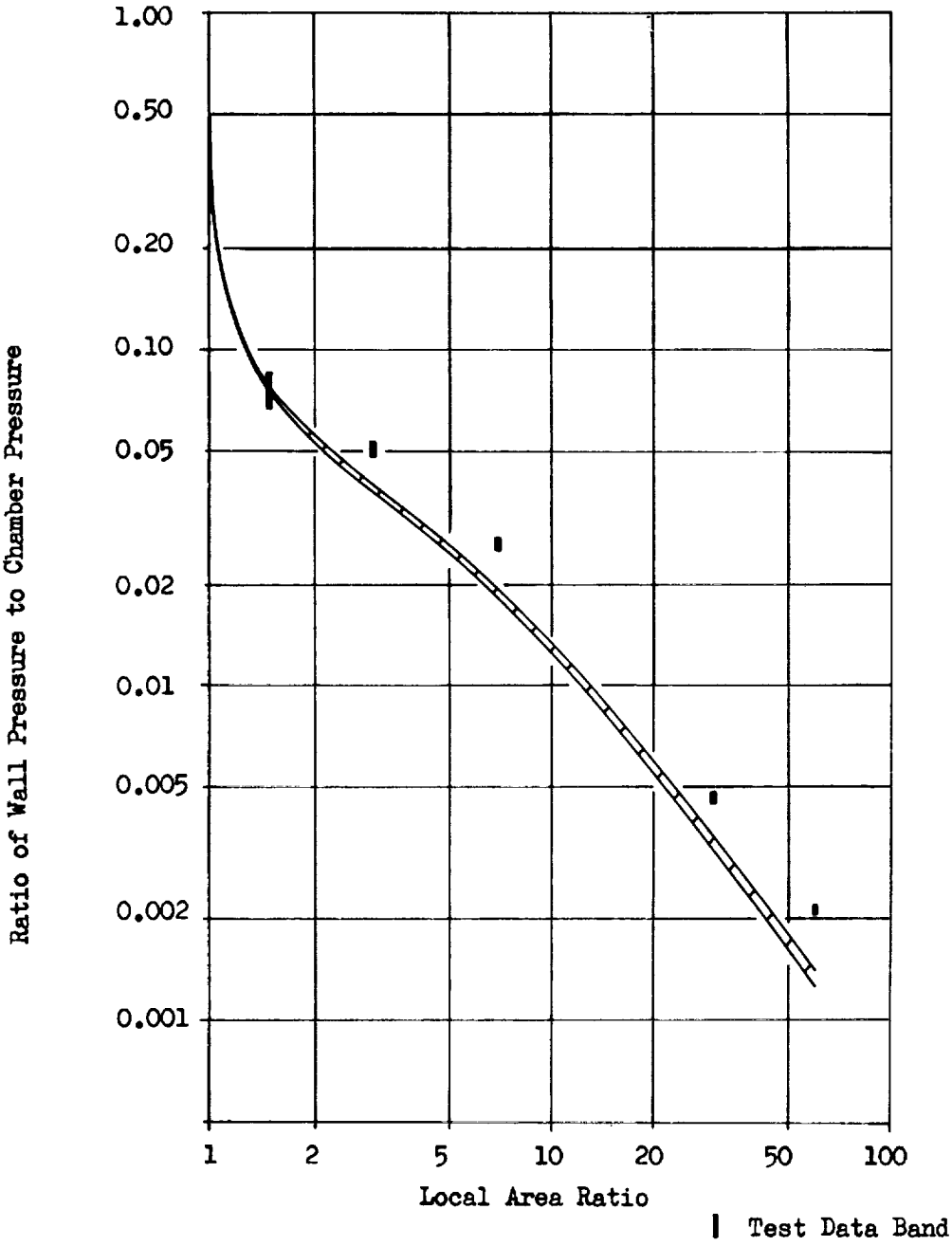

Figure 41. Area Ratio Effect on Nozzle Wall Pressure Correlation for F_2-O_2(82.5-17.5)/CH_4 for 70-percent Bell Nozzle at 100 psia Chamber Pressure

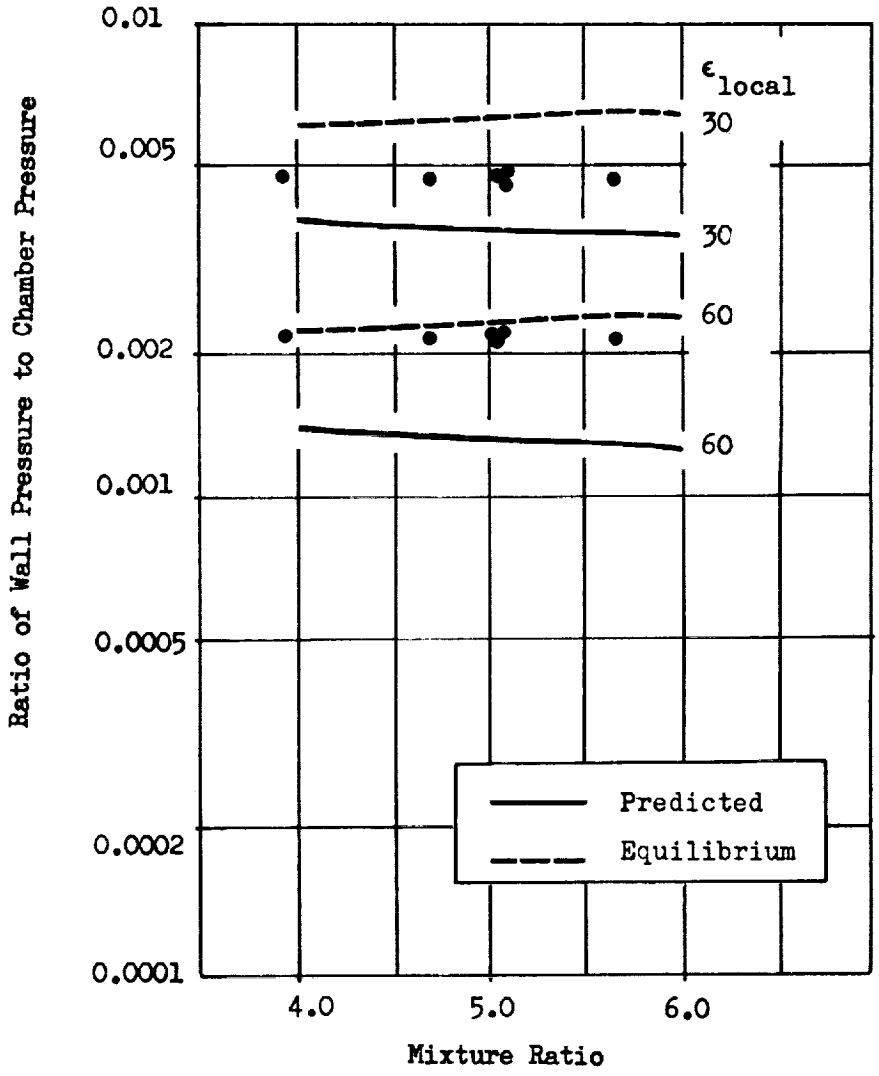

Figure 42. Effect of Mixture Ratio on Nozzle Wall Pressure Correlation for F_2-O_2(82.5-17.5)/CH_4 for the 70-percent Bell at 100 psia Chamber Pressure.

error in this loss to account for the observed performance effects. Therefore, the mainstream performance is probably the area in which unexpected trends occur.

The areas affecting mainstream performance are the aerodynamic losses, the chemical kinetic losses and basic theoretical performance data. The equilibrium reactions involved in the system are well known so the theoretical performance is probably accurate. The aerodynamic loss is a very weak function of the parameters for which unexpected trends were observed.

The loss mechanism that is least understood is the chemical kinetic process. This loss is of sufficient magnitude and varies rapidly enough with the major test parameters to account for all the observed performance trends. There are several possible physical mechanisms related to the chemical kinetic loss which could account for the observed performance trends. As shown in Fig. 43 , carbon is formed in the combustion chamber at mixture ratios below 5.5. At mixture ratios below 5.7 solid carbon could theoretically condense in the nozzle. No exact kinetic or approximate method is available that realistically includes a condensing solid and the extension of the existing methods to include this effect could not be considered in this program.

Other exhaust products that appear at mixture ratios below 5.7 could conceivably be involved in the discrepancy. The reactions involving CO and CO_2 are not completely understood and other elements such as CH, C_2H, C_2H_2, CF, C_2, C_2F, CF_2 and C_3 may not be completely characterized. There may be additional recombination paths involving these elements that are not generally known or discussed in the literature. Intermediate, unstable compounds not indicated in the equilibrium model could also enter into the chemical kinetics. For example, adding the conceptually possible reactions

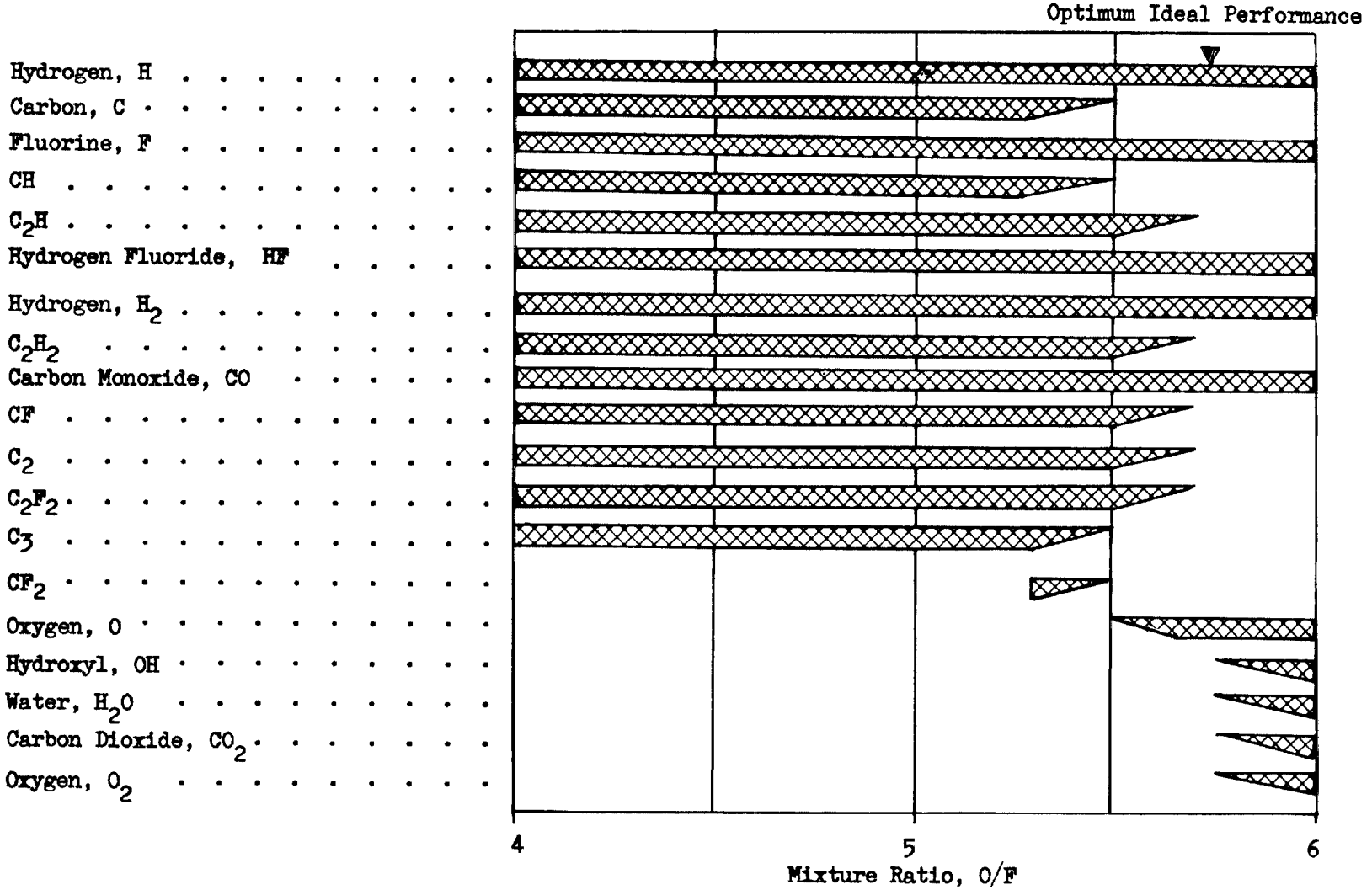

Figure 43. Species Present in Combustion Chamber for F_2-O_2(82.5-17.5)/CH_4 at Chamber Pressure 100 psia

$H + CO + M \rightarrow CHO + M$, $F + CO + M \rightarrow CFO + M$, $H_2 + M \rightarrow CH_2O$ (formaldehyde) + M and $HF + CO + M \rightarrow CHFO$ (Formyl fluoride) + M could increase the kinetic efficiency enough to correlate the data.

The strong trend of thrust chamber performance with oxidizer composition is shown by the efficiencies for OF_2 and F_2-O_2(70-30), Fig. 44 and 45. For this F_2 to O_2 ratio, the results were below the prediction, in marked contrast to the results for F_2-O_2(82.5-17.5). The predicted curves shown in Fig. 44 are for F_2-O_2(70-30) to make the figure less complex. Actually the OF_2 efficiency was predicted to be about 0.3-percent lower than F_2-O_2(70-30) as shown in Fig. E2 of Appendix E.

The fact that the strong trend in thrust chamber efficiency was coupled with a slight opposite trend in injector efficiency could indicate a problem in assigning these efficiencies and therefore in throat area or chamber pressure. However, there is sufficient corroborative data to indicate that the trend is real. Among the corroborative data are the trends in wall pressure.

The nozzle wall pressure curves for OF_2 and F_2-O_2(70-30) are shown in Fig. 46 through 49 where the data are seen to be closer to the predictions than were the data for F_2-O_2(82.5-17.5). These data provide additional confirmation of strong dependence of thrust chamber performance upon F_2 to O_2 ratio and indirectly also support the high injector efficiency for F_2-O_2(70-30).

F_2-O_2/B_2H_6 AND OF_2/B_2H_6

As with methane, the wealth of data available from the diborane tests makes a thorough scrutiny of the performance results possible. This

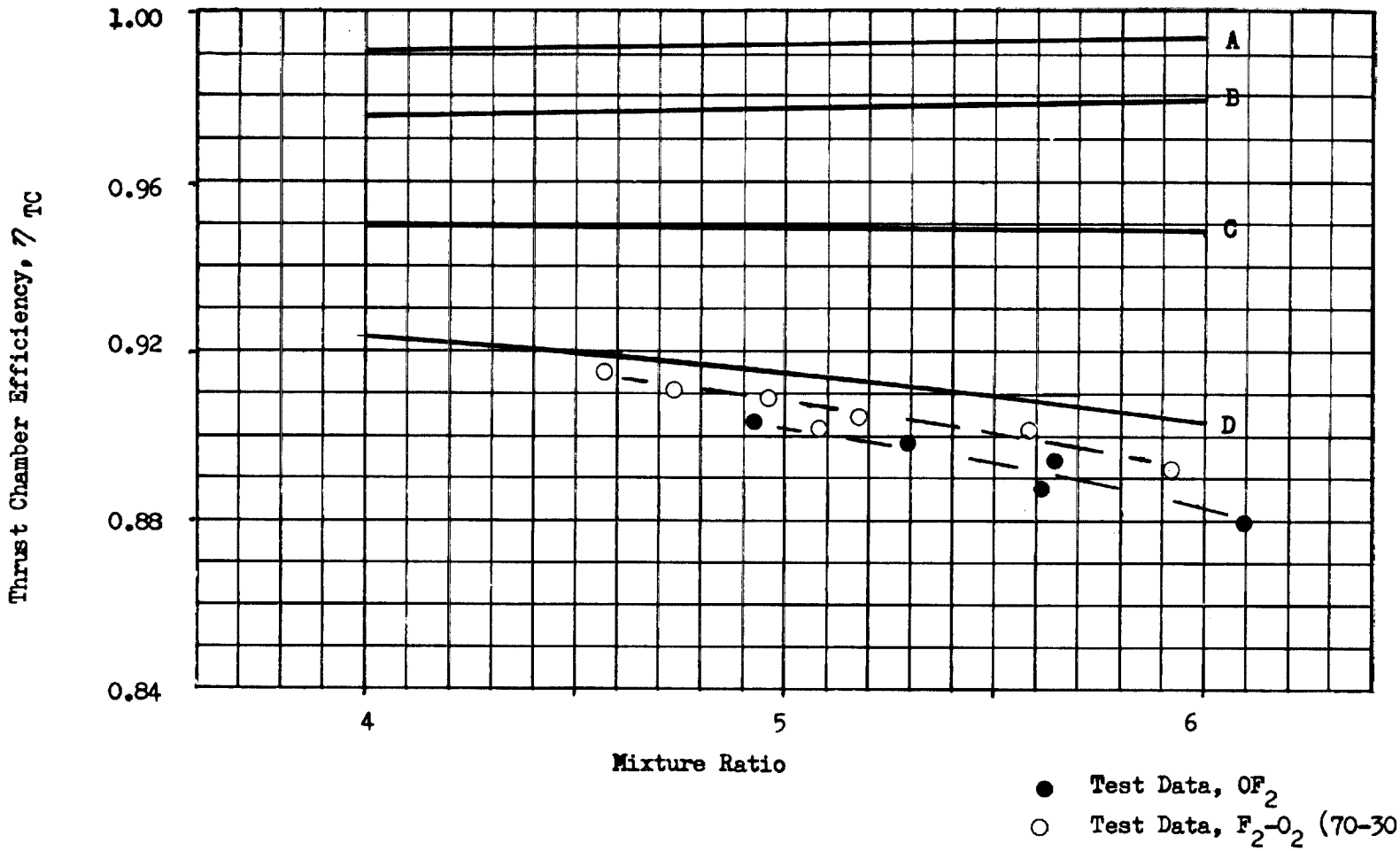

— Theoretical Curves:

A. Heat Loss
B. Heat Loss and Divergence
C. Heat Loss, Divergence and Boundary Layer
D. Heat Loss, Divergence, Boundary Layer and Kinetics

Figure 44. Thrust Chamber Efficiency for OF_2/CH_4 and F_2-O_2(70-30)/CH_4 at a Chamber Pressure of 100 psia for the 15-degree Cone

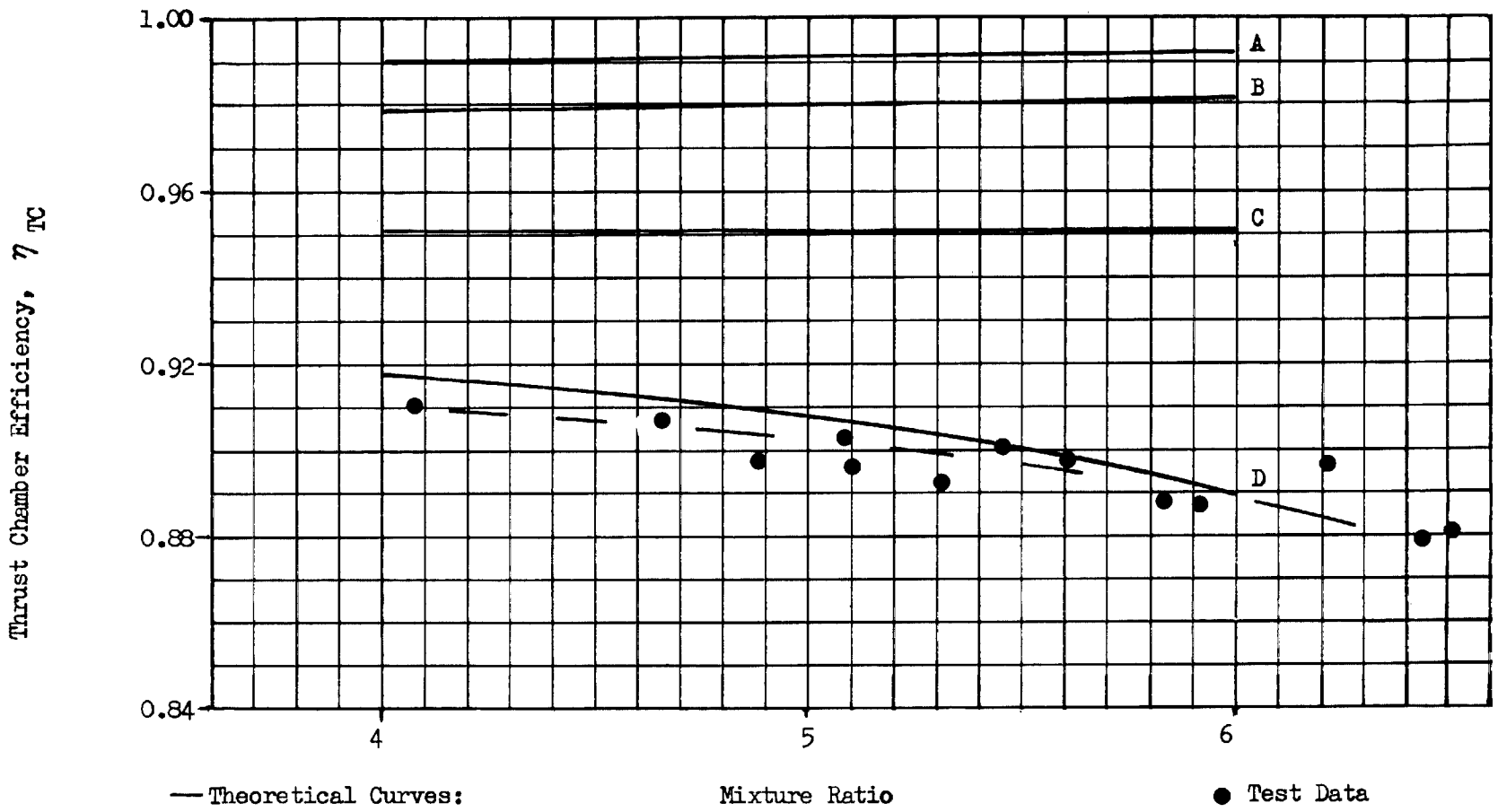

A. Heat Loss

B. Heat Loss and Divergence

C. Heat Loss, Divergence and Boundary Layer

D. Heat Loss, Divergence, Boundary Layer and Kinetics.

Figure 45. Thrust Chamber Efficiency for OF_2/CH_4 at a Chamber Pressure of 100 psia for the 70-percent Length Bell Nozzle.

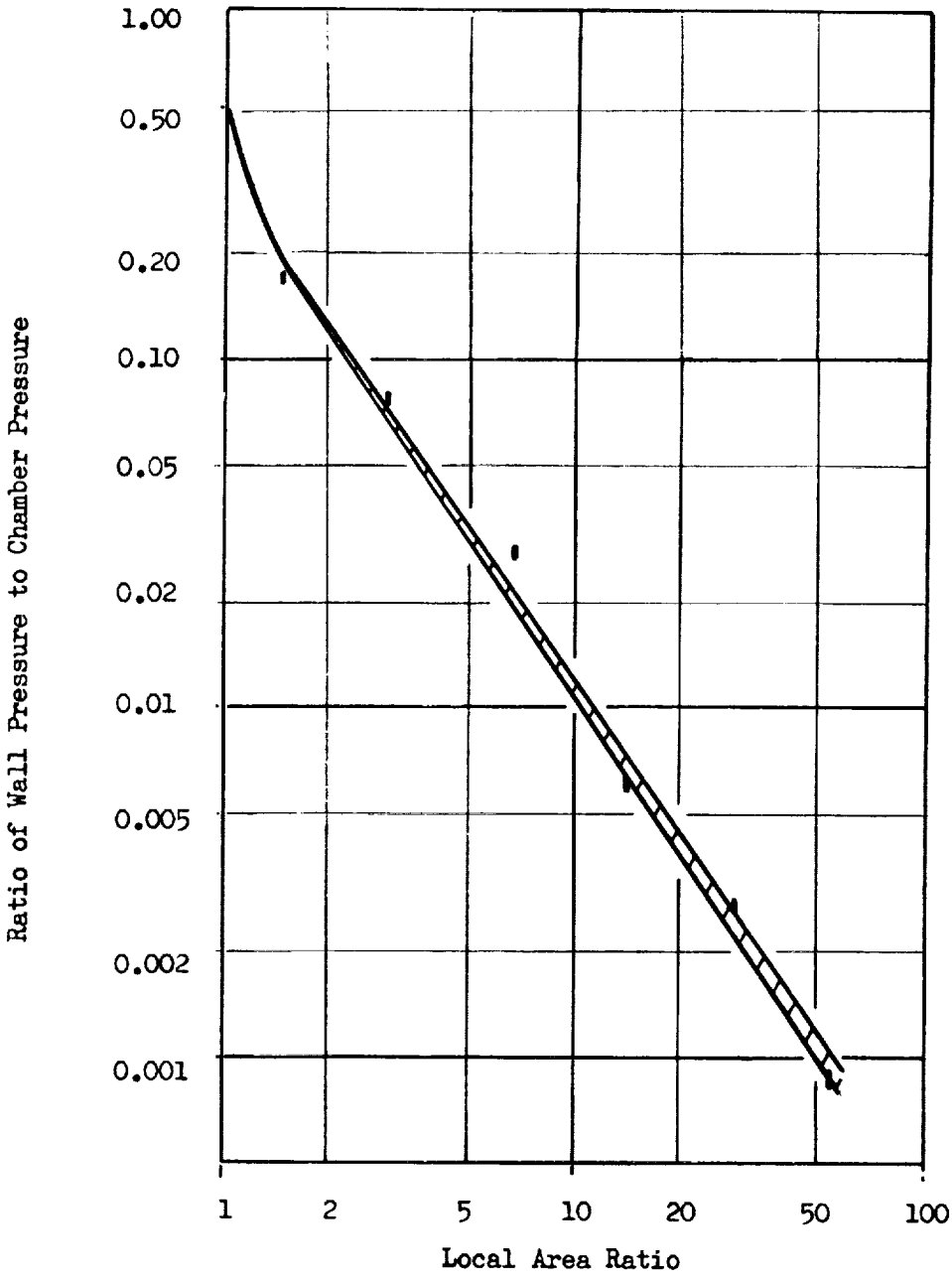

Figure 46. Effect of Area Ratio on Nozzle Wall Pressure Correlation for OF_2/CH_4 and F_2-O_2(70-30)/CH_4 Cone at 100 psia Chamber Pressure.

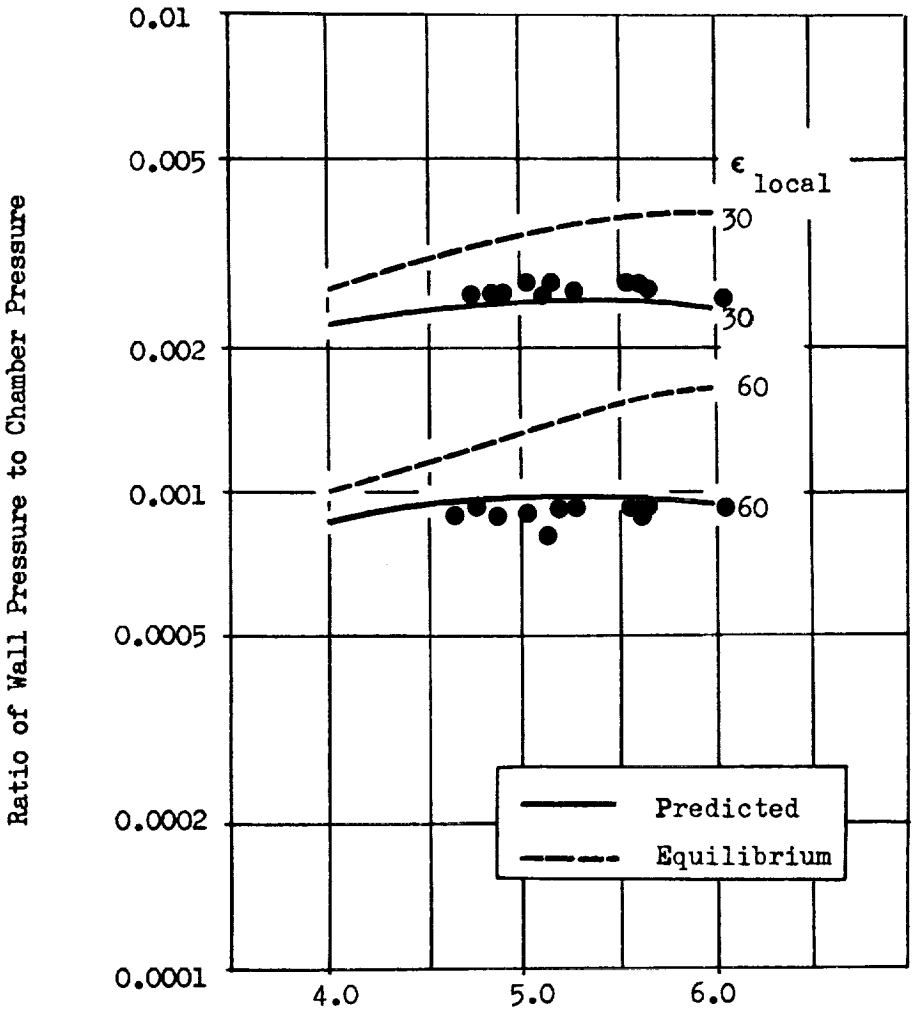

Figure 47. Effect of Mixture Ratio on Nozzle Wall Pressure Correlation for OF_2/CH_4 and F_2-O_2 (70-30)/CH_4 for 15-degree Cone at 100 psia Chamber Pressure.

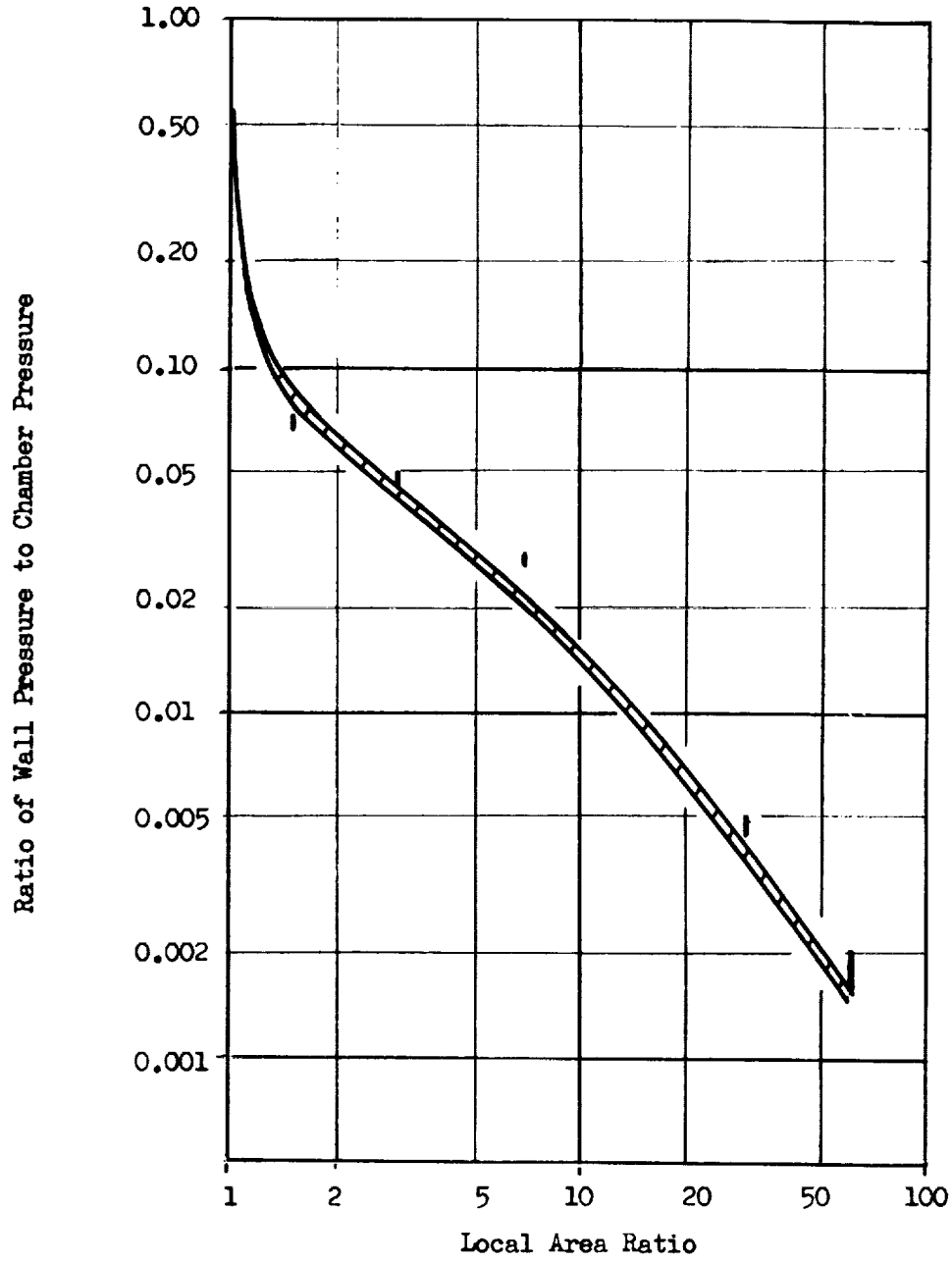

Figure 48. Effect of Area Ratio on Nozzle Wall Pressure Correlation for F_2-O_2/CH_4 for 70-percent Bell Nozzle at 100 psia Chamber Pressure.

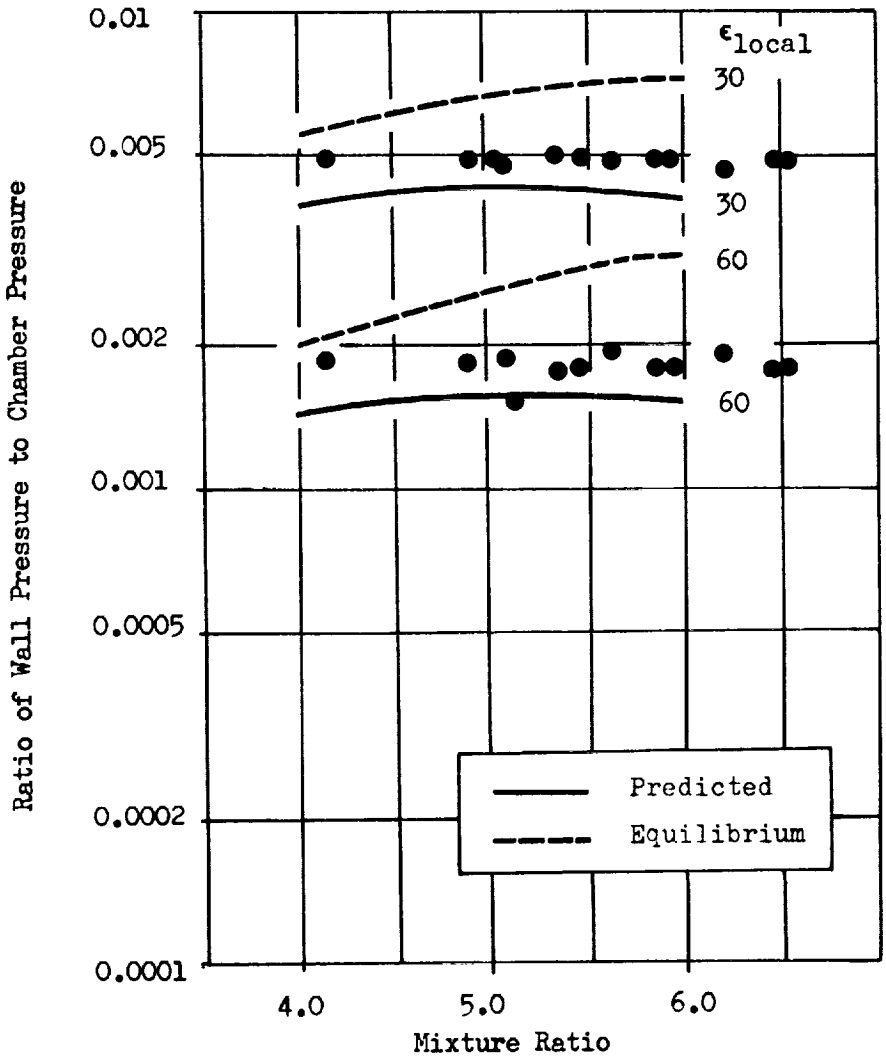

Figure 49. Effect of Mixture Ratio on Nozzle Wall Pressure Correlation for F_2-O_2/CH_4 for 70-percent Bell at 100 psia Chamber Pressure.

scrutiny ensures that the data are internally consistent and may be used in calibrating analytical techniques and physical models.

Injector Efficiency

For the B_2H_6, the injector efficiency and all the supporting data are consistent. The OF_2 and F_2-O_2(70-30) values were the same, the low area ratio injector correlation tests showed good agreement and the cold flow tests correlated the hot firing combustion chamber pressure profile (Fig. 74).

Thrust Chamber Efficiency

The most significant trend in thrust chamber efficiency for diborane was that the values were substantially higher than predicted, Figs. 50 through 52. The trend of performance with both mixture ratio and pressure was essentially as predicted. Both OF_2 and F_2-O_2(70-30) are shown on the same figure with only one predicted curve and it is seen that the OF_2 efficiencies are slightly higher. As shown in Fig. E5 of Appendix E, this slight difference between the two oxidizers was expected. As also predicted, this is opposite to the effect observed for methane.

The high thrust chamber efficiency values are supported by high nozzle wall pressures, Figs. 53 through 56, as was the case for F_2-O_2/CH_4. As seen below tests with F_2/H_2, for which the thrust chamber efficiency predictions were accurate, produced good wall pressure correlations. The extremely high heat transfer rates, usually indicative of high boundary layer losses would appear to contradict the high efficiencies except that the heat transfer is probably related to the deposition phenomenon. This condition creates a boundary layer process not amenable to analysis by currently available procedures.

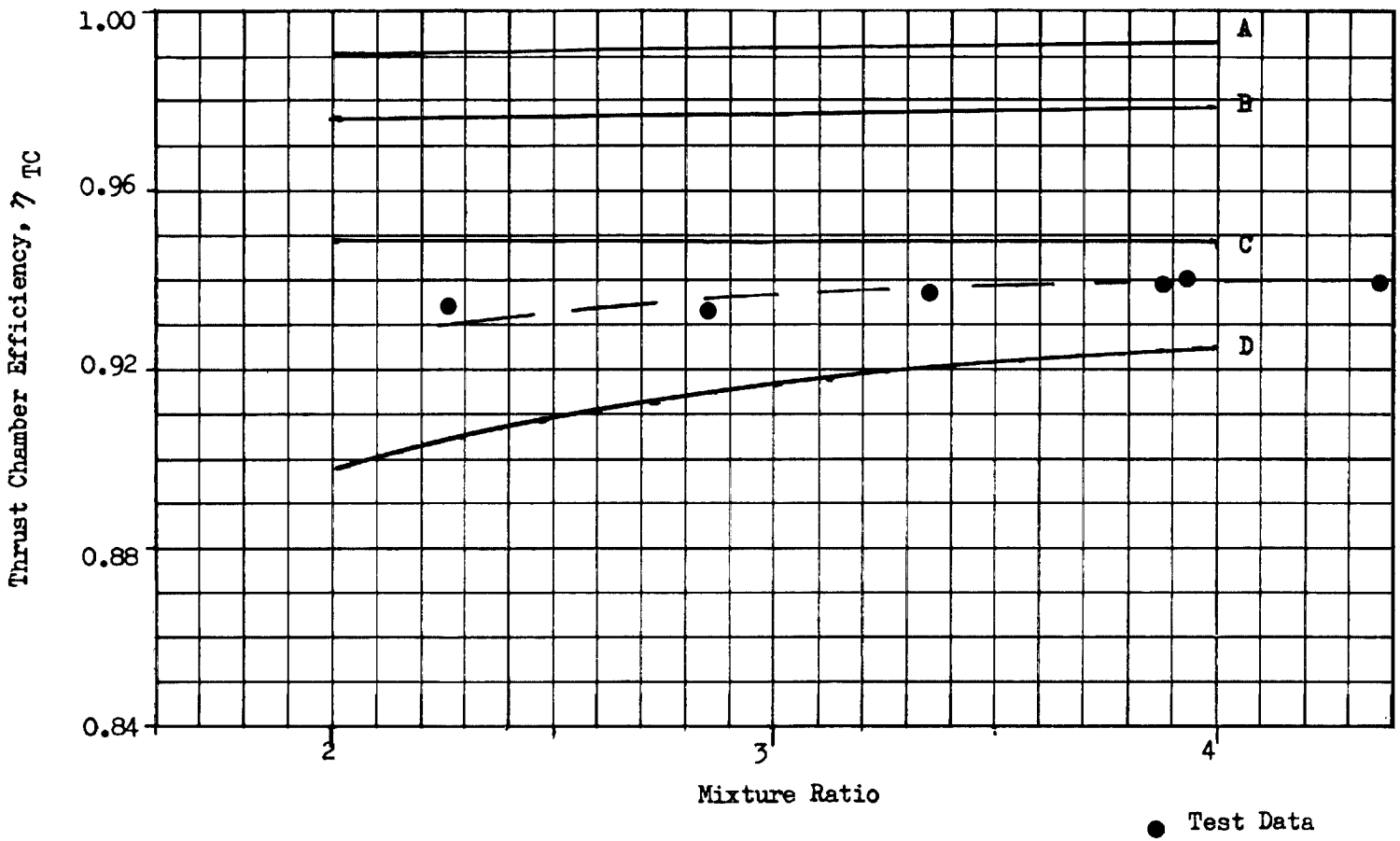

A. Heat Loss
B. Heat Loss and Divergence
C. Heat Loss, Divergence and Boundary Layer
D. Heat Loss, Divergence, Boundary Layer and Kinetics

Figure 50. Thrust Chamber Efficiency for OF_2/B_2H_6 at a Chamber Pressure of 100 psia for the 15-degree Cone.

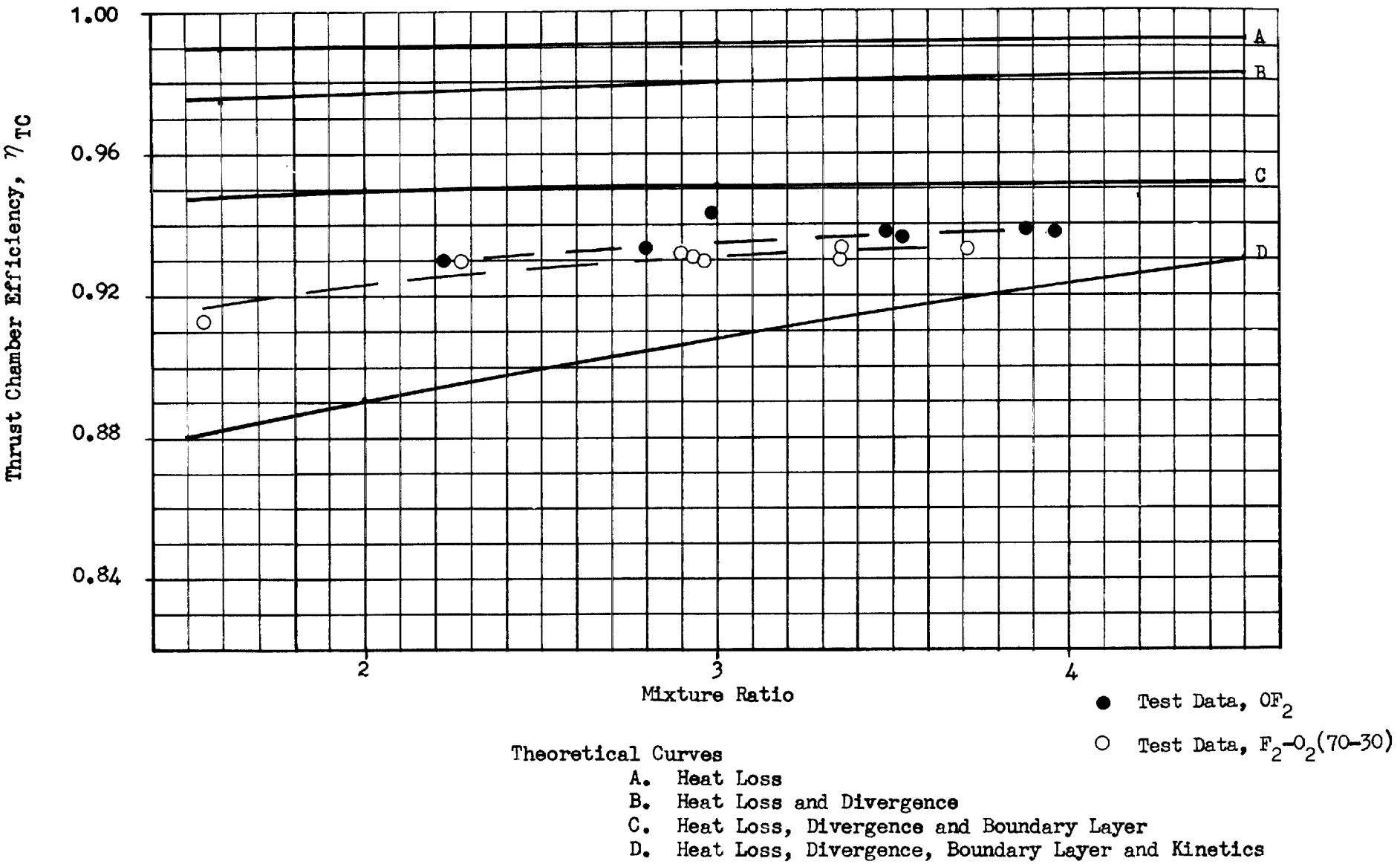

Figure 51. Thrust Chamber Efficiency for OF_2/B_2H_6 and F_2-O_2 (70-30)/B_2H_6 at a chamber pressure of 100 psia for the 70-percent Bell

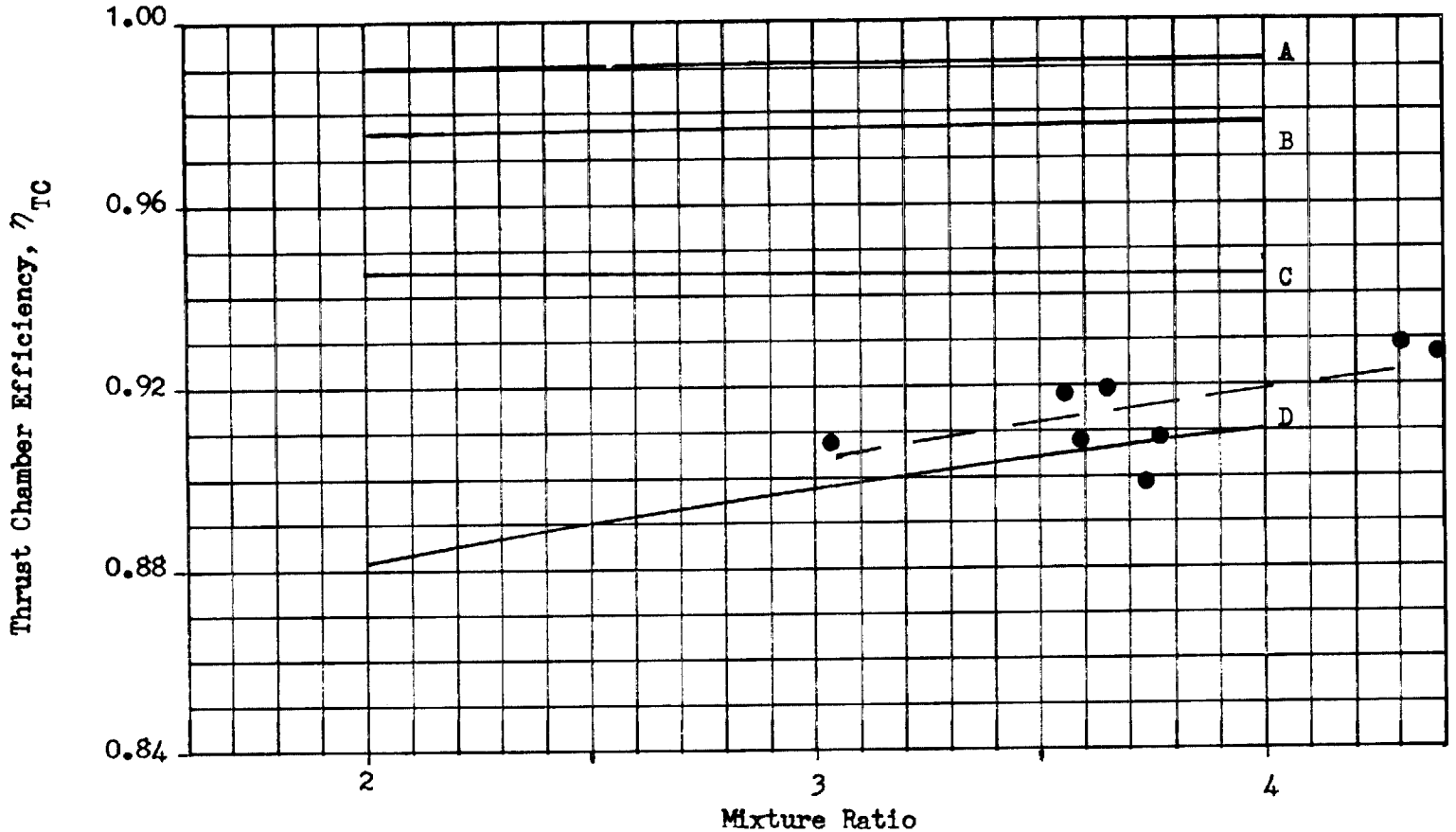

Theoretical Curves

A. Heat Loss
B. Heat Loss and Divergence
C. Heat Loss, Divergence and Boundary Layer
D. Heat Loss, Divergence, Boundary Layer and Kinetics

Figure 52. Thrust Chamber Efficiency for F_2-O_2(70-30)/B_2H_6(Gas) at a Chamber Pressure of 55 psia for the 15-degree Cone

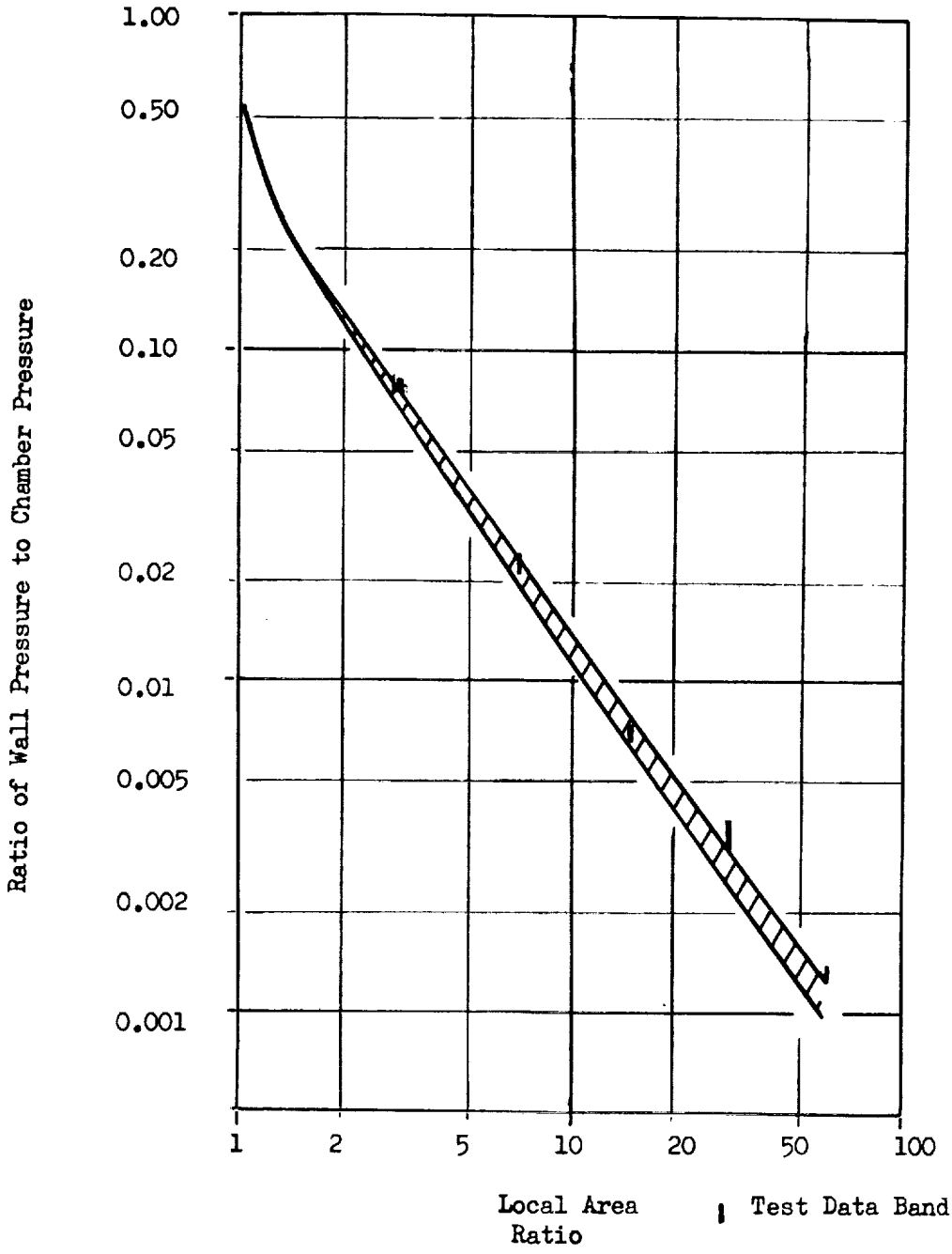

Figure 53. Effect of Area Ratio on Nozzle Wall Pressure Correlation for OF_2/B_2H_6 and F_2-O_2(70-30)/B_2H_6 Cone at 100 psia Chamber Pressure.

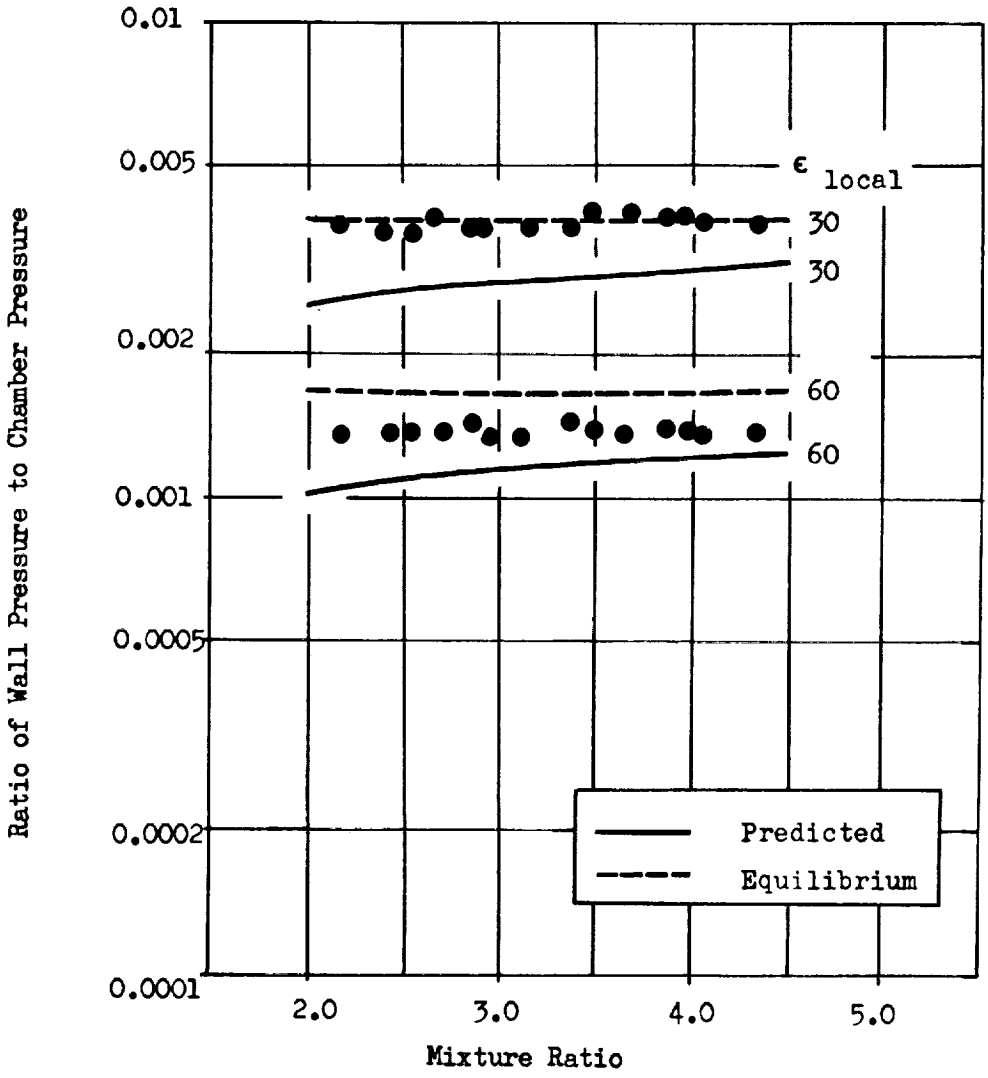

Figure 54. Effect of Mixture Ratio on Nozzle Wall Pressure Correlation for OF_2/B_2H_6 and F_2-O_2(70-30)/B_2H_6 for 15-degree Cone at 100 psia Chamber Pressure.

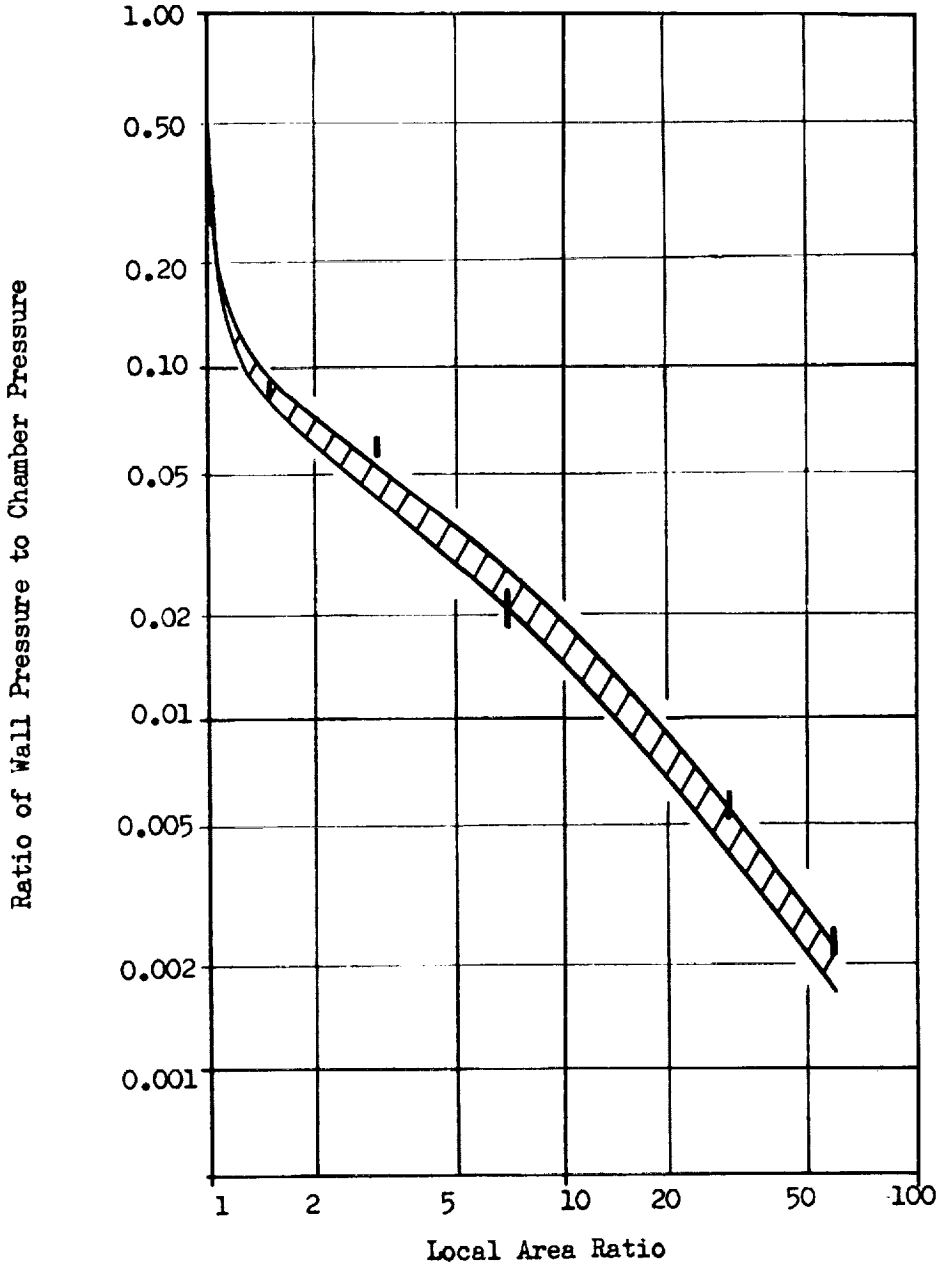

Figure 55. Effect of Area Ratio on Nozzle Wall Pressure Correlation for OF_2/B_2H_6 and $F_2-O_2(70-30)/B_2H_6$ for the 70-percent Bell at 100 psia Chamber Pressure

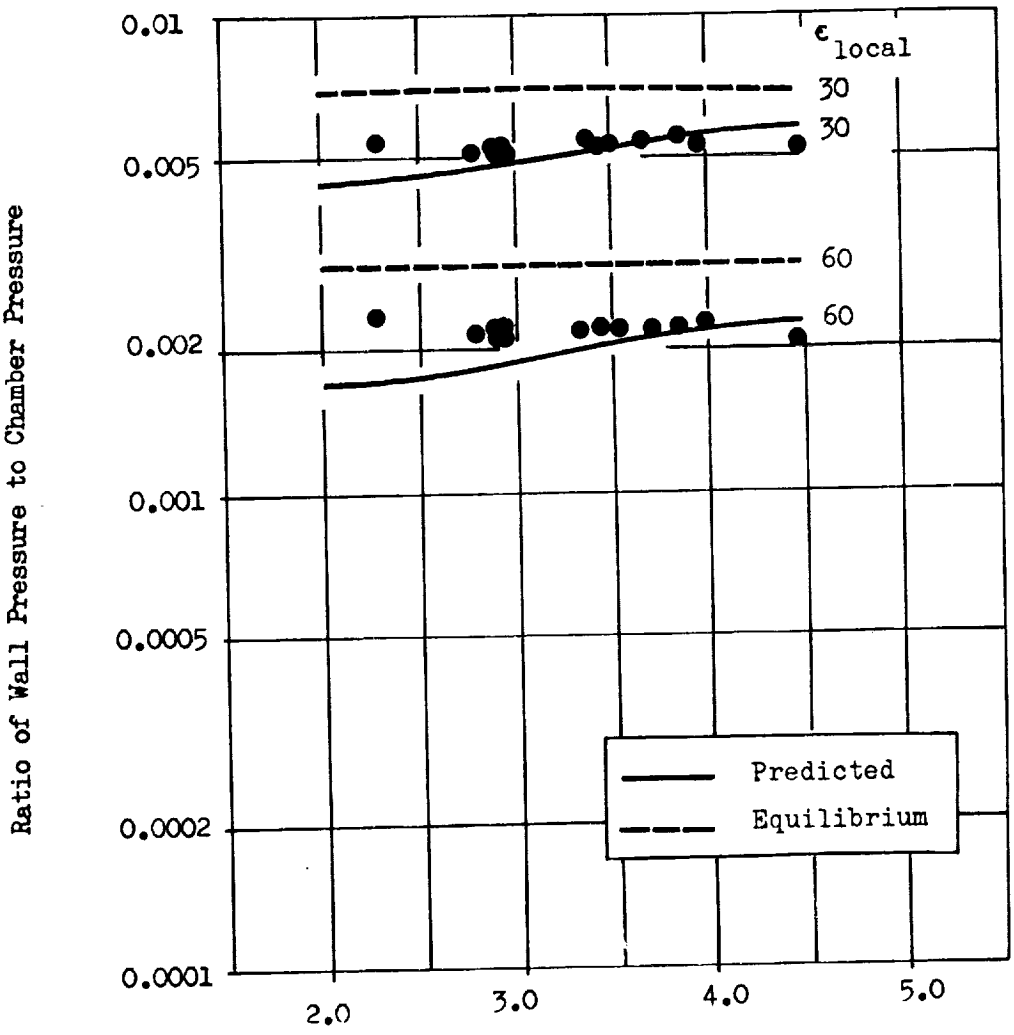

Figure 56. Effect of Mixture Ratio on Nozzle Wall Pressure Correlation for OF_2/B_2H_6 and F_2-O_2(70-30)/B_2H_6 for the 70-percent Bell at 100 psia Chamber Pressure.

The dominant presence of boron and its compounds in the exhaust makes it unlikely that the predictions of kinetic efficiency are accurate. Neither the mechanisms nor the rates for the boron related reactions are completely characterized.

One unusual trend, the increasing efficiency as mixture ratio increases, was predicted by the kinetic model. This variation is opposite to that observed for F_2-O_2/CH_4 and F_2/H_2 and there was some question as to its validity. However, the test data confirm the variation. The reasons for this reverse mixture ratio trend may be the increasing concentrations of the reaction promoting third bodies HF and H, Fig. 57. The concentrations of these species are nearly constant for F_2/H_2 and F_2-$O_2(CH_4)$, Fig. 58 and 59.

F_2/H_2

The thrust chamber efficiencies for F_2/H_2 are shown in Figs. 60 through 71. The agreement between predicted and measured values is excellent. The selected rate constants matched the data over a wide range of pressures, mixture ratios and nozzle contours. With F_2/H_2, for which thrust chamber efficiency was predictable, nozzle wall pressures were also predictable as seen for example in Fig. 72. A more comprehensive presentation of the F_2/H_2 data is in Ref. 4.

The experimental efficiencies shown in Ref. 4 are slightly different from those shown here because of the change in stagnation pressure interpretation. The predicted curves also are different because of a change in boundary layer calculation procedure. These changes are detailed in Section V. The result of the changes was to bring the theory and data into better agreement. In particular, the relative performance of the bell and cone, previously a problem area, was resolved by the new boundary layer approach.

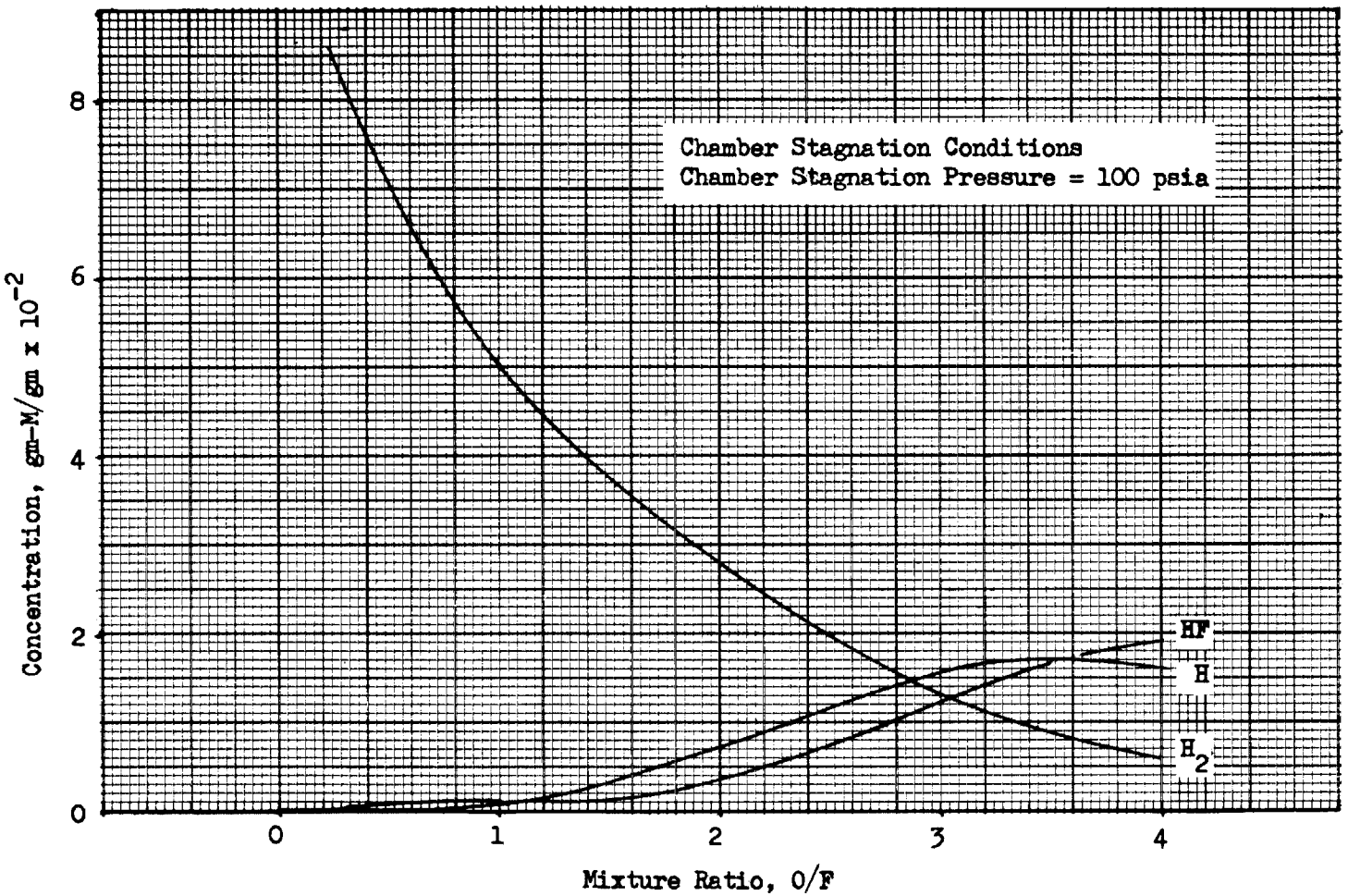

Figure 57. Concentration of Important Combustion Products for OF_2/B_2H_6

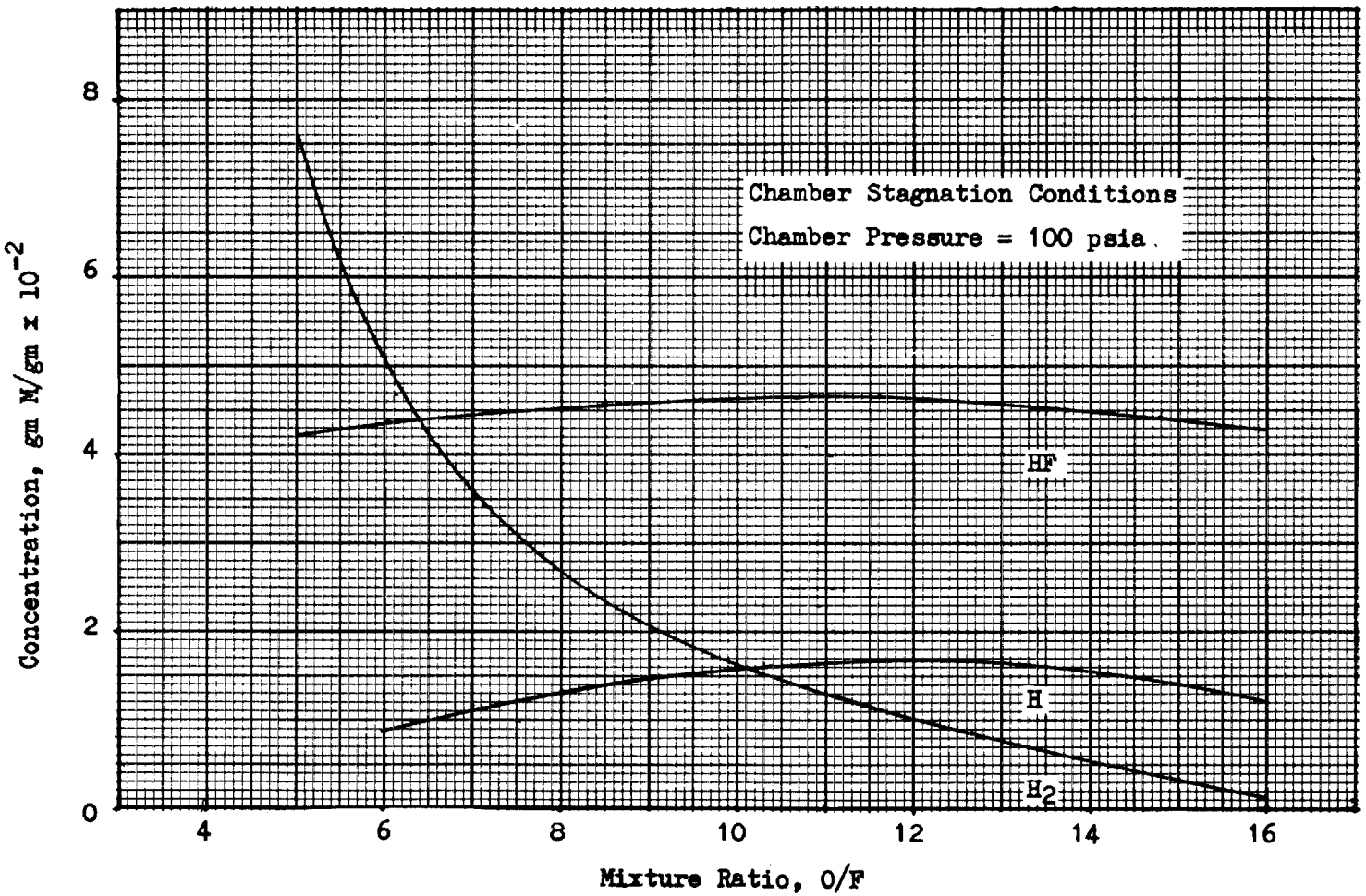

Figure 58. Concentration of Important Combustion Products for F_2/H_2.

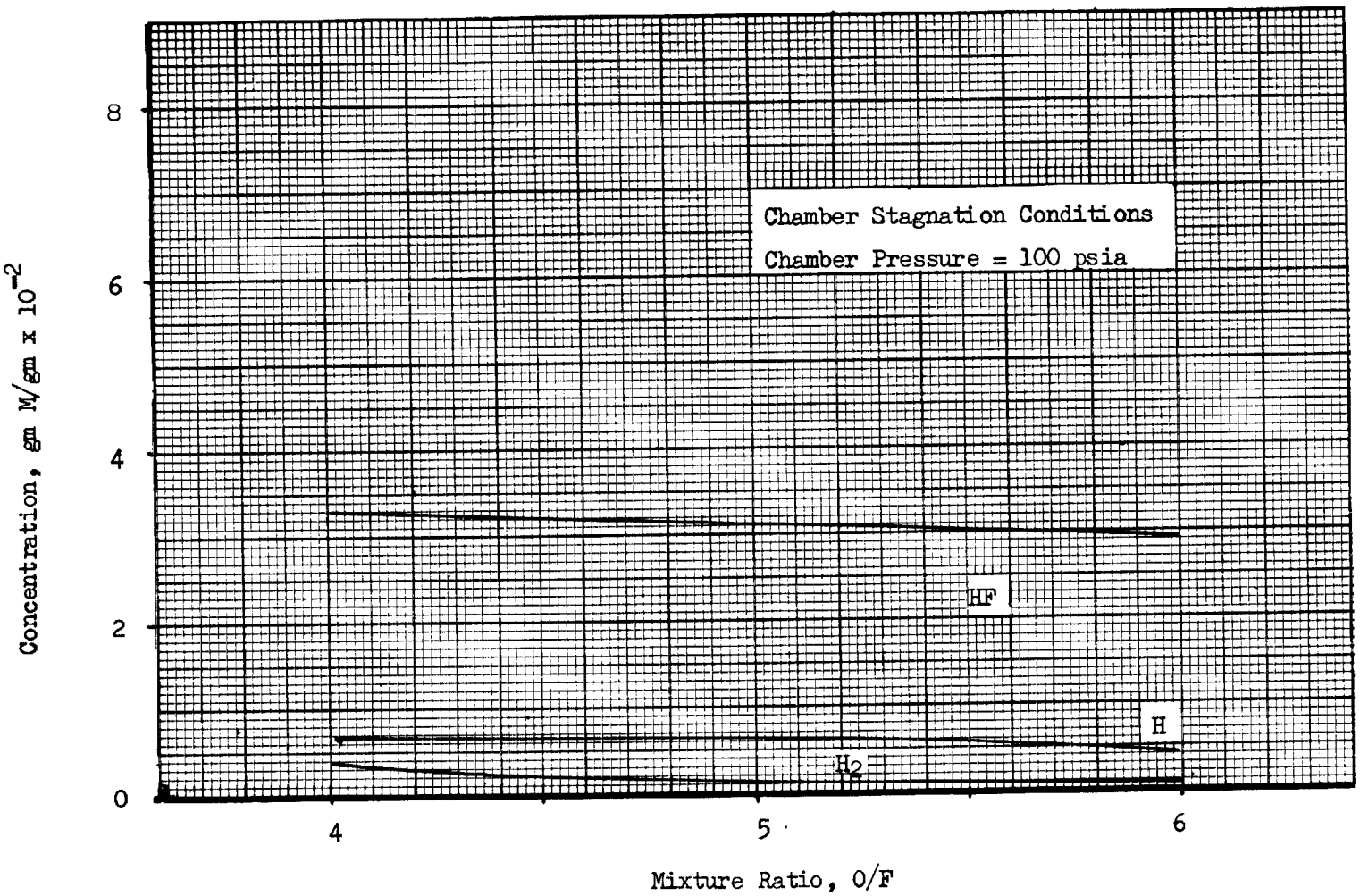

Figure 59. Concentration of Important Combustion Products for F_2-O_2(82.5-17.5)/CH_4

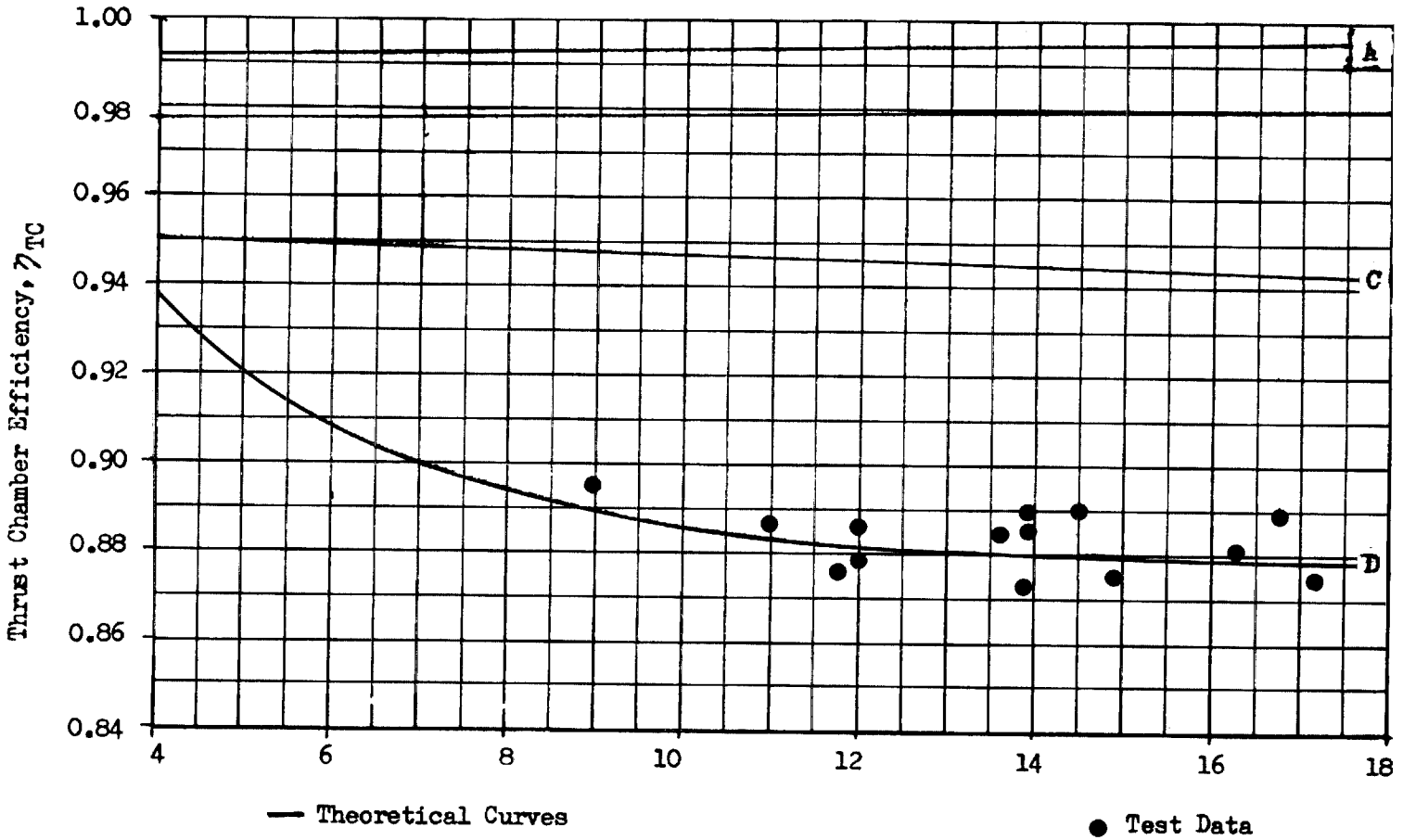

A. Heat Loss
B. Heat Loss and Divergency
C. Heat Loss, Divergence and Boundary Layer
D. Heat Loss, Divergency, Boundary Layer and Kinetics

Figure 60. Thrust Chamber Efficiency for F_2/H_2 Long Throat 15-Degree Conical Nozzle, 50 psia

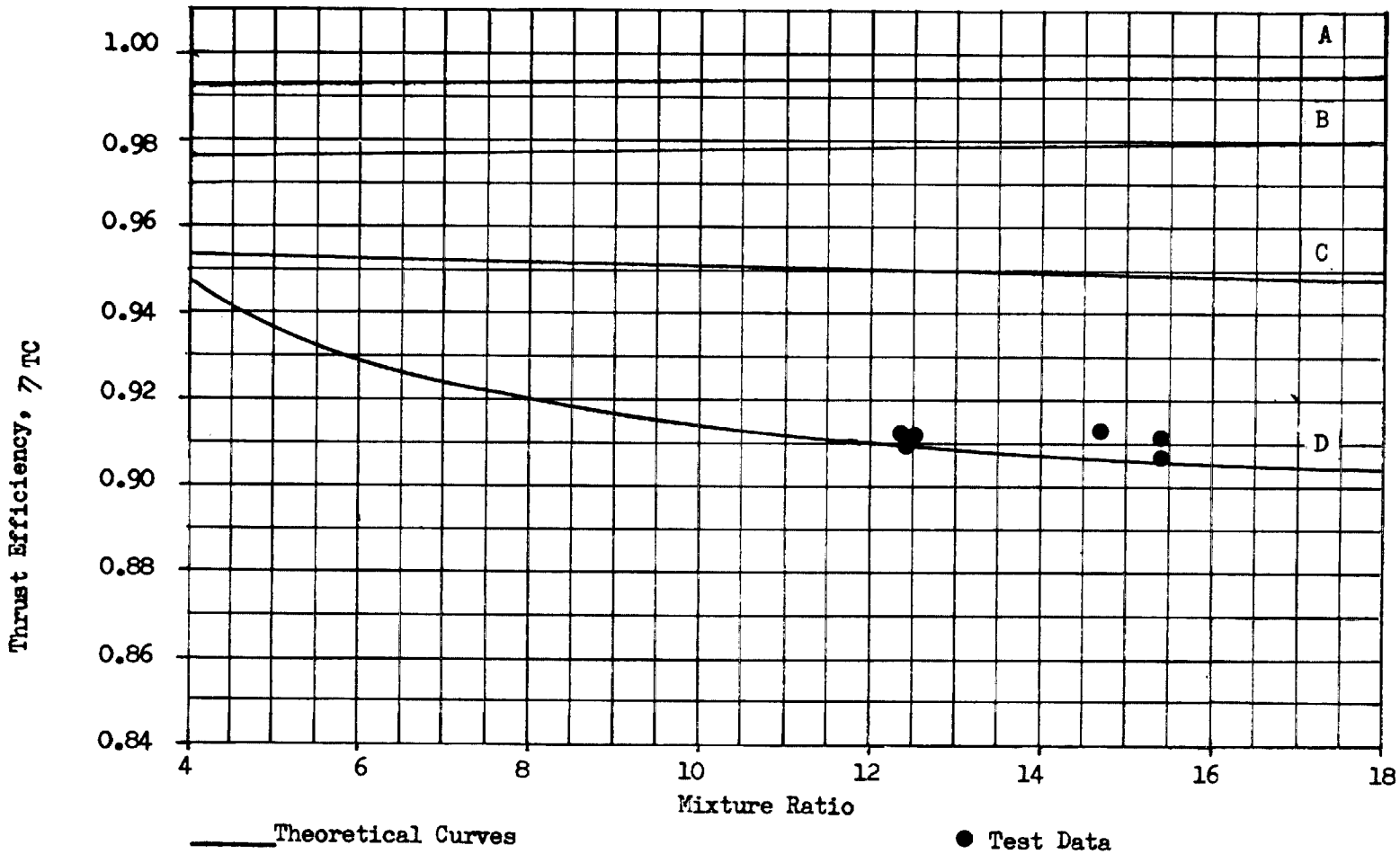

A. Heat Loss
B. Heat Loss and Divergency
C. Heat Loss, Divergence, and Boundary Layer
D. Heat Loss, Divergence, Boundary Layer and Kinetics

Figure 61. Thrust Chamber Efficiency for F_2/H_2, Long Throat 15-Degree Conical Nozzle, 100 psia

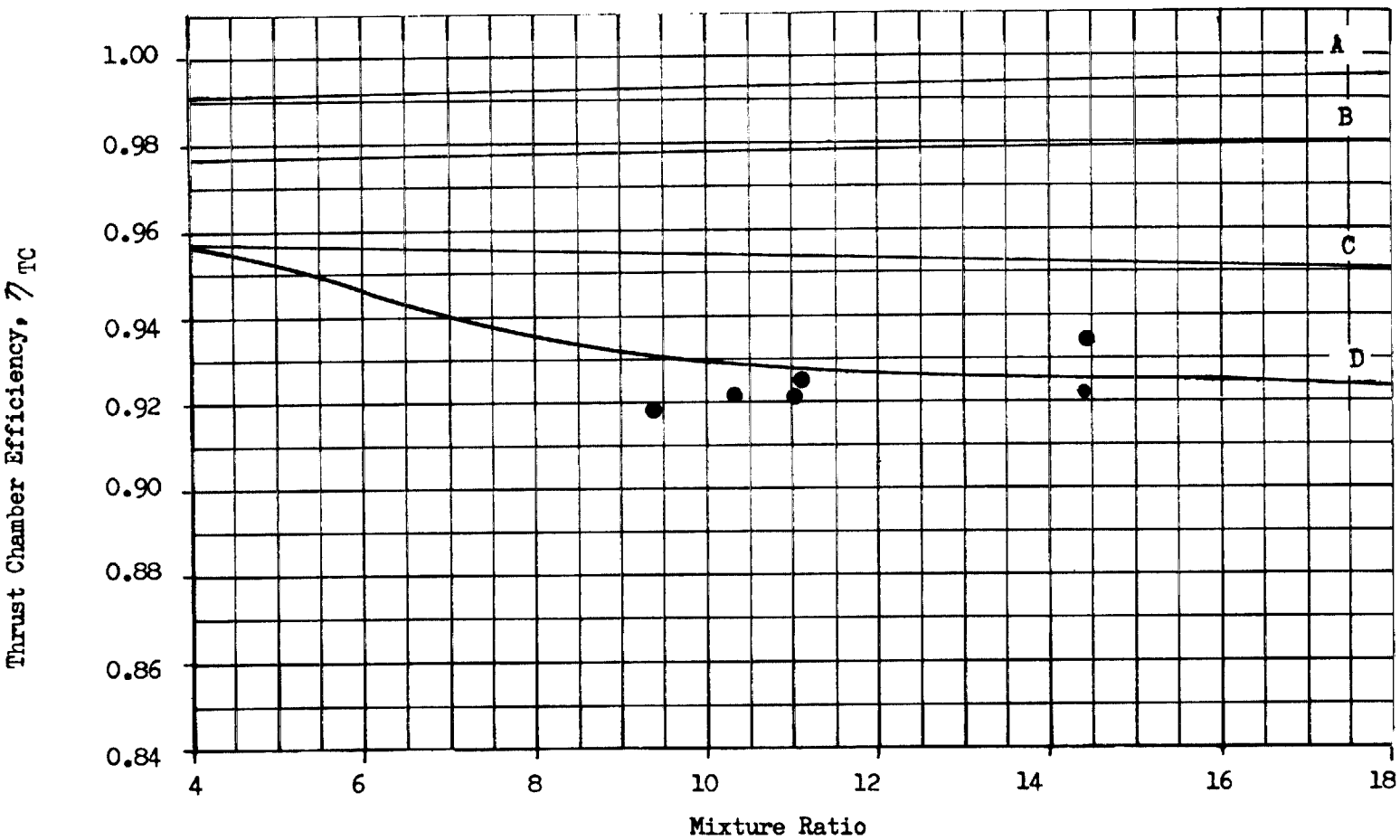

— Theoretical Curves

A. Heat Loss
B. Heat Loss and Divergence
C. Heat Loss, Divergence and Boundary Layer
D. Heat Loss, Divergence, Boundary Layer and Kinetics

● Test Data

Figure 62. Thrust Chamber Efficiency for F_2/H_2 Long Throat 15-Degree Conical Nozzle, 200 psia

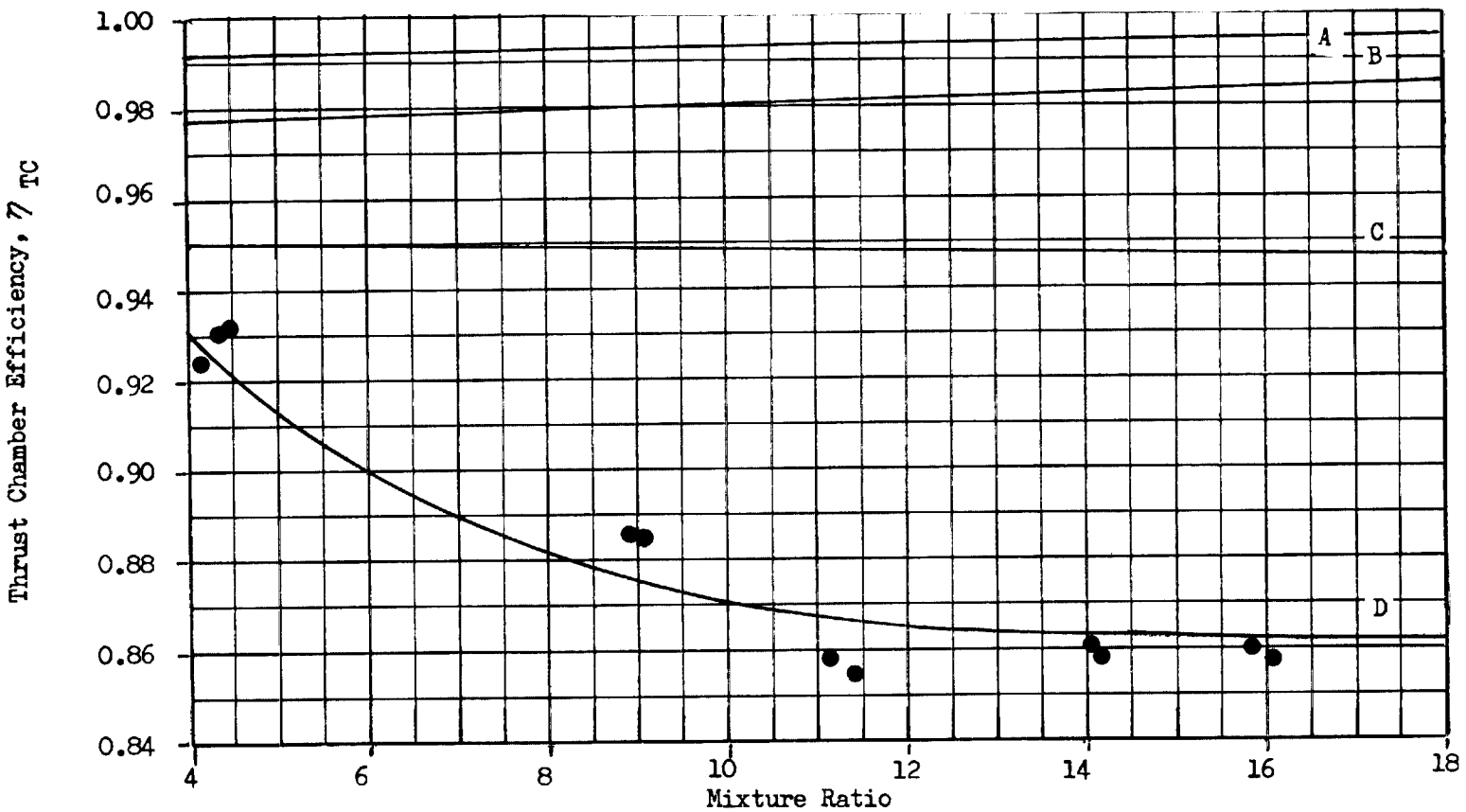

— Theoretical Curves

A. Heat Loss
B. Heat Loss and Divergence
C. Heat Loss, Divergence and Boundary Layer
D. Heat Loss, Divergence, Boundary Layer and Kinetics

● Test Data

Figure 63. Thrust Chamber Efficiency for F_2/H_2, 70-percent Bell Nozzle, 50 psia

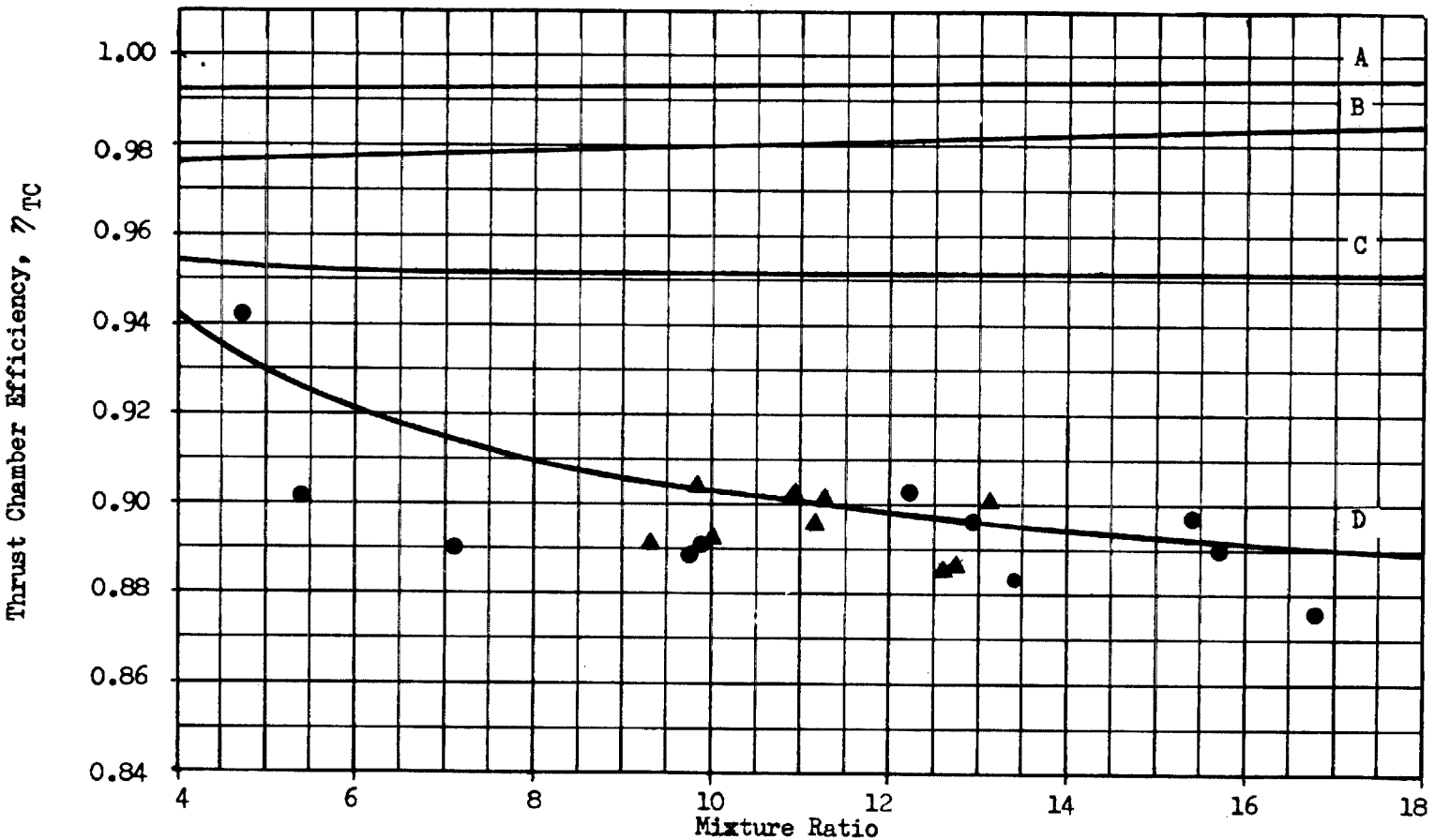

— Theoretical Curves
- A. Heat Loss
- B. Heat Loss and Divergence
- C. Heat Loss, Divergence and Boundary Layer
- D. Heat Loss, Divergence, Boundary Layer and Kinetics

▲ Test Data, Phase I

● Test Data, Activation Tests

Figure 64. Thrust Chamber Efficiency for F_2/H_2, 70-percent Bell Nozzle, 100 psia

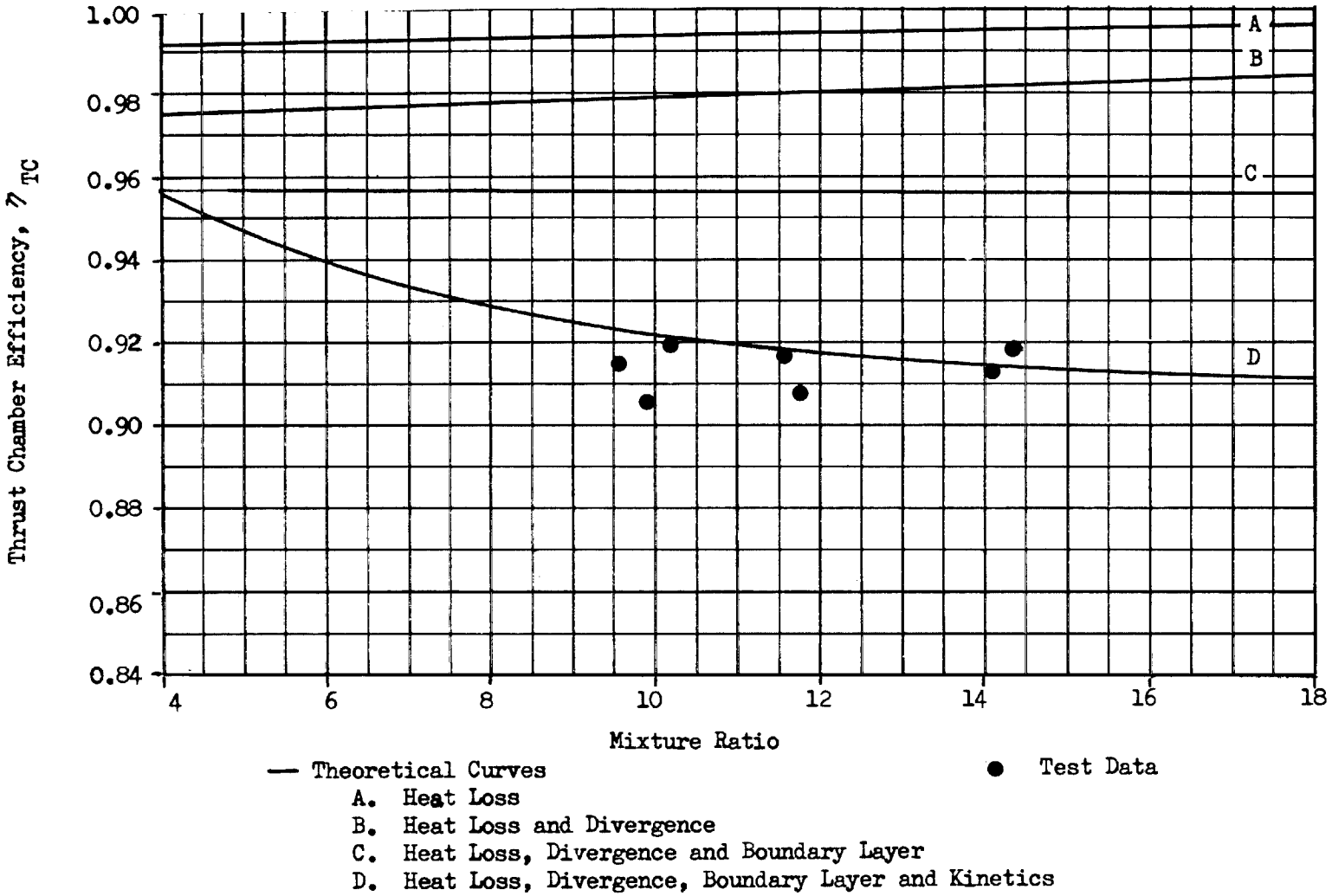

Figure 65. Thrust Chamber Efficiency for F_2/H_2, 70-percent Bell Nozzle, 200 psia

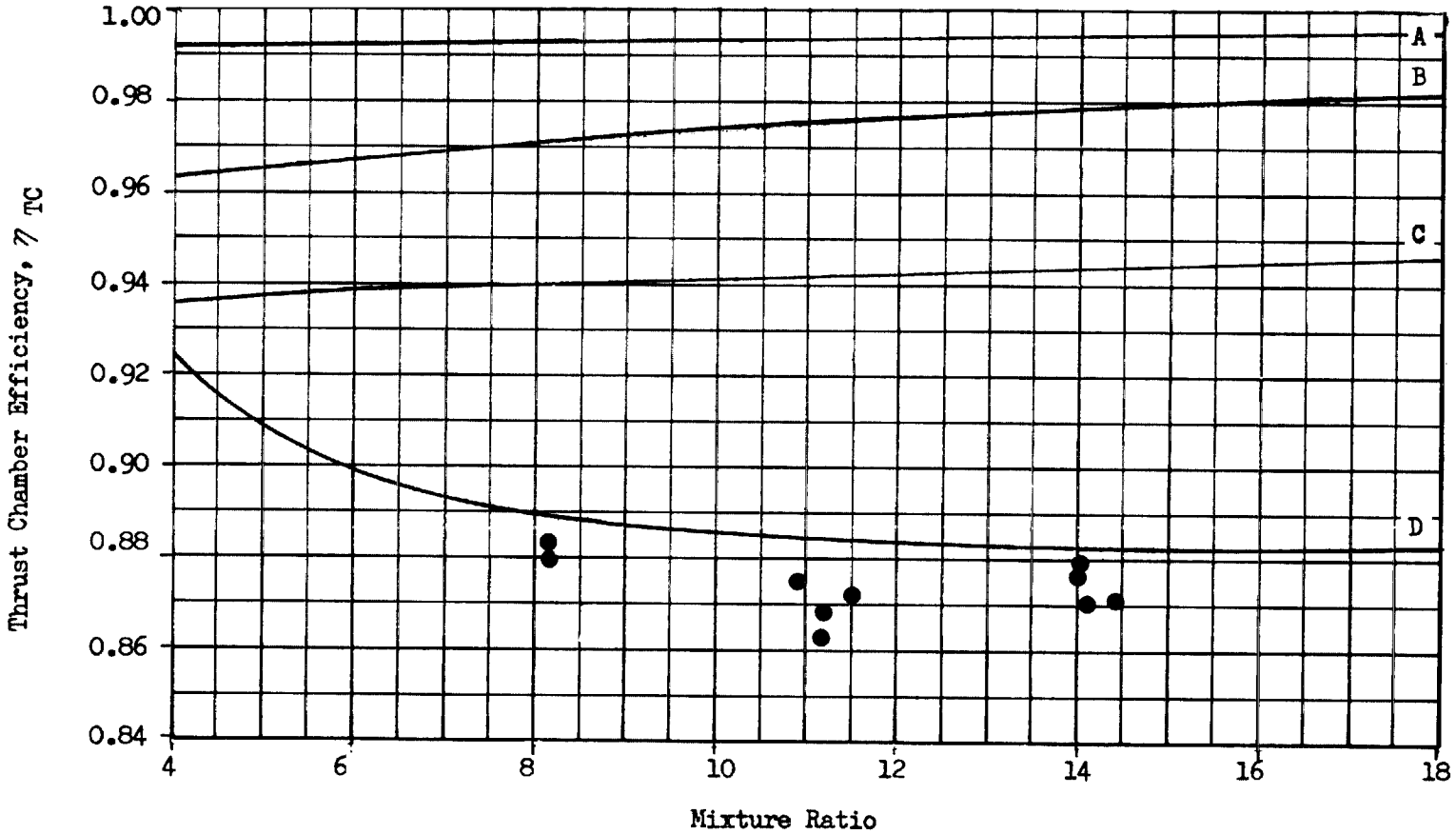

—— Theoretical Curves

A. Heat Loss
B. Heat Loss and Divergence
C. Heat Loss, Divergence and Boundary Layer
D. Heat Loss, Divergence, Boundary Layer and Kinetics

● Test Data

Figure 66. Thrust Chamber Efficiency for F_2/H_2, Controlled Expansion Nozzle, 50 psia

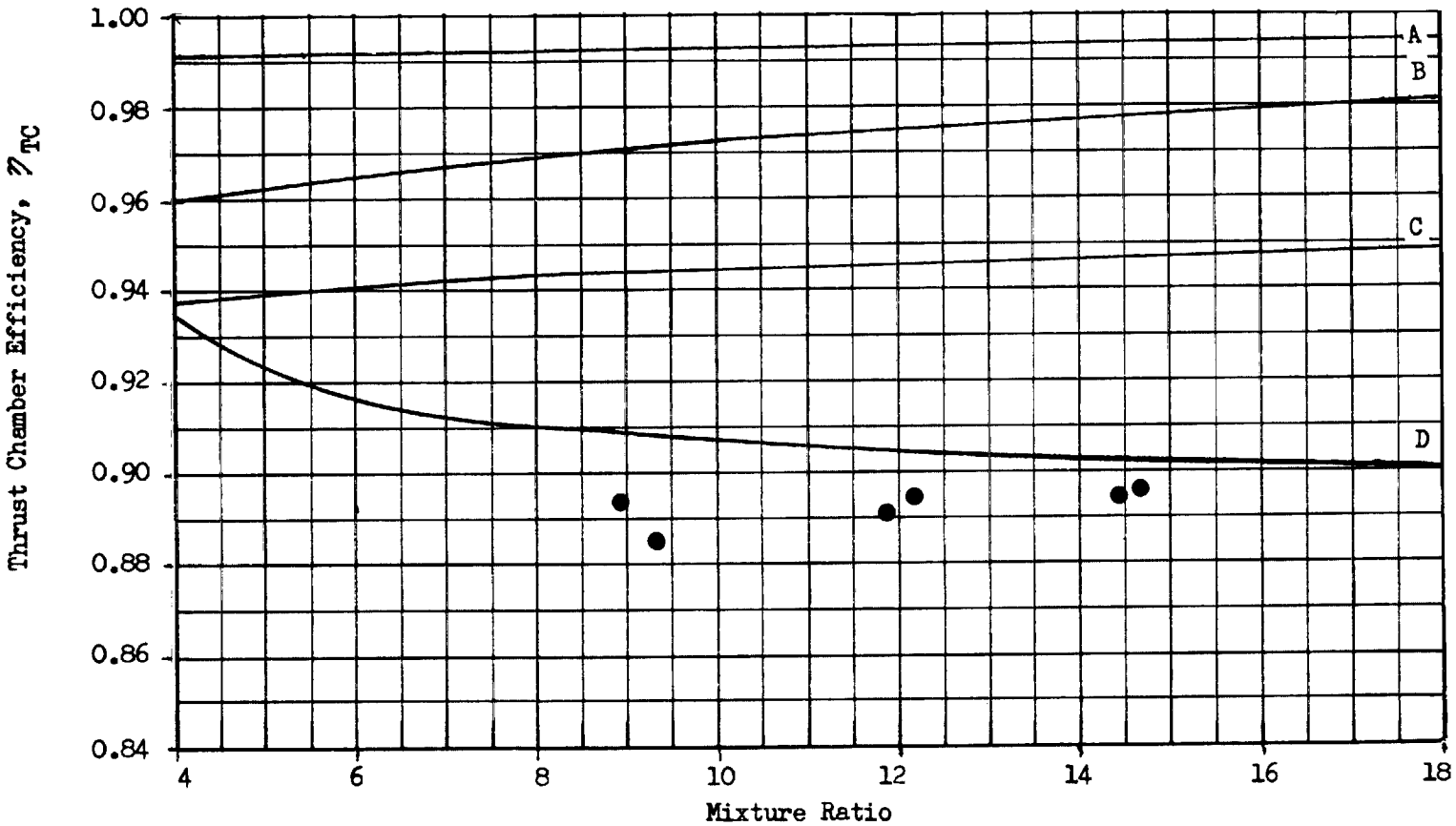

— Theoretical Curves

A. Heat Loss
B. Heat Loss and Divergence
C. Heat Loss, Divergence and Boundary Layer
D. Heat Loss, Divergence, Boundary Layer and Kinetics

● Test Data

Figure 67. Thrust Chamber Efficiency for F_2/H_2, Controlled Expansion Nozzle, 100 psia

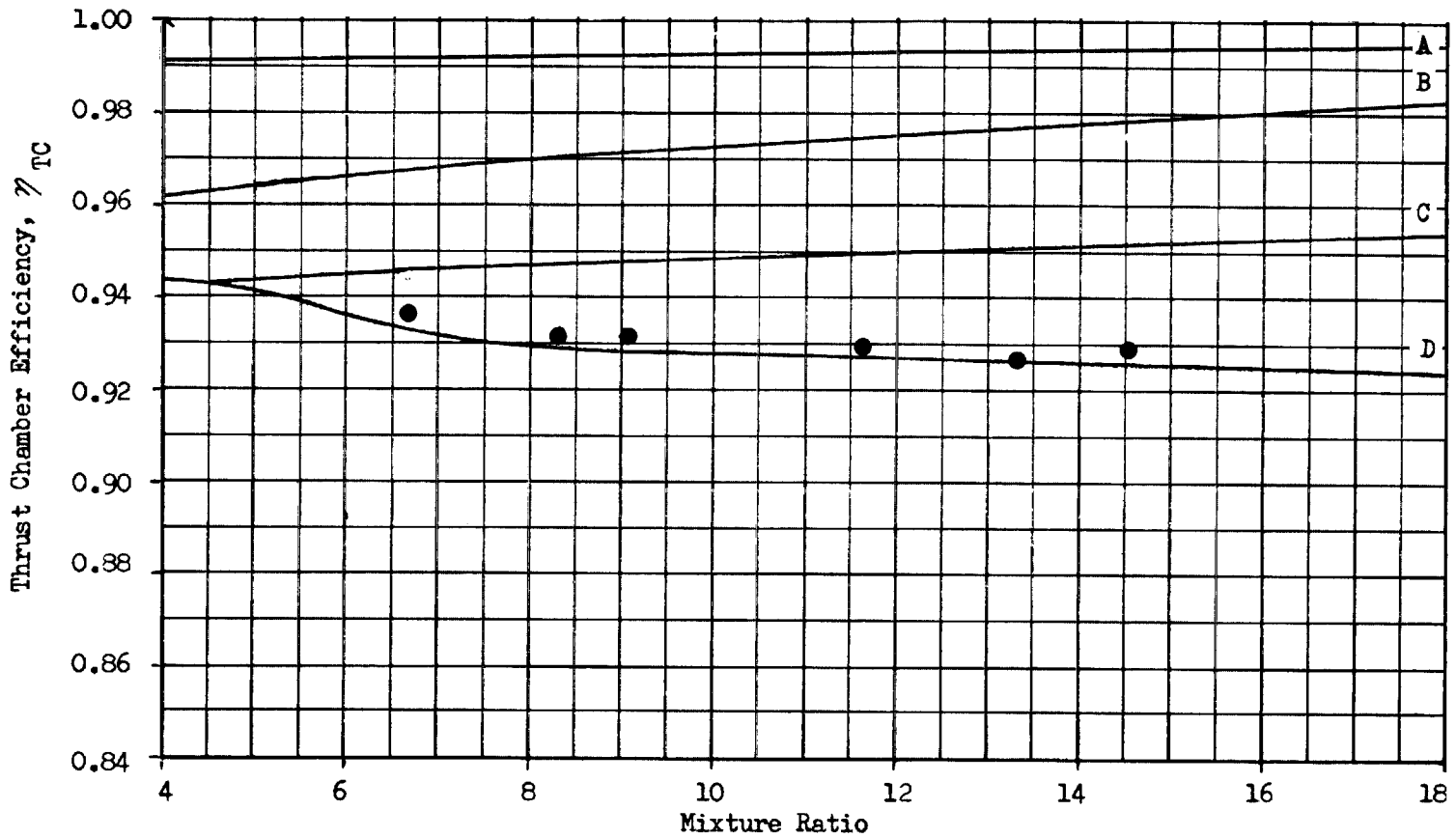

— Theoretical Curves

A. Heat Loss
B. Heat Loss and Divergence
C. Heat Loss, Divergence and Boundary Layer
D. Heat Loss, Divergence, Boundary Layer and Kinetics

● Test Data

Figure 68. Thrust Chamber Efficiency for F_2/H_2, Controlled Expansion Nozzle, 200 psia

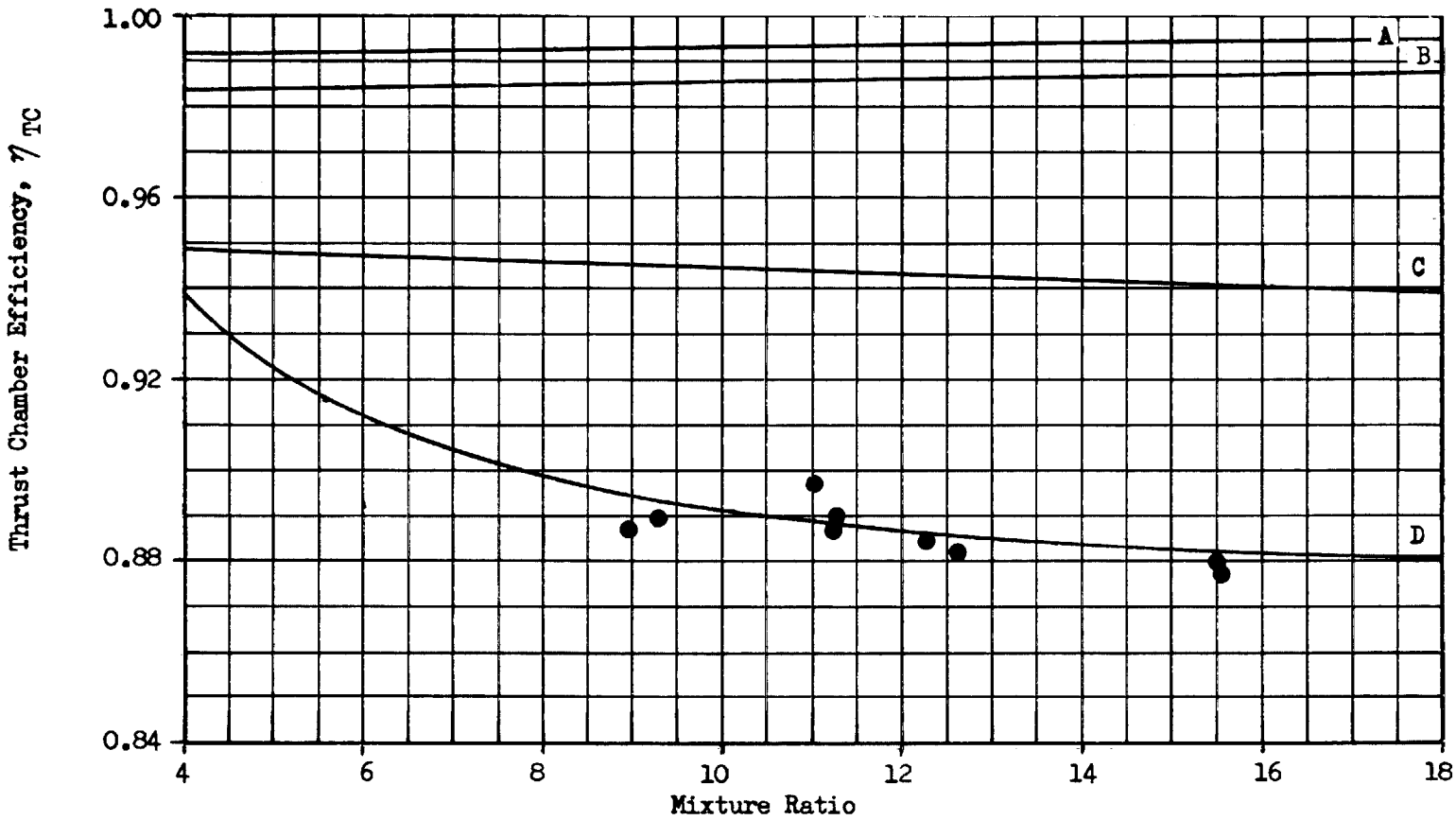

— Theoretical Curves

A. Heat Loss
B. Heat Loss and Divergence
C. Heat Loss, Divergence and Boundary Layer
D. Heat Loss, Divergence, Boundary Layer and Kinetics

Figure 69. Thrust Chamber Efficiency for F_2/H_2, 10-Degree Conical Nozzle, 50 psia

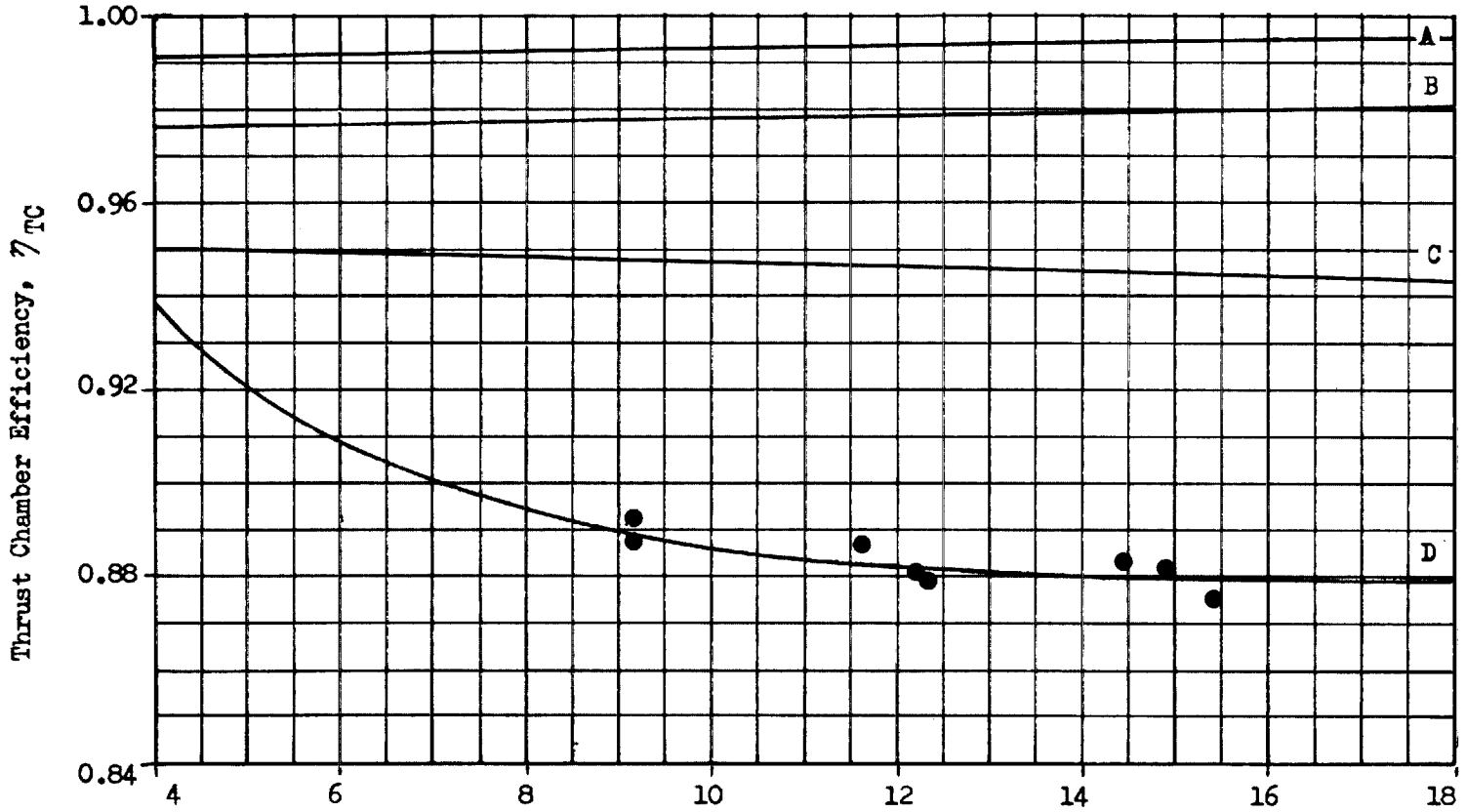

— Theoretical Curves

A. Heat Loss
B. Heat Loss and Divergence
C. Heat Loss, Divergence and Boundary Layer
D. Heat Loss, Divergence, Boundary Layer and Kinetics

● Test Data

Figure 70. Thrust Chamber Efficiency for F_2/H_2, Short Throat 15-Degree Conical Nozzle, 50 psia

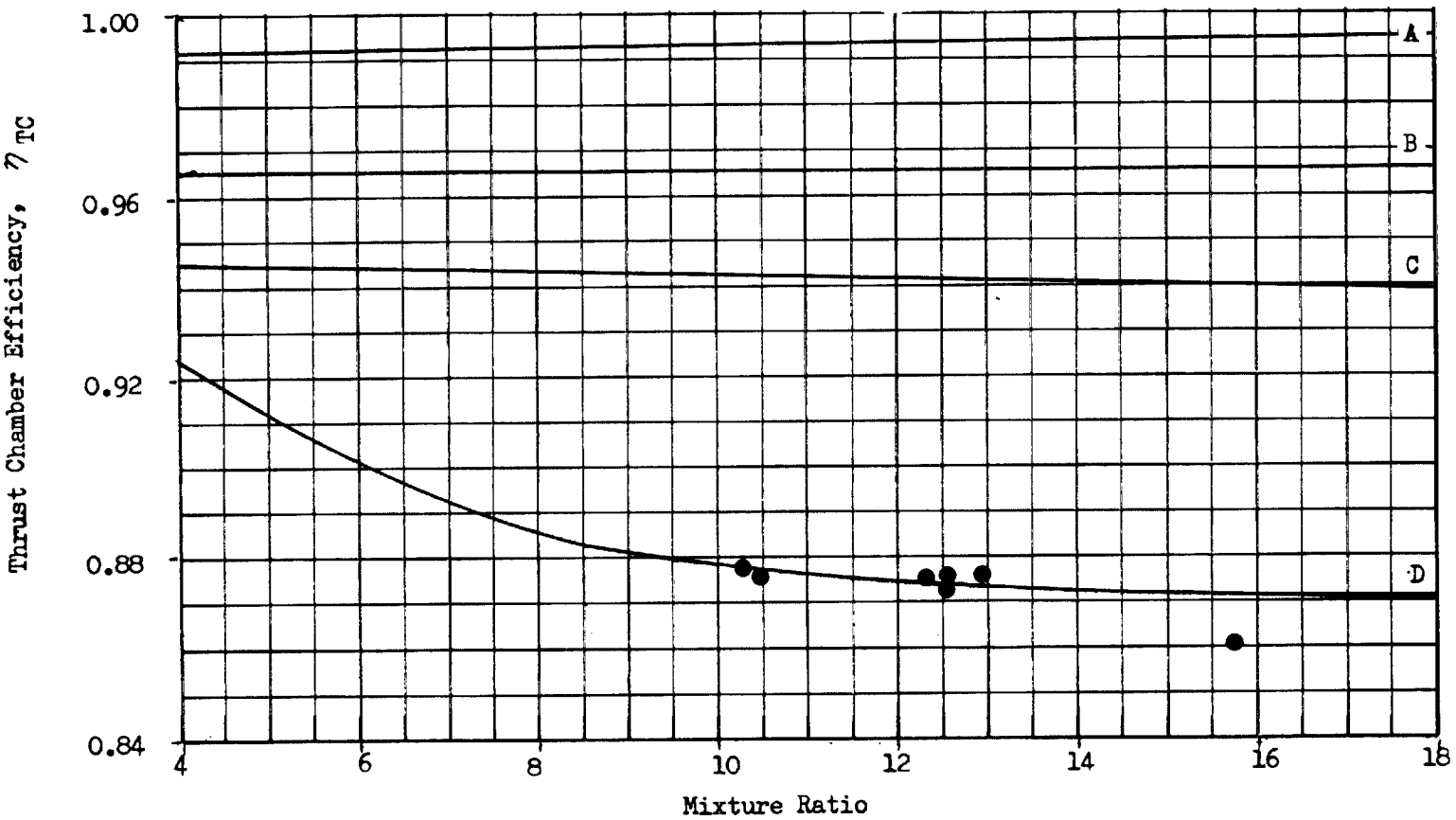

— Theoretical Curves

A. Heat Loss
B. Heat Loss and Divergency
C. Heat Loss, Divergency and Boundary Layer
D. Heat Loss, Divergency, Boundary Layer and Kinetics

● Test Data

Figure 71. Thrust Chamber Efficiency for F_2/H_2, 20-Degree Conical Nozzle, 50 psia

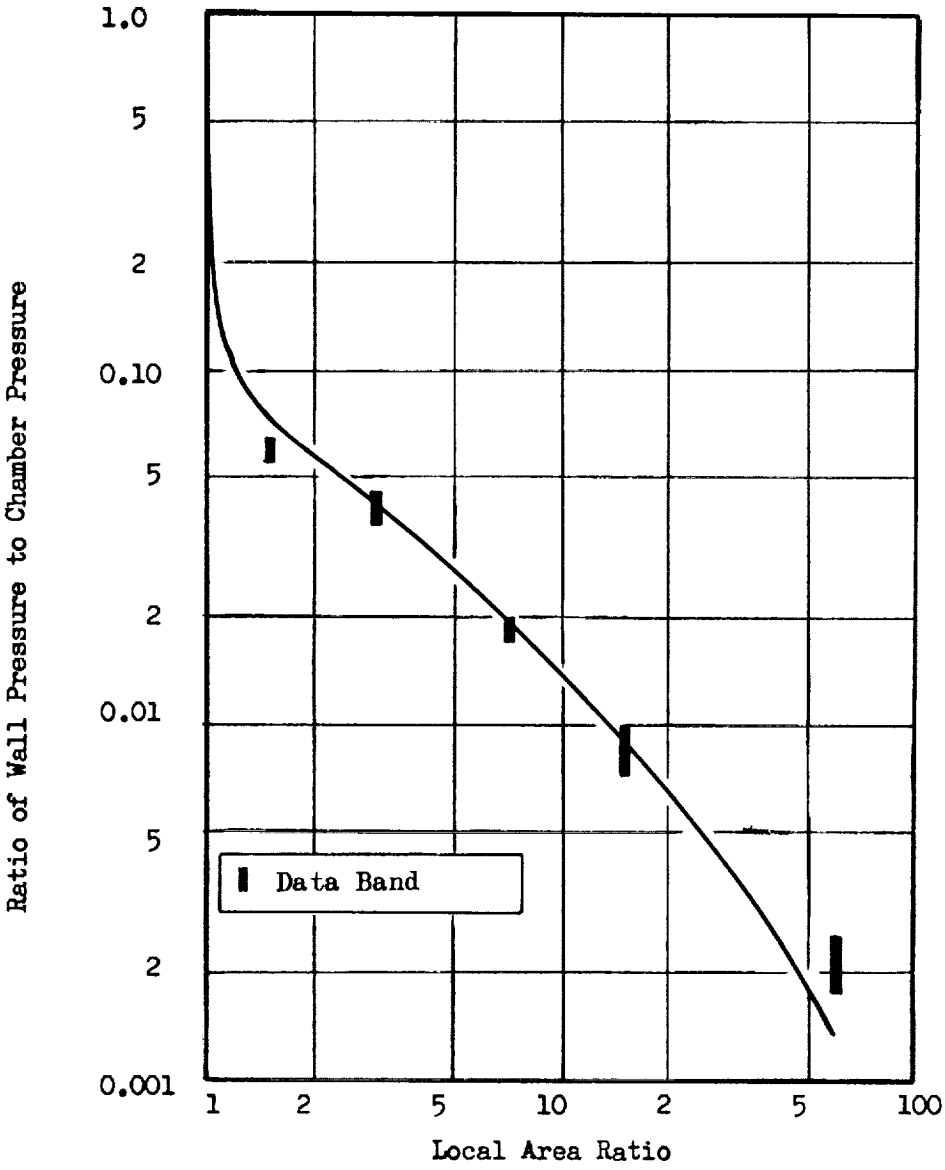

Figure 72. Effect of Area Ratio on Nozzle Wall Pressure for F_2/H_2 for the 70-percent Bell Nozzle at 50 psia Chamber Pressure

As shown in Fig. 64, the thrust chamber efficiency data from the facility activation tests were consistent with the data taken during Phase I. This consistency means that data from the two different test stands can be compared directly.

SECTION V

DATA INTERPRETATION PROCEDURES

Three terms are used in this report to describe the performance of the test engines. Specific impulse is defined as thrust divided by flowrate, corrected to vacuum conditions. For indication of loss modes and for prediction purposes, an injector efficiency including all losses caused by the nonideal propellant injector, and a thrust chamber efficiency including all losses caused by the nonideal combustion chamber and expansion nozzle are defined. The injector efficiency is the value of characteristic velocity efficiency that would have been achieved if the combustion chamber had been insulated and frictionless. The thrust chamber efficiency includes the thrust coefficient efficiency and the loss to characteristic velocity efficiency caused by the combustion chamber.

Each of the parameters used to describe the performance is calculated from test data. The specific impulse and thrust chamber efficiency are also predicted analytically. Although the manner of division of losses between injector and thrust chamber efficiencies is a matter of definition, the critical consideration is that the definitions based on test data and theory be rigorously consistent. This section contains brief descriptions of the procedures used to develop these performance parameters both from test results and from theoretical analysis.

PERFORMANCE DATA

To ensure the high reliability of the data required to determine the small performance differences expected on this program, the observable test parameters were corrected for all known effects in determining engineering

test data. Two areas in which major improvements in data reduction were made for this phase of the contract are throat stagnation pressure and fuel flowrate.

The manner of recording, averaging and converting the digital data to give engineering values of each parameter is straightforward and will not be discussed. The details of converting the measured engineering parameters to performance parameters are of interest in that failure to account for some effects such as nozzle throat size variation with temperature can make a significant difference in the calculated efficiencies.

Performance Calculation

The three performance parameters of interest are specific impulse, injector efficiency and thrust chamber efficiency.

The specific impulse is calculated as

$$I_s = \frac{F_{vacuum}}{\dot{W}_{Total}}$$

and is corrected only for exact propellant composition. For some comparisons, a normalized I_s is used as described later, however, this fact is always recorded on the figures. The injector efficiency is

$$\eta_{inj} = \frac{P_c A^*_g}{C^*_{Ideal} \dot{W}_{total}} + \left(1 - \eta_{HL_{C^*}}\right)$$

and the thrust chamber efficiency is

$$\eta_{TC} = \frac{F_{vacuum}}{P_c A^* C_{F_{Ideal}}} - \left(1 - \eta_{HL_{C^*}}\right)$$

The injector efficiency for low-area-ratio tests is also calculated from thrust as

$$\eta_{Inj} = \frac{I_s}{I_{s_{Ideal}} \left[\eta_{TC} + \left(1 - \eta_{HL_{C^*}}\right)\right]} + \left(1 - \eta_{HL_{C^*}}\right)$$

For this calculation, neither P_c nor A* needs to be known. However, the low area ratio thrust chamber efficiency prediction must be accurate.

Thrust Data

The vacuum thrust is calculated by averaging the four thrust measurements and correcting for ambient pressure by:

$$F_{vacuum} = F_{average} + P_a A_e$$

Because all tests were conducted at low environmental pressure, the correction term was small (2 to 3 percent) compared to the total; therefore, small errors for base effects or small errors in pressure or area are negligible. No other corrections are necessary because the test stand design and calibrating procedures are such that corrections for external loads on the engine are eliminated.

Flowrate Data

The gaseous fuel flowrate is measured using a venturi with choked flow. The liquid oxidizer flowrate is measured using turbine flowmeters in series. The data taken for the venturi are the pressure and temperature in the upstream portion of the venturi. For the flowmeters; pressure, temperature and rotational frequency are recorded. The relative flowmeter agreement throughout the program has been approximately 0.1 percent.

The fuel flow for choked conditions can be calculated knowing only the pressure and temperature at the entrance to the venturi. For hydrogen, the perfect gas law was used to calculate the thermodynamic properties during expansion. Methane and diborane are much closer to their critical points at the nominal temperatures used for testing than is hydrogen; and for these gases, compressibility effects had to be considered. A real gas venturi analysis procedure was developed and used for both CH_4 and B_2H_6. The development of the analytical procedure is described in Appendix D.

The oxidizer flowrate is found from the liquid pressure and temperature, and rotational frequency of the flowmeter. The density and viscosity of the liquid oxidizer are found from the pressure and temperature. The rotational frequency is converted to a Reynolds number function by dividing the frequency by the kinematic viscosity. The conversion from corrected frequency to gallons is found from the flowmeter calibration curve. This value is finally corrected for flowmeter shrinkage from the calibration temperature to the oxidizer temperature.

Throat Area

The physical throat area is measured before and after each test series. Because the hardware increases in temperature continuously during a test series, a correction must be applied to account for hardware throat growth prior to each test. This pretest throat area (A_t) is then corrected for aerodynamic and boundary layer discharge coefficients and throat shrinkage during the test to give the actual available flow area (A^*).

Chamber Pressure

The chamber pressure (throat stagnation pressure) is calculated from the wall static pressure measured prior to start of contraction but after all major combustion has taken place. The wall static pressure is corrected empirically to the core static pressure. The core static pressure is then corrected to a throat stagnation pressure using the relationship

$$P_c = P_{static}\left[1 + \frac{n-1}{2} M^2\right]^{\frac{n}{n-1}}$$

where the n used is a process exponent for the equilibrium expansion and not the local specific heat ratio.

The combustion chamber which is heavily instrumented for an examination of the complete pressure profile indicated a pressure rise just prior to start of contraction caused by aerodynamic effects. The combustion chamber geometry is shown in Fig. 73 with the position of the pressure taps. The full wall pressure profile is recorded on each hot firing test and is summarized for each of the major propellant combinations in Fig. 74.

Full-scale tests using GN_2 at a pressure of 100 psia were performed. The results of the GN_2 flow tests are also shown in Fig. 74. The pressure increase immediately upstream of the start of contraction is again evident. These results are particularly significant because there are no combustion or injector pattern effects and the hardware is the same as the hot firing hardware so there are no scale or instrumentation discrepancies.

Other checks on the validity of the pressure corrections were made by re-examination of the cold-flow tests of subscale hardware performed in Phase I and by use of a simplified electric analogy. The results of the subscale cold-flow tests confirm the full scale data. Results of the

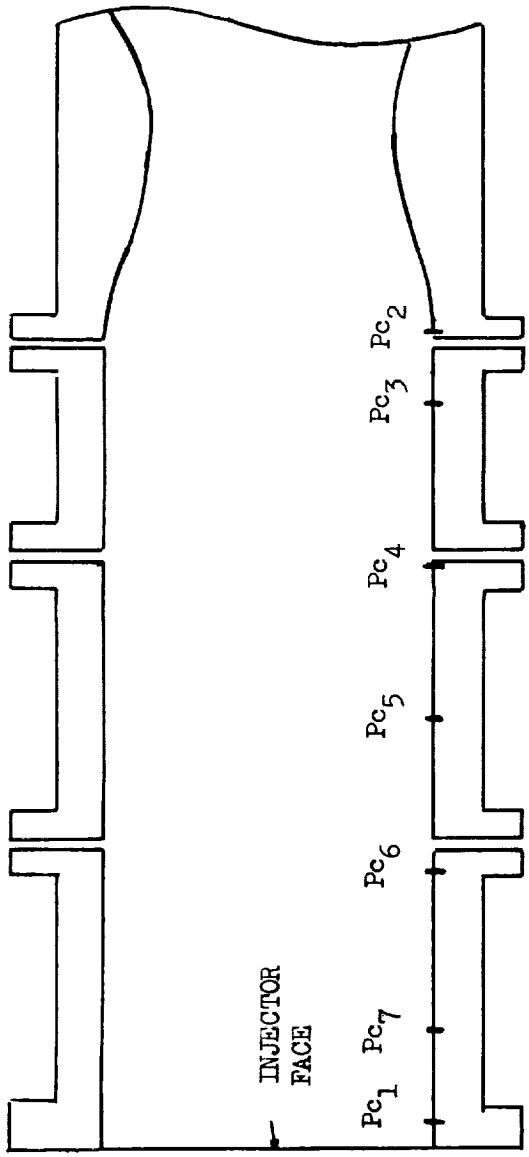

Figure 73. Pressure Tap Locations

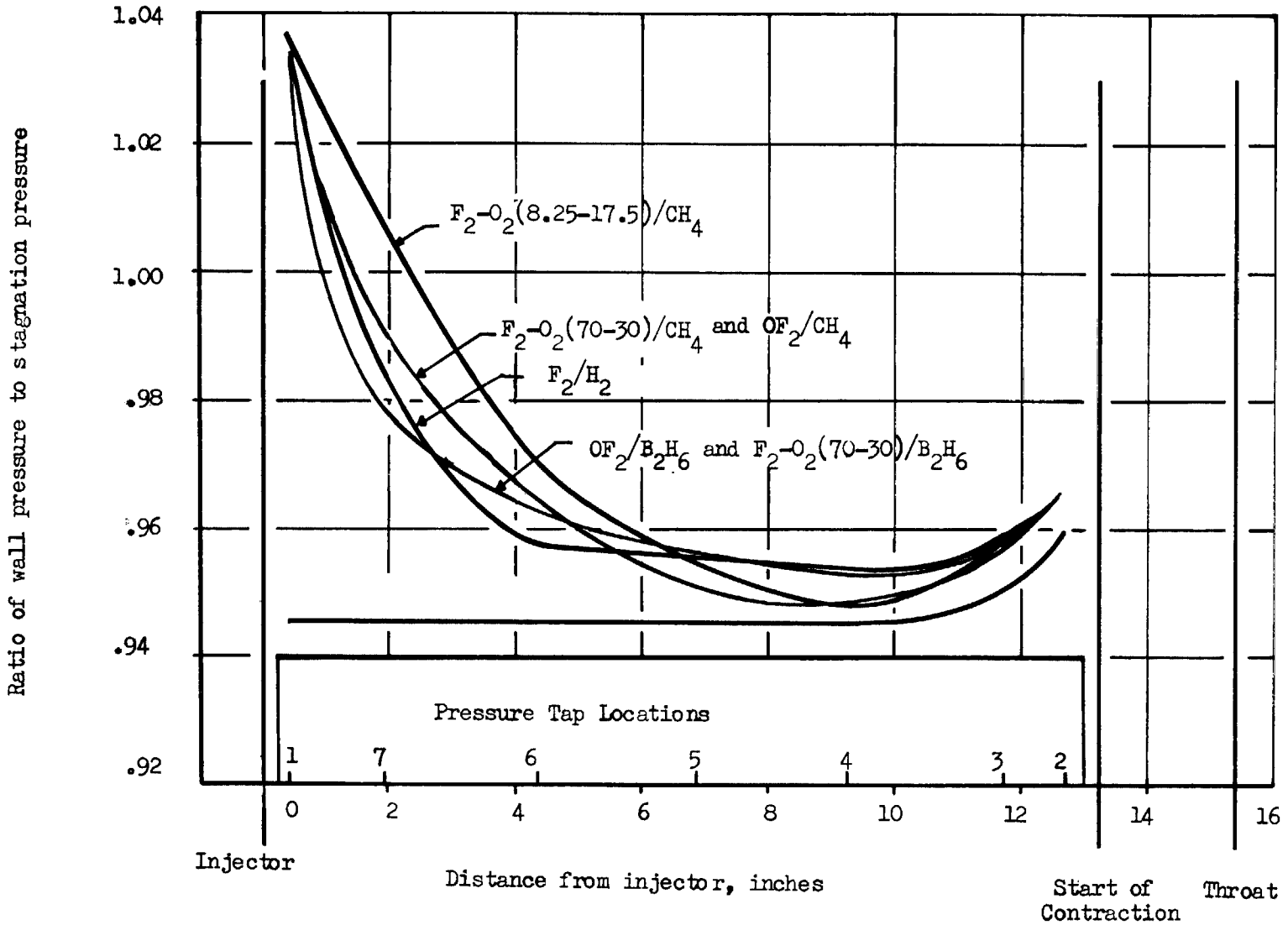

Figure 74. Comparison of Combustion Chamber Wall Pressure Profiles

electric analogy are indicated in Fig. 75, which gives a qualitative indication of the region where the turning effect is felt by the decrease in the potential velocity near the wall.

Corrections for F_2-O_2 Concentration and Impurities

All currently available propellants have some minor amounts of impurities. Because of the desired precision and following the philosophy of accounting for all calculable effects, analytical corrections for these impurities were made.

The areas affected by the impurities are the flowrates and the combustion and expansion processes. The flowrates are adjusted by taking into account the actual densities. The combustion and expansion processes are corrected by ratioing the equilibrium performance for the desired propellant. That is

$$I_{s_{corrected}} = I_{s_{measured}} + (I_{s_{ideal\ pure}} - I_{s_{ideal\ impure}})$$

with similar expressions for C* and C_F.

The propellant compositions are given in Table 2 and 3 for the various test series. F_2-O_2 composition varies slightly from series to series because of frequent tank venting and composition trimming.

Nominalization of Parameters

For purposes of comparison and for extrapolation, it is desirable to nominalize parameters to an exact chamber pressure or mixture ratio or injector efficiency. The basic assumption made in performing this nominalization is that the injector efficiency does not vary for small changes in mixture ratio and pressure and that the slope of the predicted thrust chamber efficiency is valid for small variations in pressure and mixture ratio. In addition when the specific impulse is nominalized to one injector efficiency, the assumption is made that the division of losses between injector and thrust chamber is accurate.

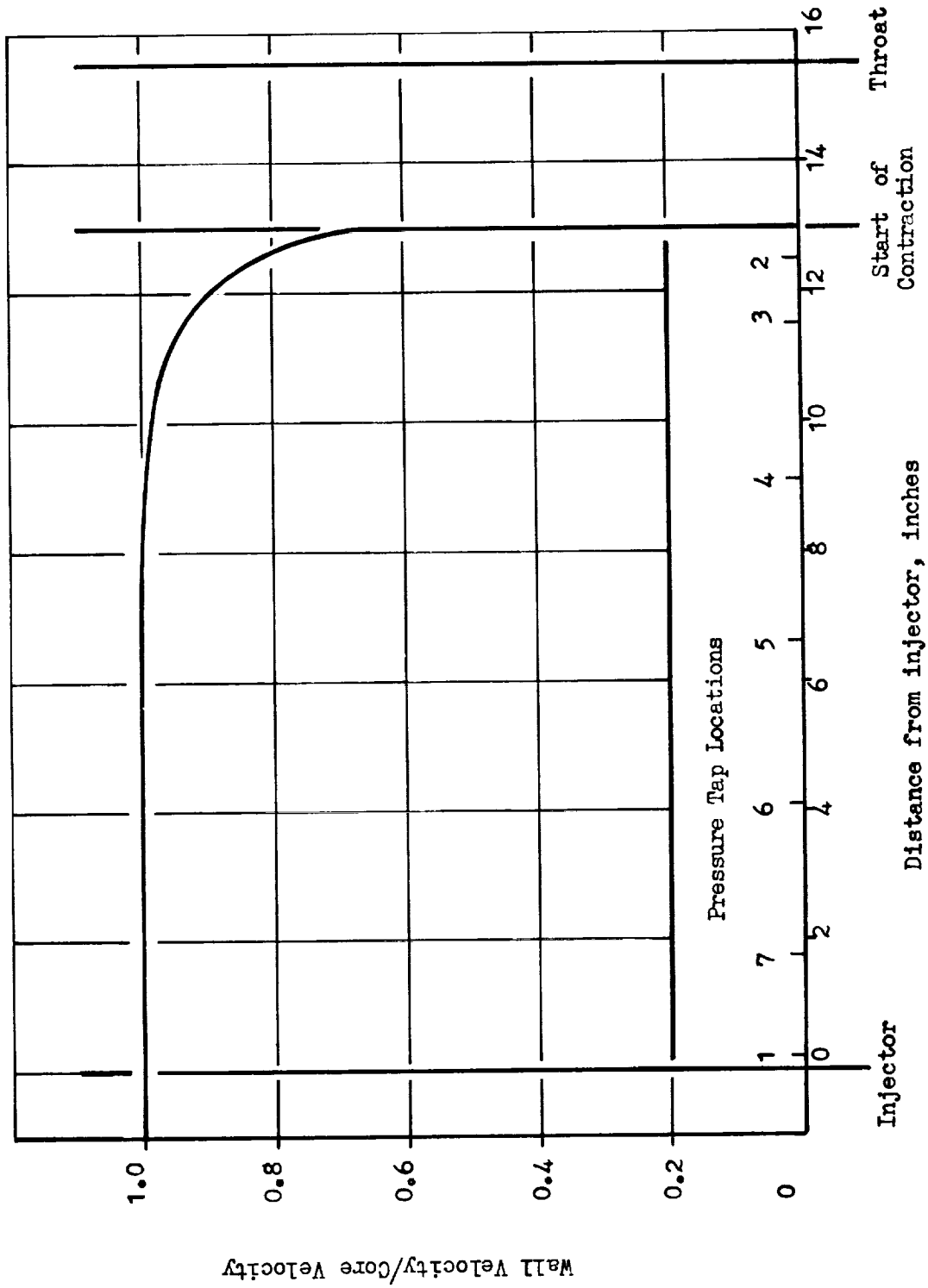

Figure 75. Electric Analog Results

TABLE 2

OXIDIZER COMPOSITION

TEST NUMBERS	33 to 42	43 to 60	61 to 62	63 to 67	68 to 72	73 to 78	79 to 86	87 to 92	93 to 100	101 to 006
Concentration in Weight Percent of										
F_2	83.8	82.3	70.4	70.0	69.6	69.2	68.8	68.3	68.0	
O_2	16.1	17.2	29.2	24.6	29.8	30.2	30.8	31.1	31.5	
HF	0.1	0.5	0.2	0.2	0.2	0.2	0.2	0.1	0.1	
CF_4			0.2	0.2	0.4	0.4	0.2	0.1	0.1	0.3
N_2								0.3	0.2	0.3
CO_2								0.1	0.1	0.1
Inerts										0.1
OF_2										99.2

TABLE 3

FUEL COMPOSITION

TEST NUMBERS	33 to 60	61 to 72	73 to 78	79 to 108	109 to 130	131 to 006
Concentration in Volume Percent of						
CH_4	99.9	0.4	99.9	0.4	99.9	0.4
N_2		0.6		0.6		0.2
H_2						0.8
Inerts	0.1		0.1		0.1	
B_2H_6		99.0		99.0		98.6

The relationships used in the nominalization for pressure and mixture ratio are

$$I_{s_{nominal}} = I_{s_{delivered}} \left[\frac{I_{s_{ideal\ nominal}}}{I_{s_{ideal}}}\right] \left[\frac{\eta_{TC_{predicted\ nominal}}}{\eta_{TC_{predicted}}}\right]$$

and for injector efficiency is

$$I_{s\,\eta_{inj}} = I_{s_{nominal}} \frac{\eta_{Inj_{nominal}} - \left[1\ \eta_{H.L.C.*}\right]}{\eta_{inj} - \left[1-\eta_{H.L.C.*}\right]}$$

HEAT TRANSFER DATA

Heat transfer data were taken using thermal isolation sections as described in Section VI. The resultant data were in the form of temperature-time histories. When nondimensionalized, these histories were compared with results of a one dimensional transient heat conduction model to establish the film coefficients.

The theoretical, non-dimensional, back side wall temperature-time histories wereobtained from a transient heat conduction analysis assuming an infinite plate solution with one surface exposed to the combustion gas and the other surface insulated. The assumption of the infinite plate (one-dimensional conduction) is reasonable because of the insulating effect of the air and/or 347 stainless steel that surrounds the measuring plug. Small corrections are made for the true geometry of the plugs where necessary to reduce the test data to infinite plate form.

The following equation was solved to obtain the backwall temperature as a function of time:

$$\frac{T_{AW}-T_{BW}}{T_{AW}-T_i} = 2 \sum_{n-1}^{\infty} \frac{\sin\ \lambda_n\, l}{\lambda_n l + \sin\ \lambda_n l \cos\ \lambda_n l}\ e^{-(\lambda_n l)^2 F_o} \cos\left(\lambda_n l\ \frac{x}{l}\right)$$

where

$$(\lambda_n \ell)/Bi = \cot(\lambda_n \ell)$$

and ℓ is the wall thickness, λ_n is the n^{th} eigenvalue. This equation defines the values of λ_n for each term in the infinite series shown above. The controlling dimensionless parameters are seen to be:

Fraction of wall thickness, $\frac{x}{\ell}$

Biot number = $Bi = \frac{h\ell}{k}$ (h is film coefficient and k is thermal conductivity)

Fourier number = $F_o = \frac{\alpha t}{\ell^2}$ (α is thermal diffusivity)

The solution has been programmed for the IBM 360 digital computer. An example of the solution is shown in Fig. 76 where the curves are for parametric values of film coefficient.

The pertinent measured test data include:

1) Initial segment temperature

2) Segment thickness

3) Backwall temperature-time history

The adiabatic wall temperature was calculated from the following equation:

$$T_{AW} = T_C \frac{1 + N_{Pr}^{1/3} \frac{\gamma - 1}{2} M^2}{1 + \frac{\gamma - 1}{2} M^2}$$

A typical temperature-time history for a nozzle probe location is shown in Fig. 77. For each temperature location, the ratio $(T_{AW}-T_W)/(T_{AW}-T_i)$ was

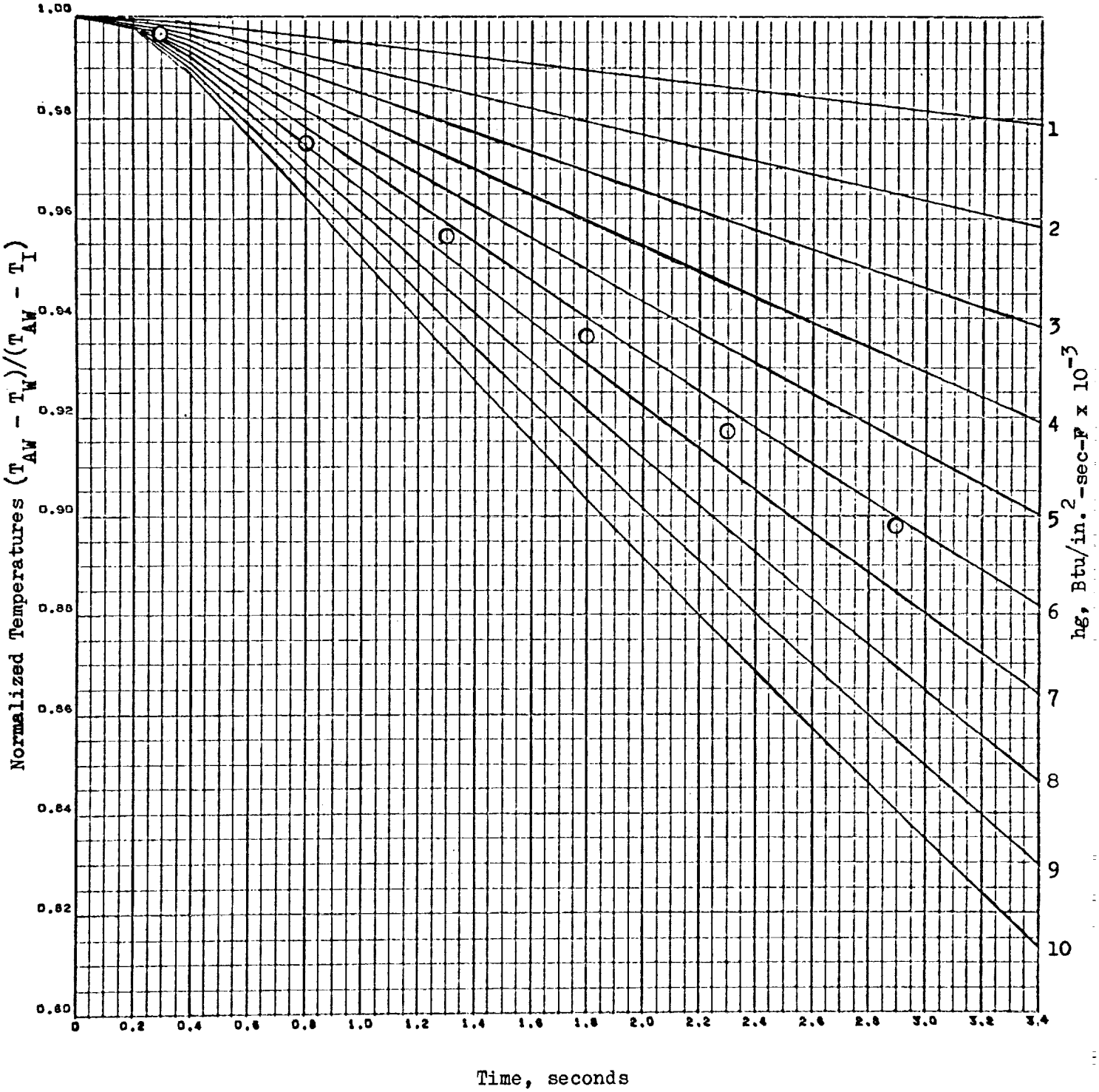

Figure 76. Theoretical Normalized Temperature-Time History for a Typical Thermal Plug

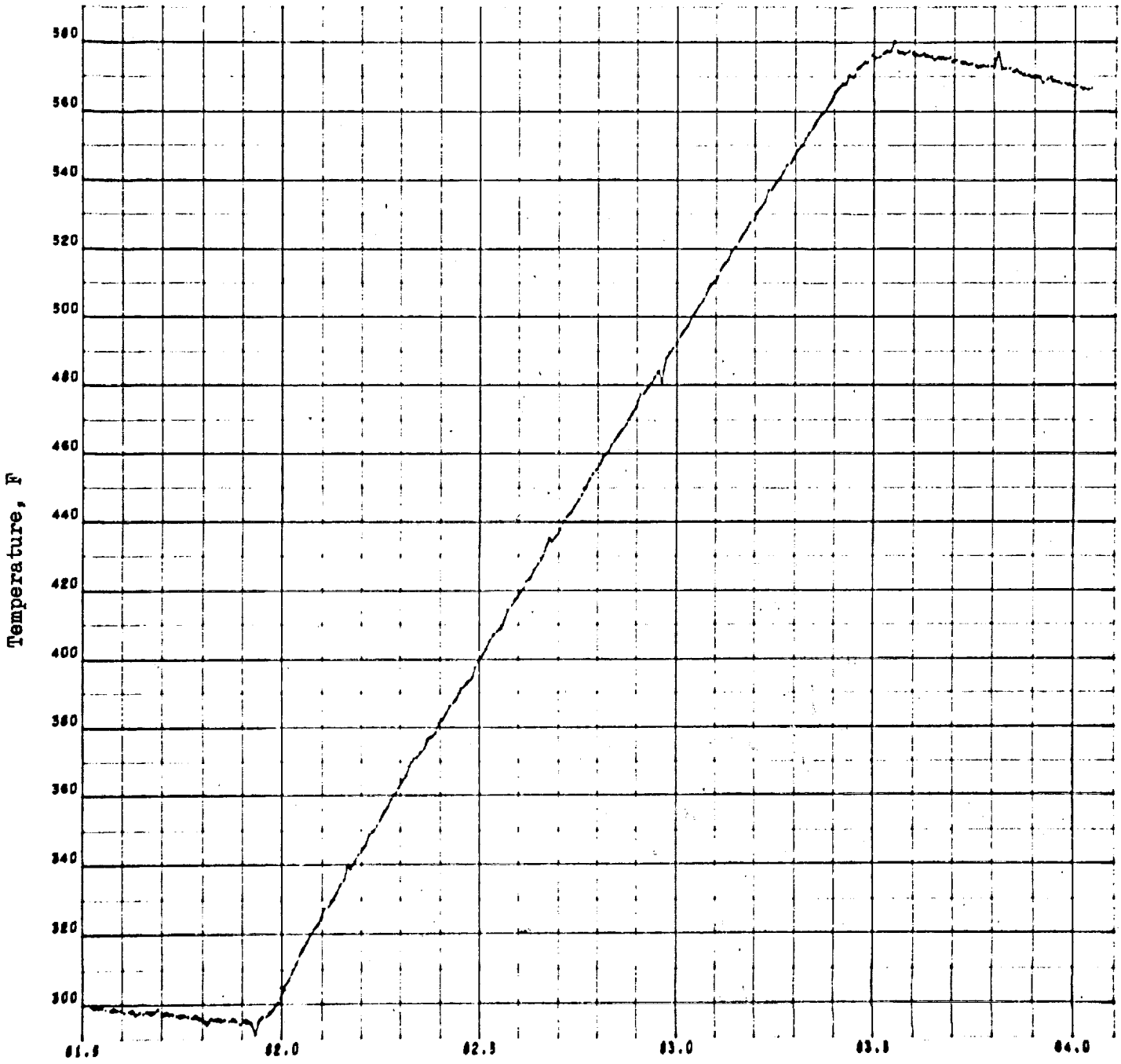

Figure 77. Experimental Temperature-Time History for a Typical Thermal Plug

computed for different time slices and these values, corrected for three-dimensional effects, were superimposed on the theoretical curves, Fig. 76. The resultant gas-side film coefficient was read directly from the plot.

PERFORMANCE PREDICTION

The performance prediction procedure used is basically similar to that used in Phase I (Ref. 4). Modifications have been made in the treatment of the boundary layer loss and heat loss. The basic ideal performance is the one dimensional isentropic chemical equilibrium expansion with the propellants at the injection temperatures. This performance is used to define all efficiencies and losses. Losses from this ideal performance and interactions of these losses are calculated analytically except for injector effects.

The losses considered in the performance prediction are given in Fig. 78. Efficiencies are defined as:

$$\eta = 1 - \frac{\text{loss}}{\text{reference value}}$$

The predicted thrust chamber efficiency is calculated as:

$$\eta_{TC} = 1 - \left(1 - \eta_G\right) - \left(1 - \eta_K\right) - \left(1 - \eta_{BL}\right) - \left(1 - \eta_{HL_{I_s}}\right)$$

The predicted specific impulse is given by

$$I_s = I_{s_{Ideal}} \eta_{C^*} \eta_{C_F}$$

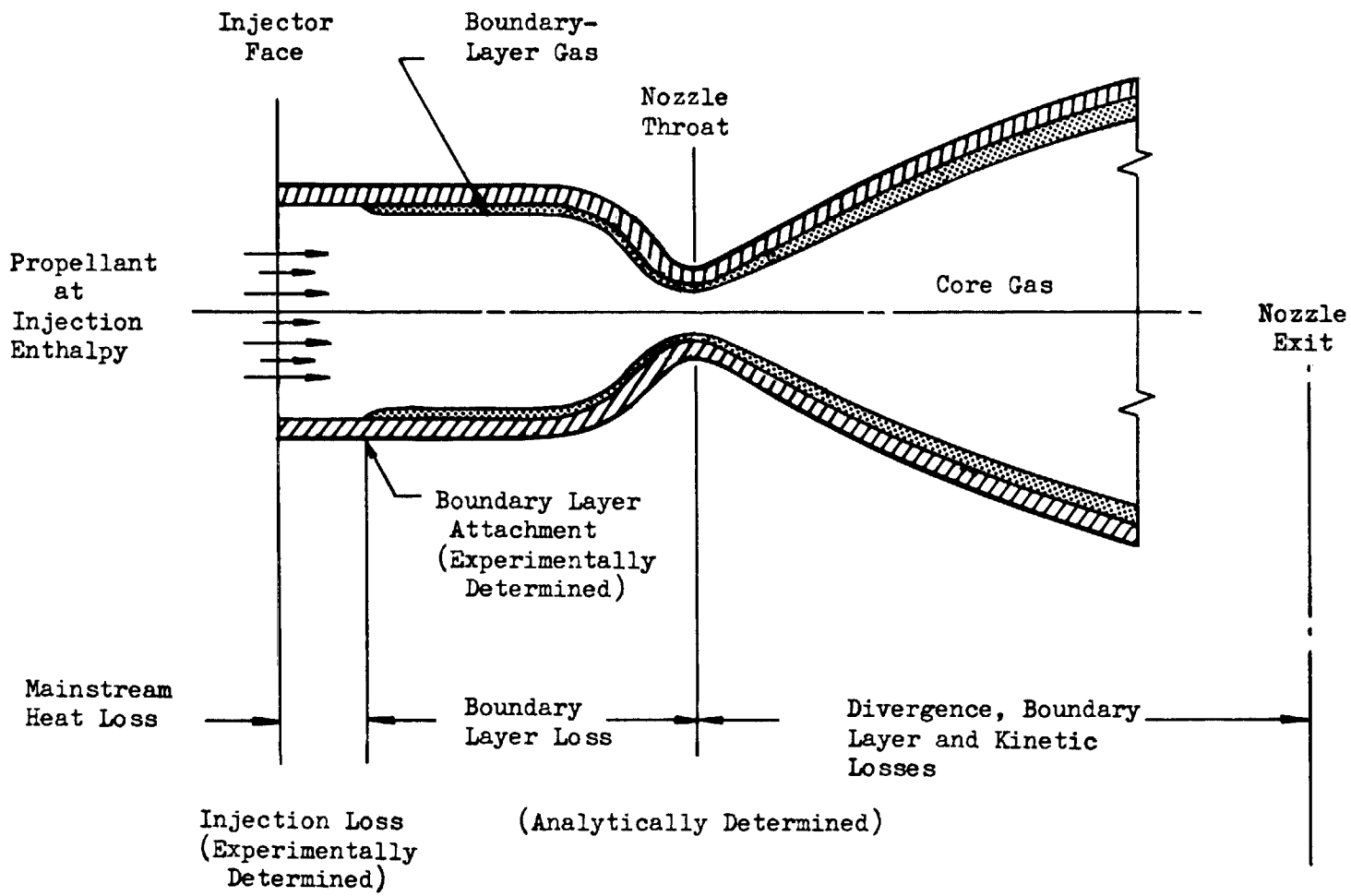

Figure 78. Performance Loss Occurrence

or

$$I_s = I_{s_{Ideal}} \left[\eta_{TC} + \left(1 - \eta_{HL_{C^*}}\right)\right]\left[\eta_{Inj} - \left(1 - \eta_{HL_{C^*}}\right)\right]$$

The injector efficiency can be assumed, measured on low area ratio tests or calculated from static pressure on the high area ratio tests. The C^* heat loss efficiencies are given in Appendix E, the ideal performance can be found in Appendix B.

Aerodynamic Analysis

The nozzle flow field is calculated by the method of characteristics, which has proven accurate both in cold flow and in hot firing tests. In the transonic region the method of characteristics cannot be employed. Therefore, the flow field in this region is computed by a series expansion of the equations of flow for Mach numbers near unit. The Rocketdyne transonic analysis has been verified using cold flow test data and is quite accurate.

In the calculational procedure, the gas state properties are input as a numerical table for a gas flow that is reacting. The chemical equilibrium properties of the propellants are used, since the flow for the parameters of interest is most closely approximated by the equilibrium gas properties. The aerodynamic calculations result in a geometric efficiency, η_G, which is a measure of the loss caused by the nonuniform divergent flow in the nozzle.

Boundary Layer Analysis and Mainstream Heat Loss

The concept of a thin continuous boundary layer is useful for flow having small mainstream turbulence. However, there is evidence that in the combustion region of rocket thrust chambers, large-scale turbulence may occur, preventing the development of a boundary layer early in the chamber.

The starting point of boundary layer growth for such thrust chambers must be determined experimentally from heat transfer data.

The point in the flow at which the boundary layer calculation is begun is determined by examining the parameter $St(Pr)^{2/3}$ as derived from heat transfer data. This parameter decreases continuously after the boundary layer has formed. For the combustion chambers tested in this program the boundary layer method became valid at the start of contraction.

For analysis, the thrust chamber wall was divided into two regions: the region between the injector and the point where boundary layer attachment occurs, and the region between this point and the nozzle exit. The region prior to boundary layer initiation is marked by the presence of violent turbulence. In this region, it is assumed that the heat transferred to the thrust chamber wall is lost uniformly by all the gas; a molecule that transfers heat to the wall may reach the center of the flow field or by a series of collisions receive some energy from the gas in the center of the flow field. The reaction rates are high in this area and stay time is long; thus it can be deduced that the gas composition will achieve the equilibrium associated with the reduced energy level. The gas will then proceed through the remaining length of the thrust chamber as though the lost heat had never been present. Therefore, in relation to the potential performance at the injector conditions, a heat loss has occurred. This heat loss is defined as the difference in the equilibrium specific impulse values at the two energy levels divided by the value used for reference.

Once the boundary layer calculation is initiated, the heat transferred to the wall is lost entirely from the boundary layer. Cross diffusion, conduction and radiation between boundary layer and core gas are assumed to be negligible. The core gas proceeds through the nozzle without further loss of heat. As the heat is lost, the boundary layer grows to include an

increasing portion of the total flow; but for any boundary layer thickness, the portion of the mass outside the boundary layer has lost no heat or it would become part of the boundary layer. The loss modes of heat transfer and shear both occur exclusively in the boundary layer once a well-defined boundary layer has begun to exist. The boundary-layer analysis accounts for these shear and heat transfer losses and the interrelations between them.

In the Rocketdyne boundary layer approach a finite difference solution of the integral momentum equations is used that includes terms to account for the effects of a pressure gradient, a compressible shape factor, a nonadiabatic wall condition, compressible flow condition, and a variable, turbulent boundary layer velocity profile. The von Karman integral momentum equation is used in the computations which are valid for both laminar and turbulent boundary layer conditions.

Using the potential flow conditions (velocity, density and temperature) determined from the inviscid axisymmetric flow analysis to define conditions at the outer edge of the boundary layer, the finite difference solution is pursued from the boundary layer starting point along the entire length of the wall. This solution finally results in a momentum thickness at the nozzle exit. When converted to a momentum deficit and corrected by the cosine of the wall angle at the exit, this calculation produces the loss in thrust resulting from the boundary layer. The loss in thrust is given by

$$\Delta F = 2\pi r_e \cos \alpha_e \left[\rho_e U_e^2 \theta_e - \left(P_e - P_a \right) \delta_e^* \right]$$

Two efficiencies are derived from the mainstream heat loss and boundary layer analysis; the mainstream heat loss efficiency, defined as

$$\eta_{HL_{I_s}} = 1 - \frac{I_{s_{ideal}} - I_{s_{Heat\ Loss}}}{I_{s_{ideal}}}$$

(where $I_{s_{Heat\ Loss}}$ is calculated for equilibrium one-dimensional isentropic flow at the reduced energy level). Also, the effect upon C* is given as

$$\eta_{HL_{C^*}} = 1 - \frac{C^*_{ideal} - C^*_{Heat\ Loss}}{C^*_{ideal}}$$

The boundary layer loss is given by

$$\eta_{BL} = 1 - \frac{I_{s_{Boundary\ Layer}}}{I_{s_{Ideal}}}$$

Reaction Kinetic Analysis

The calculation of reaction kinetic effects in the nozzle is performed by dividing the nozzle flow into a large number of streamtubes derived from the aerodynamic analysis. The one-dimensional reaction kinetic analysis is then applied to the flow in each streamtube. The reaction kinetic loss for the nozzle is calculated by integrating the impulse function across the streamtubes at the nozzle exit for both equilibrium flow and for flow calculated using the kinetic model. Rate constants are tabulated in Table 4. Details of the procedure are described in Ref. 4.

TABLE 4 REACTION RATE CONSTANTS

Reaction Rate Constant with Argon as Third Body

$H + H + Ar = H_2 + AR$	$1.6 \times 10^{18} \times T^{-1}$
$H + OH + Ar = H_2O + Ar$	$4.5 \times 10^{19} \times T^{-1}$
$H + O + Ar = OH + Ar$	$6.0 \times 10^{18} \times T^{-1}$
$O + O + Ar = O_2 + Ar$	$2.0 \times 10^{18} \times T^{-1}$
$H + F + Ar = HF + Ar$	$4.0 \times 10^{18} \times T^{-1}$
$F + F + Ar = F_2 + Ar$	$8.0 \times 10^{15} \times T^{-1}$

Third Body Efficiencies Relative to Argon

H	25
OH	25
H2	10
O	5
F	5
HF	4
H_2O	4
CO_2	4
CO	3
O_2	2
All other species	1

WALL PRESSURE PREDICTION

The wall pressure profile is determined by predicting the pressure as a function of position in the wall streamtube. Once the transition from shifting to frozen in this streamtube is calculated using the Reaction Kinetic Analysis Program, the wall pressure profile is completely determined.

The relationship between the streamtube area ratio and the nozzle axial length is known from aerodynamic and streamline analysis. The relationship between streamtube area ratio and local geometric area ratio is shown in Fig. 79. Using the curves of streamtube area ratio vs local geometric area ratio and the wall pressure ratio vs streamtube area ratio data, the curves of wall pressure vs local nozzle area ratio are obtained.

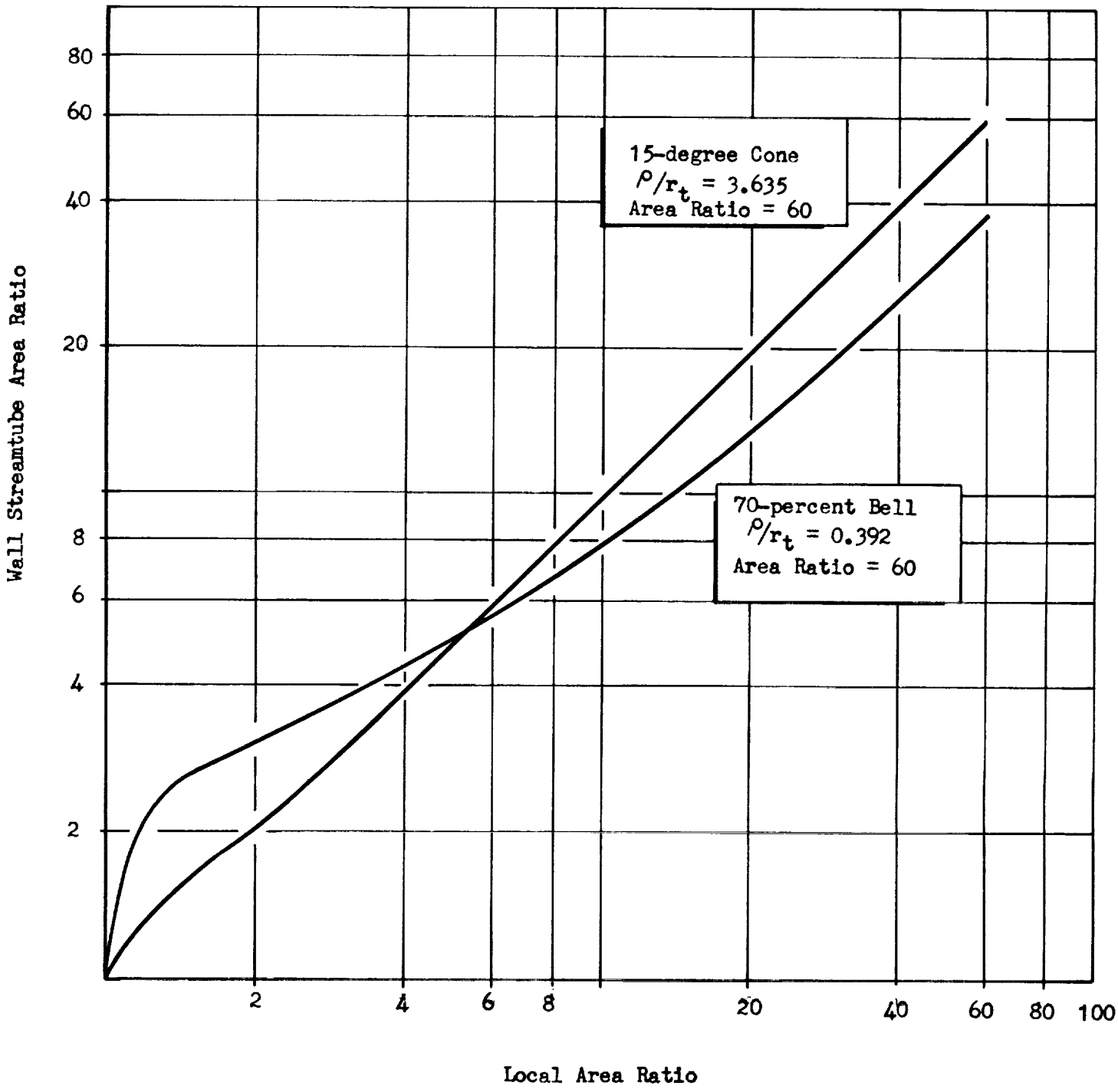

Figure 79. Wall Streamtube Area Ratio as a Function of Local Geometric Area Ratio.

SECTION VI

TEST APPARATUS AND PROCEDURES

The apparatus and procedures used to conduct the experimental portion of the program are described in this section. The test facility and instrumentation are discussed at length because of the unusual features of the fuel feed systems and the emphasis on high quality test data. The hardware, identical to that used in Phase I, is described only briefly. More details are available in Refs. 3 and 4.

The test program was conducted at the Rocketdyne Nevada Field Laboratory Altitude simulation facility B-3 test stand shown in Fig. 80. This facility produces a simulated altitude of 120,000 feet. The propellant feed systems provide the oxidizer as a liquid under liquid nitrogen controlled conditions and the fuels as a gas under conditions established by heat exchangers. The diborane is stored in a liquid condition and converted to a gas for each test.

Instrumentation is designed for precise specific impulse performance determination. Data acquisition is by digital recorder. The specific impulse test results have consistently been able to resolve performance effects of 1-percent magnitude. The difference between OF_2 and F_2-O_2 (70-30), a 6 lbf-sec/lbm effect has been clearly evident in the test results. The relative performance of the bell and conical nozzles, different by only about 2 lbf-sec/lbm, was reproducibly indicated.

All engine hardware was of heat sink design intended for short duration tests. The combustion chamber was fabricated of heavy wall copper and was of two-piece construction: a cylindrical section and throat section.

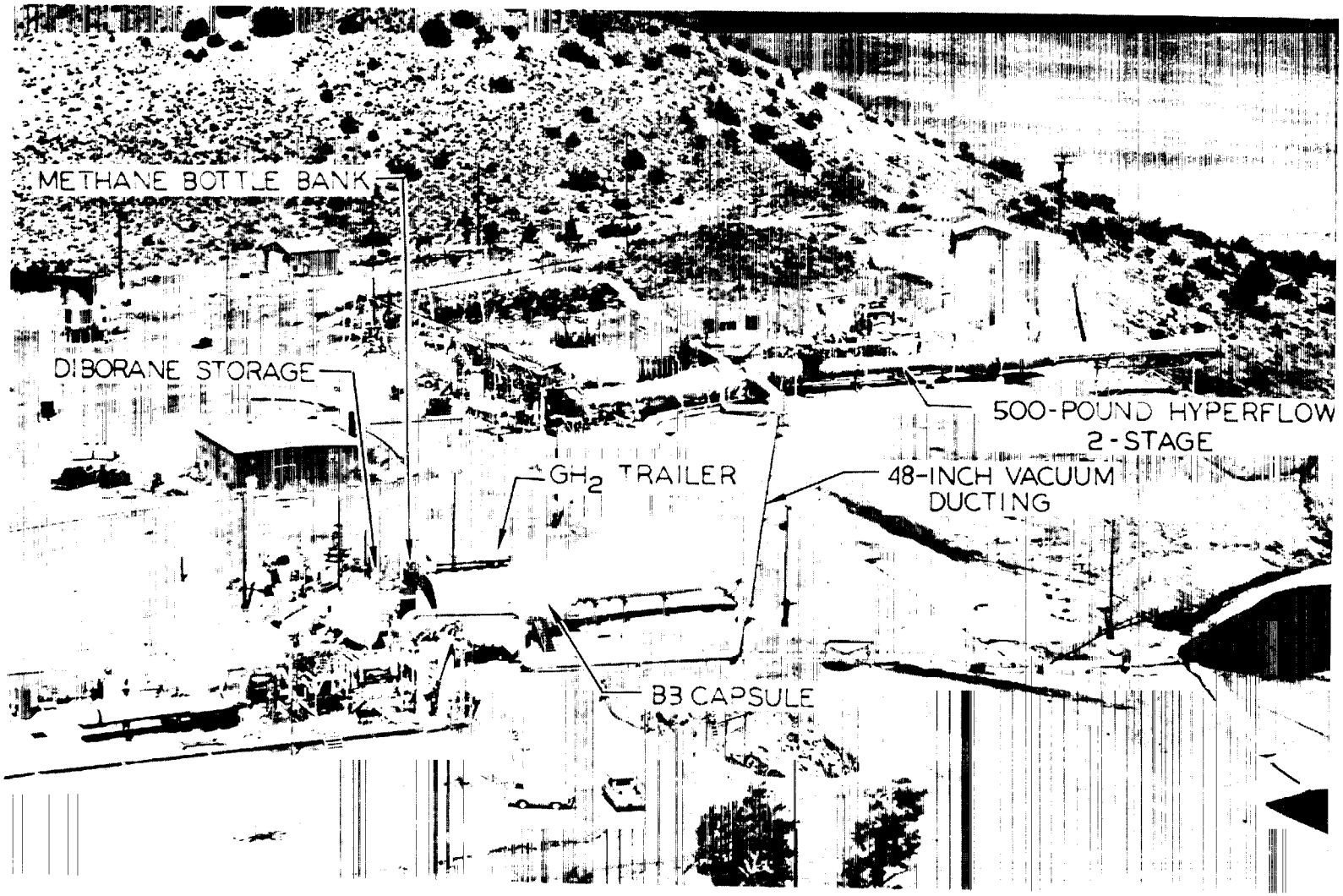

6RE11-3/21/68-R1A

Figure 80. Nevada Field Laboratory Small Engines Area

The stainless steel nozzle extensions used were a 15-degree cone and a 70-percent bell, each of area ratio 60. The copper injector was designed for liquid oxidizers and gaseous fuels.

PROPELLANT SYSTEMS

The test stand had essentially three separate propellant feed systems: an oxidizer system and two fuel systems, one system for methane, and one system for diborane. The need for separate fuel systems stemed from the unique characteristics of diborane.

Oxidizer Feed System

The oxidizer feed and storage system is designed for use with any fluorinated cryogenic oxidizer. The storage-test tank is a triple-walled 500-gallon stainless steel tank having a liquid nitrogen inner jacket and an insulation-filled vacuum outer jacket. The tank is shown in Fig. 81 next to the LN_2 tank.

The liquid oxidizer system is liquid nitrogen-jacketed and insulated from the test tank to the main valve just upstream of the engine, Fig. 82. The flowmeters are within 4 feet of the injector and measure representative flow conditions at a specific data slice. Just downstream of the main valve in the oxidizer system, a liquid nitrogen bleed is connected for chilling the injector assembly prior to engine start.

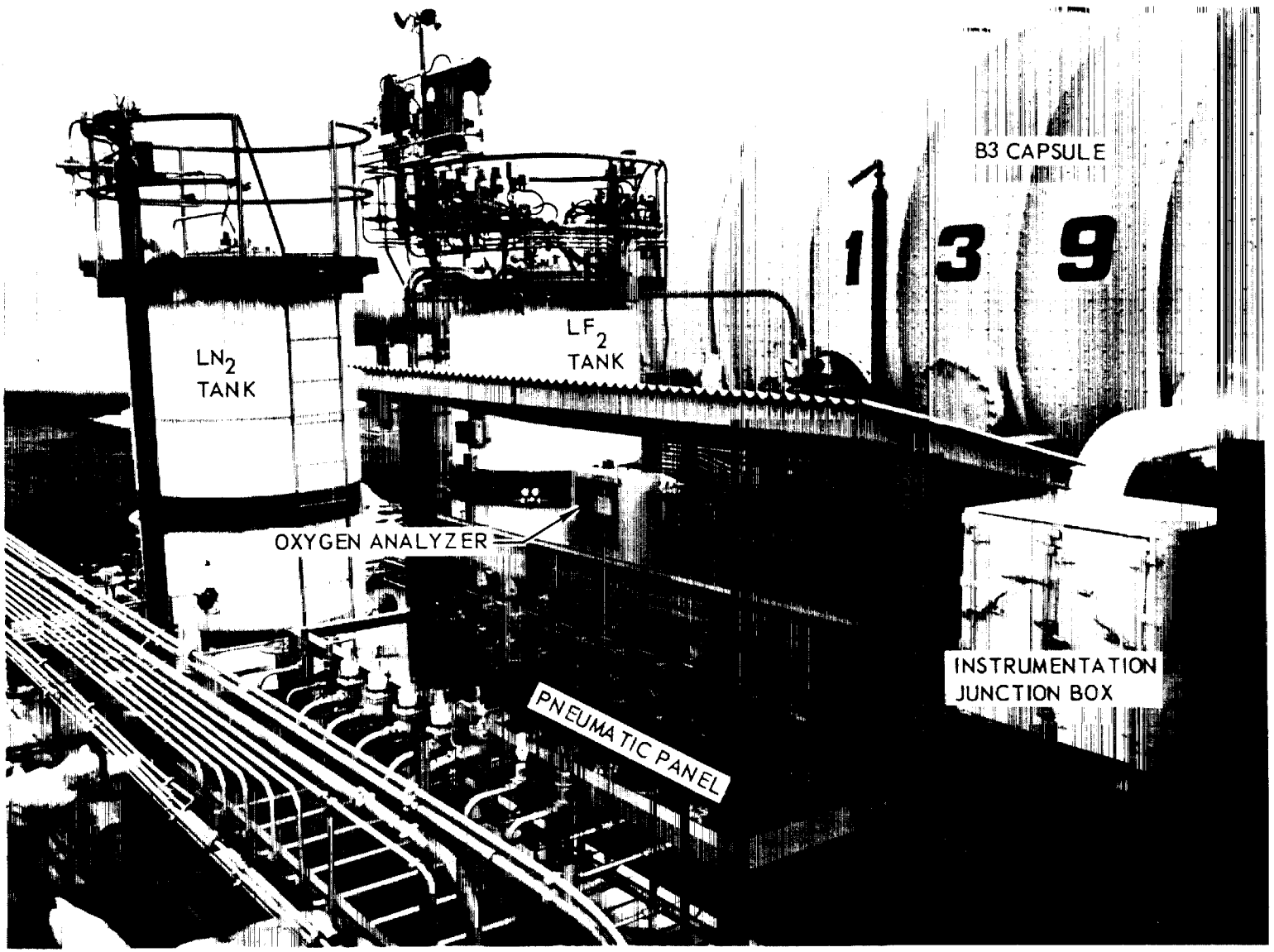

Figure 81. B3 Oxidizer Storage Area

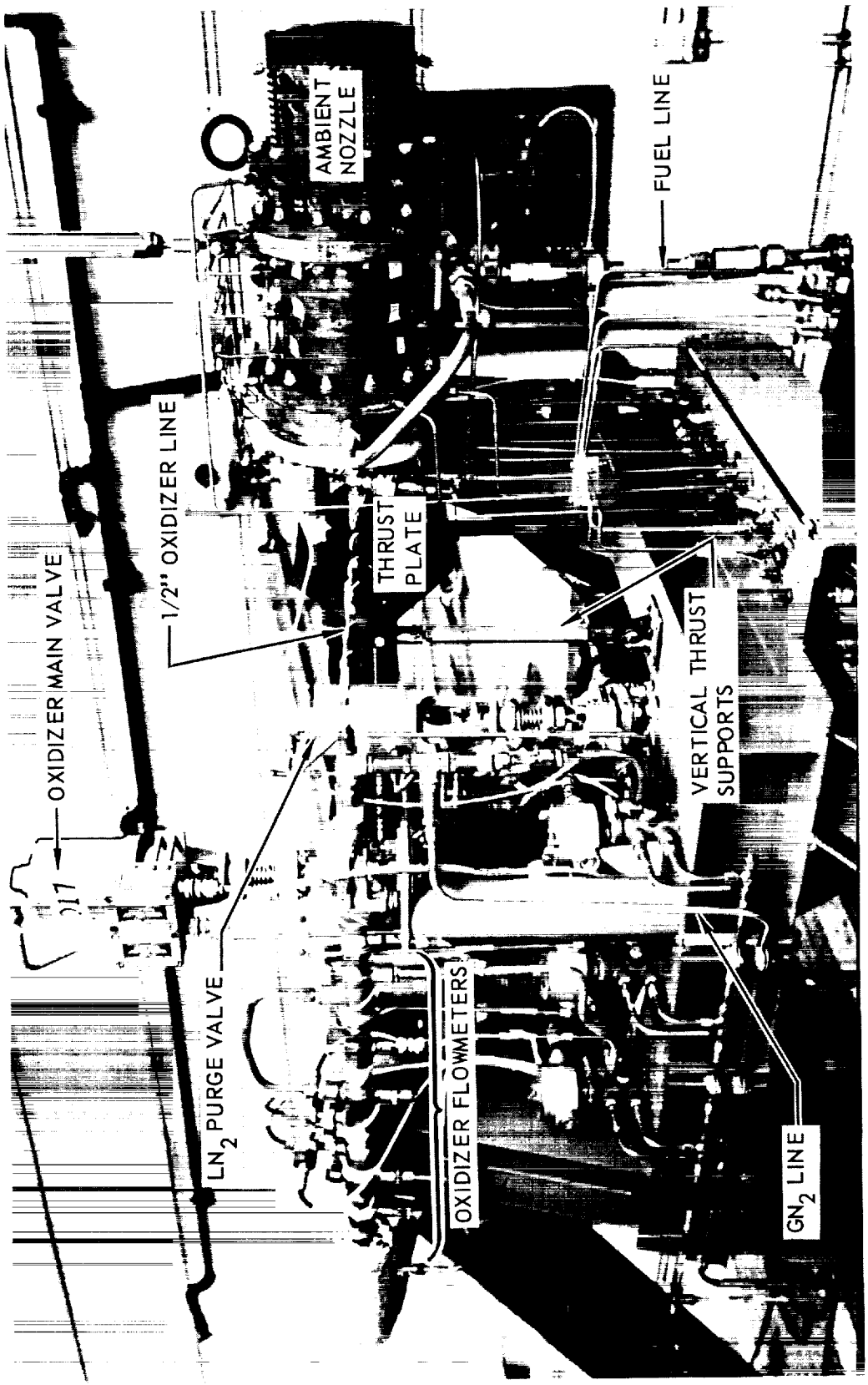

Figure 82 . B3 Engine Installation

The stand includes provisions for making and analyzing F_2-O_2 mixtures on site. The mixture is produced by introducing gaseous oxygen into the bottom of the LF_2 tank and allowing it to bubble through and condense in the LF_2. Additional mixing is accomplished by cycling the liquid through the feed lines and return system and by bubbling helium gas through the propellant in the tank.

An oxygen analyzer, Fig. 81, was used in monitoring the LF_2 concentration in the tank. The gas analysis is based upon a measurement of the magnetic susceptibility of the gas that is being analyzed. More precise analysis of the concentration is made by laboratory analysis.

During the OF_2/CH_4 portion of the program an ignition system was installed in the oxidizer system because hypergolicity is considered unreliable for this propellant. The modification consisted of the installation of a high pressure fluorine bottle and associated plumbing. Gaseous fluorine was introduced through the oxidizer system 250 msec before the methane. When the oxidizer main valve reached full open, the gaseous fluorine main valve was closed. GF_2 injection was limited to 0.5 seconds. This ignition system worked reliably throughout the test series. No attempt was made to conduct OF_2/CH_4 tests without using the ignition system.

Fuel Feed System

For the methane feed system, K bottles at 2250 psi were manifolded together. This gaseous bottle bank, illustrated in Fig. 83, was connected to the propellant feed line.

The diborane feed system was designed for liquid diborane storage and gaseous diborane injection. The use of gaseous diborane was

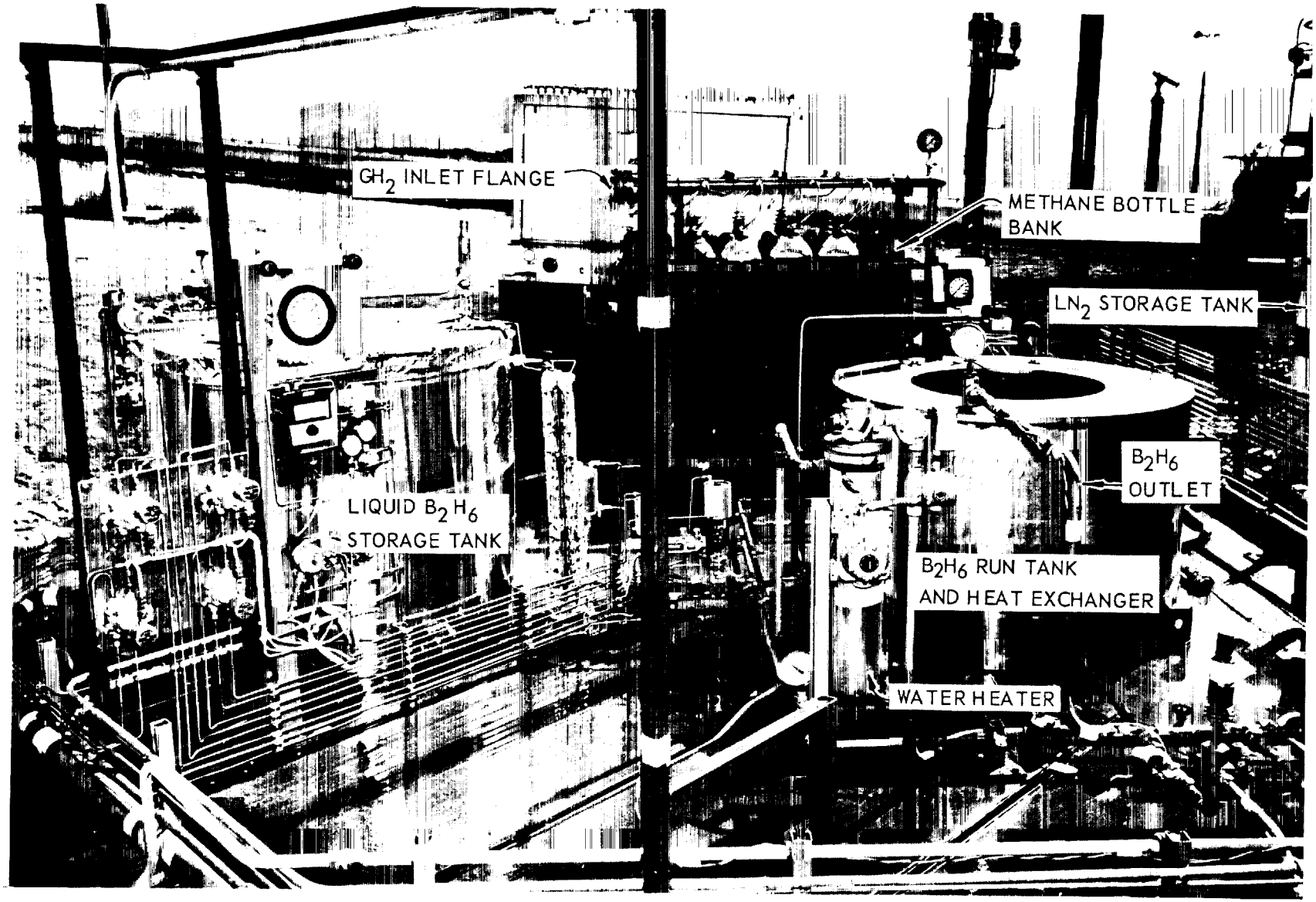

Figure 83. B3 Fuel Storage Area

necessitated by the requirement of comparing the three fuels, H_2, CH_4 and B_2H_6, under the same operating conditions. Gaseous fuels ensure high combustion efficiency for all propellant combinations and eliminated the need for injector development. The required phase change and heating resulted in a unique feed system design approach.

The required quantity of liquid diborane is converted to a gas before the test but cannot be held at the optimum test temperature of 140 degrees F for long periods of time because of the high decomposition rate at this temperature (lower temperatures bring the gas too close to a two-phase regime as it expands through the flow measurement sonic venturi). Therefore, a two-stage heat exchanger was devised. The first stage maintains the gas at approximately 70 degrees F where long delays in the test can be tolerated with no danger of decomposition, (Appendix C). The second stage is used immediately before the test and raises the temperature to the desired 140 degrees. The second-stage heat exchanger was also used to regulate the fuel temperature on H_2 and CH_4 tests.

The liquid storage tank (Fig. 83) consists of three tubes inside an annular container which is used as an LN_2 jacket. The LN_2 flow is regulated to control the B_2H_6 storage temperature. This type of system is more flexible than the simpler dry-ice system sometimes used. Its extra cooling capacity was essential to the diborane recovery operation performed after each test, during which unused gaseous diborane was recondensed in the liquid storage tank. During this procedure, the temperature controller was overriden and the container was filled with LN_2, freezing the diborane and speeding the recovery process.

The run tank and first-stage heat exchanger (Fig. 83) is of similar physical construction to the storage tank but uses a heated water system

as the heat source to vaporize and regulate the temperature of the diborane. The water is heated by a closed loop pumping and heating cycle and the temperature can be controlled to within a few degrees.

The second-stage heat exchanger is located inside the test capsule and consists of three parallel copper pipes filled with copper rivets. The pipes are wrapped with heater tapes and insulated, Fig. 84. In a test, diborane was not admitted to this section until the vacuum system and all electrical systems had been checked out, minimizing the chance of any delay. The gas remained in this section for three minutes before the test began.

After the test was completed, all valves between the second-stage heat exchanger and the liquid storage tank were opened and the diborane is reliquefied. High-pressure helium was added at the downstream end of the system to help force the diborane back into the tank.

The only time that safety equipment was required was in the initial transfer of diborane into the storage tank from the shipping cylinders. All other operations were performed remotely with the area cleared. Since the storage tank contained sufficient diborane for several hyperflow series, personnel exposure was minimized. Additional safety was also provided on occasion by storing the diborane frozen minimizing the vapor pressure in the storage tank. This capability of freezing also made the recovery of almost all unused gas possible.

In the activation of the diborane facility, a major safety precaution was taken in the use of nontoxic ethane as a simulant for the diborane. The physical properties of the two compounds are close enough that all major facility features could be checked by using ethane. All problems with

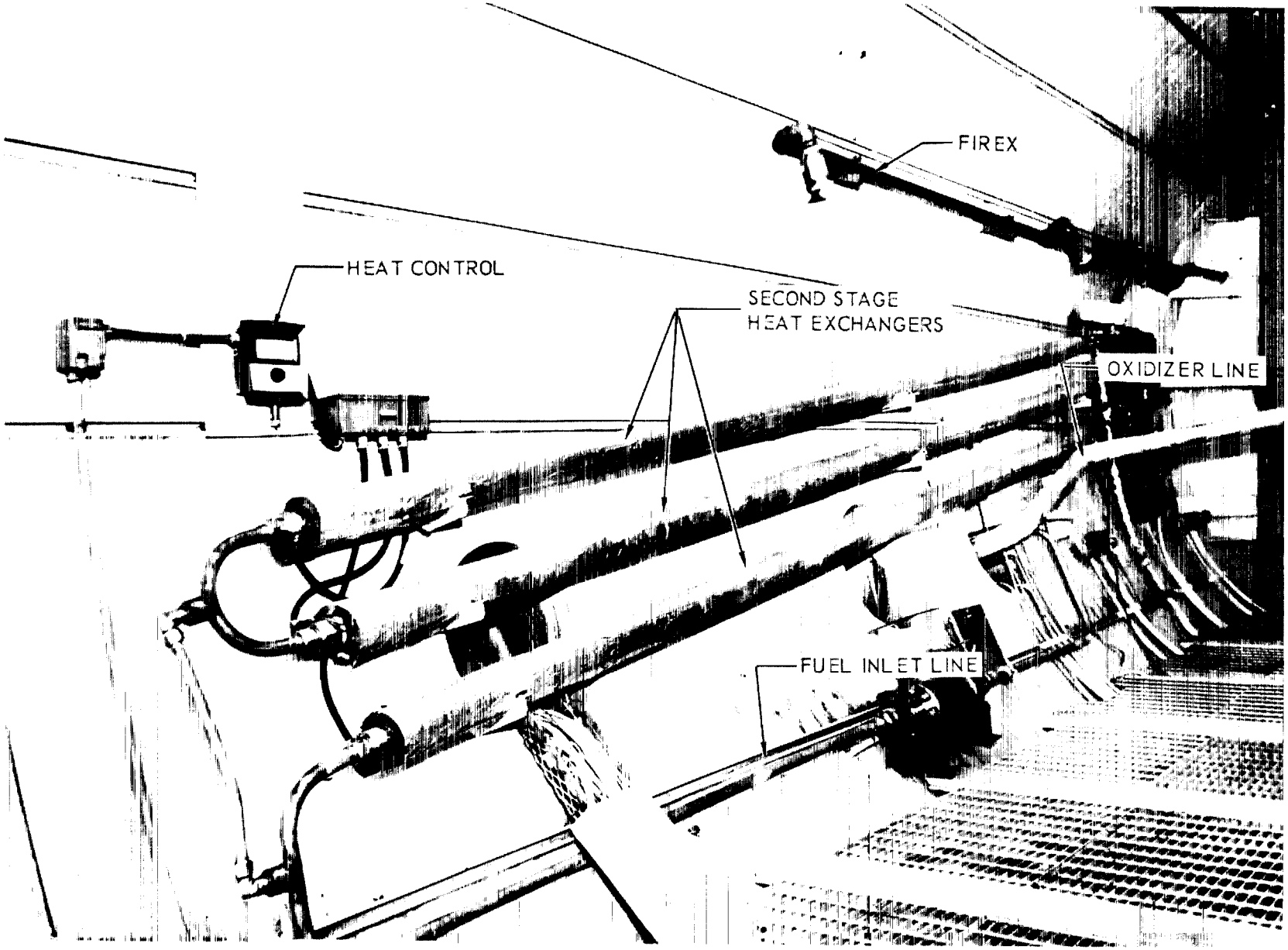

Figure 84. Gaseous Fuel Heat Exchanger System

the original facility design and operation were uncovered using ethane and corrected so that all operations were routine by the time the diborane was first introduced.

ALTITUDE SIMULATION SYSTEM

A twofold altitude-simulation system was used in this phase, the main steam ejector and an auxiliary small steam ejector. The main system, consisting of three diffuser stages, is capable of maintaining an altitude of 120,000 feet for 150 seconds of test operation. The first stage is driven by the engine, while the other two stages are powered by supersonic steam ejectors. The overall system is shown in Fig. 85.

The auxiliary ejector unit is supplied by steam from the main boiler plant. This ejector, although not capable of maintaining altitude conditions during test operation, permits evacuation and facility checkout before starting the large system. This served three objectives.

1. All systems were checked out before an engine test was committed (of the unsuccessful tests in the previous tasks, many were caused by problems which could have been found during a pretest altitude checkout).
2. This procedure eliminated the large jolt to the thrust system which can be caused by the rush of air past the nozzle when the main hyperflow is started.
3. This system prevented the main hyperflow cutoff transients from affecting the engine hardware by blocking the high-pressure wave that travels up the diffuser sections.

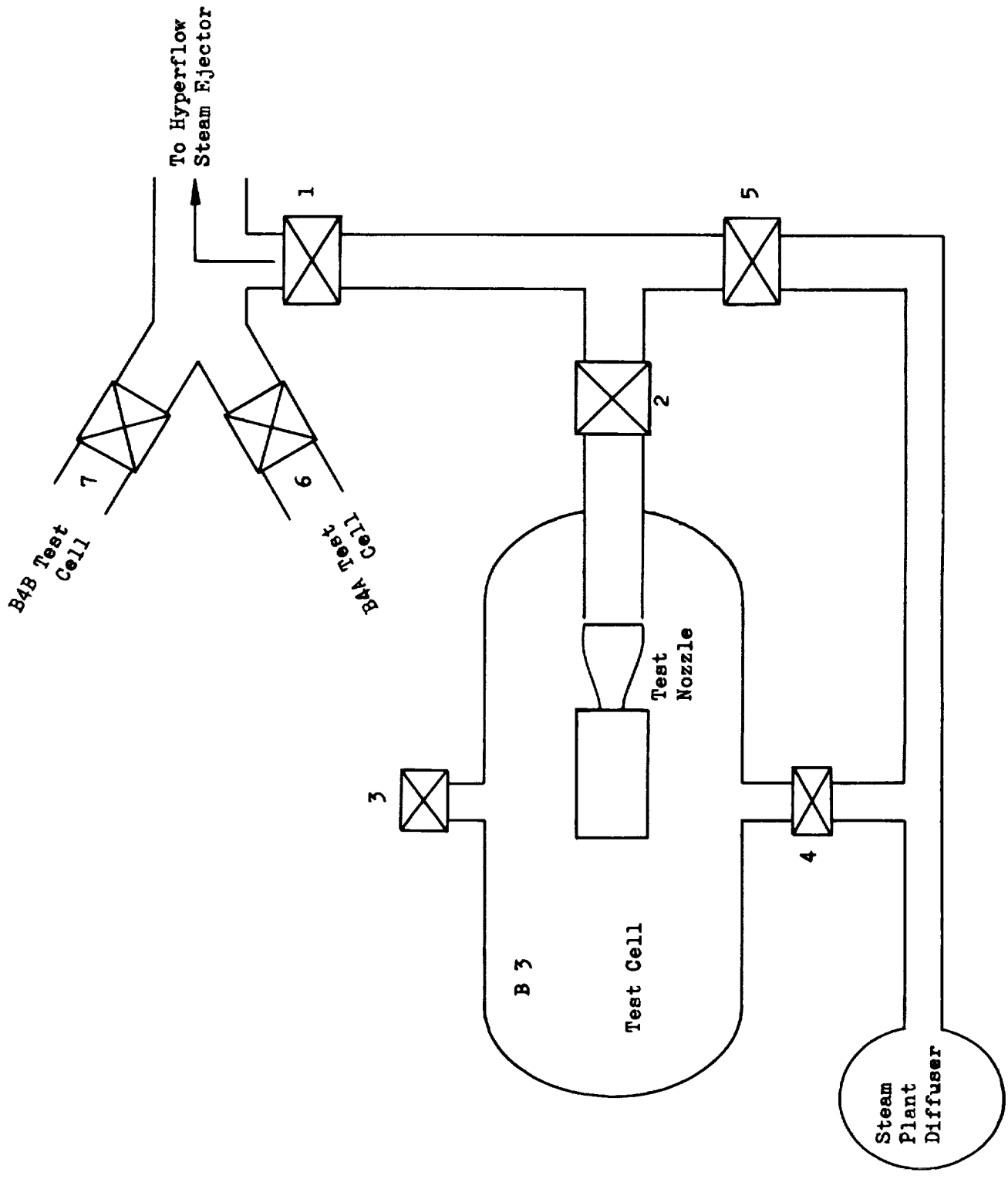

Figure 85. Vacuum System Schematic

These objectives were achieved by proper sequencing of the facility ducting valves.

The sequence of the valves, illustrated in Fig. 85 and operation of the vacuum system were as follows:

1. Close valves 1, 3, 4, 6 and 7
2. Open valves 2 and 5
3. Evacuate the B3 capsule and vacuum duct using the steam plant diffuser
4. Start the large hyperflow steam ejector
5. Close valve 5 and open valve 1
6. Conduct tests
7. Close valve 1 and open valve 5
8. Terminate large hyperflow
9. Close valve 2
10. Terminate small diffuser
11. Open valves 1 and 3 and return test capsule to ambient pressure

The altitude test capsule consists of a cylinder approximately 16 feet in diameter and 40 feet long with hemispherical ends. The aft end is connected to the altitude-simulation system by a 48-inch duct. The forward end of the capsule is mounted on a movable trolley for access. The opened capsule is shown in Fig. 86. The ducting leading to the main ejectors and the isolation valve are also evident in this figure. Fig. 87 is a view of the inside of the capsule with the 70-percent bell nozzle installed.

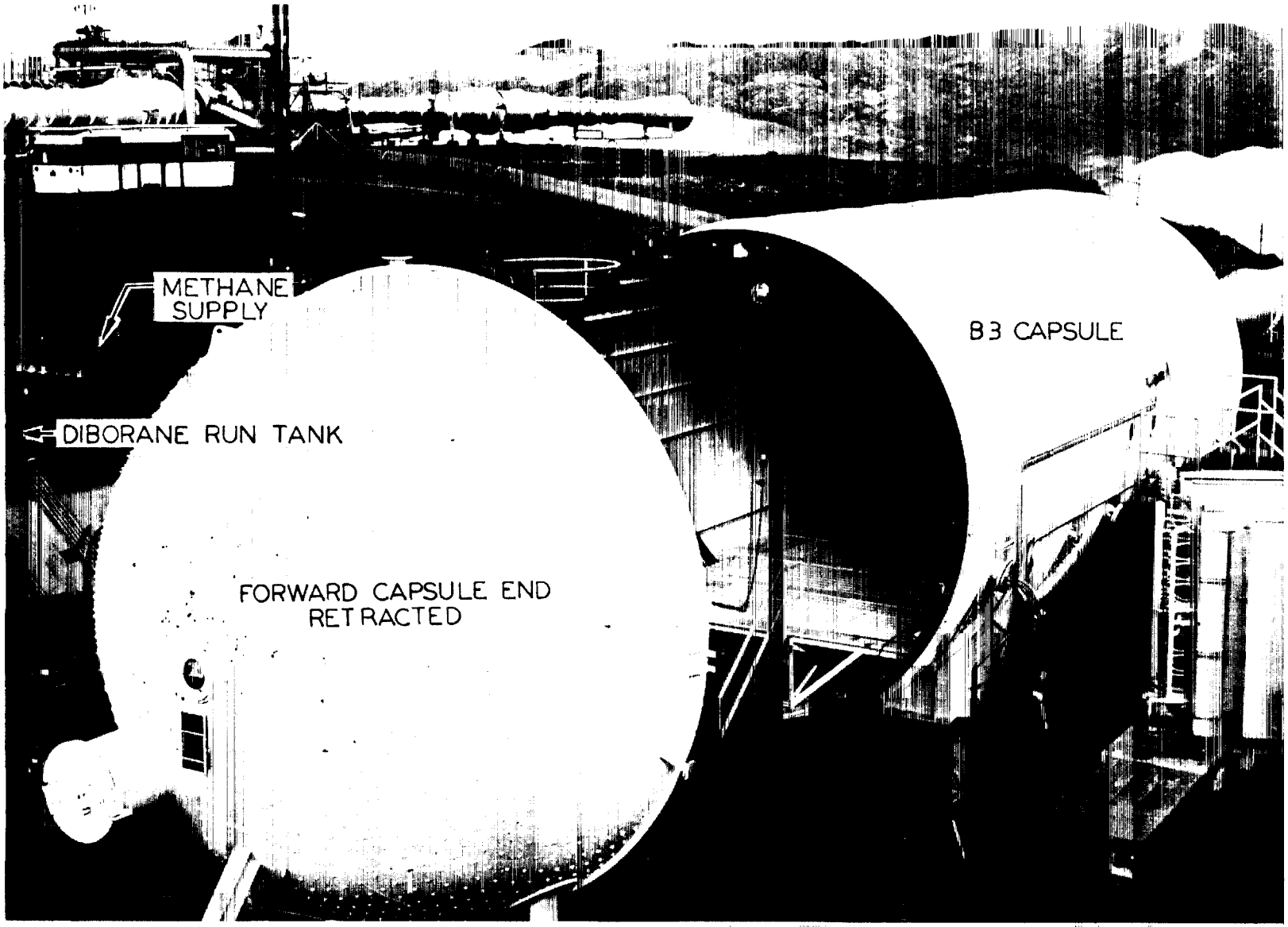

6RE36-2/7/68 - R1F

Figure 86. B3 Test Position

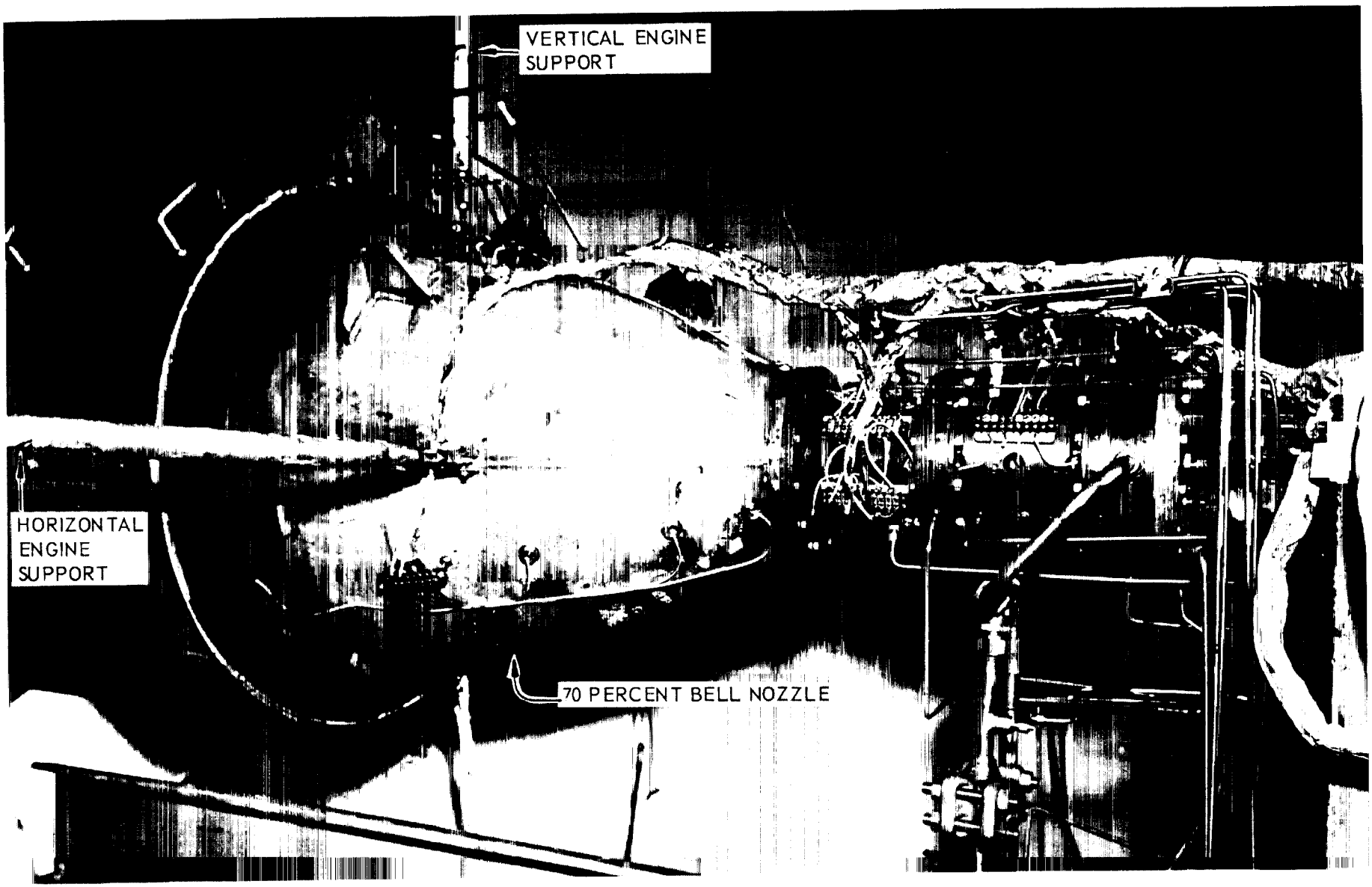

1XW21 10/11/68-R1A

Figure 87. Engine Installation and Facility

ENGINE INSTALLATION

The engine is installed in the test stand in such a way that it is free of external interference. No corrections have to be made for thrusts caused by supports or propellant lines. The diffuser inlet is adjusted to ensure that there is no effect of the engine plume within the capsule.

Engine Mounts

The thrust system is illustrated in Fig. 88. The injector (not shown) is mounted to the thrust plate by three longitudinal standoffs. This plate is supported by one horizontal and two vertical tie rods. Mounted to the thrust plate is a flexure and spacer followed by a dual-element load cell. Two alignment plates separate the two load cells and flexures. This assembly is mounted to a rigid I-beam. Also mounted to this I-beam is an hydraulic ram and the calibration load cell. At the end of the calibration cell is a ball joint in a yoke that is tied to the thrust plate by two tension rods. To minimize the cantilevered engine weight, a vertical rod and a horizontal rod are attached to the nozzle skirt, Fig. 87. These rod supports are mounted in clevis fittings through swivel tie rod ends.

The engine thrust is simulated by pressurizing the hydraulic ram which moves the calibration cell putting the two tie rods in tension. In this manner, the simulated engine thrust is transmitted through the centerline of the thrust system putting the dual-bridge load cells in compression in the same way the engine puts them into compression. During test operation the tie rods were loosened and do not interfere with engine movement.

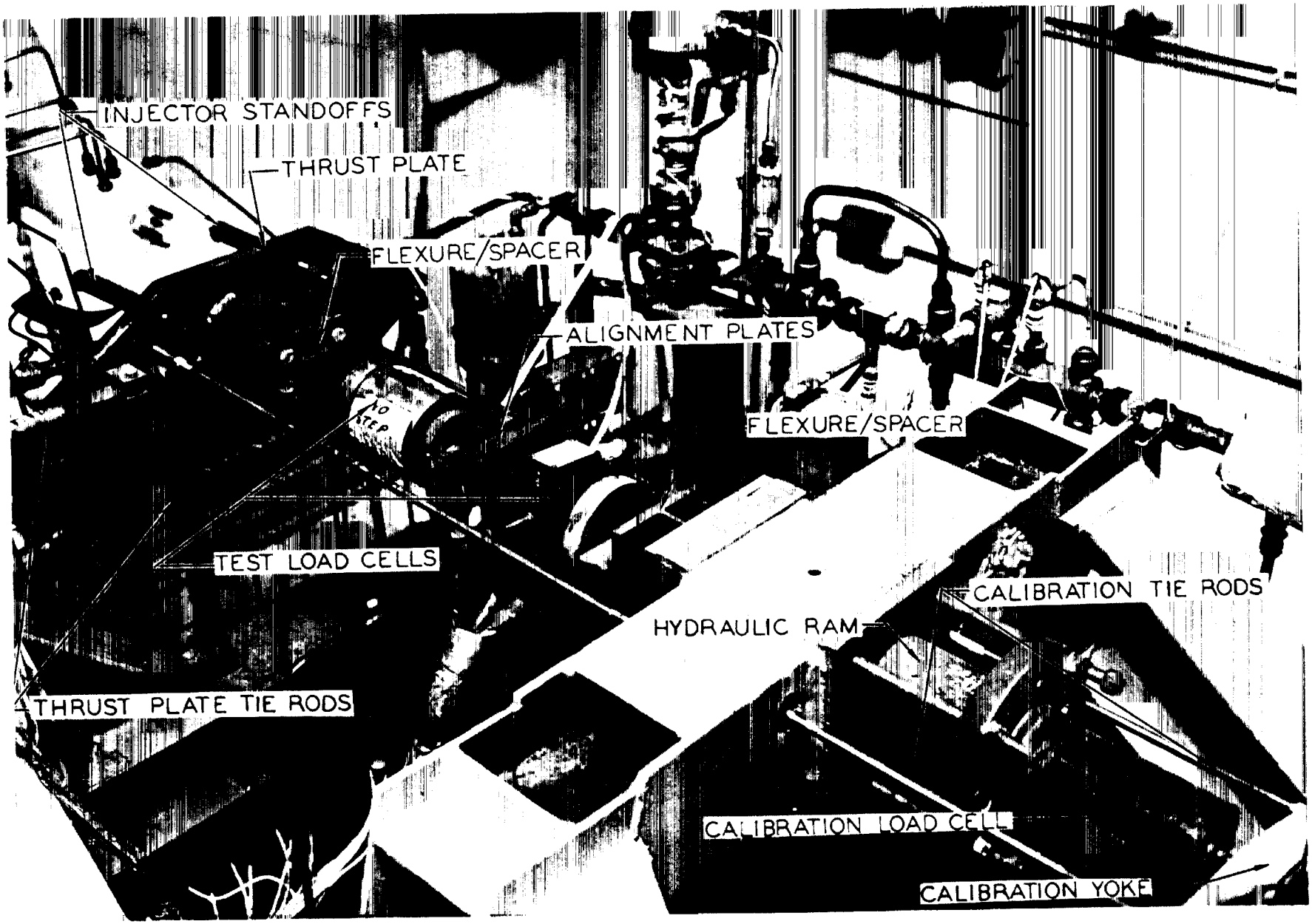

Figure 88. Engine Thrust Mount System

Propellant Lines

The engine plumbing consists of instrumentation lines and propellant feed lines. To minimize test stand effect, all the propellant plumbing is introduced to the injector radially, with relatively long straight actions to allow unrestrained movement of the chamber assembly. The engine instrumentation also has the same feature. The lines are "S" shaped with long leg sections and are fabricated from 1/4-inch light wall tubing. There is no insulation or jacketing on any lines downstream of the rigidly mounted valves or transducers.

Electrical Connections

The engine electrical connections consist of numerous thermocouple wiring and electrical connections which are attached to the temperature probes. These wires (Fig. 87) are connected to a "Jones" strip physically mounted to the hardware. From the terminal strip, the wires are bundled and wrapped in aluminum foil, terminating at a master strip mounted to the stand support.

Diffuser

The diffuser extension (Fig. 87) is 40 inches in diameter. When the 70-percent bell hardware is installed in the stand, there is a 1-inch axial gap from the exit of the bell to the inlet of the diffuser. When the 15-degree cone is installed, the nozzle protrudes into the diffuser 16 inches. When the low-area-ratio nozzle is used, a cylindrical diffuser extension is installed to encapsulate the engine exhaust plume.

INSTRUMENTATION

Throughout this program, the sole test objective has been the acquisition of high quality data. Therefore, special emphasis was placed upon instrumentation and instrumentation systems. In this phase of the program small differences in performance between different propellants and nozzles were to be determined. To ensure still more accurate data, further improvements were made in the instrumentation system for Phase II, including the use of a new digital data acquisition system.

In this task, one nominal value of chamber pressure was used for most tests with only a minimal deviation in propellant flows occurring during mixture ratio surveys. Therefore, it was possible to select instruments that operated in the optimum portion of their range. Because certain parameters are critical in determining engine performance (e.g., flowrates, thrust and chamber pressure) the critical items in these measurements were made redundant.

The location of major test stand instrumentation is shown schematically in Fig. 89. The exact location of the thrust chamber instrumentation for the 70-percent bell is shown in Fig. 90 and 91. The instrumentation for the cone is similar.

Data Acquisition System

During this phase of the program, primary data acquisition was by means of a digital recorder. This digital recorder provides high accuracy with immediate response and is used for precise performance characterization. The digital unit is an Astrodata Model 2013-100

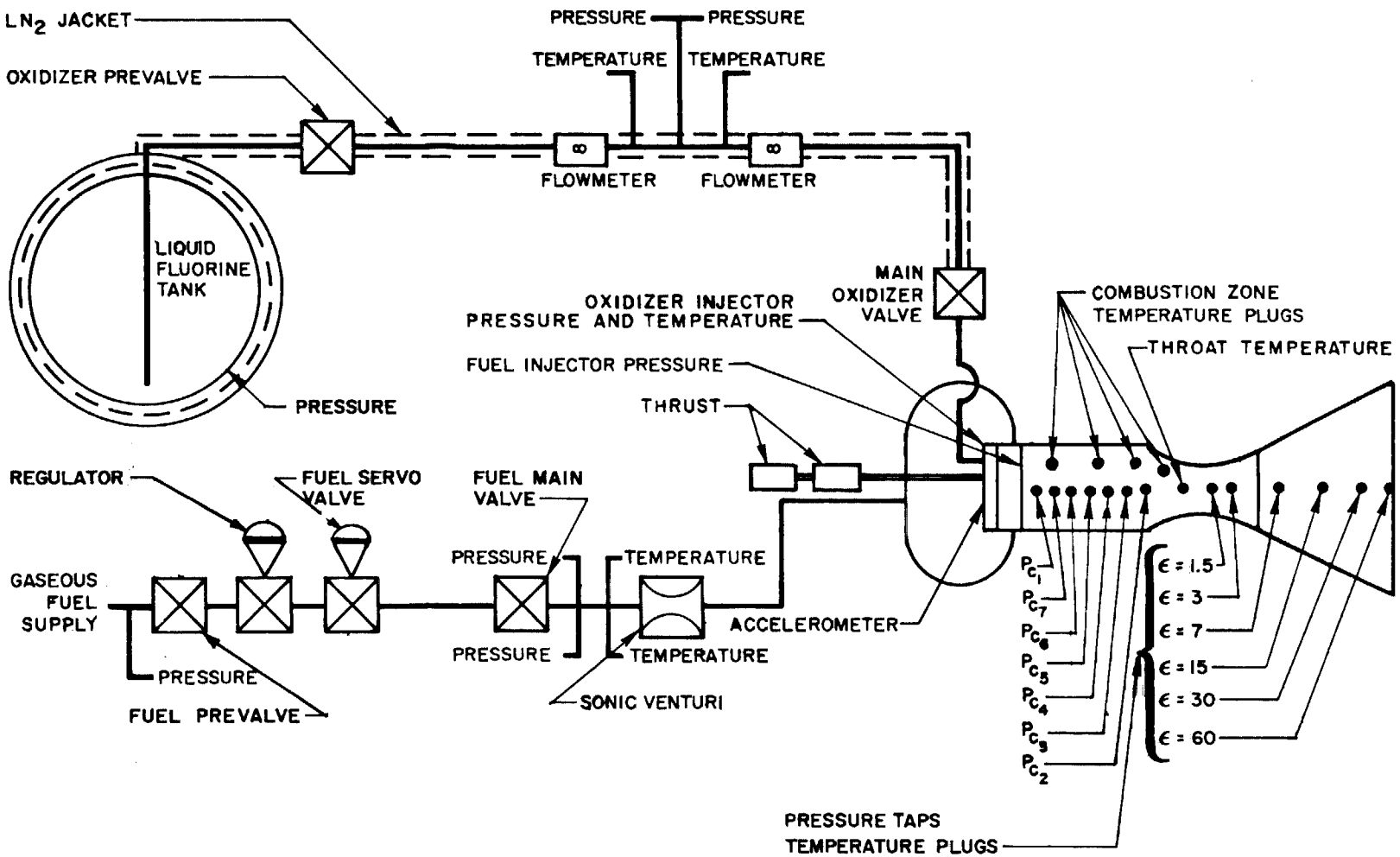

Figure 89. NFL B3 Test Stand Instrumentation Schematic

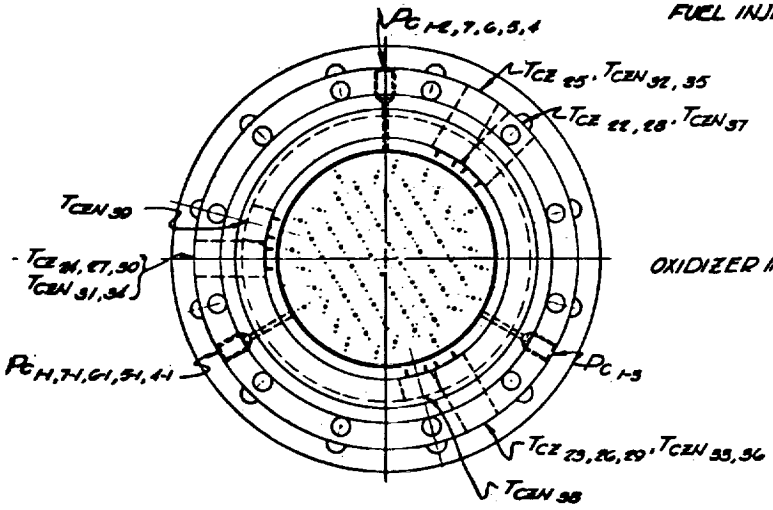

VIEW B-B
NOZZLE OMITTED

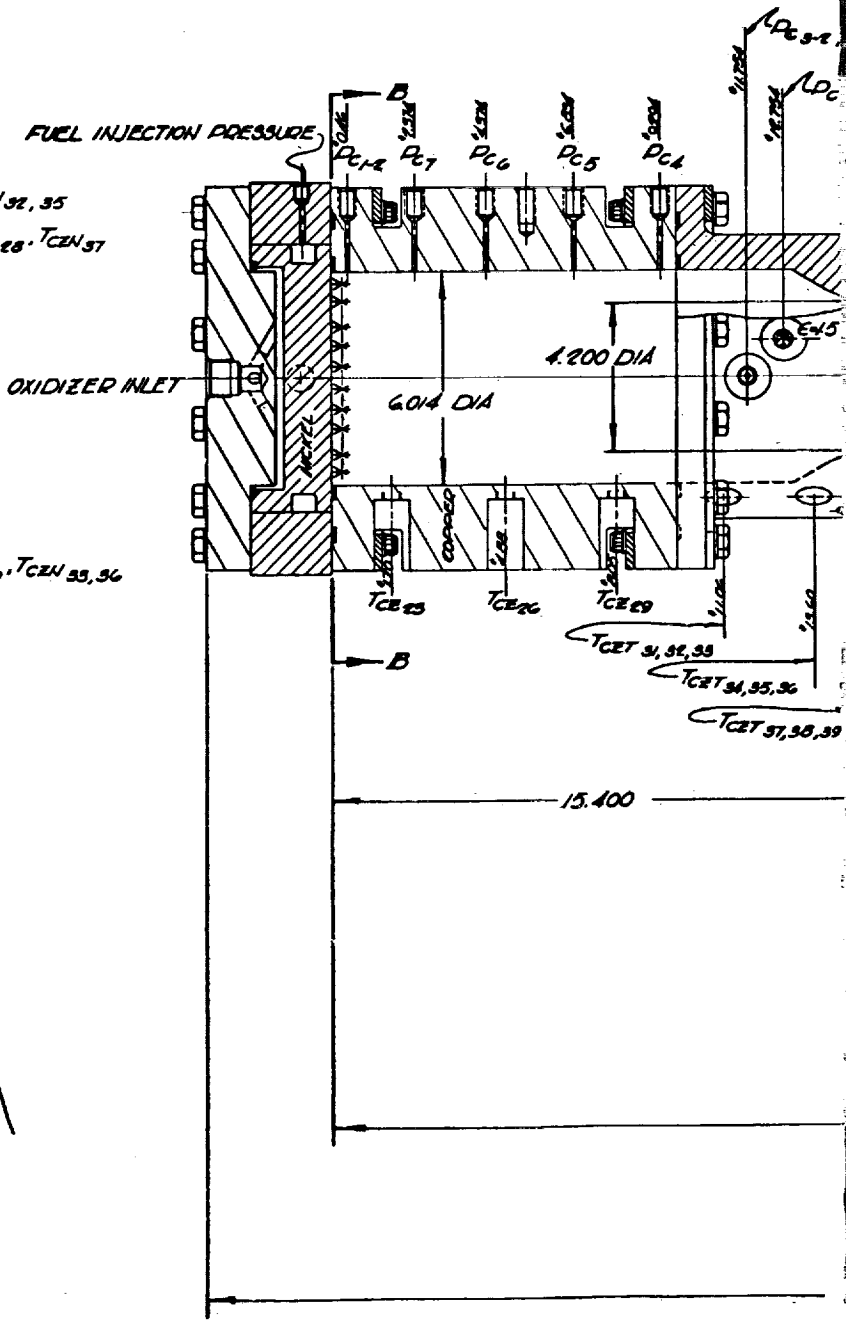

FOLDOUT FRAME

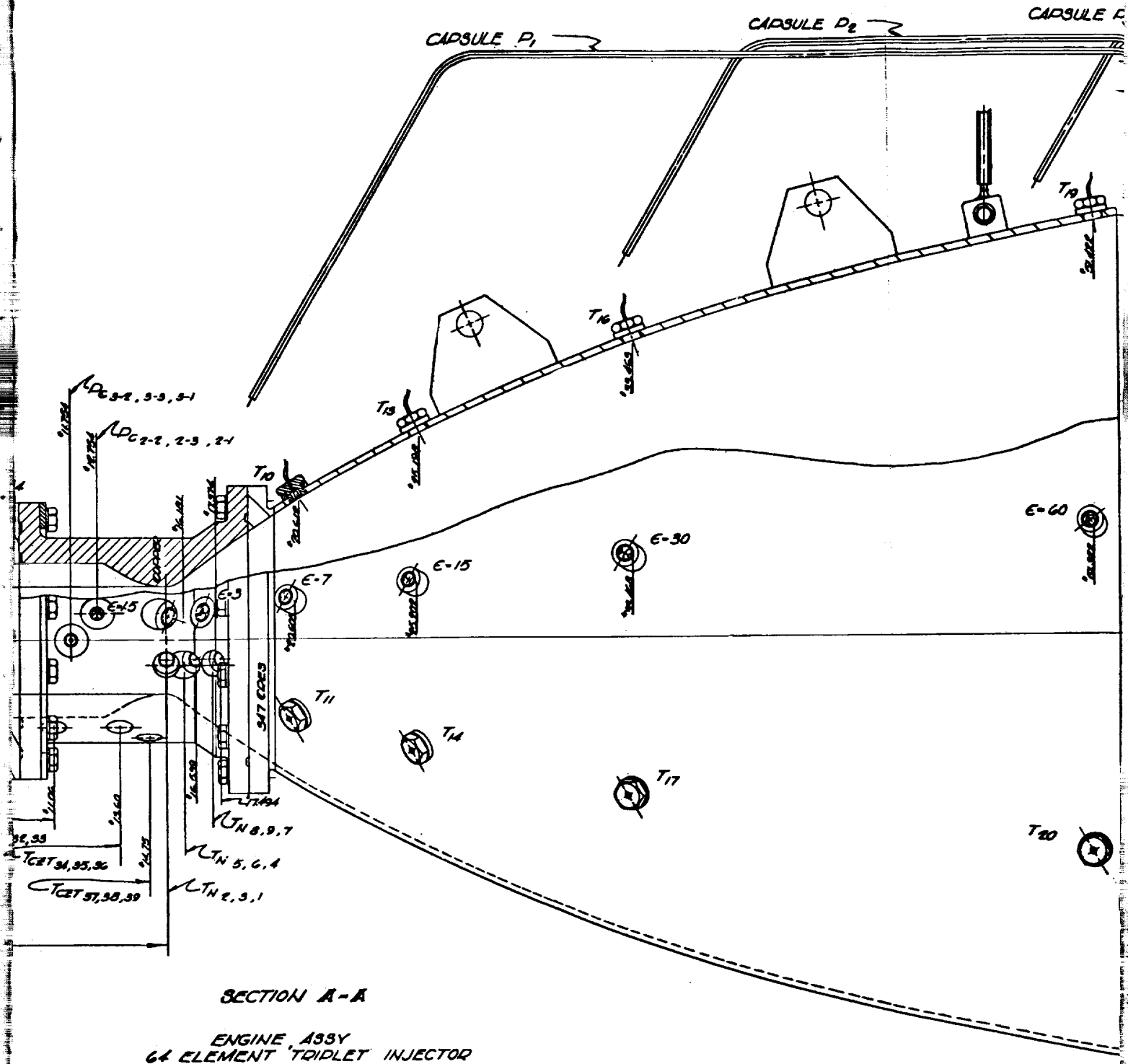

SECTION A-A

ENGINE ASSY
64 ELEMENT TRIPLET INJECTOR

FOLDOUT FRAME

*DIMENSIONS FOR INNER SURFACE

Figure

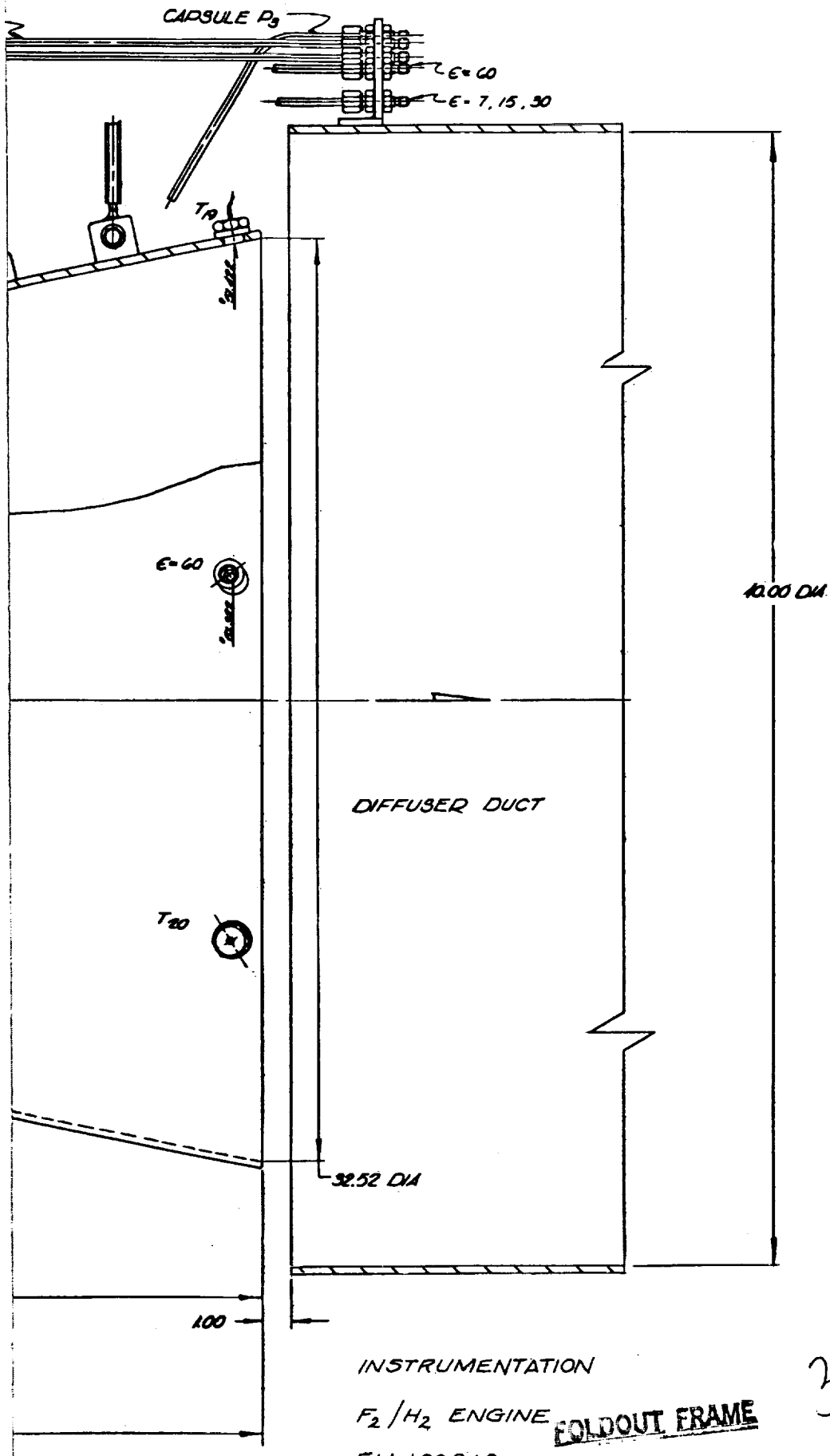

Figure 90. Nozzle Instrumentation Location, Side View

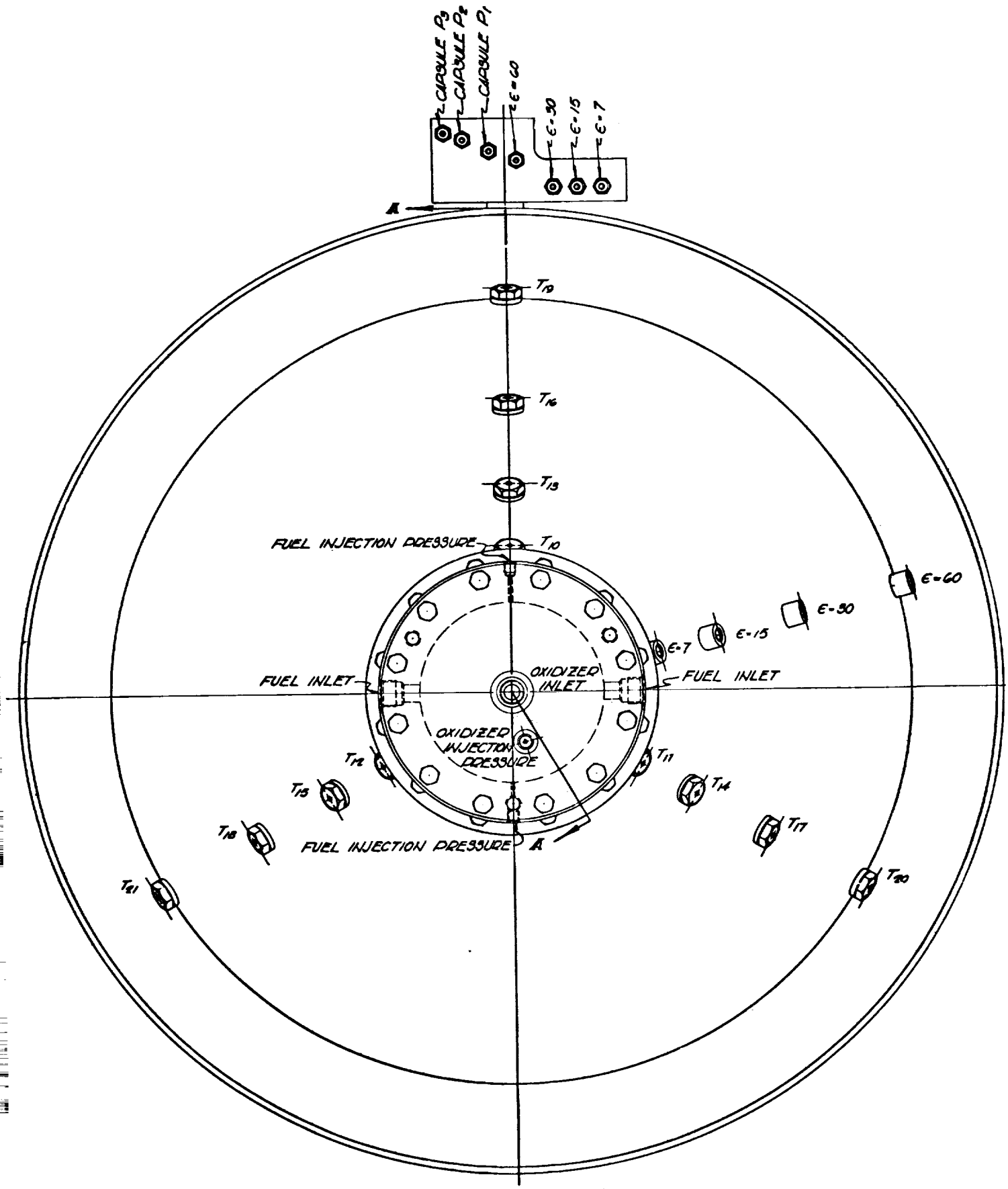

Figure 91. Nozzle Instrumentation Location, End View

portable, a 100 channel system. The recorder has a sampling rate fixed at 11,120 samples per second. Using all channels, as on this program, the sampling time is approximately 11 milliseconds. Oscillograph measurements are used to monitor transient engine performance.

One of the system improvements which resulted from the installation of the digital data acquisition system was the capability of greatly reducing the required test duration to achieve stable high-quality data. After the early activation tests with the digital system, it was found that the critical engine and feed system measurements were stable after approximately 250 msec of start transient as shown in Fig. 92 for a typical activation test. With this new capability, individual test durations were decreased to 2.4 and 1.2 seconds. The first test of each series is long and the remaining tests are short.

Thrust Measurement

Thrust measurement is made by two-series Baldwin-Lima-Hamilton double-bridge load cells. Each cell (2000 pounds) provides a redundant measurement by the double-bridge network, resulting in four separate thrust measurements. Calibration of the load cells is conducted before and after each test series by means of the calibration load cell and a hydraulic loader, Fig. 88. The calibration load cell is calibrated against a proving ring traceable to the National Bureau of Standards.

Pressure Measurement

Pressure transducers are of the bonded strain gage, d-c type. The calibration and verifications of the pressure transducers are accomplished with a dead weight tester or similarly precise calibration device traceable

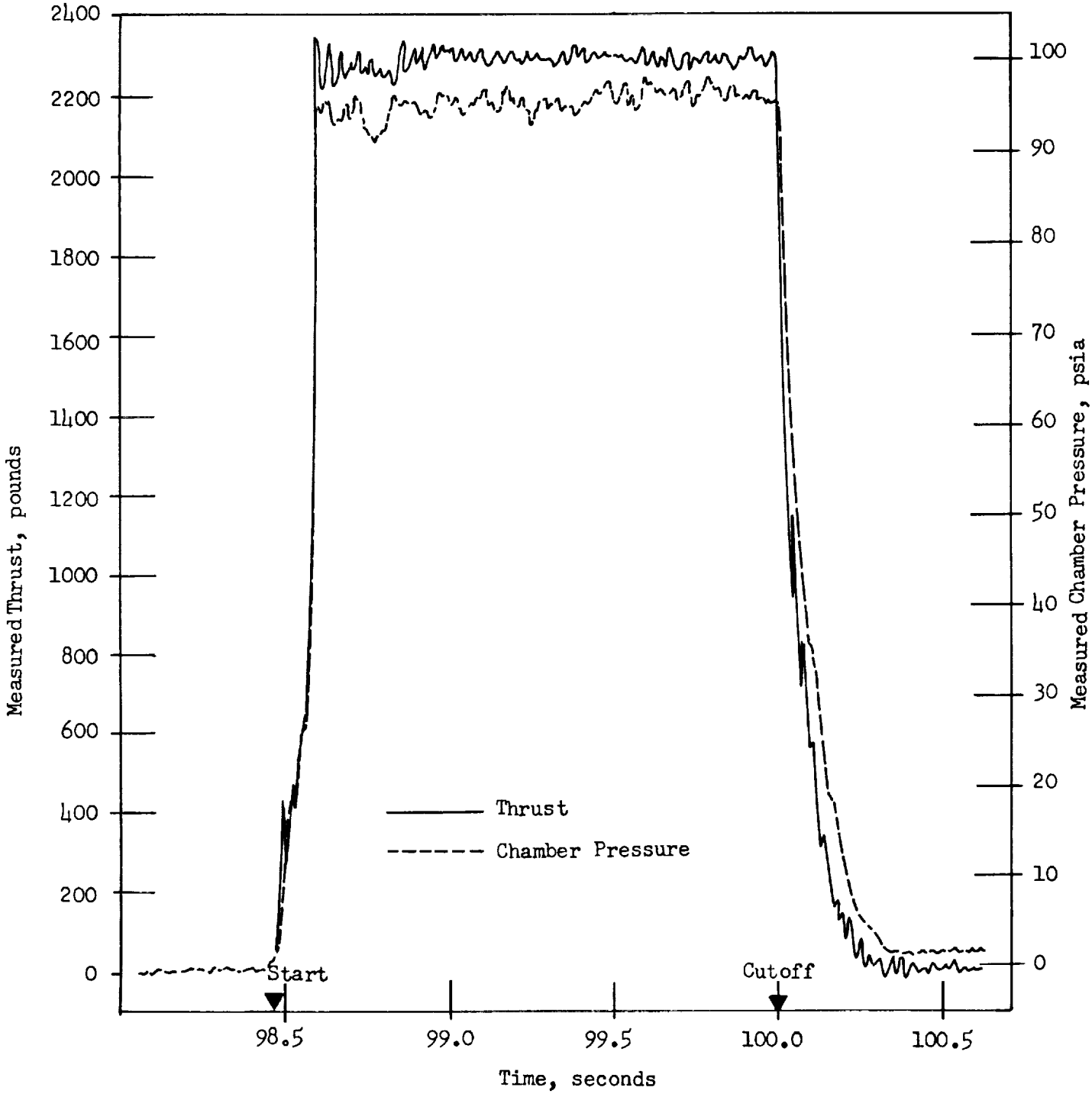

Figure 92. Thrust and Pressure from Digital Data System for Test 377-031.

to the National Bureau of Standards. For LOX clean certified pressure transducers, the calibration and verifications are accomplished by introducing GN_2 and measuring the pressure on a Heise gage.

Flow Measurement

Fuel flowrate is measured by a specially fabricated flow section containing a sonic venturi. This section, having upstream pressure and temperature and downstream pressure measurement, was calibrated by the manufacturer and is the same unit as previously used in Phase I. When measuring B_2H_6 flowrate, a second venturi is used in parallel.

Fluorine flowrate is measured using redundant 1-inch Foxboro turbine-type volumetric flowmeters, Fig. 82. These meters were calibrated using liquid freon. These meters resulted in a more accurate flow measurement than achieved in Phase I for which water calibrated meters were used. Flowmeter disagrement throughout the program was normally approximately 0.1 percent.

Temperature Measurement

Oxidizer temperature is measured using Rosemount shielded platinum resistance bulbs, immersed in the liquid stream. Iron-constantan thermocouples are used for the hydrogen temperature measurements and for the major portion of the thrust chamber temperatures used in the heat transfer calculations. Chromel-Alumel thermocouples are used in the remaining positions.

Heat Flux Measurement

Heat flux determination is based upon the temperature-time history of special control sections embedded in the thrust chamber wall. The temperature measuring device consists of a thermal isolation segment with a thermocouple located on the back side of the segment.

The isolation segments used in the test program are of two types. These are depicted in Fig. 93. Type (a) is installed in the combustor and throat regions to measure high heat flux levels, whereas Type (b) is installed in the nozzle section where heat flux is low. Type (a) is made by cutting isolation grooves into the copper wall to reduce three dimensional heat transfer effects. Thermal plug Type (b) is made by inserting steel plugs into the steel nozzle wall. Each plug contains a thin copper wafer to which is bonded a thermocouple. In this way, heat loss from the plug is minimized and the maximum possible temperature response is obtained.

Visual Recording

Hot-fire test coverage is made by two Gazap 16-64 frps, 16 mm color cameras. These cameras are located high in the capsule, one on each side, and view the engine and associated plumbing immediately behind the engine. In addition, all tests are monitored with a closed circuit television camera.

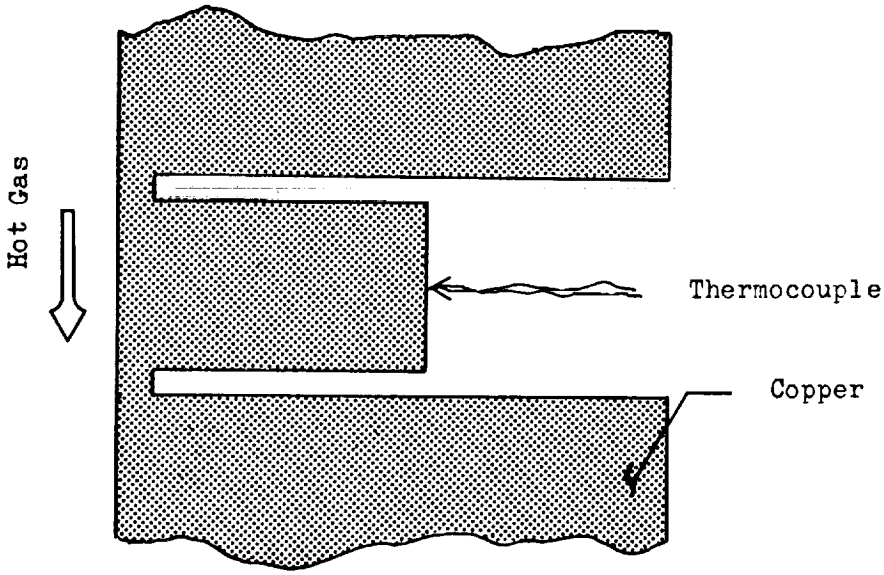

Type (a)

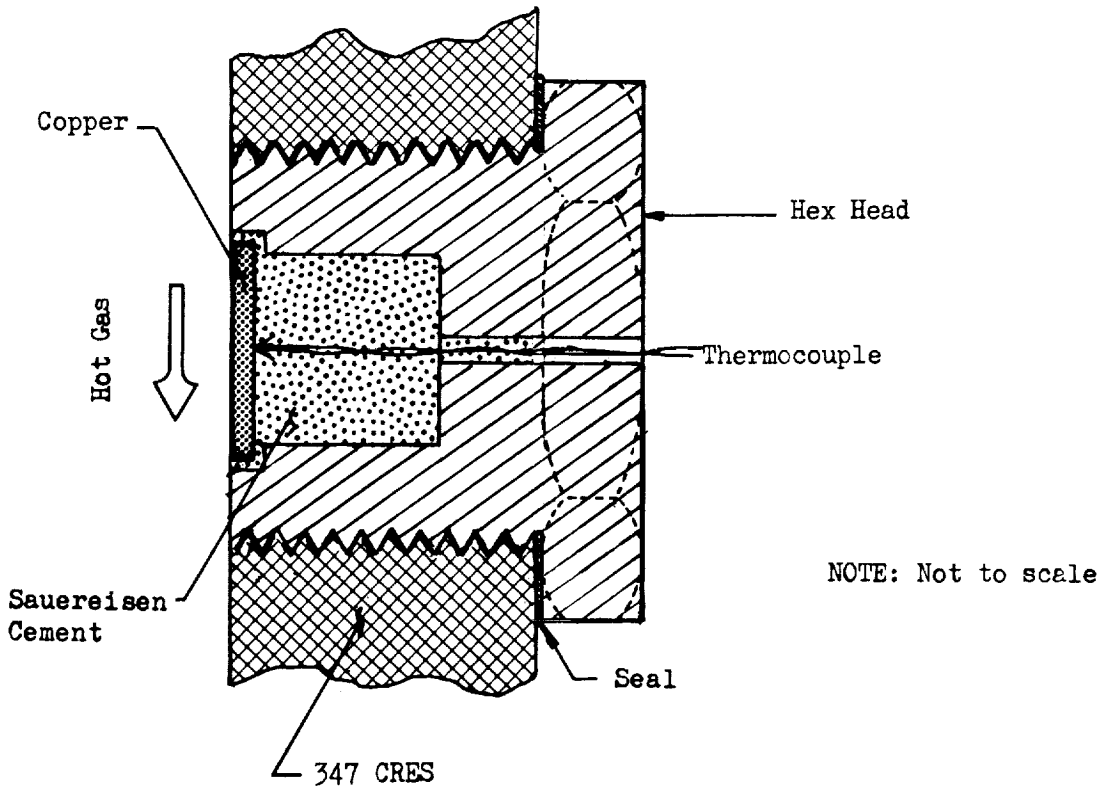

Type (b)

Figure 93 . Schematic Cross-Sections of Heat Transfer Isolation Segments

TEST HARDWARE

The major items of test hardware were identical with those used in the earlier portions of the test program and are described in detail in Ref. 4. The only exception was a new combustion chamber needed to replace the original chamber which had undergone nearly 300 tests. The only test to test hardware variation was the nozzle, of which two were used, an aerodynamic optimum 70-percent bell and a 15-degree cone. The cone was used in two configurations, 4:1 area ratio for injector verification and 60 for performance tests.

Injector

The injector configuration used for all Phase II testing is shown in Fig. 94. It is designed for gaseous fuel and liquid oxidizer and consists of triplet elements in a square pattern. Each triplet element has two impinging oxidizer ports and a central fuel port. The outer elements of the grid are rotated to prevent direct impingement of the oxidizer fan on the chamber wall. The same injector was used for all propellant combinations tested in Task VI.

Combustion Chamber

The combustion chambers consist of heavy wall copper cylinders designed for heat sink operation. This differs from the original chamber in the thickness of the chamber wall, 2 inches rather than 1 inch. The heavier wall has permitted larger numbers of tests in a hyperflow series.

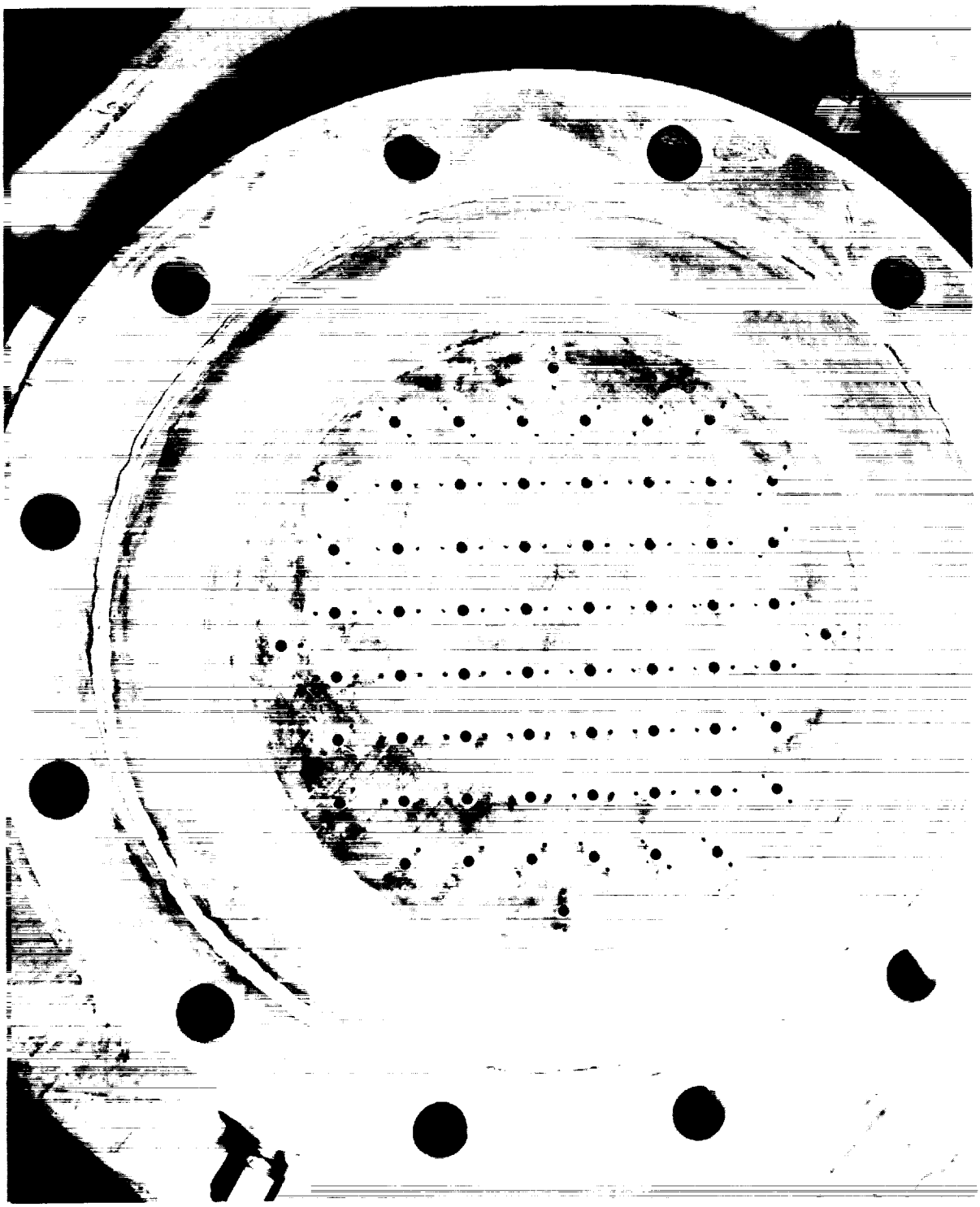

Figure 94. Liquid Fluorine/Gaseous Hydrogen Injector

Nozzles

The nozzle includes the contraction zone, the throat, and the expansion zone. The contraction region, throat and expansion region to an area ratio of four are copper. The expansion region, from area ratio four to sixty, is steel. The wall radius of curvature upstream of the throat is 1.5 times the throat radius of 2.1 inches.

The 15-degree conical nozzle (Fig. 95) has a wall radius of curvature downstream of the throat of 3.635 times the throat radius. For low area ratio injector tests, the steel skirt is removed leaving an area ratio four nozzle.

The 70-percent length bell nozzle (Fig. 96) has a wall radius of curvature downstream of the throat of 0.392 times the throat radius. This value was chosen as being machineable but close in performance to an ideal point expansion. The wall contour was aerodynamically optimized for 60:1 area ratio and 70-percent length, using actual exhaust products.

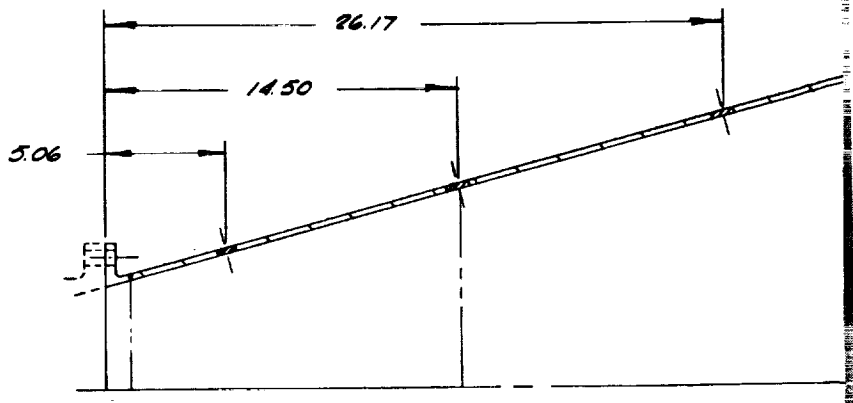

SECTION B-B
(TYP) 3 PLACES

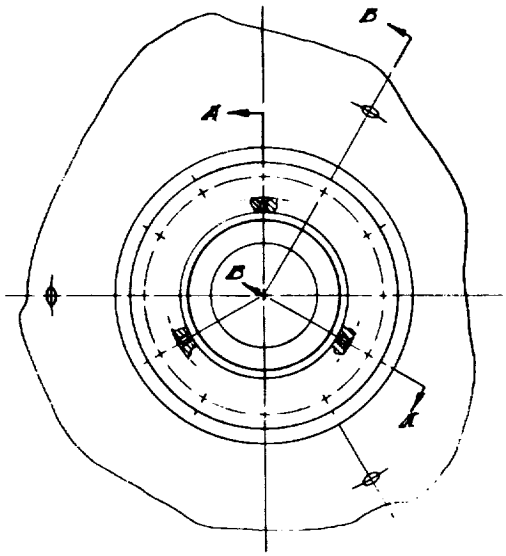

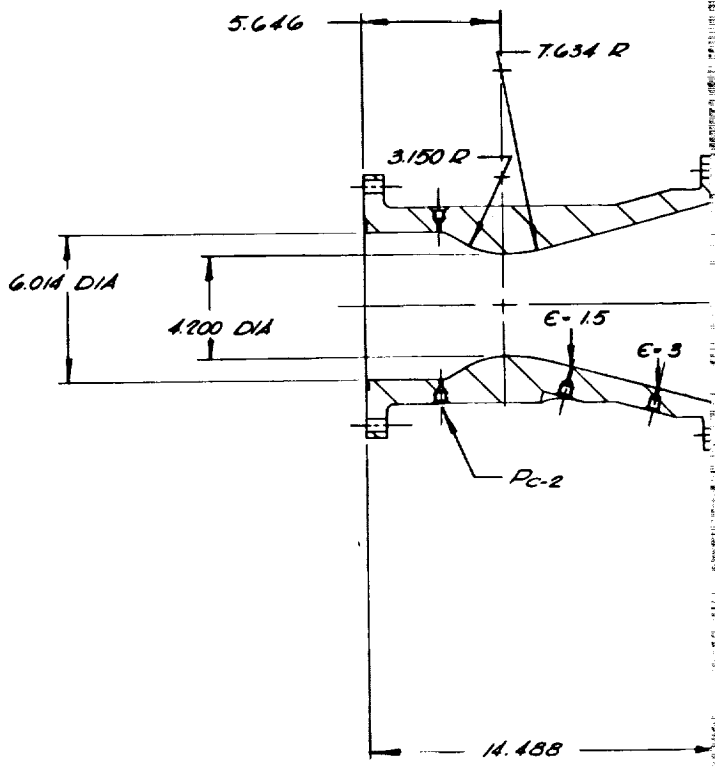

FOLDOUT FRAME

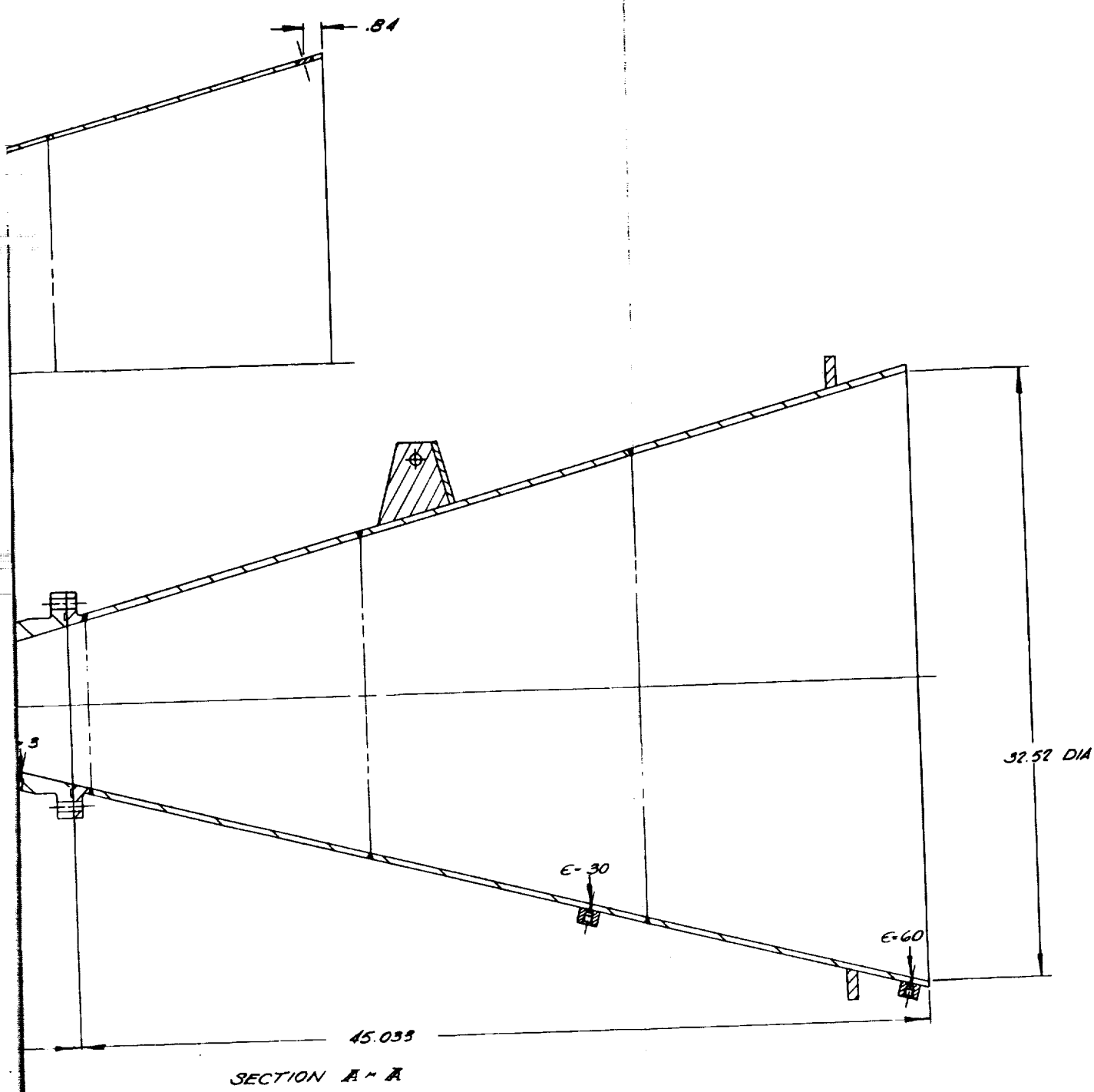

Figure 95. Long Throat 15-Degree Conical Nozzle Design

FOLDOUT FRAME 2

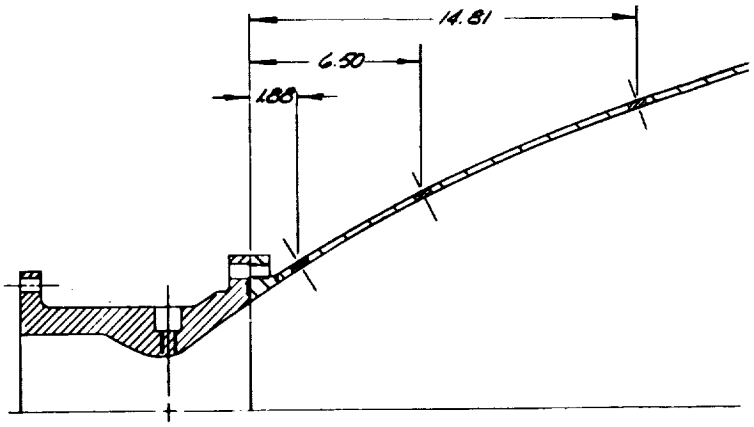

SECTION B-B
(TYP) 3 PLACES

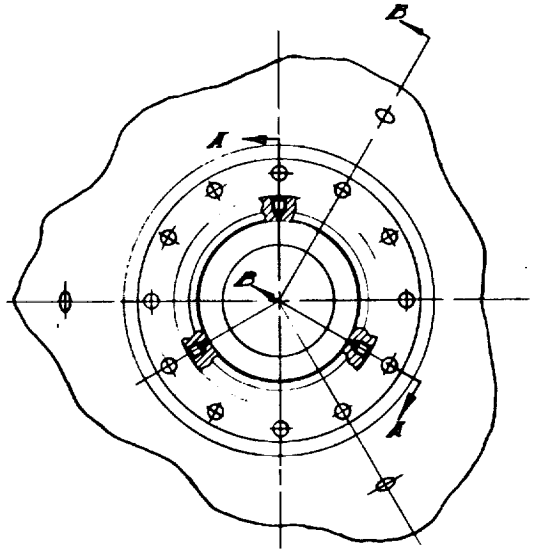

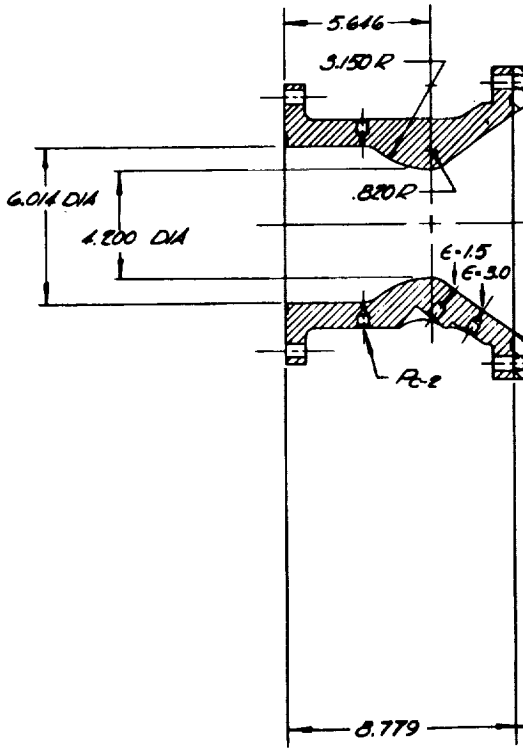

FOLDOUT FRAME

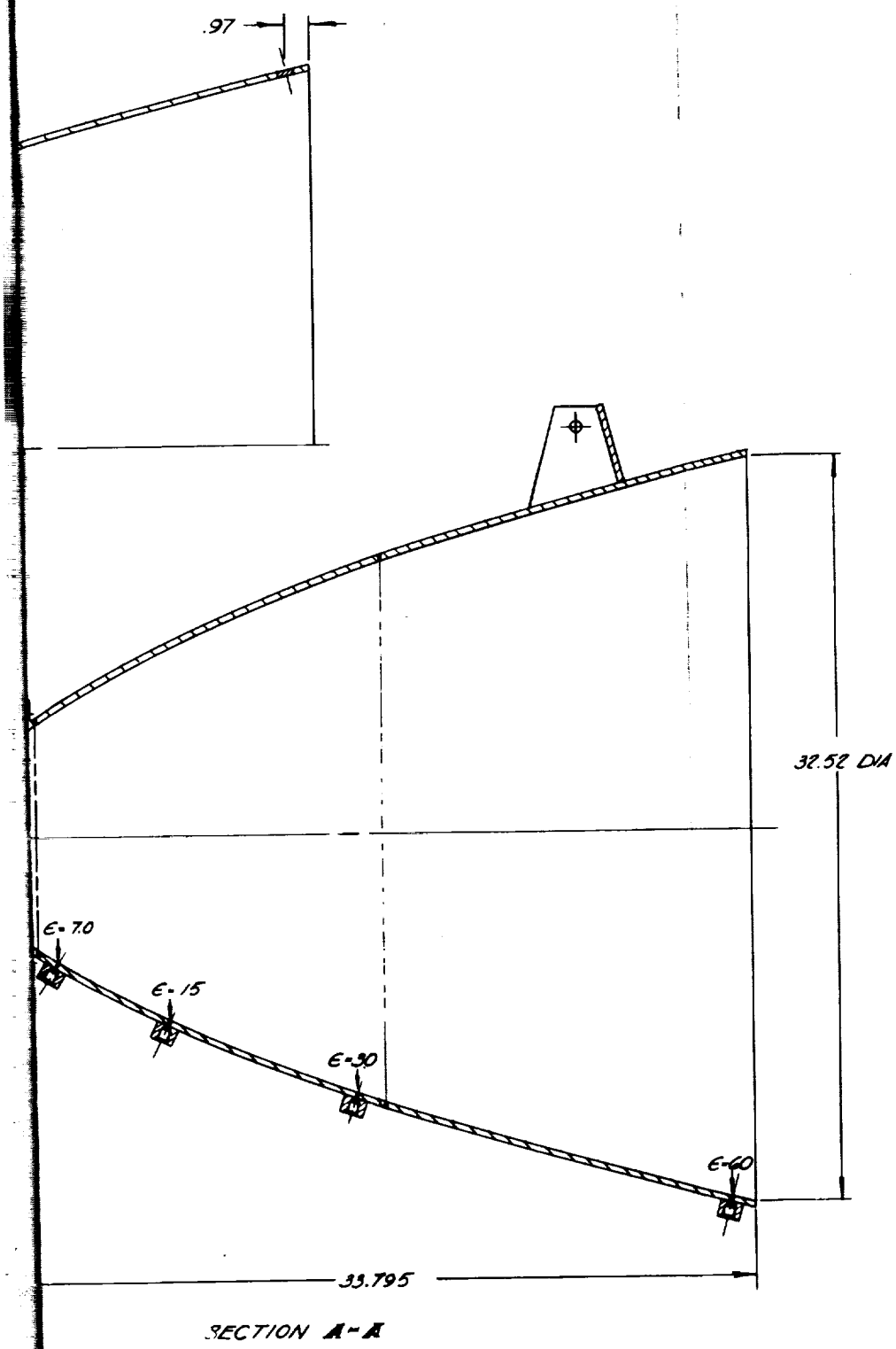

FOLDOUT FRAME 2

Figure 96. 70-Percent Bell Nozzle Design

NOMENCLATURE

Measured Performance Variables

F	Thrust
MR	Ratio of oxidizer mass flowrate to fuel mass flowrate
P	Local static pressure
P_a	Ambient pressure of the engines surroundings
P_c or $P_{c_{NS}}$	Stagnation pressure for nozzle throat conditions
P_e	Exit pressure at the nozzle wall
$\dot{w}$	Mass flowrate

Defined Performance Variables

C_F	Thrust coefficient, $\frac{F_{nozzle}}{P_c A^*}$
C^*	Characteristic velocity, $\frac{P_c A^* g}{\dot{w}_{nozzle}}$
g or g_o	Force conversion constant in equation $F = \frac{ma}{g_o}$, $32.174 \frac{lb_{in}\text{-ft/sec}^2}{lb_f}$
I_s	Specific impulse, $F_{engine} / \dot{w}_{engine}$

Performance Efficiencies

η	Efficiency, $\frac{\text{delivered}}{\text{reference value}}$
η_{BL}	Boundary layer efficiency
η_{CF}	Thrust coefficient efficiency
η_{c^*}	Characteristic velocity efficiency
η_G	Geometric or divergency efficiency
$\eta_{HC_{IS}}$	Specific impulse heat loss efficiency
$\eta_{HL_{C^*}}$	Characteristic velocity heat less efficiency
η_{Inj}	Injector efficiency

η_{IS}	Specific impulse efficiency
η_{k}	Reaction kinetic efficiency
η_{TC}	Thrust chamber efficiency

Heat Transfer, Thermodynamic and Boundary Layer Variables

B_i	Biot number $\frac{h\,l}{k}$
c	Specific heat capacity
C_p	Specific heat capacity for a constant pressure process
C_v	Specific heat capacity for a constant volume process
F_o	Fourier number, $\frac{\alpha t}{l^2}$
h	Specific enthalpy
h or h_g	Heat transfer coefficient of exhaust gases
H	Enthalpy
k	Thermal conductivity
M	Mach number
MW	Molecular weight
n	Isentropic coefficient defined so that PV^n = constant for an isentropic process. For ideal gases n = γ
N_{Pr}	Prandtl number $\frac{c\,\mu}{k}$
R	Gas constant, R/MW
R	Universal gas constant
s	Specific entropy
S	Entropy
T	Local static temperature
T_{BW}	Back wall temperature

T_C	Stagnation temperature
T_i	Initial temperature
T_{uw}	Adiabatic wall temperature
U_e	Exhaust gas velocity at the nozzle exit at the wall
v	Velocity
V	Volume
Z	Compressibility, $P = Z \rho RT$
α	Thermal diffusifity, $k/\rho c$
γ	Specific heat ratio, Cp/Cv
δ_{e^*}	Displacement thickness at the nozzle exit
θ_e	Momentum thickness at the nozzle exit
λ_n	Eigen value in solution of second order differential equation for heat conduction
μ	Viscosity
ρ	Density
ρ_e	Exhaust gas density at the nozzle exit at the wall

Geometric Variables

A	Local area
A_e	Nozzle exit area
A_T	Nozzle Throat Area
A^*	Effective nozzle throat area, $\frac{\dot{w}}{\rho^* V^*}$
L^*	Combustion Chamber characteristic length $\frac{\text{Volume C.C.}}{A_T}$
ℓ	Nozzle wall thickness
r_e	Nozzle exit radius
α_e	Nozzle wall angle with the axis at the nozzle exit
$\frac{\rho}{r_T}$	Wall radius of curvature nominalized to throat radius, usually refers to throat wall contour

Subscripts

$(\quad)_{Corrected}$	Adjusted from a measured value using an analytical or empirical factor
$(\quad)_{Delivered}$	Actual performance as contrasted with $(\quad)_{Ideal}$
$(\quad)_{Ideal}$ or $(\quad)_{Theor.}$	Reference value
$(\quad)_{measured}$	Actual data
$(\quad)_{nominal}$	Adjusted to some nominal conditions using analytical corrections
$(\quad)_{R}$	Reduced value, actual value divided by critical conditions
$(\quad)_{Vac}$	Vacuum conditions

REFERENCES

1. King, R. C. and G. T. Armstrong: "Constant Pressure Flame Calorimetry with Fluorine, II Heat of Formation of Oxygen Difluoride," Journal of Research of the National Bureau of Standards, A. Physics and Chemistry, Vol. 72A, No. 2, March-April 1968.

2. Investigations of Space Storable Propellants (OF_2/B_2H_6), NASA CR-54741, Reaction Motors Division of Thiokol Chemical Corporation, Denville, New Jersey, 10 June, 1966.

3. Arbit, H. A. and S. D. Clapp: Fluorine-Hydrogen Performance Evaluation Phase I, Part I: Analysis, Design, and Demonstration of High-Performance Injectors for the Liquid Fluorine-Gaseous Hydrogen Propellant Combination, NASA CR-54978, Report No. R-6636-1, Rocketdyne, a Division of North American Rockwell Corporation, Canoga Park, California, July 1966.

4. Waldman, B. J. and E. B. Shuster, Fluorine-Hydrogen Performance Evaluation Phase I, Part II: Nozzle Performance Analysis and Demonstration, NASA CR-72038, Report No. R-6636-2, Rocketdyne, a Division of North American Rockwell Corporation, Canoga Park, California, April 1967.

5. Waldman, B. J.: "Performance Prediction and Demonstration for Fluorine/Hydrogen," Proceedings of Ninth Liquid Propulsion Symposium, CPIA No. 155, Vol. 1, September 1967.

6. Galbraith, H. J. and J. F. Masi: "A Generalized Data Fitting Routine for the LGP-30 Computer; Application to Real Gas Properties of Diborane," Thermodynamic and Transport Properties of Gases, Liquids and Solids, ASME.

7. Eads, D. K. and A. Murchison: Pyrolysis of Diborane, Callery Chemical Company, CCC-1024-TR-278, 1 November 1959.

8. Gas Engineers Handbook, The Industrial Press, New York, 1965

9. Rossini, F. D. et al: Selected Values of Physical and Thermodynamic Properties of Hydrocarbons and Related Compounds, Carnegie Press, Pittsburgh, 1952.

APPENDIX A

TEST DATA SUMMARY

The basic test measurements are summarized in Table A-1. In each case the value shown represents the average of the redundant measurements. The efficiencies shown are uncorrected values defined as:

$$\eta_{C^*} = \frac{P_{C_{NS}} A_T B}{\dot{W}_{total} C^*_{theo}}$$

$$\eta_{C_F} = \frac{F_{vac}}{P_{C_{NS}} A_T C_{F_{theo}}}$$

$$\eta_{I_s} = \frac{F_{vac}}{\dot{W}_{total} I_{vac_{theo}}}$$

TABLE A-

TEST DATA SU

1968 Tests

TEST NO. 377-	PROPELLANT	NOZZLE TYPE	OXID DENSITY (lbm/ft^3)	OXID TEMP (°F)	OXID PRESS (psia)	OXID FLOW-RATE (lbm/sec)	FUEL VENTURI PRESS (psia)	FUEL VENTURI TEMP (°F)	FUEL FLOW-RATE (lbm/sec)	MIXT RAT
033 -2	$F_2 - O_2$	$\epsilon = 4$	89.65	-303.70	410.43	5.160	500.44	52.43	1.003	5.1
034	(83.8)/	$\epsilon = 4$	89.69	-303.96	394.10	4.997	578.14	58.89	1.159	4.3
035	CH_4	$\epsilon = 4$	89.35	-302.47	404.19	5.100	510.34	58.12	1.019	5.0
036		$\epsilon = 4$	88.70	-299.60	422.74	5.228	451.30	56.61	0.898	5.8
037		$\epsilon = 4$	88.22	-297.64	413.80	5.163	472.53	58.48	0.941	5.4
038		$\epsilon = 4$	88.02	-296.90	388.26	4.952	651.95	66.73	1.296	3.8
039		$\epsilon = 4$	85.98	-288.51	404.65	5.011	481.16	55.52	0.961	5.2
040 *		$\epsilon = 4$	87.49	-294.57	416.84	4.903	461.32	58.89	0.917	5.3
041 *		$\epsilon = 4$	87.00	-292.64	402.33	4.967	512.40	60.29	1.021	4.8
042 *		$\epsilon = 4$	85.67	-287.33	398.81	4.779	556.21	61.11	1.110	4.3
043 -2	$F_2 - O_2$	15° Cone	86.77	-292.78	423.54	5.078	532.12	46.98	1.073	4.7
044	(82.3)/	15° Cone	86.95	-293.58	410.79	4.998	626.41	55.35	1.262	3.9
045	CH_4	15° Cone	86.58	-292.03	414.55	5.109	556.27	56.54	1.115	4.5
046		15° Cone	86.04	-289.74	431.53	5.226	500.04	56.67	0.999	5.2
047		15° Cone	85.55	-287.78	427.06	5.134	515.73	58.87	1.030	4.9
048		15° Cone			Facility Malfunction					
049 -1		15° Cone	85.84	-289.07	409.81	5.089	555.94	50.86	1.120	4.5
050		15° Cone	86.44	-291.40	422.82	5.135	497.65	60.27	0.991	5.1
051		15° Cone	86.43	-291.42	416.72	5.131	511.12	64.50	1.012	5.0
052		15° Cone	86.24	-290.72	400.54	5.031	600.55	71.63	1.182	4.2
053		15° Cone	85.88	-289.27	401.90	5.034	629.72	76.82	1.230	4.0
054		15° Cone	85.71	-288.48	417.28	5.066	537.58	75.98	1.047	4.8
055 -2		70% Bell	88.44	-300.15	427.90	5.229	525.72	50.43	1.057	4.9
056		70% Bell	87.78	-297.34	434.40	5.342	477.53	49.90	0.957	5.5
057		70% Bell	87.16	-294.80	419.37	5.207	557.26	56.62	1.117	4.6
058		70% Bell	85.61	-289.23	419.89	5.035	657.10	64.85	1.310	3.8
059		70% Bell	84.71	-284.90	412.55	4.977	734.80	70.42	1.456	3.4
060		70% Bell	84.70	-284.74	430.79	5.083	516.32	62.16	1.026	4.
	* Ambient Tests									

LE A-1

A SUMMARY

MIXTURE RATIO	TOTAL FLOW-RATE (lbm/sec)	P_{c_2} (psia)	P_c Ns (nozzle stag-nation) (psia)	VACUUM THRUST (lbf)	THROAT AREA (sq in.)	EXIT AREA (sq in.)	η c* (unc)	η c_f (unc)	η ISP (unc)	VACUUM SPECIFIC IMPULSE (lbf-sec/lbm)
5.144	6.163	92.1	95.4	2032.0	13.73	55.40	98.21	95.60	93.89	329.7
4.313	6.155	91.5	94.8	2029.3	13.77	55.40	99.39	95.93	95.34	329.7
5.005	6.120	91.0	94.3	2022.2	13.79	55.40	98.29	95.95	94.31	330.5
5.821	6.126	89.7	92.9	2001.0	13.81	55.40	96.80	95.92	92.86	326.6
5.489	6.104	90.3	93.5	2004.3	13.83	55.40	97.70	95.40	93.21	328.4
3.821	6.248	91.1	94.3	2031.8	13.84	55.40	98.88	95.85	94.78	325.2
5.215	5.971	88.4	91.6		13.75	55.40	97.78	98.05		
5.345	5.820	90.9	94.1		13.78	55.40				
4.863	5.988	88.5	91.7		13.83	55.40	98.17			
4.304	5.889	87.6	90.8		13.78	55.40	99.63			
4.730	6.151	91.7	95.0	2364.1	13.71	829.58	98.33	93.13	91.57	384.3
3.961	6.260	92.5	95.8	2379.9	13.73	829.58	99.33	92.96	92.33	380.2
4.580	6.224	92.6	95.9	2390.5	13.74	829.58	98.55	93.17	91.83	384.0
5.231	6.225	92.9	96.2	2380.5	13.75	829.58	98.07	91.92	90.15	382.4
4.986	6.163	91.7	95.0	2364.9	13.76	829.58	98.10	92.67	90.91	383.7
4.544	6.209	92.8	96.1	2387.1	13.71	829.58	98.87	93.06	92.01	384.5
5.181	6.126	90.9	94.2	2329.9	13.73	829.58	97.53	92.03	89.75	380.3
5.070	6.143	91.4	94.7	2348.3	13.74	829.58	97.93	92.32	90.41	382.2
4.258	6.213	92.0	95.3	2377.7	13.75	829.58	98.96	93.21	92.24	382.7
4.092	6.265	92.0	95.3	2390.3	13.76	829.58	98.68	93.62	92.39	381.6
4.839	6.113	89.1	92.3	2296.5	13.77	829.58	96.41	92.63	89.30	375.7
4.946	6.287	93.4	96.7	2410.9	13.75	823.21	97.96	92.83	90.93	383.5
5.580	6.299	93.2	96.5	2371.3	13.79	823.21	97.38	90.64	88.26	376.5
4.660	6.324	93.5	96.9	2417.8	13.80	823.21	98.31	92.81	91.24	382.3
3.843	6.345	91.5	94.8	2360.3	13.82	823.21	98.08	92.54	90.77	372.0
3.418	6.433	92.5	95.9	2396.3	13.83	823.21	98.95	93.17	92.19	372.5
4.952	6.110	89.9	93.1	2320.2	13.85	823.21	97.76	92.12	90.05	379.8

LAYOUT FORMS 7

TABLE A-1
TEST DATA SUMMARY

TEST NO. 377-	PROPELLANT	NOZZLE TYPE	OXID DENSITY (lbm/ft^3)	OXID TEMP (^oF)	OXID PRESS (psia)	OXID FLOW-RATE (lbm/sec)	FUEL VENTURI PRESS (psia)	FUEL VENTURI TEMP (^oF)	FUEL FLOW-RATE (lbm/sec)	MIXTUR RATIO
061 -5	F_2-O_2	15° Cone	86.25	-303.02	389.39	4.848	436.54	92.41	1.516	3.19
062.-3	(70.4)/	15° Cone	85.86	-301.25	393.67	4.892	483.10	101.28	1.678	2.91
063 -3	B_2H_6	15° Cone	84.06	-293.17	411.54	4.900	436.58	96.16	1.502	3.26
064		15° Cone	84.55	-295.31	408.43	4.954	451.94	89.30	1.590	3.11
065		15° Cone	84.47	-294.98	406.03	4.919	480.84	98.26	1.679	2.92
066		15° Cone	83.67	-291.37	433.13	5.053	403.96	89.54	1.387	3.64
067		15° Cone	84.00	-292.79	437.82	5.100	373.36	89.98	1.268	4.02
068 -4		15° Cone	85.00	-297.31	412.88	4.944	464.22	111.10	1.569	3.15
069		15° Cone	84.59	-295.63	380.21	4.703	567.14	119.96	1.948	2.41
070		15° Cone	84.36	-294.59	388.89	4.744	553.80	125.37	1.874	2.53
071		15° Cone	84.05	-293.13	412.62	4.888	535.82	127.08	1.809	2.70
072		15° Cone	83.94	-292.63	418.49	4.919	429.24	119.07	1.414	3.47
073-9	F_2-O_2/CH_4	15° Cone	83.44	-291.61	412	5.399	545	96.97	1.074	5.026
074			83.01	-289.87	395	5.304	611	98.32	1.163	4.560
075			83.18	-290.58	396	5.366	598	98.42	1.138	4.713
076			82.74	-288.81	413	5.481	585	99.91	1.111	4.931
077			82.87	-289.17	411	5.470	560	100.03	1.062	5.151
078			83.18	-290.43	424	5.582	529	100.17	1.001	5.576
079-4	F_2-O_2/	15° Cone	82.28	-286.94	427	2.946	324	76.06	0.828	3.459
080	B_2H_6		82.65	-288.97	346	2.628	242	71.48	0.611	4.303
081			81.95	-286.03	349	2.617	280	78.49	0.700	3.787
082			81.86	-285.65	348	2.616	293	84.54	0.729	3.591
083			82.02	-286.26	352	2.622	345	92.46	0.864	3.036
084			82.10	-286.60	353	2.628	242	84.55	0.600	4.379
085			82.14	-286.77	354	2.631	282	88.66	0.698	3.770
086			82.34	-287.61	354	2.632	292	90.83	0.721	3.650
087-5	F_2-O_2/	$\epsilon = 4$	80.55	-280.25	413	4.428	395	86.25	1.364	3.248
088	B_2H_6		80.74	-281.01	414	4.539	410	90.26	1.414	3.210
089			81.05	-282.36	406	4.519	426	95.46	1.465	3.084
090			81.30	-283.25	429	4.726	368	90.89	1.250	3.780
091			81.97	-286.03	439	4.810	356	92.00	1.200	4.007
092			82.32	-287.64	418	4.704	398	96.49	1.353	3.477
093-3	F_2-O_2/	70% Bell	77.06	-267.62	295	3.132	570	103.21	2.041	1.535

FOLDOUT FRAME

tinued

TOTAL FLOW-RATE (lbm/sec	P_{c_2} (psia)	$P_{c_{Ns}}$ (Nozzle stagnation) (psia)	VACUUM THRUST (lbf)	THROAT AREA (sq in.)	EXIT AREA (sq. in.)	η_{C^*} (unc)	η_{C_F} (unc)	η_{ISP} (unc)	VACUUM SPECIFIC IMPULSE (lbf-sec/lbm)
6.364	96.1	99.6	—	13.71	823.21	97.19	Facility Malfunction		
6.570	99.5	103.1	—	13.77	823.21	98.41	Facility Malfunction		
6.402	96.2	99.6	2603.9	13.64	823.21	96.11	95.87	92.15	406.7
6.544	99.4	103.0	2661.0	13.69	823.21	97.74	94.41	92.27	406.6
6.598	100.1	103.6	2684.5	13.73	823.21	98.21	94.37	92.68	406.9
6.440	97.8	101.3	2644.5	13.77	823.21	97.80	94.76	92.67	410.6
6.368	96.2	99.6	2623.5	13.80	823.21	97.70	95.23	93.04	412.0
6.513	99.1	102.7	2670.7	13.66	823.21	97.67	95.25	93.03	410.0
6.651	100.1	103.7	2680.3	13.72	823.21	98.70	94.43	93.20	403.0
6.618	100.0	103.6	2681.0	13.75	823.21	98.94	94.33	93.33	405.1
6.697	100.4	104.0	2706.1	13.78	823.21	97.96	94.54	92.61	404.0
6.333	95.6	99.1	2599.1	13.81	823.21	97.63	95.01	92.76	410.4
6.473	95.9	98.8	2421.5	13.65	823.21	.989	.928	.878	374.1
6.467	95.5	98.9	2421.9	13.68	823.21	.988	.916	.905	375.4
6.504	96.2	99.6	2441.9	13.70	823.21	.992	.912	.915	375.4
6.594	97.3	100.8	2481.4	13.72	823.21	.994	.910	.905	376.4
6.531	95.9	99.3	2450.8	13.74	823.21	.994	.905	.901	375.2
6.533	95.8	99.2	2459.6	13.75	823.21	.993	.901	.875	376.7
3.774	56.7	58.8	1497.8	13.64	823.21	.969	.921	.892	396.9
3.238	47.9	49.6	1268.7	13.69	823.21	.962	.932	.897	391.8
3.318	50.4	52.2	1313.9	13.71	823.21	.984	.892	.878	396.0
3.345	50.5	52.3	1323.1	13.73	823.21	.982	.911	.894	395.6
3.486	53.1	55.0	1377.3	13.75	823.21	.998	.910	.908	395.1
3.229	47.7	49.4	1268.2	13.77	823.21	.968	.931	.900	392.8
3.329	49.6	51.3	1319.5	13.78	823.21	.971	.912	.886	396.4
3.353	49.7	51.5	1327.3	13.80	823.21	.969	.922	.893	395.8
5.792	88.4	91.5	1959.2	13.62	55.40	.977	.967	.944	338.3
5.952	90.3	93.6	2012.1	13.68	55.40	.976	.968	.944	338.0
5.984	90.2	93.4	2013.6	13.71	55.40	.973	.967	.941	336.5
5.977	89.9	93.1	2021.1	13.74	55.40	.968	.972	.940	338.2
6.010	90.1	93.3	2030.2	13.76	55.40	.967	.972	.940	337.8
6.057	91.0	94.2	2049.1	13.79	55.40	.970	.971	.942	373.4
5.173	75.1	77.8	1931.9	13.75	823.21	.998	.912	.910	373.4

FOLDOUT FRAME 2

TABLE A-1 (Continued)

TEST NO.	PROPEL-LANT	NOZZLE TYPE	OXID DENSITY (lbm/ft^3)	OXID TEMP (F)	OXID PRESS (PSIA)	OXID FLOW-RATE (lbm/sec)	FUEL VENTURI PRESS (PSIA)	FUEL VENTURI TEMP (deg F)	FUEL FLOW-RATE (lbm/sec
094	B_2H_6		80.65	-281.15	375	4.176	510	92.04	1.838
095			81.34	-283.81	407	4.495	439	91.42	1.532
096			81.57	-284.72	416	4.596	405	96.91	1.378
097			81.44	-284.10	433	4.725	381	95.91	1.283
098			81.23	-283.30	415	4.581	406	101.70	1.372
099			81.57	-284.79	409	4.548	461	109.28	1.563
100			82.60	-287.01	399	4.528	463	114.04	1.559
101-3	OF_2/B_2H_6	70% Ball	96.10	-244.52	332	4.503	541	88.5	2.011
102			98.06	-256.69	354	4.774	477	87.8	1.712
103			97.82	-255.05	372	4.934	427	90.3	1.485
104			98.17	-257.26	378	5.082	382	93.4	1.295
105			98.68	-260.38	414	5.346	355	94.3	1.190
106			98.20	-257.44	383	5.060	380	98.3	1.277
107			98.32	-258.21	378	5.012	424	102.6	1.436
108			98.61	-260.17	355	4.814	470	105.8	1.612
122	OF_2/CH_4	15° Cone							Facility
123									Facility
124									Facility
125			100.18	-270.24	398	5.794	540	90.8	1.033
126			100.05	-269.32	413	5.943	511	89.9	.976
127			99.55	-266.07	402	5.826	542	93.8	1.033
128			99.80	-267.69	398	5.782	575	98.8	1.092
129			98.44	-258.91	393	5.668	608	103.9	1.151
130			98.71	-260.67	388	5.942	166	83.9	.298

1969 Tests

001-3	OF_2/B_2H_6	15° Cone	99.20	-264.11	323	4.625	554	90.5	2.049
002			100.69	-273.99	284	4.893	480	89.8	1.715
003			100.76	-274.49	279	5.127	438	90.5	1.532
004			100.92	-275.57	279	5.267	397	91.5	1.359
005			100.82	-274.81	295	5.417	365	90.0	1.239
006			97.75	-254.96	288	5.300	397	95.8	1.349

FOLDOUT FRAME

TABLE A-1 Continued

MIXTURE RATIO	TOTAL FLOW-RATE (lbm/sec)	P_c (PSIA)	P_{cN_s} (nozzle stagnant (PSIA)	VACUUM THRUST (lbf)	THROAT AREA (sq in)	EXIT AREA (sq in)	η_{c^*} (unc)	η_{C_F} (unc)	η ISP	VACUUM SPECIFIC IMPULSE I_{SP} lbf-sec/lbm
2.272	6.014	89.3	92.5	2364.6	13.78	823.21	.987	.931	.919	393.2
2.934	6.027	91.2	94.5	2424.2	13.80	823.21	.987	.930	.917	402.3
3.337	5.974	90.4	93.7	2416.1	13.84	823.21	.983	.933	.916	404.4
3.683	6.008	90.6	93.8	2428.5	13.86	823.21	.978	.933	.913	404.2
3.340	5.952	90.0	93.2	2409.3	13.89	823.21	.985	.931	.917	404.8
2.910	6.111	91.9	95.2	2460.0	13.90	823.21	.987	.930	.918	402.5
2.904	6.087	91.1	94.3	2445.1	13.92	823.21	.984	.932	.917	401.7
2.240	6.514	98.0	101.5	2578.8	13.72	823.21	.986	.931	.918	395.9
2.789	6.485	98.7	102.3	2620.7	13.74	823.21	.980	.934	.915	404.1
3.322	6.419	98.5	102.1	2629.4	13.77	823.21	.981	.936	.918	409.6
3.885	6.327	96.7	100.2	2595.3	13.80	823.21	.988	.937	.916	410.2
4.491	6.537	99.6	103.2	2683.8	13.82	823.21	.982	.938	.921	410.6
3.964	6.336	96.8	100.2	2602.5	13.85	823.21	.980	.936	.917	410.7
3.490	6.449	98.2	101.7	2642.6	13.87	823.21	.978	.937	.917	409.8
2.987	6.426	97.4	100.9	2618.8	13.74	823.21	.972	.945	.919	407.5
idizer	Valve Malfunction									
idizer	Valve Malfunction									
idizer	Valve Malfunction									
5.609	6.827	102.1	105.8	2568.0	13.70	823.21	1.002	.888	.890	376.1
6.087	6.920			2577.5	13.71	823.21			.891	372.5
5.640	6.859	101.9	105.6	2588.2	13.73	823.21	.998	.894	.893	377.4
5.293	6.875	102.7	106.4	2614.2	13.74	823.21	.999	.899	.898	380.3
4.926	6.819	102.9	106.6	2618.5	13.76	823.21	1.005	.904	.908	384.0
19.922	6.240	60.6	62.8	1507.8	13.77	823.21	Facility	Fuel Servo	Valve Malfunction	
2.257	6.674	101.7	105.4	2676.8	13.64	823.21	0.992	0.936	0.928	401.1
2.854	6.607	101.0	104.6	2670.3	13.70	823.21	0.979	0.933	0.914	404.2
3.348	6.659	102.2	105.9	2722.6	13.73	823.21	0.977	0.937	0.916	408.9
3.877	6.626	101.7	105.3	2719.3	13.76	823.21	0.977	0.937	0.916	410.4
4.371	6.656	101.9	105.6	2734.3	13.78	823.21	0.982	0.937	0.920	410.8
3.928	6.650	102.3	106.0	2751.9	13.81	823.21	0.984	0.938	0.924	413.8

FOLDOUT FRAME 2

APPENDIX B

IDEAL PERFORMANCE MAPS

This appendix contains theoretical one dimensional isentropic equilibrium performance maps for the five propellant combinations of interest: OF_2/B_2H_6, F_2-O_2(70-30)/B_2H_6, OF_2/CH_4, F_2-O_2(70-30)/CH_4, and F_2-O_2(82.5-17.5)/CH_4. Data are presented in the forms of characteristic velocity, vacuum thrust coefficient, and vacuum specific impulse.

The performance curves were generated for liquid oxidizers at their normal boiling points and gaseous fuels at 77F. Heats of Formation of the propellants are listed in Table B-1. The value for OF_2 is that recommended by the National Bureau of Standards, Ref. 1. The properties of the combustion products are the recommended JANAF values as of September 1968.

The organization of the figures is shown in Table B-2.

TABLE B-1

Heats of Formation for Propellants

Propellant	Heat of Formation (kcal/mole)
Oxidizers	
F_2	-3.0299
O_2	-3.0795
OF_2	1.95
F_2-O_2(70-30)	-8.4684
F_2-O_2(82.5 - 17.5)	-8.2622
Fuels	
CH_4	-17.895
B_2H_6	9.8

Table B-2

Figure Numbers for Theoretical Performance Maps

Propellant \ Figure Number	Vacuum Specific Impulse vs Mixture Ratio	Characteristic Velocity vs Mixture Ratio	Vacuum Thrust Coefficient vs Mixture Ratio	Vacuum Thrust Coefficient vs Area Ratio
OF_2/B_2H_6	B-1	B-4	B-7	B-10
F_2-O_2(70-30)/B_2H_6	B-1	B-4	B-7	B-11
OF_2/CH_4	B-2	B-5	B-8	B-12
F_2-O_2(70-30)/CH_4	B-2	B-5	B-8	B-13
F_2-O_2(82.5-17.5)/CH_4	B-3	B-6	B-9	B-14

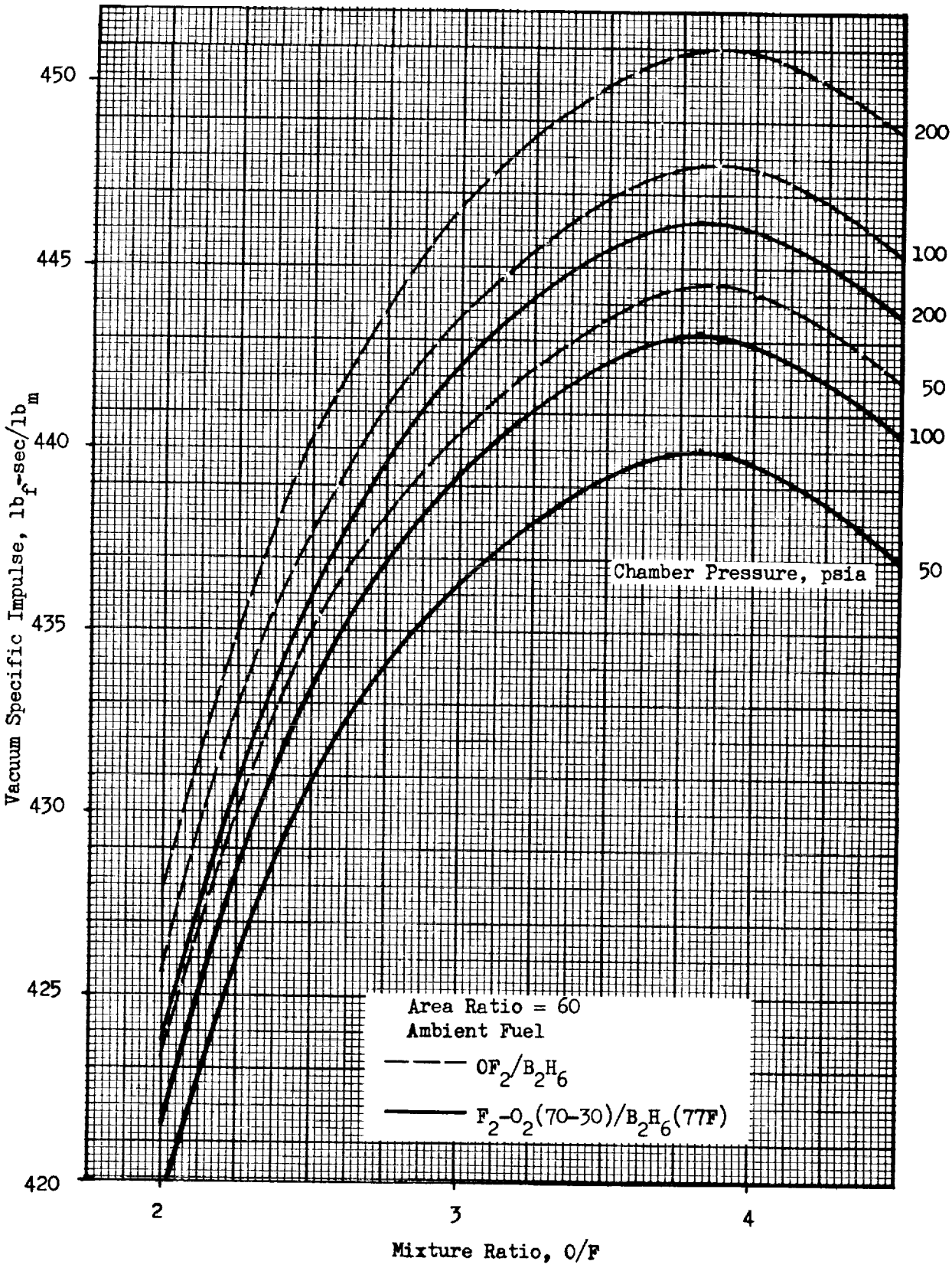

Figure B-1 . Vacuum Specific Impulse vs Mixture Ratio, Chemical Equilibrium, for OF_2/B_2H_6 and F_2-O_2(70-30)/B_2H_6(77F)

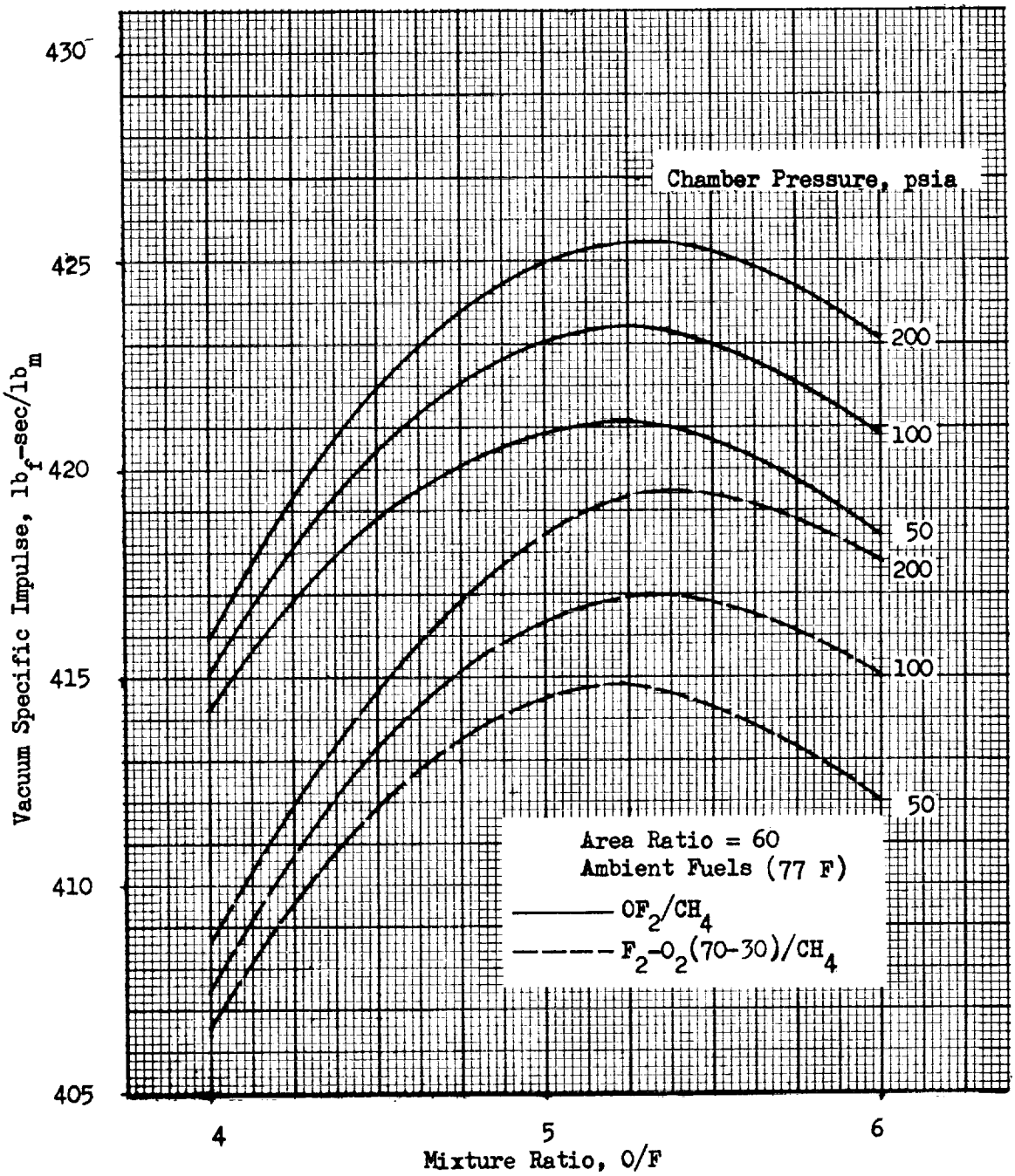

Figure B-2. Vacuum Specific Impulse vs Mixture Ratio, Chemical Equilibrium, for OF_2/CH_4 and F_2-O_2(70-30)/CH_4.

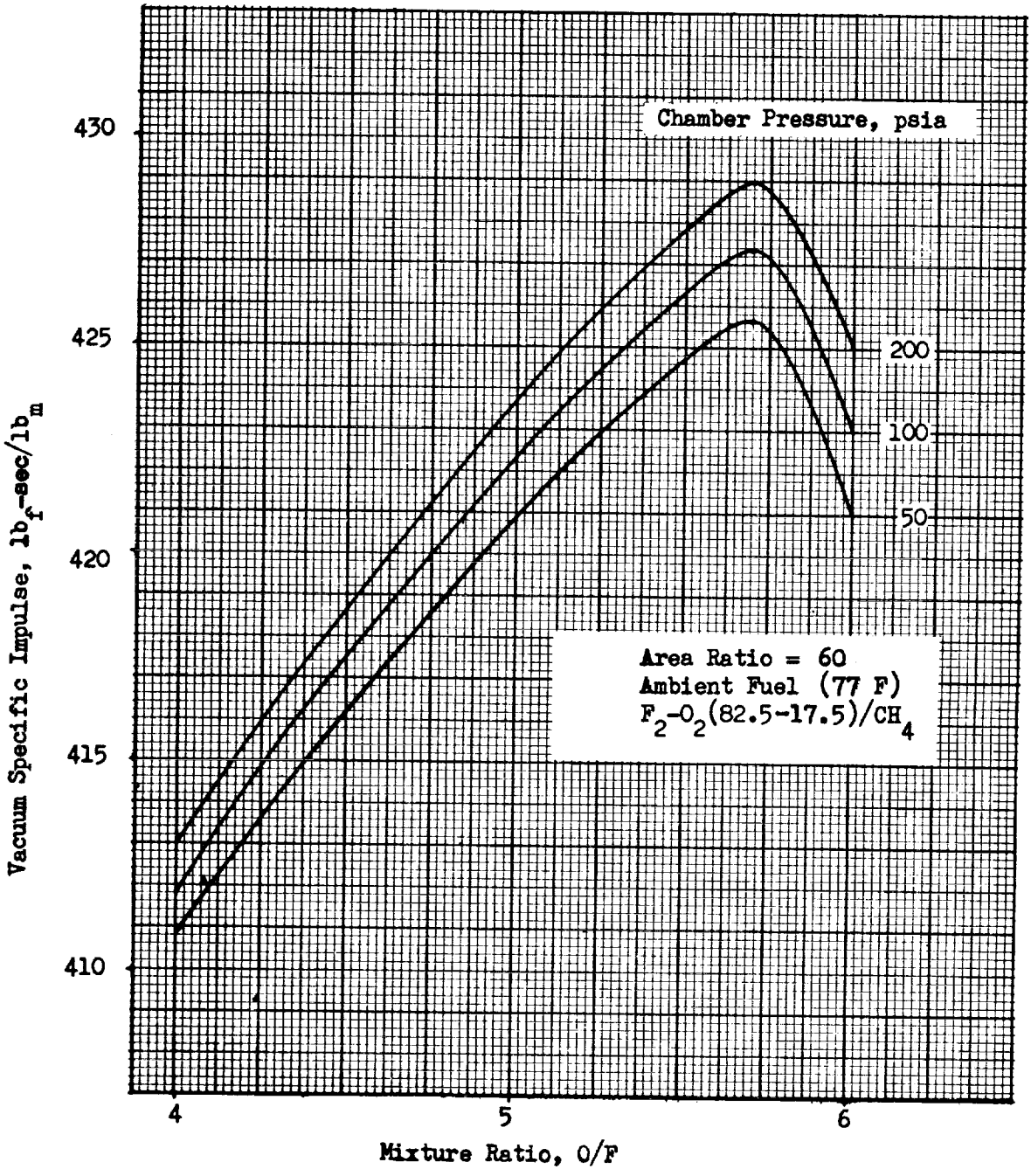

Figure B-3. Vacuum Specific Impulse vs Mixture Ratio, Chemical Equilibrium, for F_2-O_2(82.5-17.5)/CH_4.

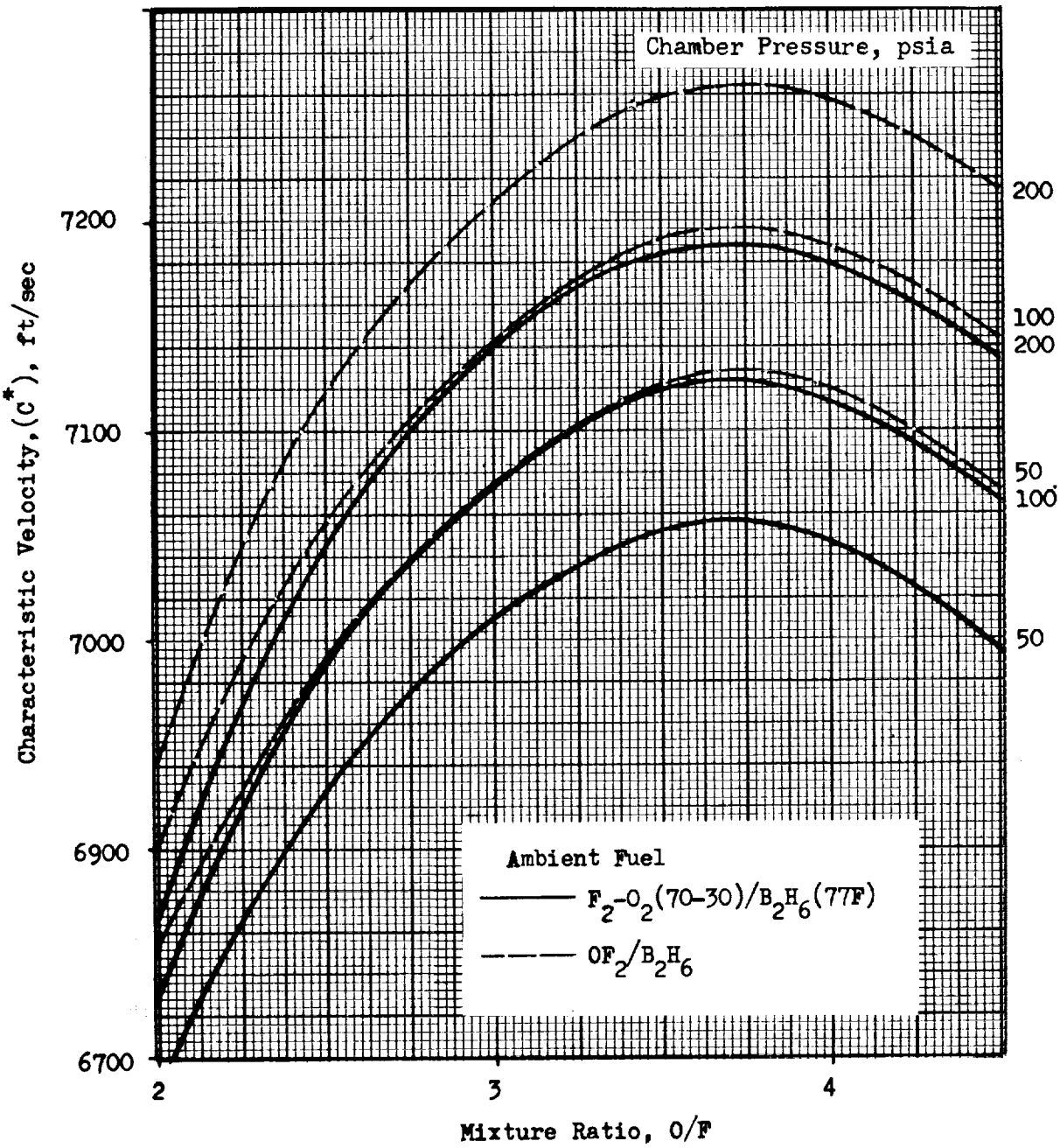

Figure B-4. Characteristic Velocity vs Mixture Ratio, Chemical Equilibrium, for OF_2/B_2H_6 and $F_2-O_2(70)/B_2H_6$

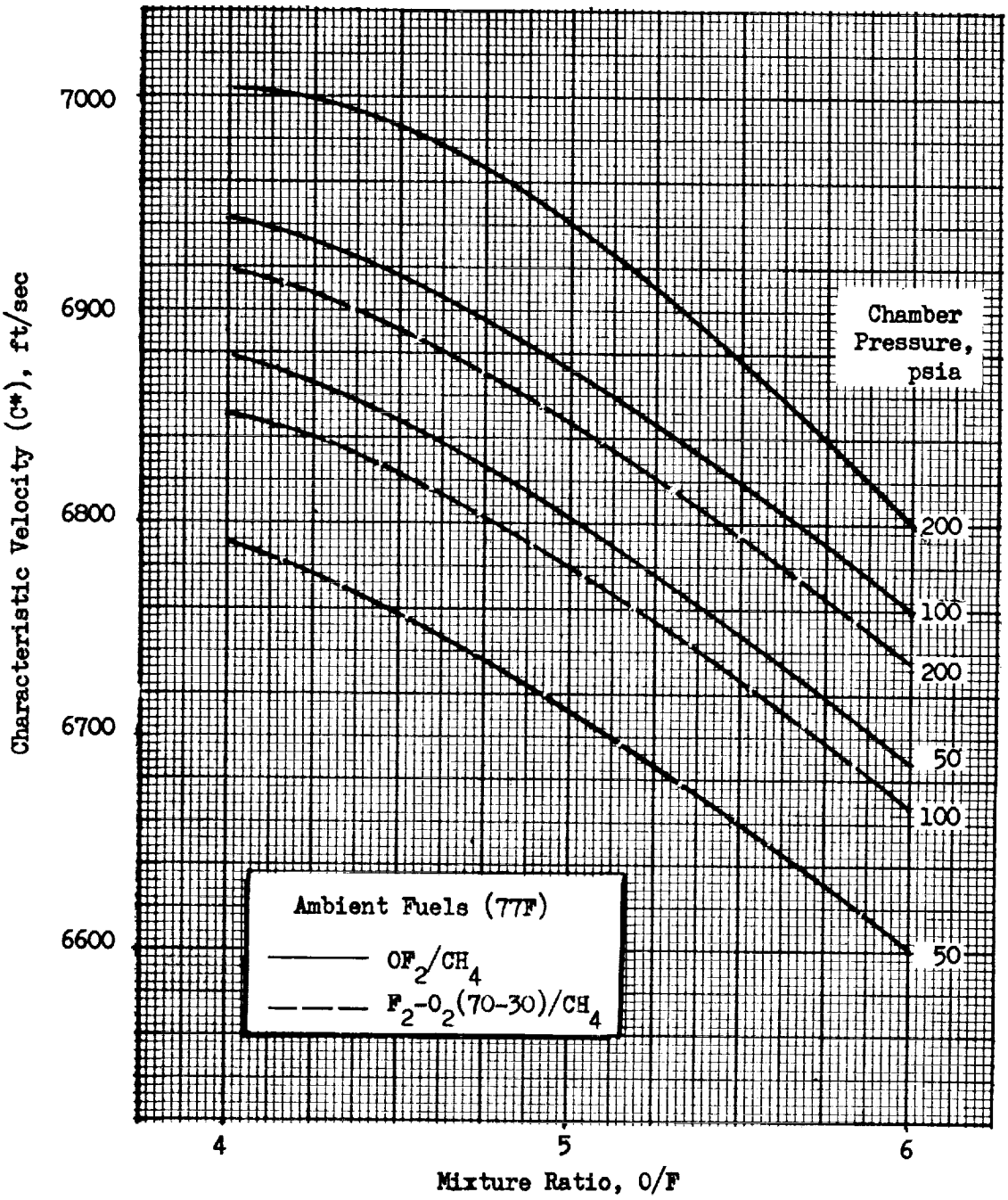

Figure B-5. Characteristic Velocity vs Mixture Ratio, Chemical Equilibrium, for OF_2/CH_4 and F_2-O_2(70-30)/CH_4.

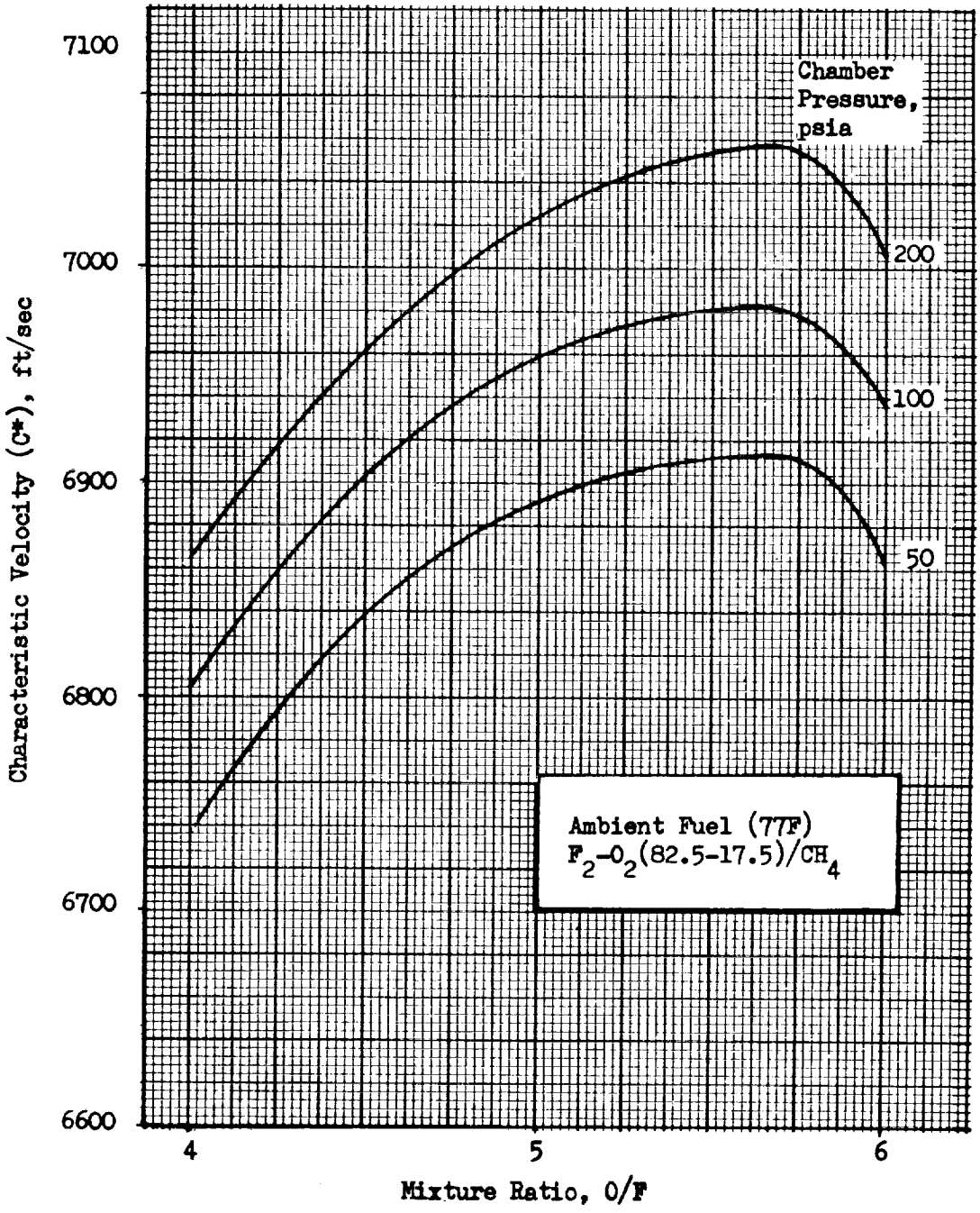

Figure B-6. Characteristic Velocity vs Mixture Ratio, Chemical Equilibrium, for F_2-O_2(82.5-17.5)/CH_4.

Area Ratio = 60:1

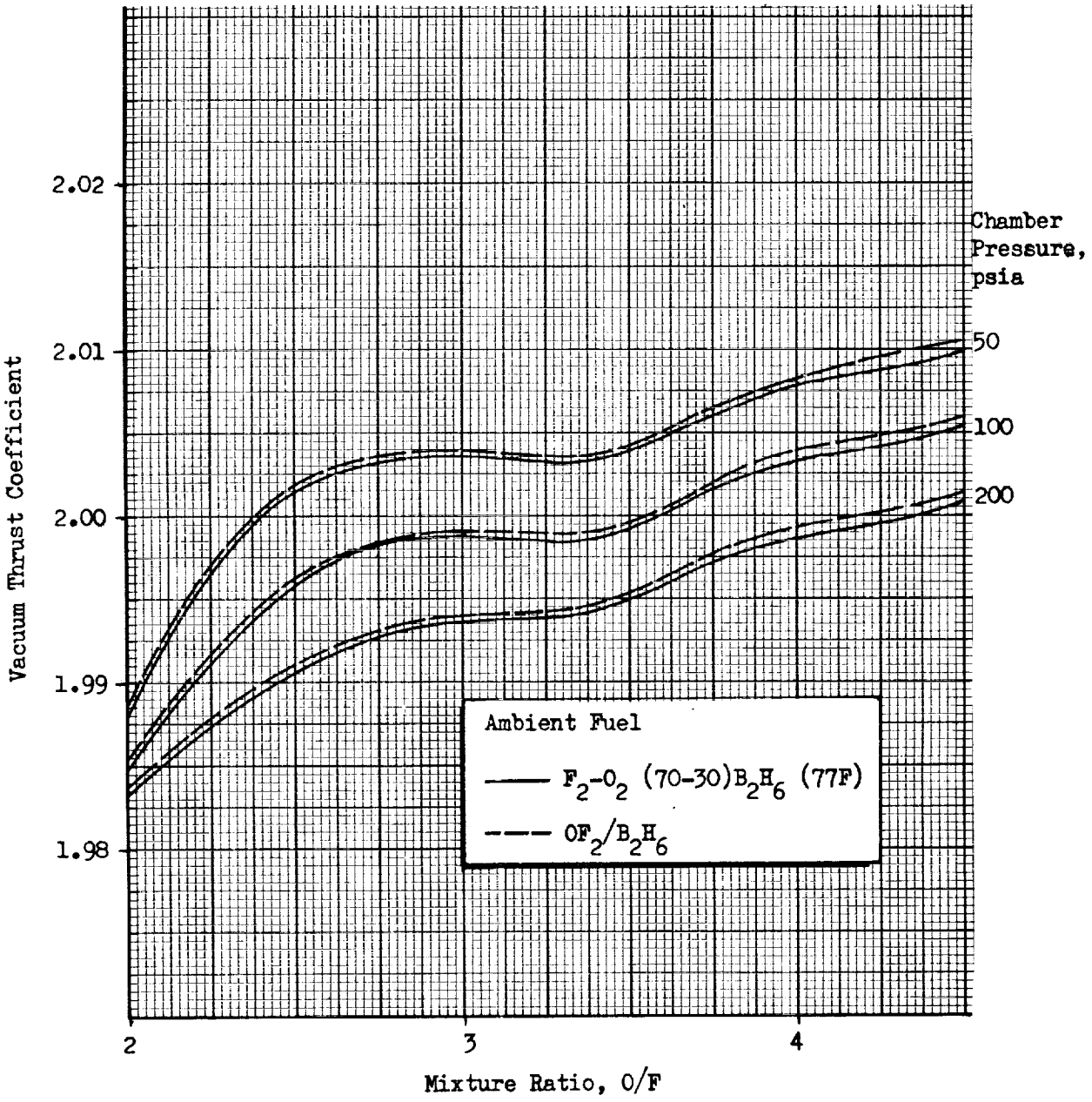

Figure B-7 . Vacuum Thrust Coefficient vs Mixture Ratio— Chemical Equilibrium for OF_2/B_2H_6 and F_2-O_2(70-30)B_2H_6(77F) .

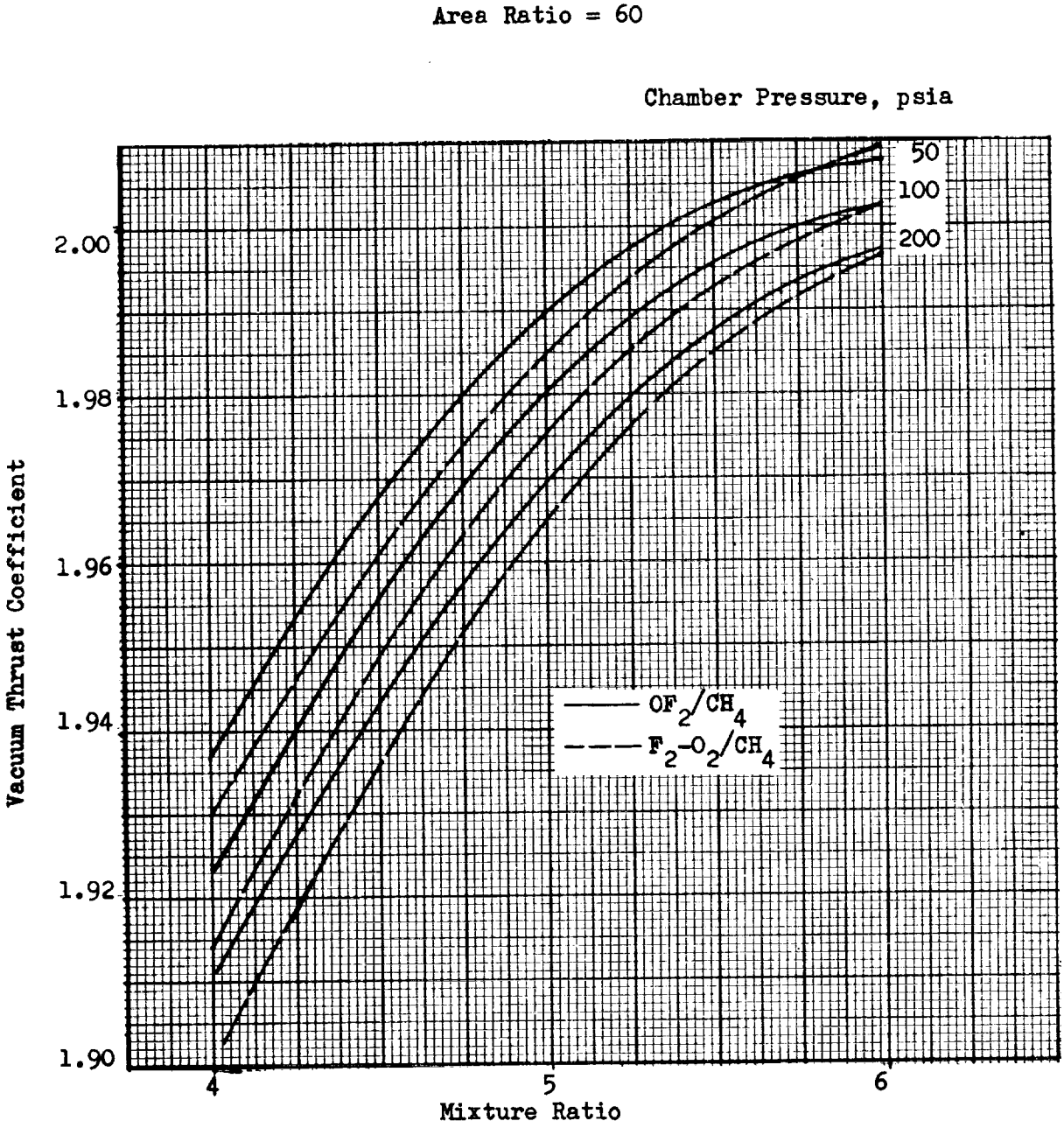

Figure B-8. Vacuum Thrust Coefficient vs Mixture Ratio--Chemical Equilibrium for OF_2/CH_4 and F_2-O_2(70-30)/CH_4

Area Ratio = 60

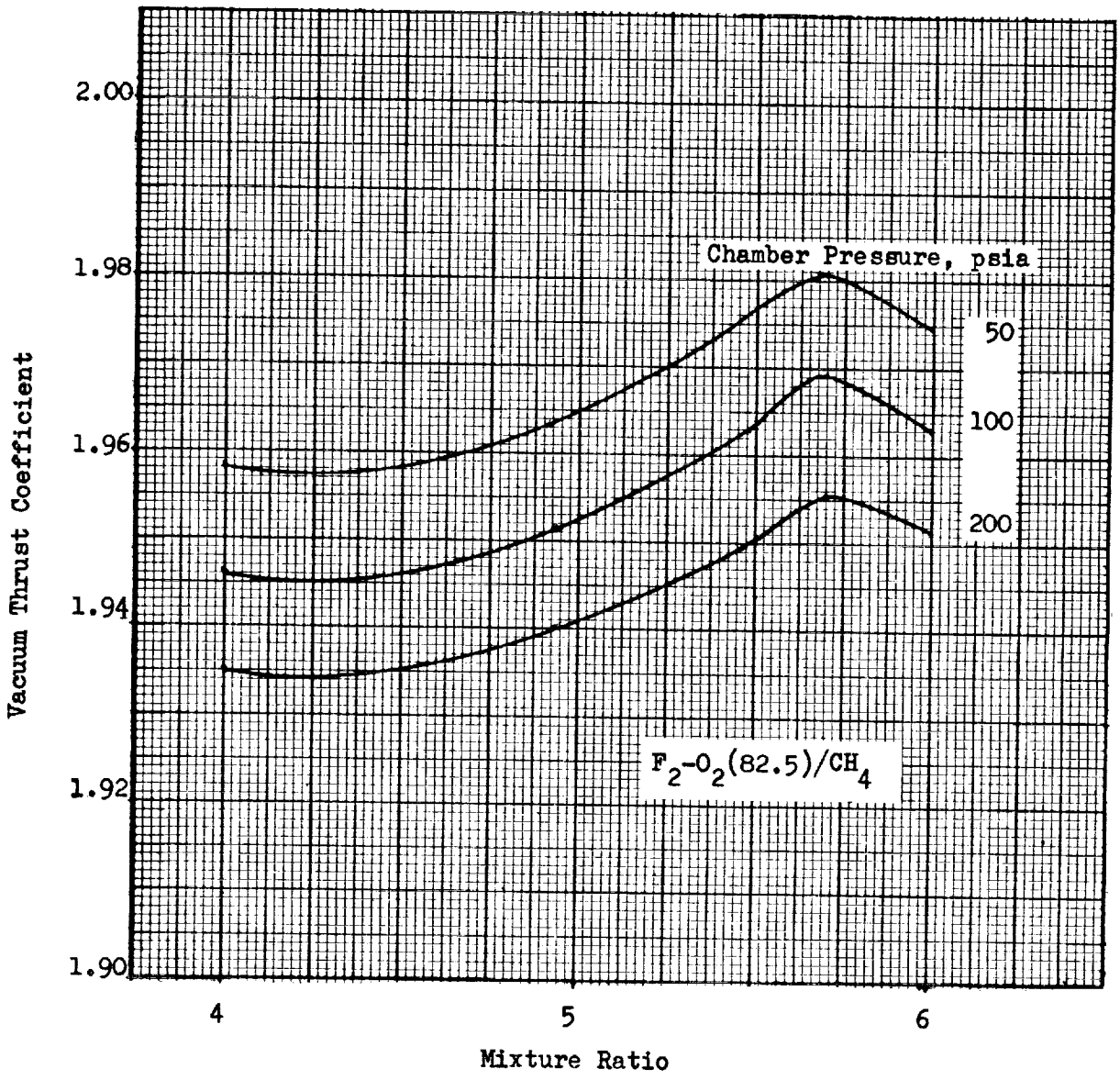

Figure B-9. Vacuum Thrust Coefficient vs Mixture Ratio-- Chemical Equilibrium for F_2-O_2(82.5 - 17.5)/CH_4

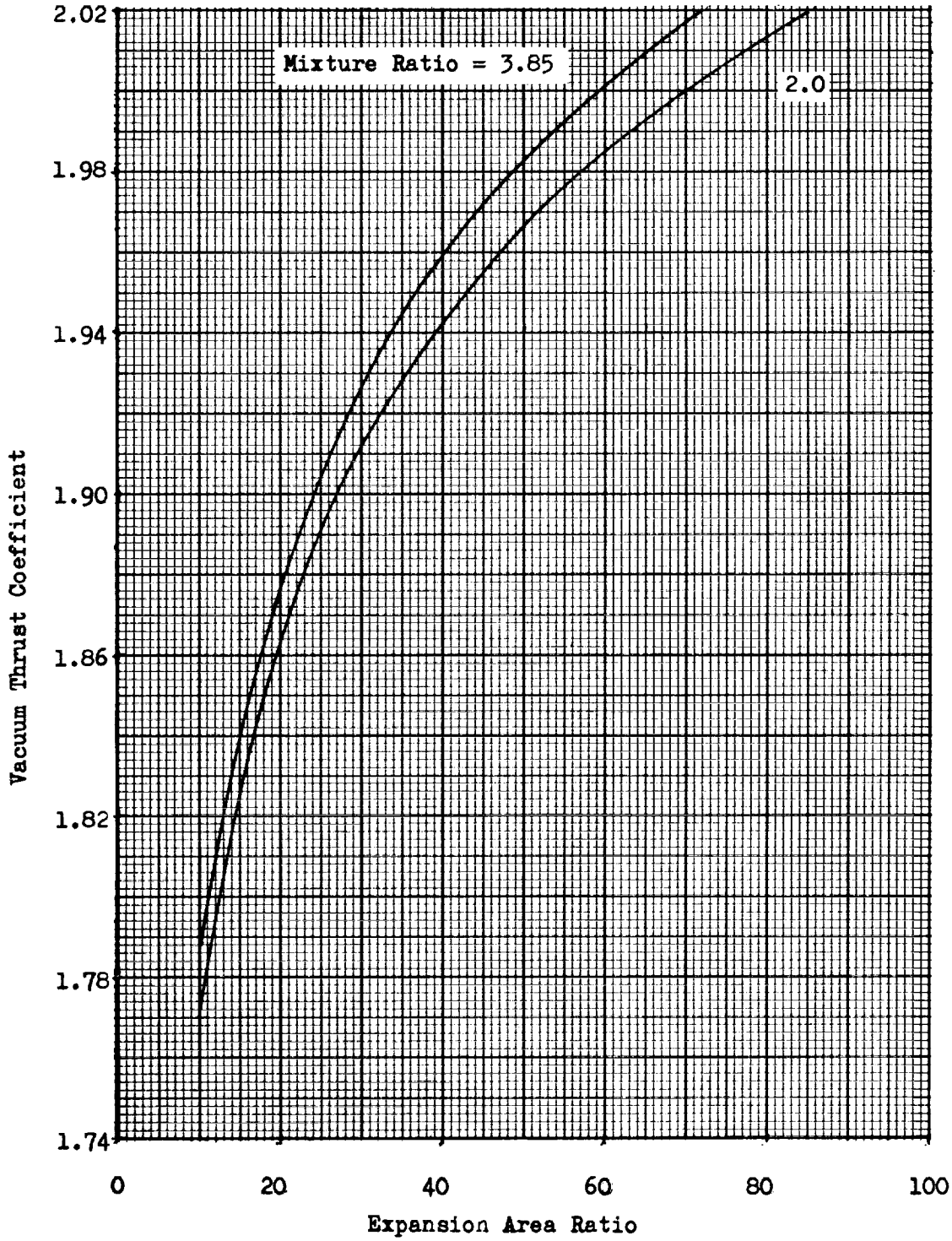

Figure B-10. Vacuum Thrust Coefficient vs Expansion Area Ratio Chemical Equilibrium for OF_2/B_2H_6

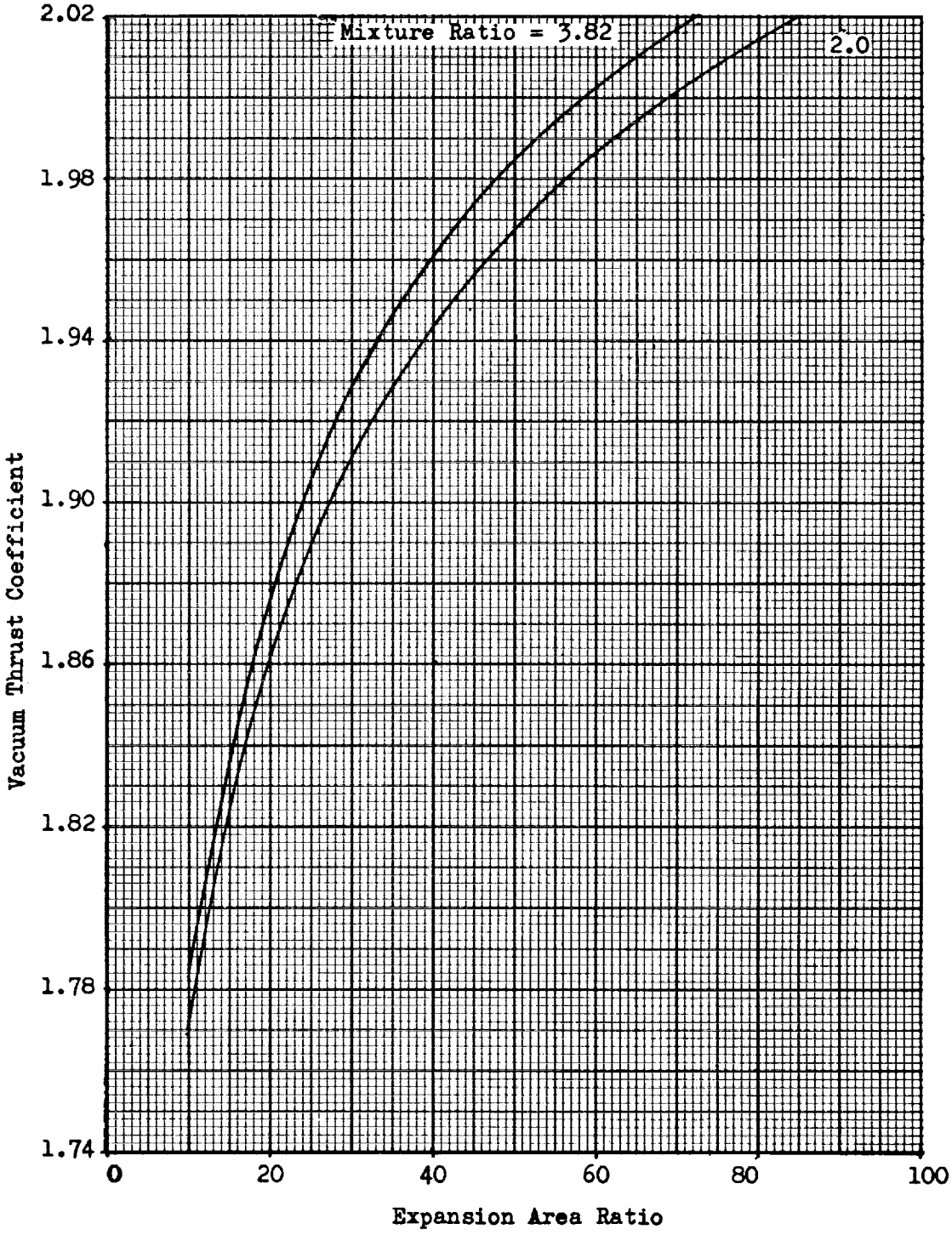

Figure B-11. Vacuum Thrust Coefficient vs Expansion Area Ratio Chemical Equilibrium for F_2-O_2(70-30)/B_2H_6

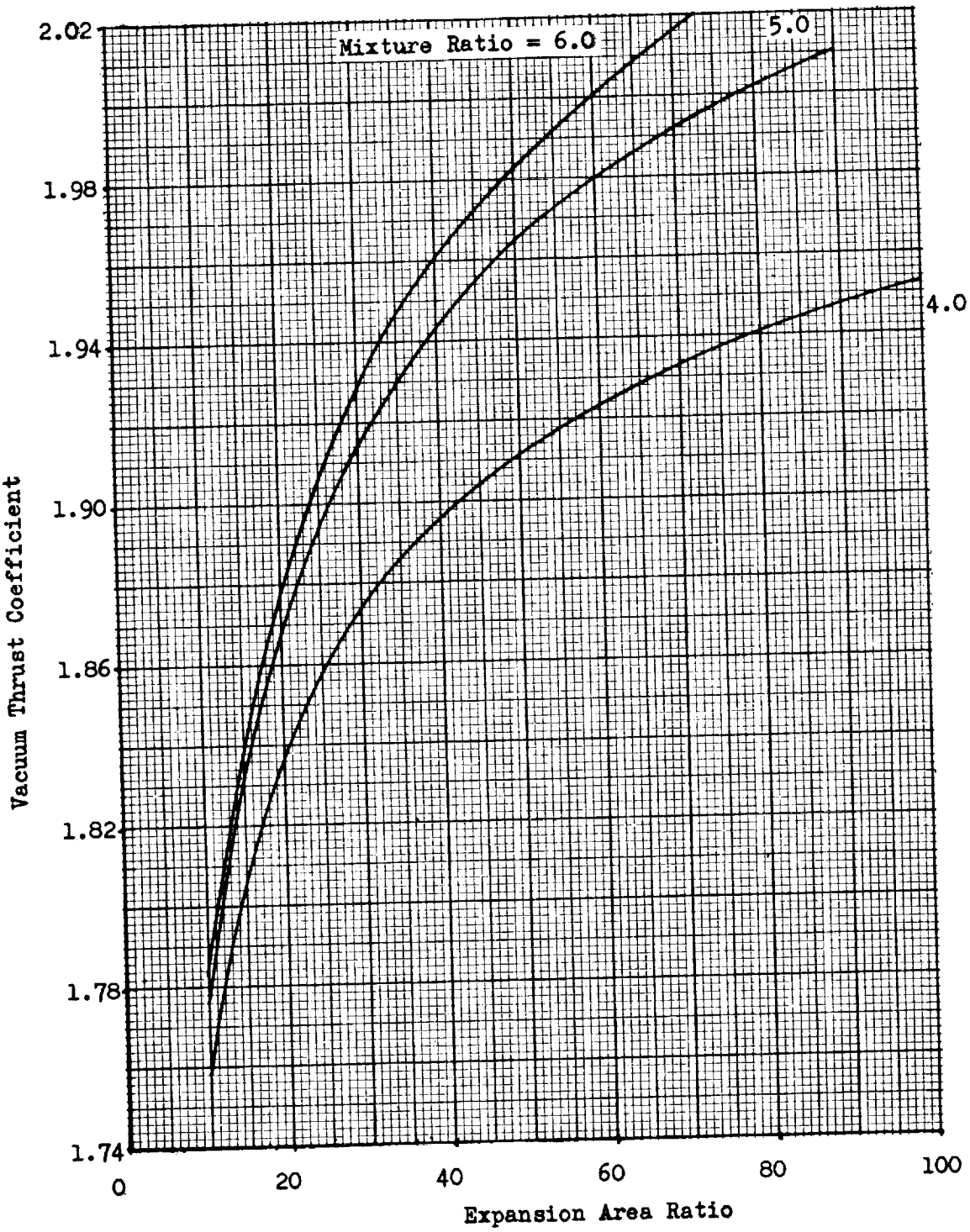

Figure B-12. Vacuum Thrust Coefficient vs Expansion Area Ratio Chemical Equilibrium for OF_2/CH_4

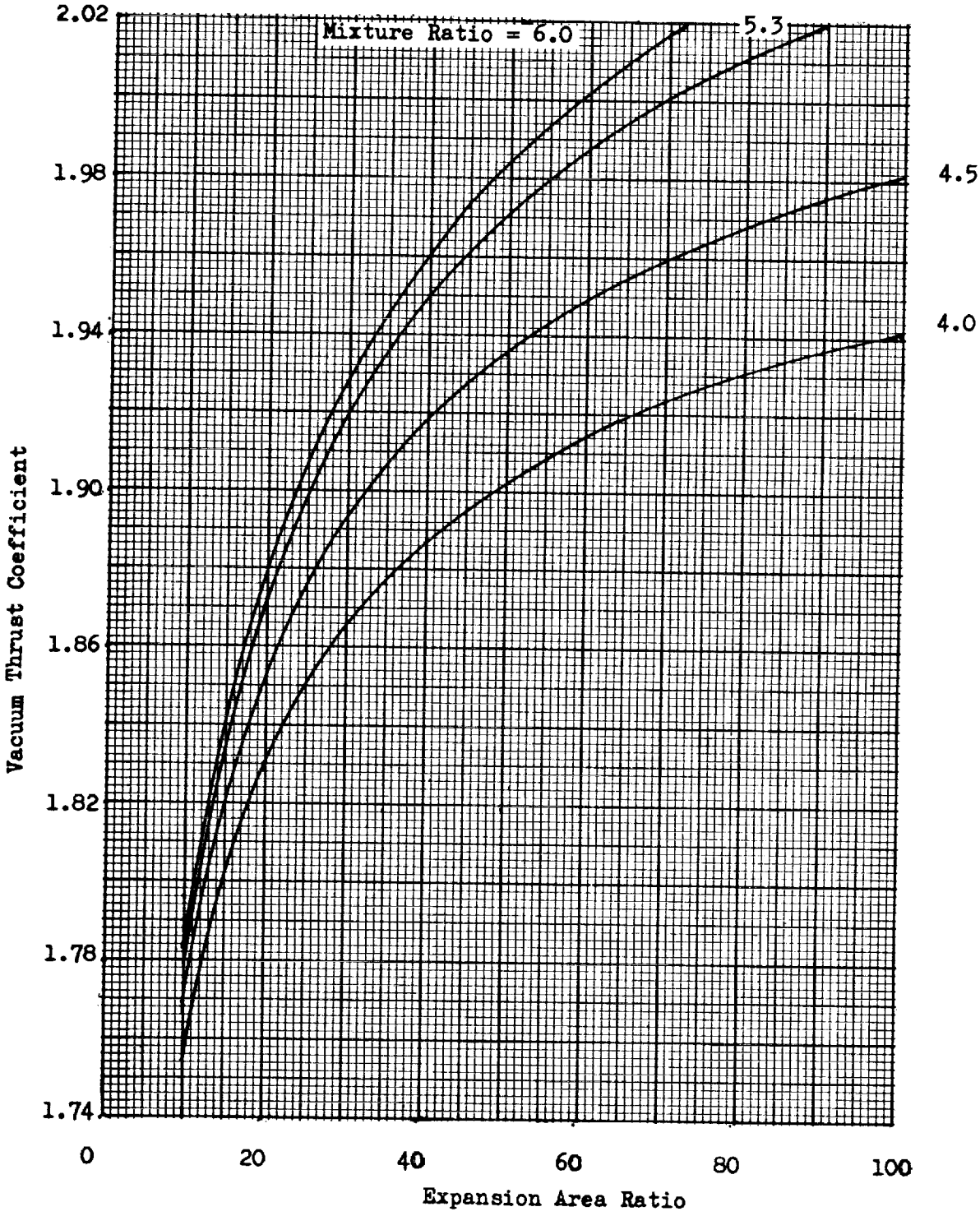

Figure B-13. Vacuum Thrust Coefficient vs Expansion Area Ratio Chemical Equilibrium for F_2-O_2(70-30)/CH_4

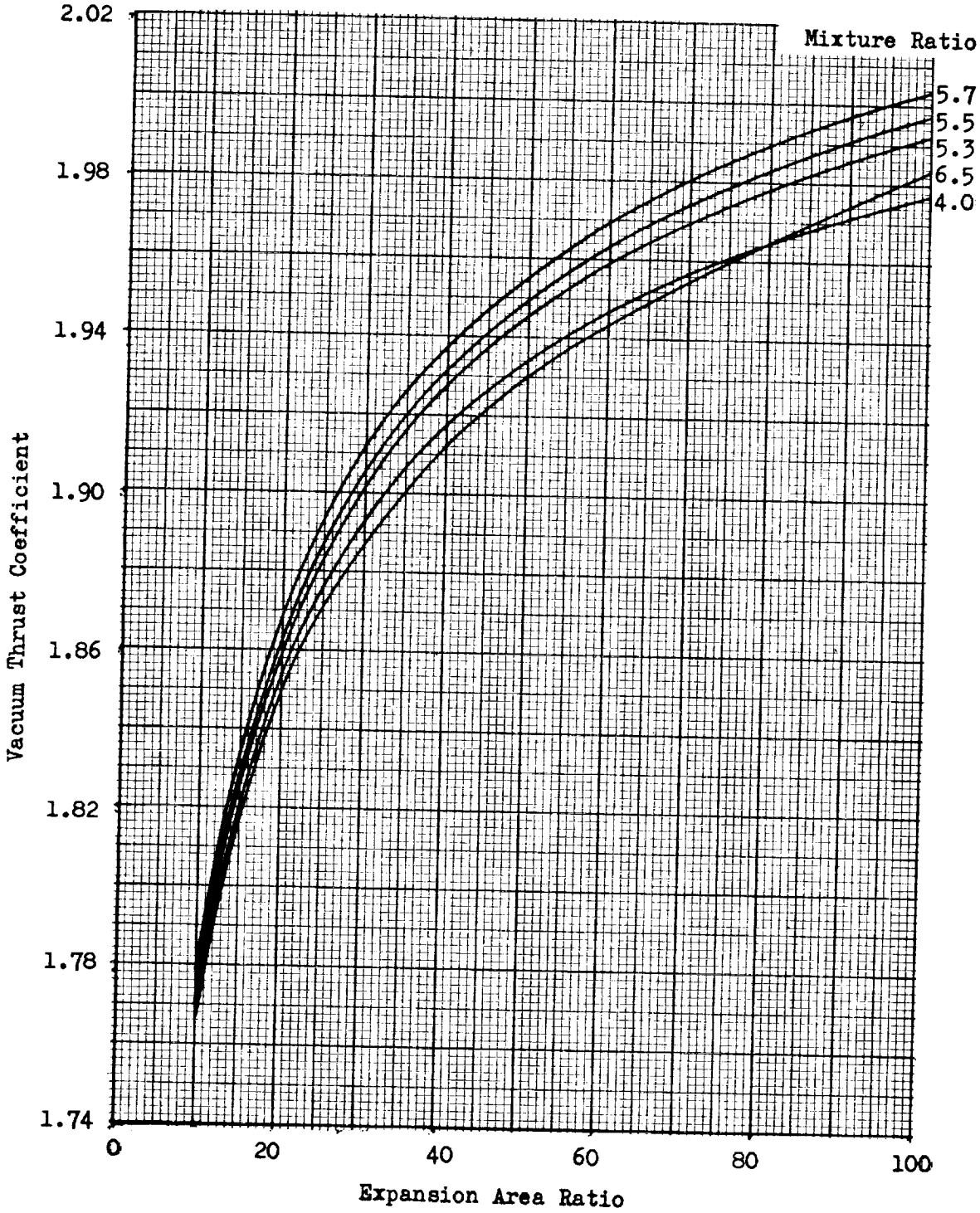

Figure B-14. Vacuum Thrust Coefficient vs Expansion Area Ratio Chemical Equilibrium for F_2-O_2(82.5-17.5)/CH_4

APPENDIX C

DIBORANE PROPERTIES

Because the properties of gaseous diborane are not conveniently available in the literature, some of the more useful information was compiled and is presented in this appendix. Thermodynamic data based on Ref. 6 are presented as outlined in Table C-1.

TABLE C-1

Information	Figure
Compressibility vs Temperature	C-1
Compressibility vs Pressure	C-2
Enthalpy vs Entropy	C-3
Temperature vs Entropy	C-4
Pressure vs Enthalpy	C-5
Density vs Temperature	C-6
Density vs Pressure	C-7

Diborane decomposition data were obtained from Ref. 7 and are shown in Fig. C-8 and C-9. The original data were taken as pressure rise as a function of time for selected temperatures. These results were reinterpreted in terms of percent decomposition for use here. At room temperature the decomposition is slow and produces hydrogen and higher molecular weight boron hydrids. At high temperatures the decomposition rate increases and the products change in the direction of higher molecular weight hydrids and more hydrogen. Boron is not produced until approximately 900°F. The data as interpreted from Ref. 7 are in Fig. C-8 Figure C-9 contains a useful crossplot of the data.

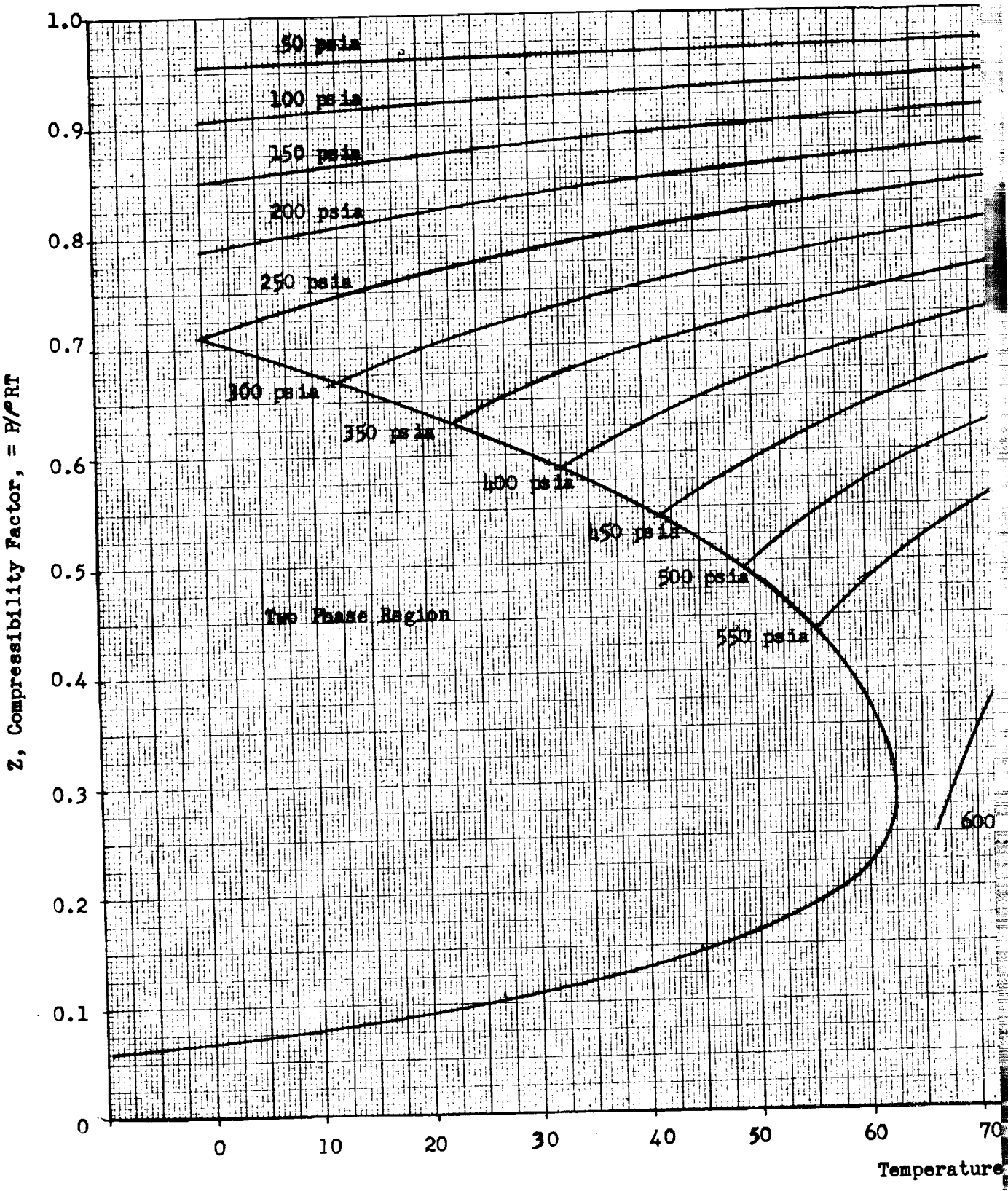

FOLDOUT FRAME

Gaseous Diborane

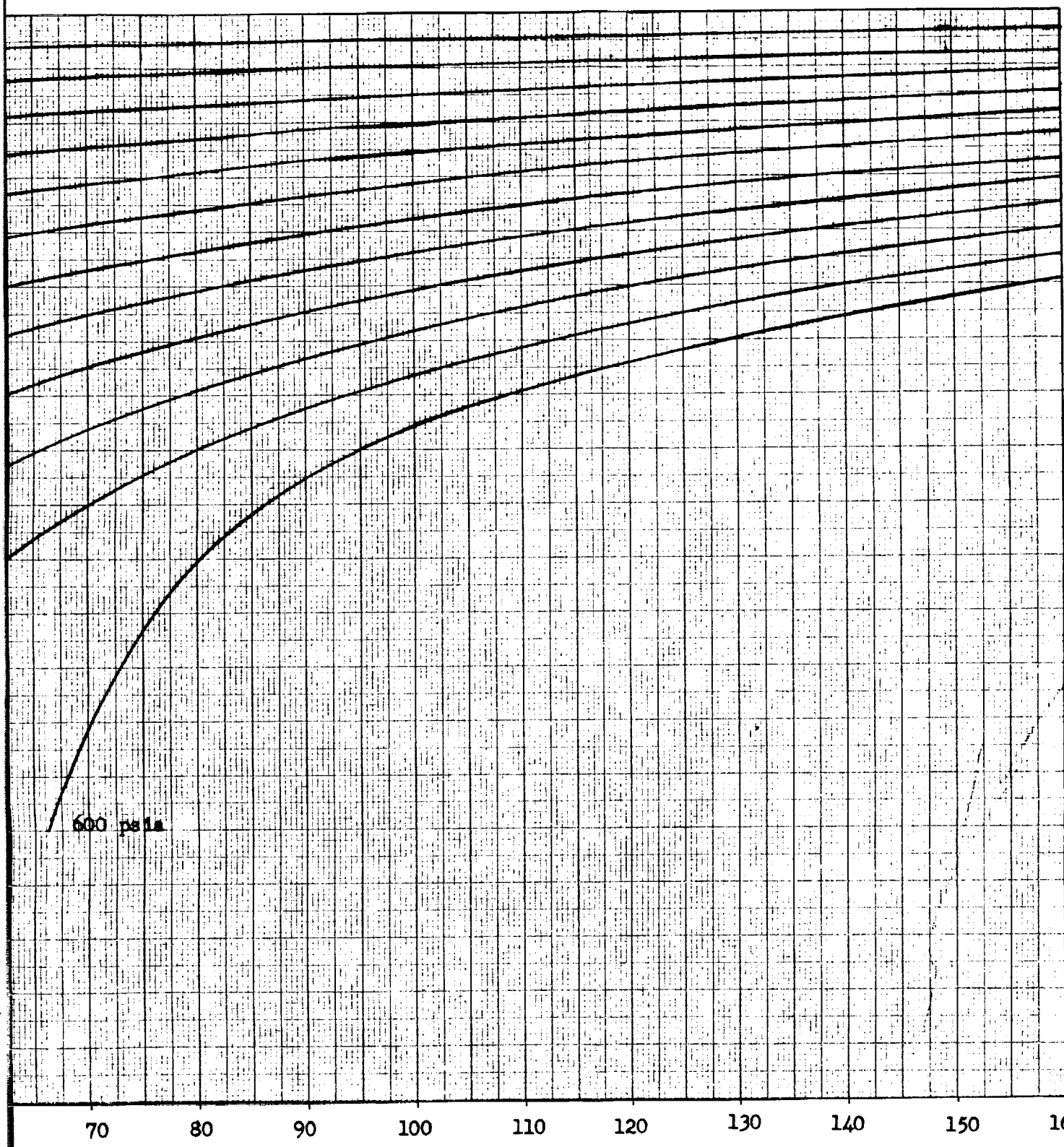

Figure C-1. Compressibility Factor vs Temperature for Diborane

FOLDOUT FRAME

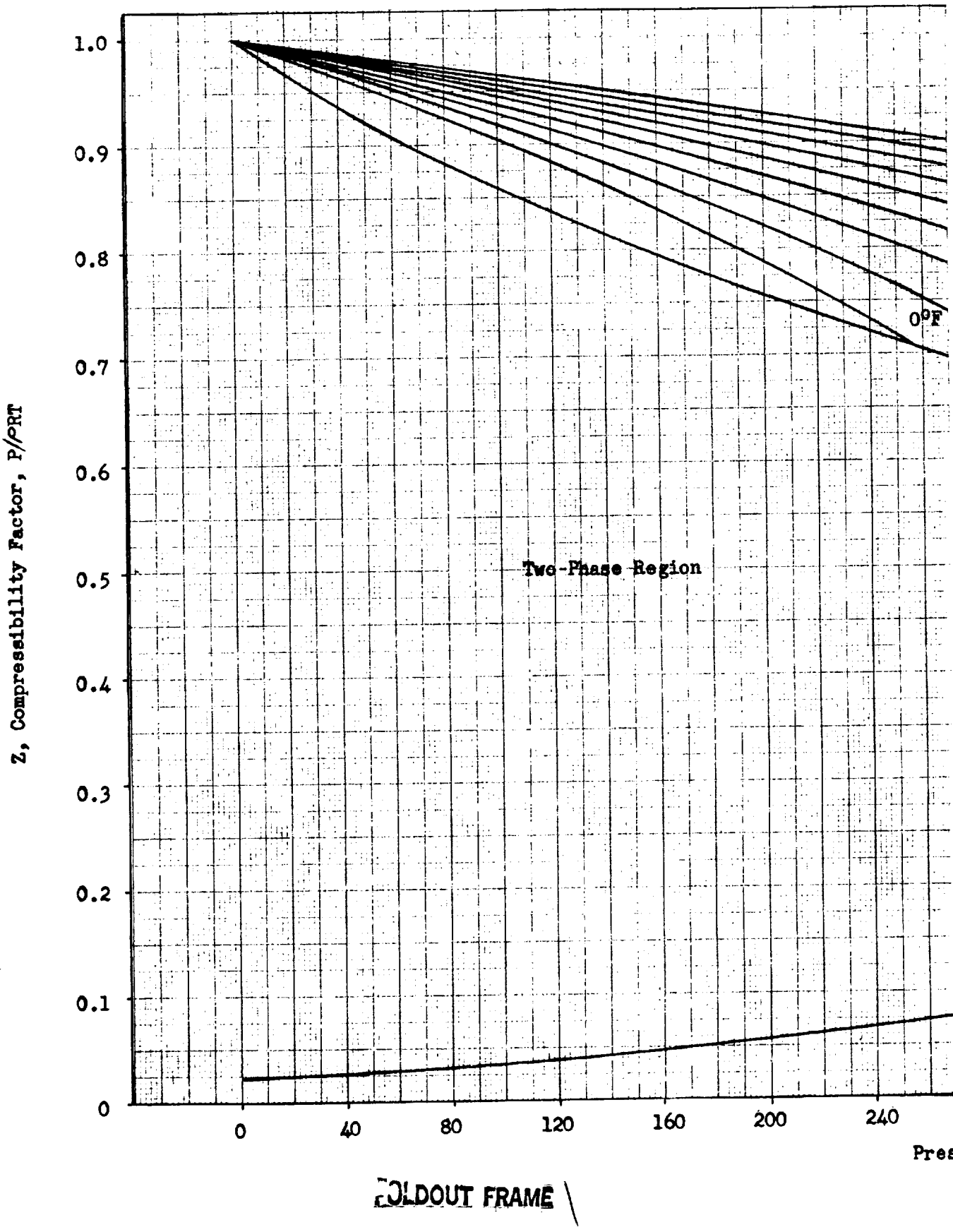

FOLDOUT FRAME

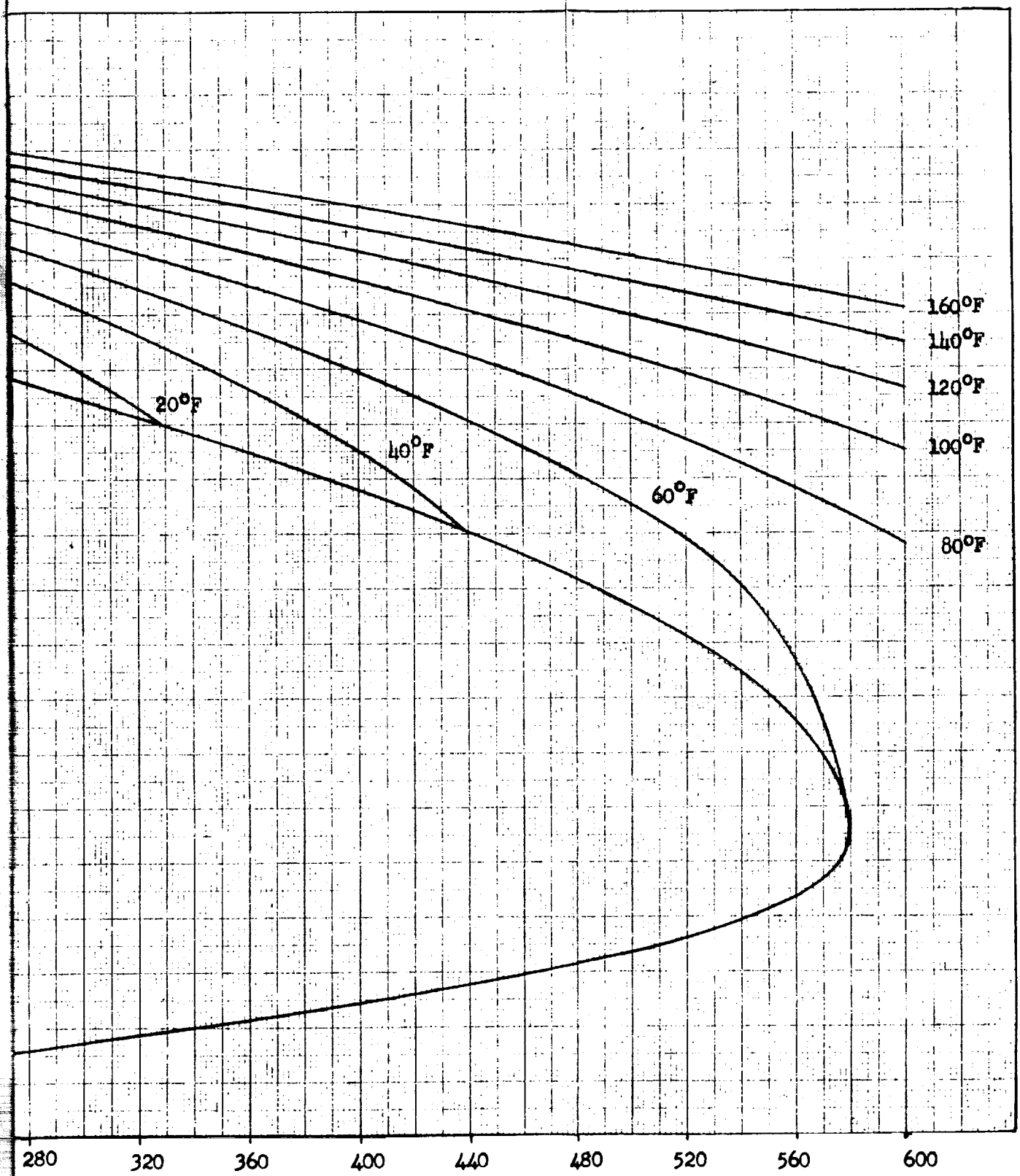

ure, psia

FOLDOUT FRAME 2

Figure C-2. Compressibility of Diborane as a Function of Pressure

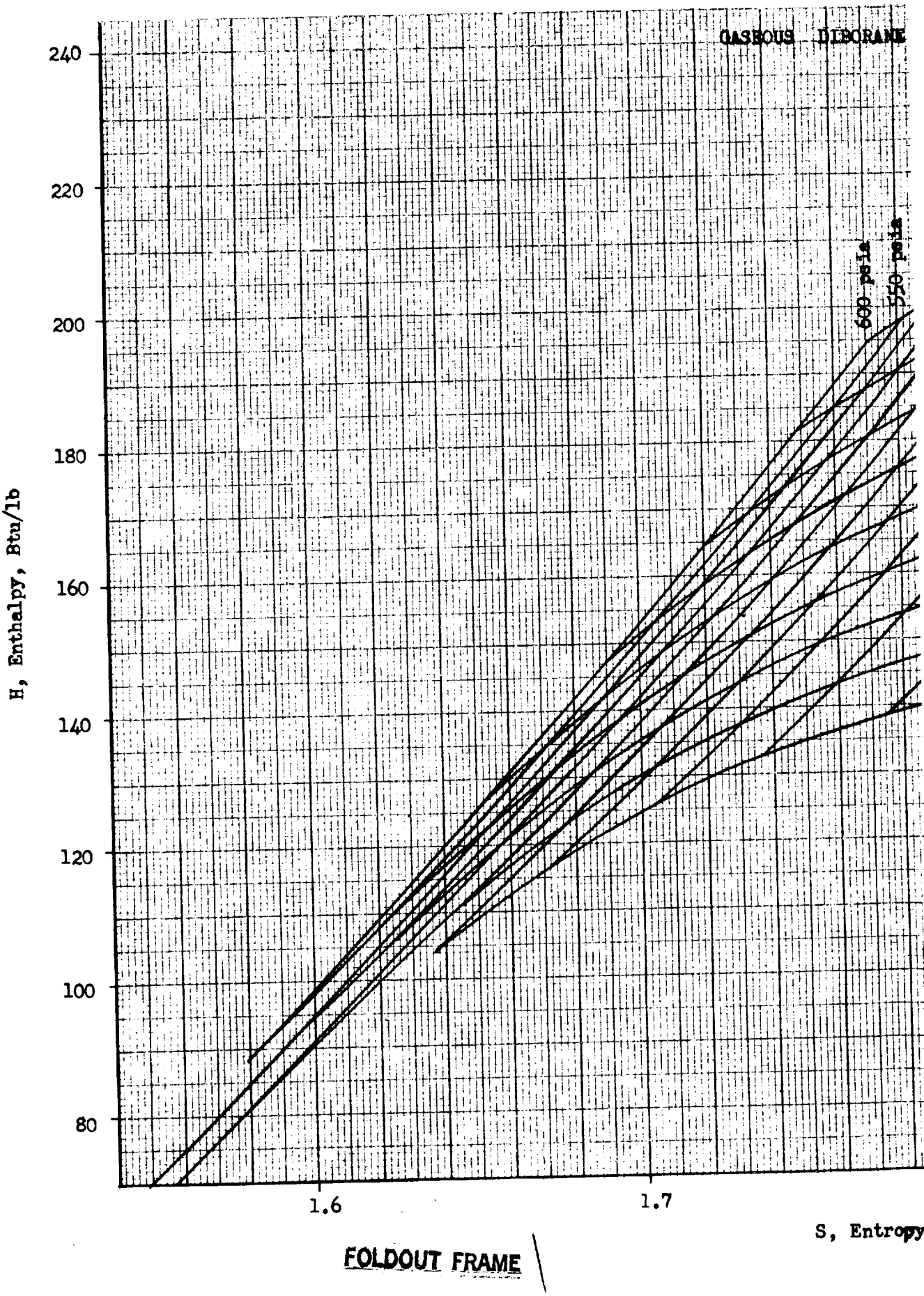

FOLDOUT FRAME

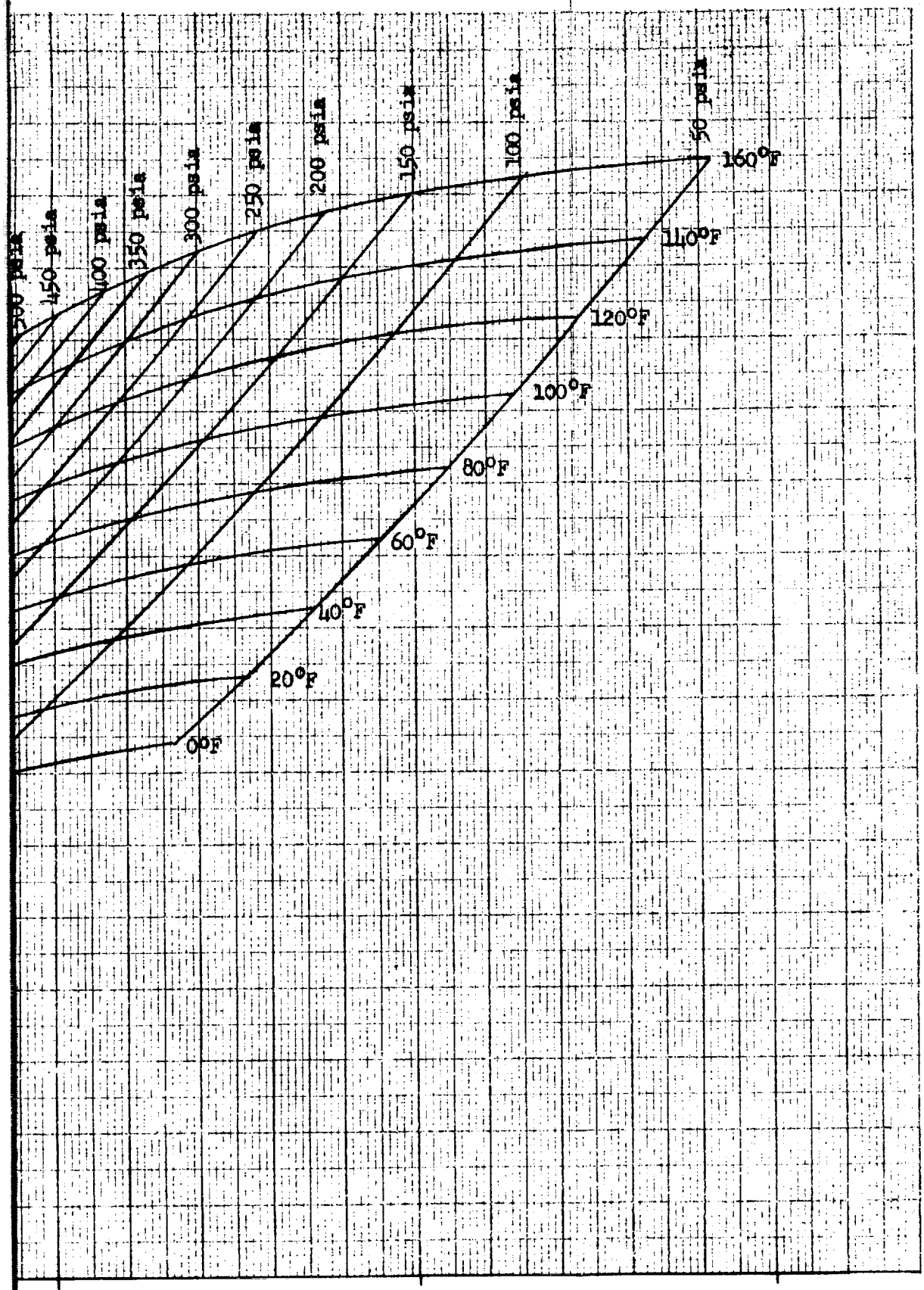

Figure C-3. Enthalpy-Entropy Diagram for Diborane

FOLDOUT FRAME 2

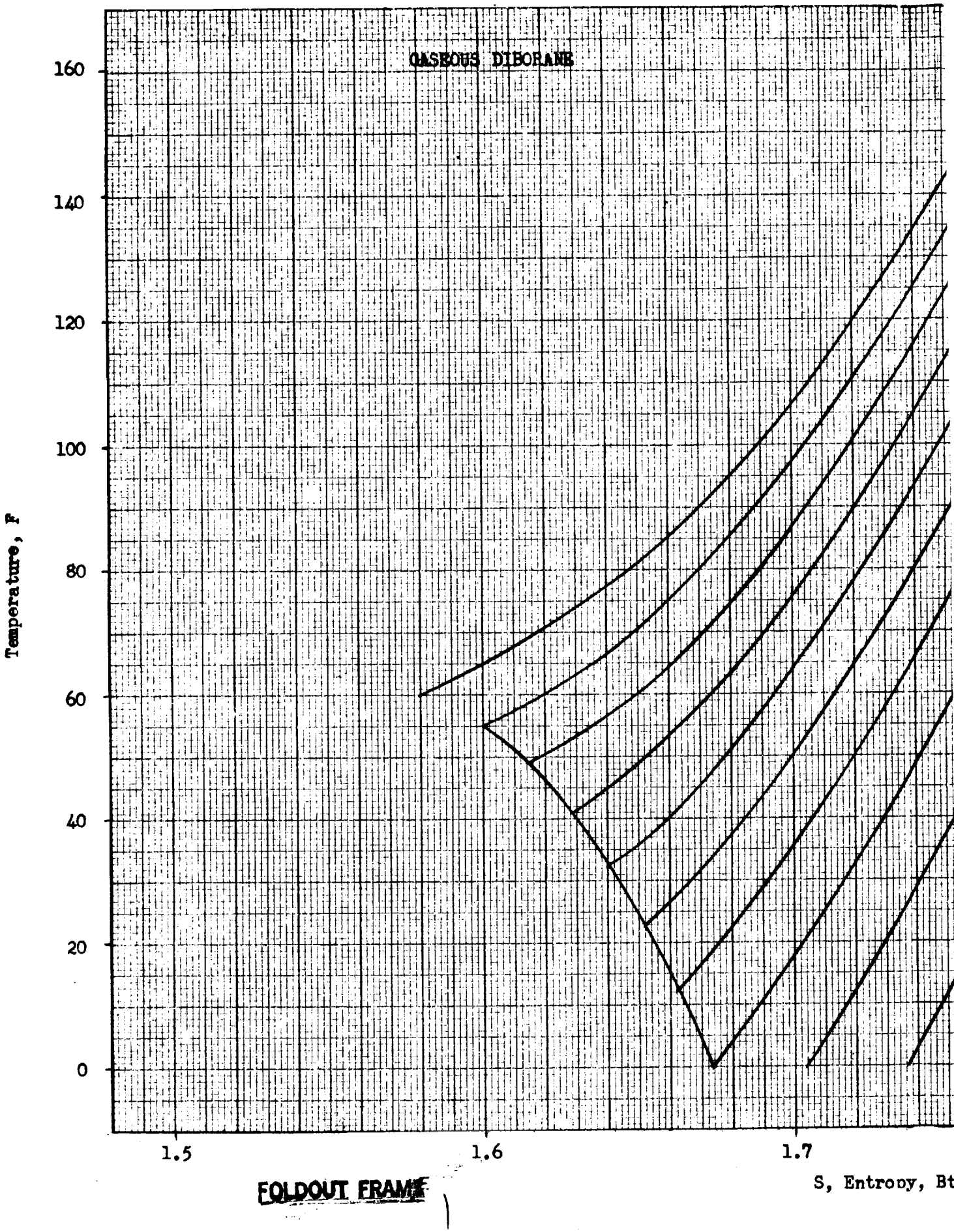

FOLDOUT FRAME

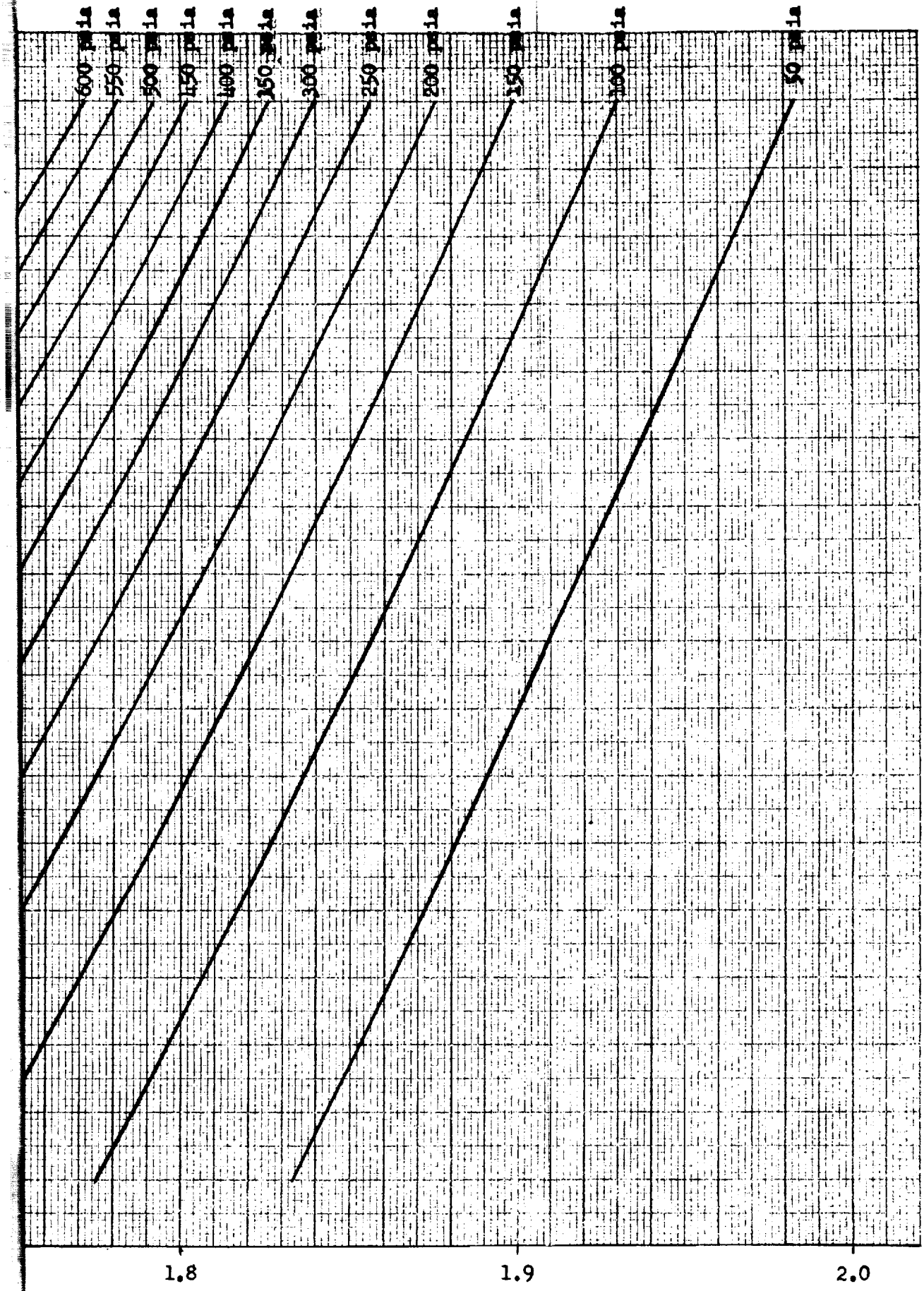

FOLDOUT FRAME

Figure C-4. Temperature-Entropy Diagram for Diborane

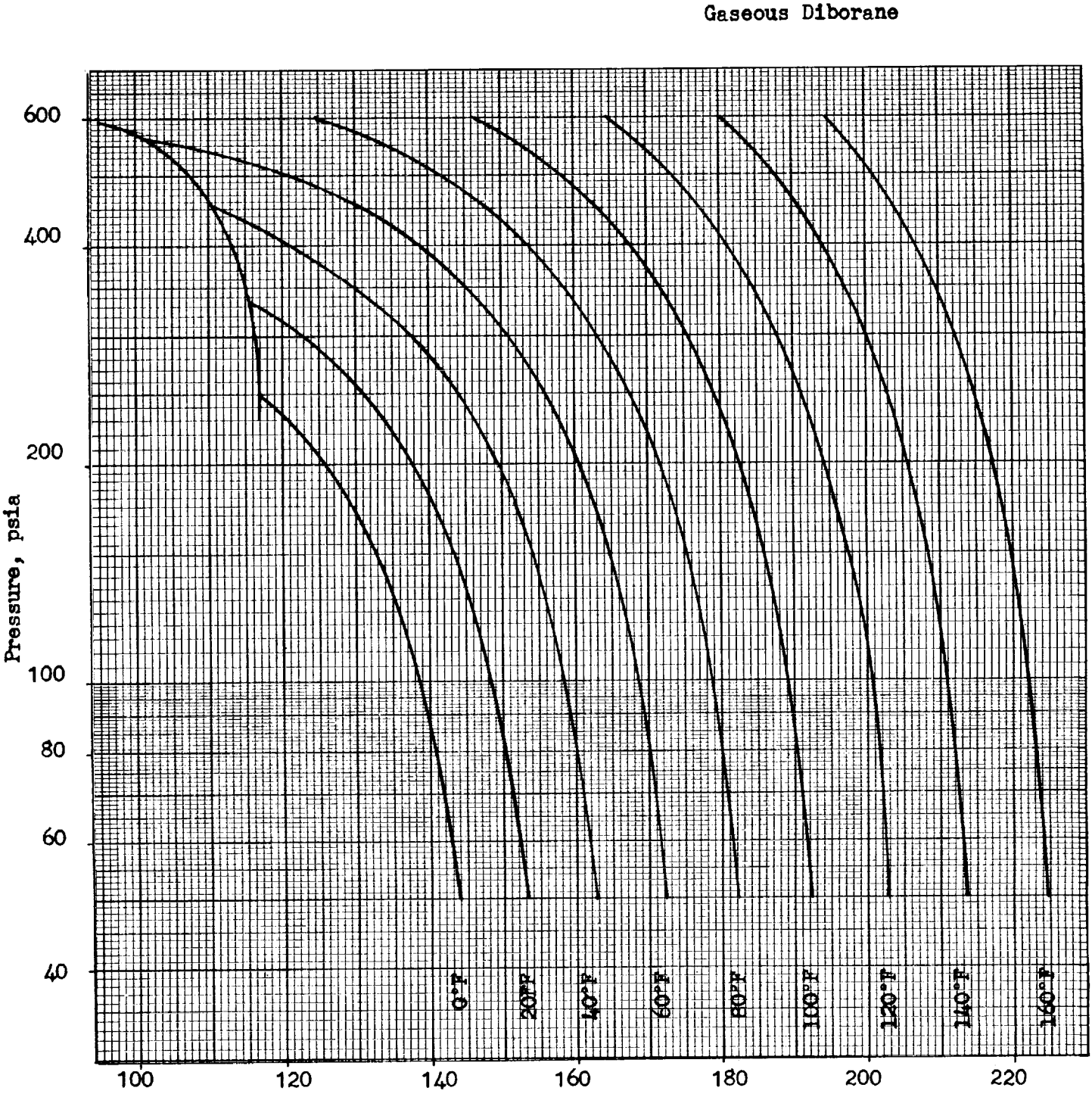

Figure C-5. Pressure - Enthalpy Diagram for Gaseous Diborane

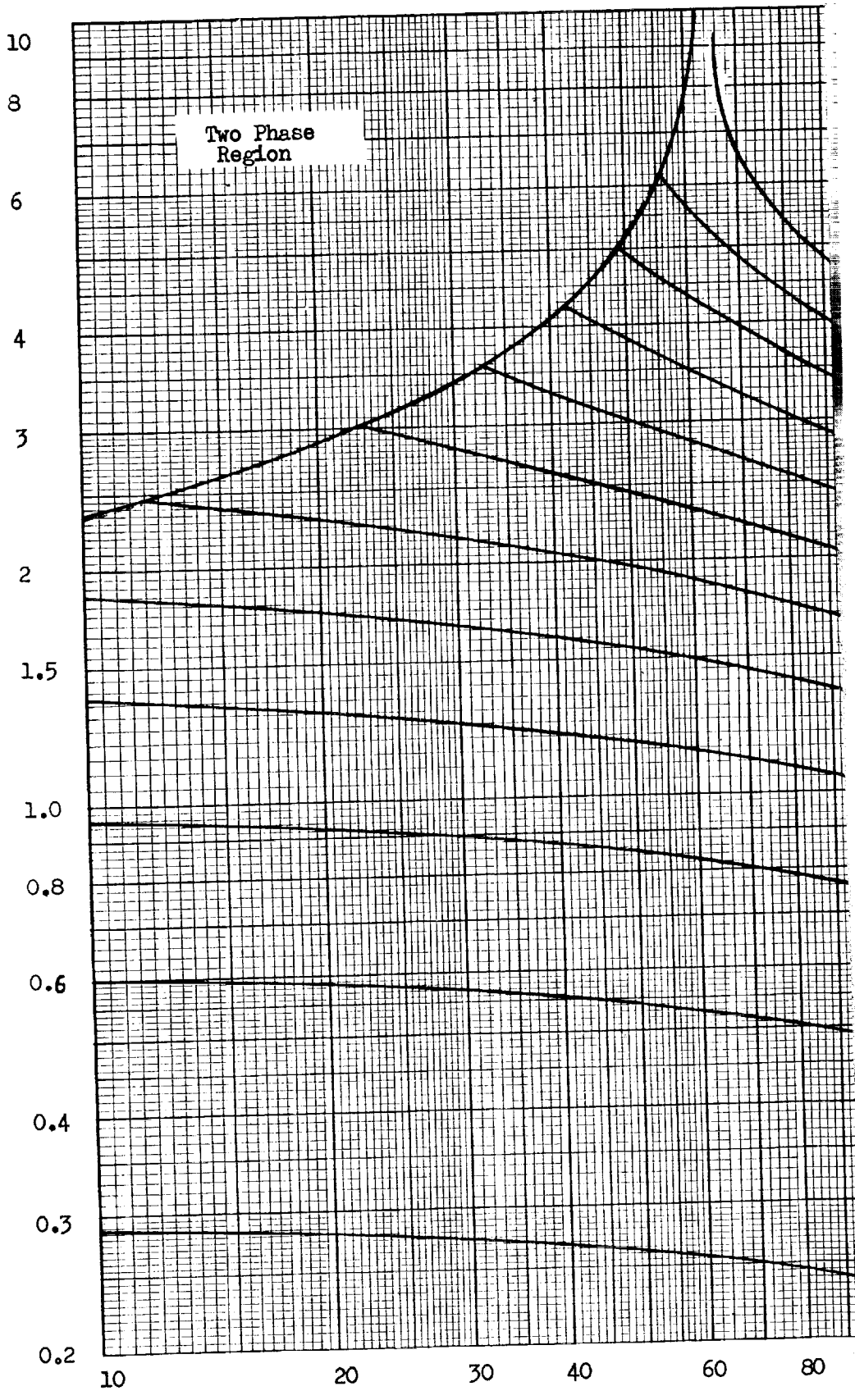

FOLDOUT FRAME

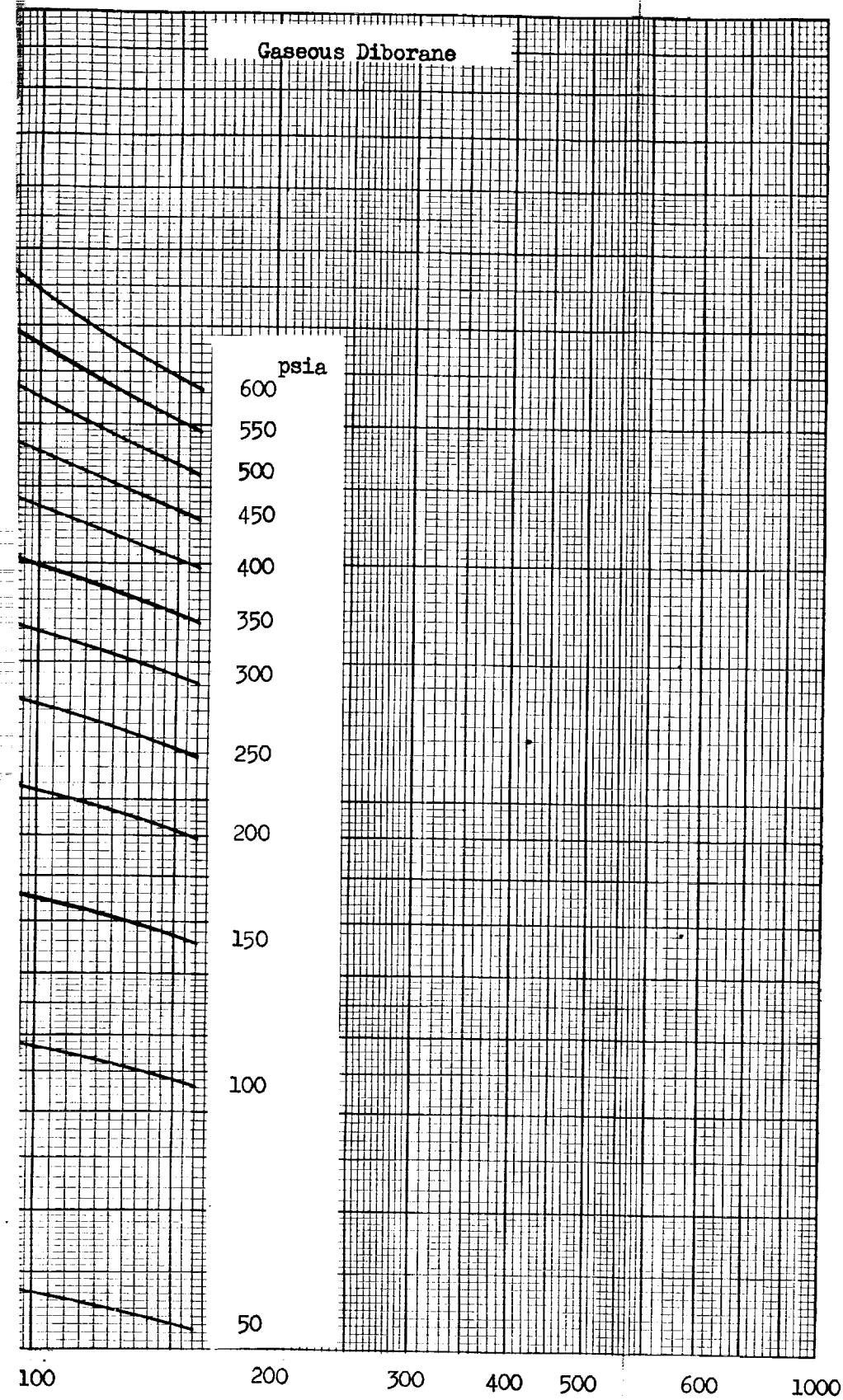

Figure C-6. Density vs Temperature for Diborane.

FOLDOUT FRAME

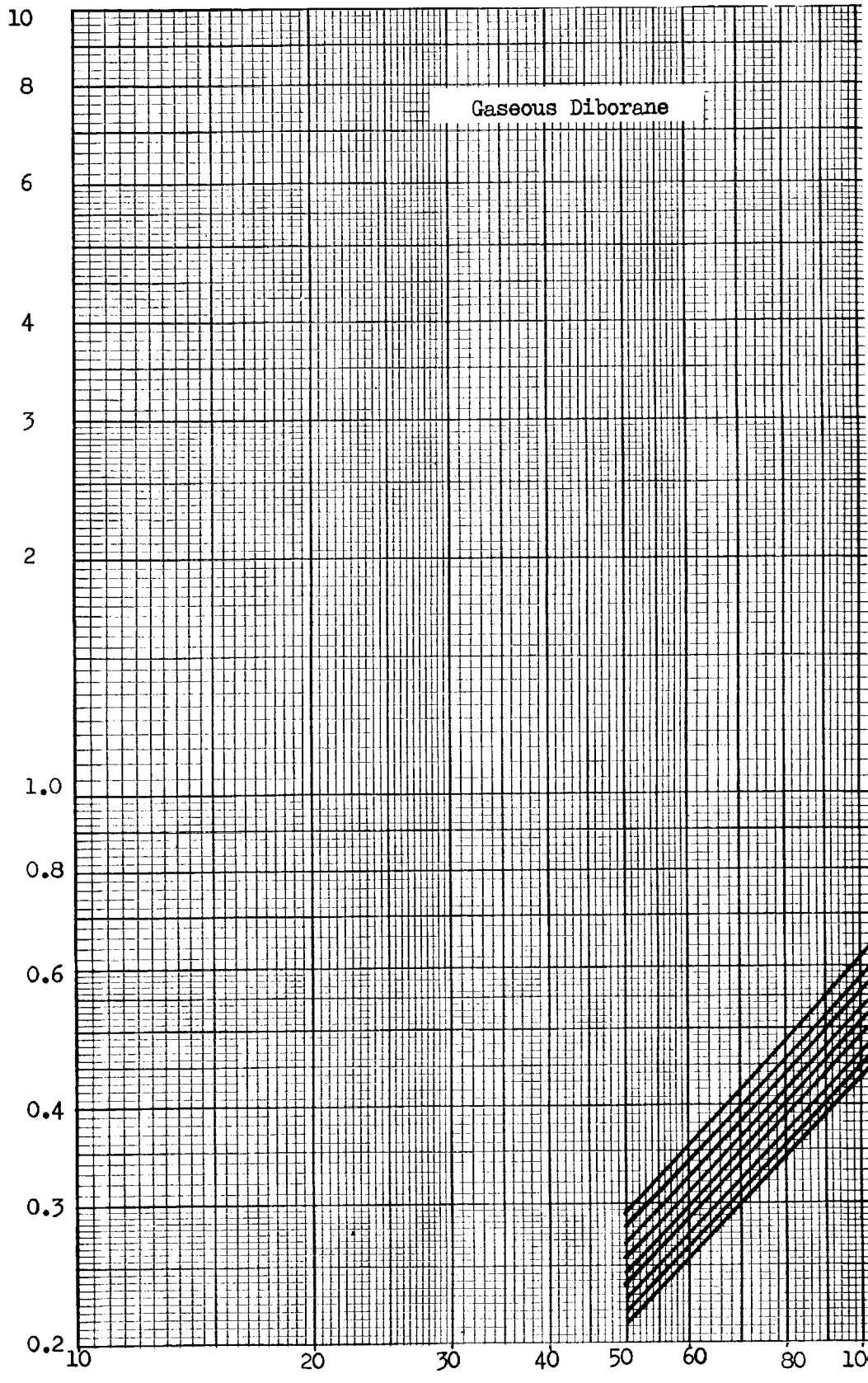

FOLDOUT FRAME

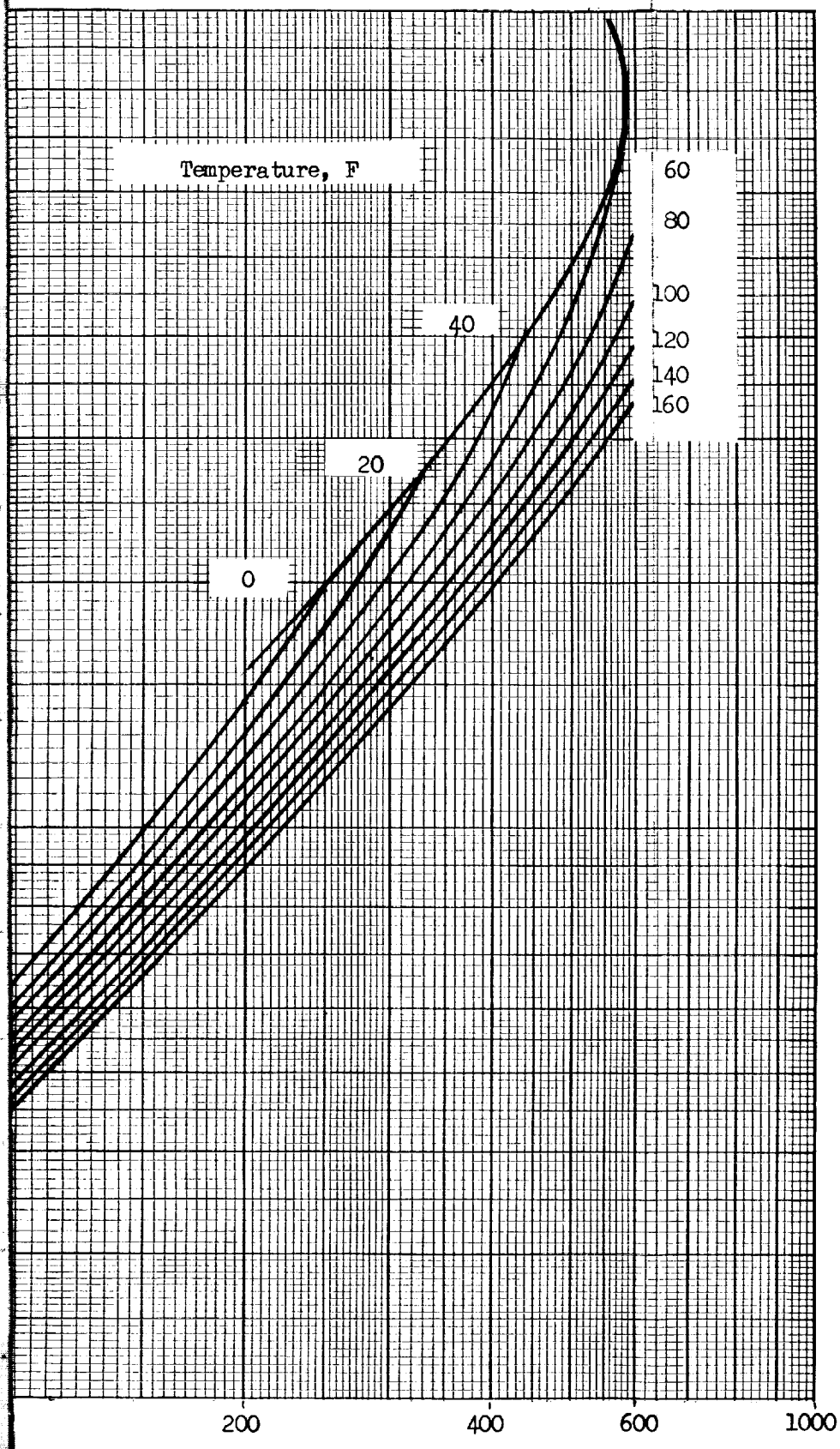

FOLDOUT FRAME

Figure C-7. Density vs Pressure for Diborane

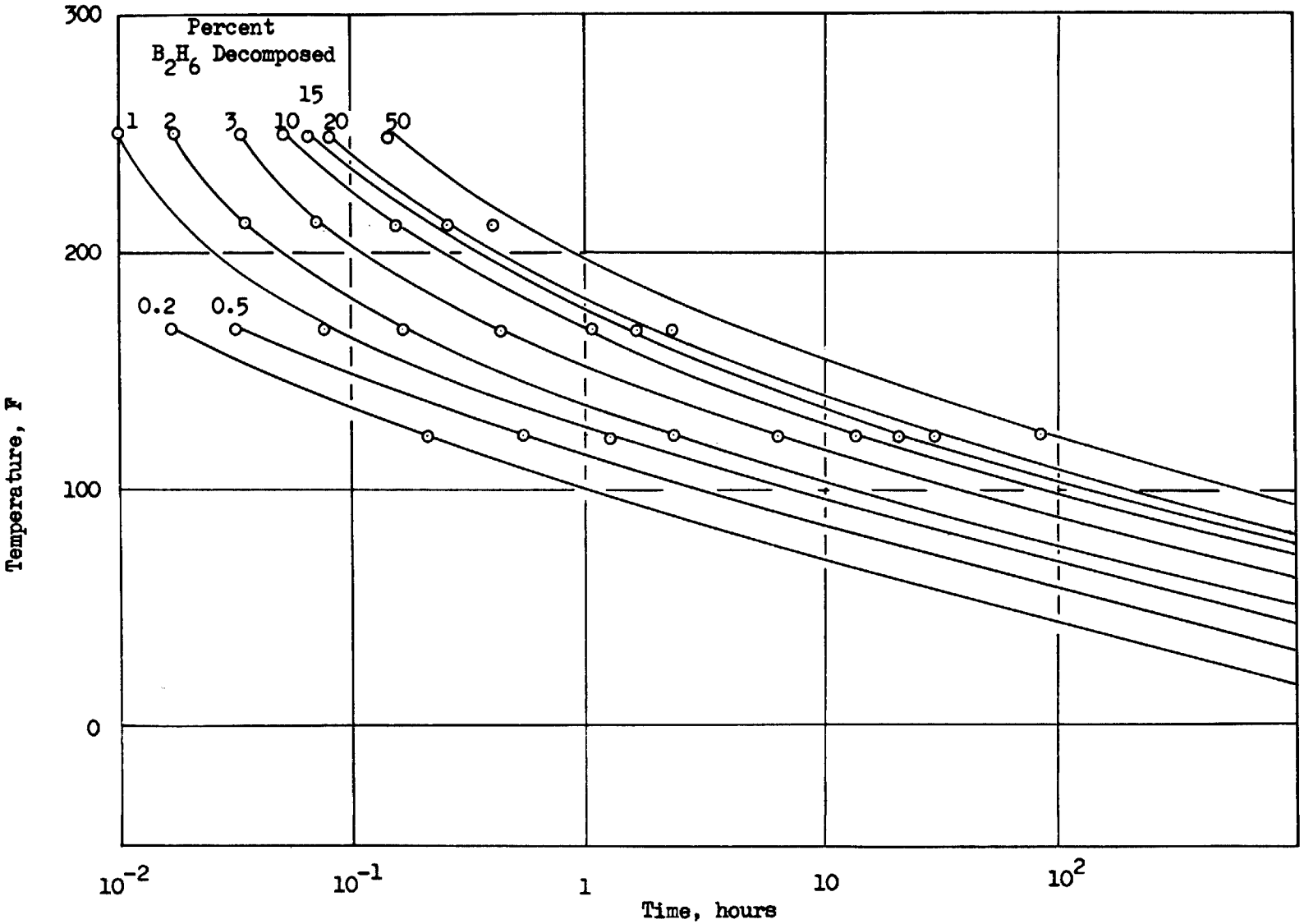

Figure C-8. Diborane Decomposition

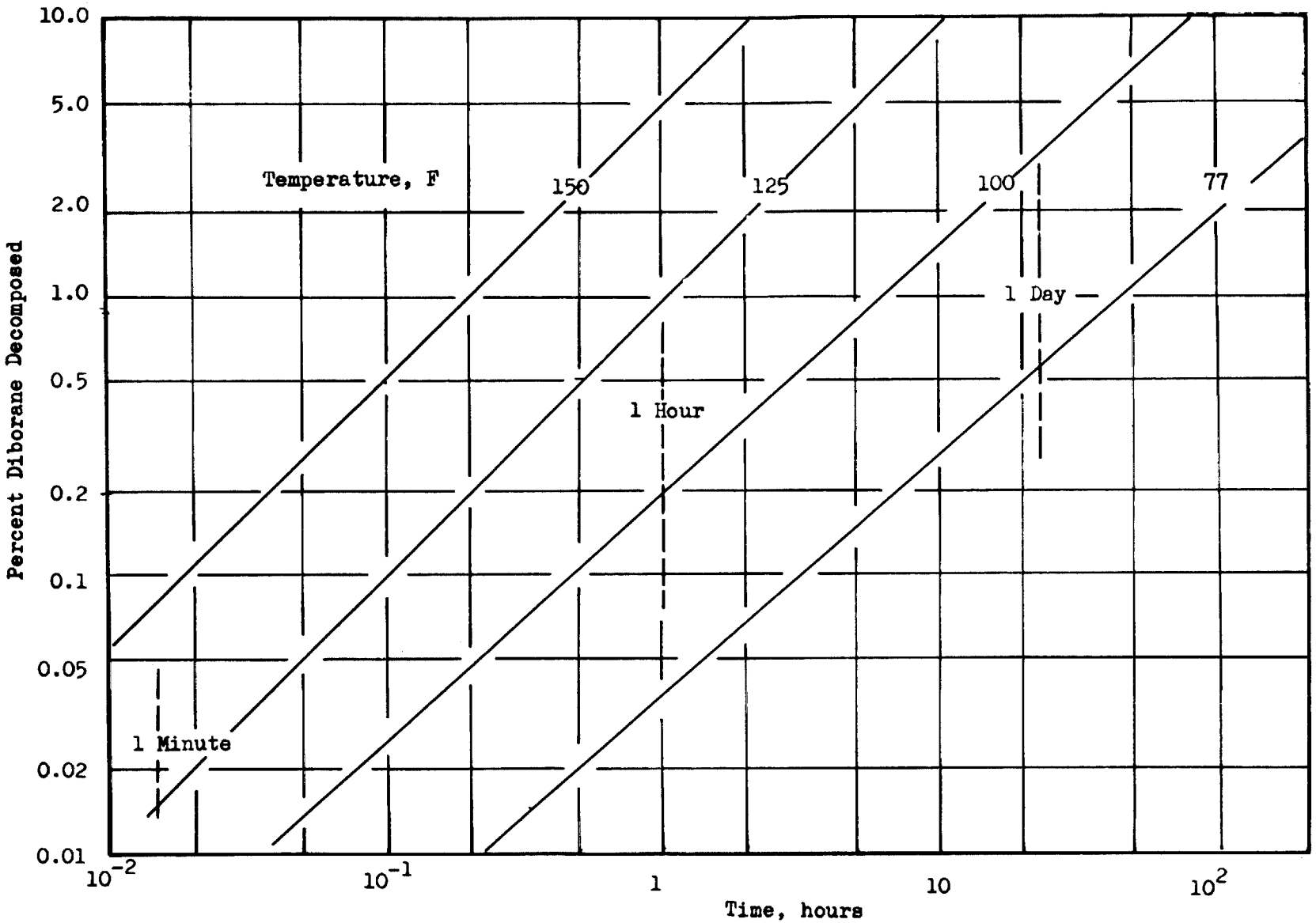

Figure C-9. Crossplot of Diborane Decomposition Data

APPENDIX D

DEVELOPMENT OF REAL GAS SONIC VENTURI ANALYSIS

Because diborane and methane gas are close to their critical points for the flow conditions of interest, the standard ideal gas venturi equations cannot be used. Therefore, a calculational procedure including the real gas effects was developed. The analysis is presented in this appendix.

In the procedure, the virial equation of state is used to generate a table of thermodynamic properties for an expansion from the initial conditions. The mass flux at each expansion table point is found and a power fit of the properties in the region of highest mass flux is used to find the exact point of maximum mass flux or throat.

All the methods used in calculating flowrate of gases through sonic venturis start with the steady flow energy equation:

$$h_1 + \frac{\dot{W}^2}{2g_o \rho_1^2 A_1^2} = h_2 + \frac{\dot{W}^2}{2g_o \rho_2^2 A_2^2}$$

where

$$\dot{W} = \rho_1 A_1 V_1 = \rho_2 A_2 V_2$$

Rewriting the equation in terms of flowrate yields

$$\dot{W} = \left[\frac{2g_o (h_1 - h_2)}{\frac{1}{\rho_2^2 A_2^2} - \frac{1}{\rho_1^2 A_1^2}} \right]^{\frac{1}{2}}$$

The basic problem in solving for the flowrate lies in determining the relationship of h_2 and ρ_2 to h_1 and ρ_1 for an isentropic expansion from A_1 to A_2.

The exact solution is based upon the fact that the mass flux is maximum at the sonic throat. Solving for the throat mass flux gives

$$\left(\frac{\dot{W}}{A_2}\right)^2 = \left[\frac{2g_o\,(h_1 - h_2)\,\rho_2^2}{\left(1 - \frac{\rho_2^2 A_2^2}{\rho_1^2 A_1^2}\right)}\right]$$

Differentiating with respect to density squared and holding entropy constant

$$\left[\frac{d\left(\dot{W}^2/A_2^2\right)}{d(\rho_2^2)}\right]_s = \left[\frac{2g_o(h_1 - h_2)}{\left(1 - \frac{\rho_2^2 A_2^2}{\rho_1^2 A_1^2}\right)^2}\right]_s - \left[\frac{\rho_2^2\left(\frac{dh_2}{d(\rho_2^2)}\right)_s A_2^2}{1 - \frac{\rho_2^2 A_2^2}{\rho_1^2 A_1^2}}\right]_s$$

Rearranging terms and using a power relationship for enthalpy as a function of density and introducing throat conditions (*) and conditions immediately above the throat (x) gives:

$$kB\left(\rho_x^2 - \rho^{*2}\right)^{k-1} = \frac{\left[h_{v/s} + B\left(\rho_x^2 - \rho^{*2}\right)^k - h_x\right]}{\rho^{*2}\left[1 - \left(\frac{\rho^* A^*}{\rho_{v/s} A_{v/s}}\right)\right]}$$

This equation can be solved for ρ^* by iterative means. With ρ^* known, h^* and $\dot{W}$ can be calculated.

The calculation procedure used in the numerical solution is to input a table of pressure, temperature, enthalpy and density along the constant entropy line corresponding to the upstream pressure and temperature. The mass flux for each point in the table is then calculated. When the peak in mass flux is passed, three points are used to find the constants for the power fit equation. The throat density, enthalpy and the flowrate are then found.

The simplest and most consistent method of tabulating pressure, temperature, enthalpy and density for constant entropy was found to be the use of the virial equation of state using coefficients of the form recommended by Benedict, Webb and Rubin. The form of the virial equation used is

$$P_R = Z \rho_R R T_R$$

With the compressibility given by:

$$Z = 1 + A_1 \rho_R + A_2 \rho_R^2 + A_4 \rho_R^4 + A_5 \rho_R^5$$

where

$$\rho_R \equiv \frac{\rho}{P_{critical}/RT_{critical}}$$

$$P_R \equiv P/P_{critical}$$

$$T_R \equiv T/T_{critical}$$

$$A_1 \equiv B_0 + B_1/T_R + B_3/T_R^3$$

$$A_2 \equiv C_0 + C_1/T_R + C_3/T_R^3$$

$$A_4 \equiv C_3 C_3''/T_R^3$$

$$C_3 \equiv C_3' e^{-C_3'' \rho_R^2}$$

$$A_5 \equiv E_1/T_R$$

The form of the equation is determined by examining the intermolecular forces. The constants can be derived either theoretically or empirically. The constants used for methane were taken from Ref. 8 and gave highly accurate values when checked against the graphical values shown in Ref. The constants for diborane were taken from Ref. 6. The values used are shown in Table D-1.

The deviation from perfect gas value of the entropy is given by:

$$(S - S_o')/R = \left[\frac{2C_3'}{C_3'' T_R^3}\right]\left[1 - e^{-C_3'' \rho_R^2}\right] -$$

$$\left[B_o - 2\frac{B_3}{T_R^3}\right]\rho_R -$$

$$\left[\frac{C_o}{2} + \frac{C_3'}{T_R^3}\right] e^{-C_3'' \rho_R^2} \rho_R^2 +$$

$$R \ln (ZR)$$

and

$$S_o' = \int_o^T C_{P_o} \frac{dt}{t} - R \ln P$$

The function $\int_o^T C_{P_o} \frac{dt}{t}$ is the ideal gas state entropy and is tabulated in Ref. 9 for hydrocarbons.

TABLE D-1

VIRIAL COEFFICIENTS AND

CRITICAL CONSTANTS

	CH_4	B_2H_6
$T_{critical}$	343.3 R	521.7 R
$P_{critical}$	673.3 psia	580.9 psia
B_o	0.12469	0.032529
B_1	-0.34697	-0.207653
B_3	-0.11609	-0.167886
C_o	0.028956	-0.1890356
C_1	-0.027045	0.261514
C_3'	0.038313	-0.0963183
C_3''	0.051401	0.0827739
E_1	0.84333×10^{-4}	-0.00048395

The deviation from perfect gas values for the enthalpy is given by:

$$(h-h_o)/RT = \frac{3C_3'}{C_3'' T_R^3}\left[1-e^{-C_3''\rho_R^2}\right] +$$

$$\left[B_o + 2\frac{B_1}{T_R} + \frac{4B_3}{T_R^3}\right]\rho_R +$$

$$\left[C_o + \frac{3C_1}{2T_R} - \frac{C_3'}{2T_R^3}\, e^{-C_3''\rho_R^2}\right]\rho_R^2 +$$

$$\frac{C_3' C_3''}{T_R^3}\, e^{-C_3''\rho_R^2}\,\rho_R^4 +$$

$$\frac{6E_1\rho_R^5}{5T_R}$$

where $h_o = \int_o^T C_{P_o}\, dT$ is the ideal gas state enthalpy as tabulated in Ref. 9.

For given values of inlet pressure and temperature; the density, enthalpy and entropy are calculated using the equations of state. Pressure, temperature and enthalpy are then tabulated by solving the equations with the same value of entropy at a set series of densities in the range needed to find the sonic throat.

APPENDIX E

THRUST CHAMBER EFFICIENCY PREDICTIONS

The method of predicting thrust chamber efficiency is described in Section V. The calculations required involve the computation of a number of individual efficiencies to account for the specific loss modes. Each figure shows all propellant combinations for ease of comparison. The C^* heat loss efficiencies are also used in calculating predicted specific impulse from thrust chamber efficiency and injector efficiency as described in Section V.

The individual efficiencies and the thrust chamber efficiencies for all cases studied are presented in this Appendix. The organization of the figures is shown in Table

TABLE E-1

ORGANIZATION OF THRUST CHAMBER EFFICIENCY FIGURES

Nozzle	P_c	η_{TC}	η_G	η_{BL}	$\eta_{HL_{I_s}}$	$\eta_{HL_{C^*}}$	η_K
Cone	50	E-1	—	E-8	E-11	E-14	E-17
	100	E-2	—	E-9	E-12	E-15	E-18
	200	E-3	—	E-10	E-13	E-16	E-19
Bell	50	E-4	E-7	E-8	E-11	E-14	E-20
	100	E-5	E-7	E-9	E-12	E-15	E-21
	200	E-6	E-7	E-10	E-13	E-15	E-22

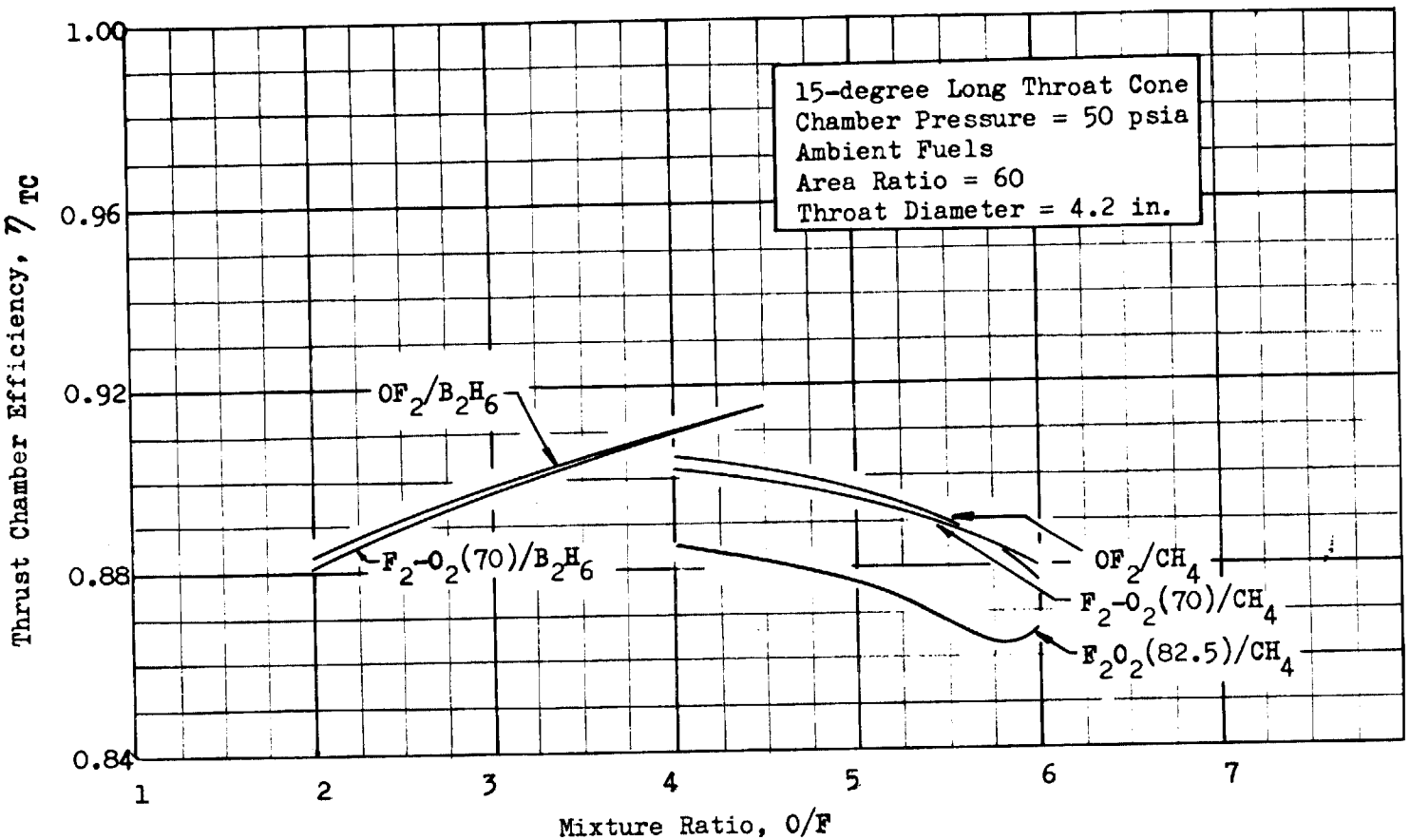

Figure E-1. Thrust Chamber Efficiency for 15-degree Long Throat Cone for 50 psia Chamber Pressure

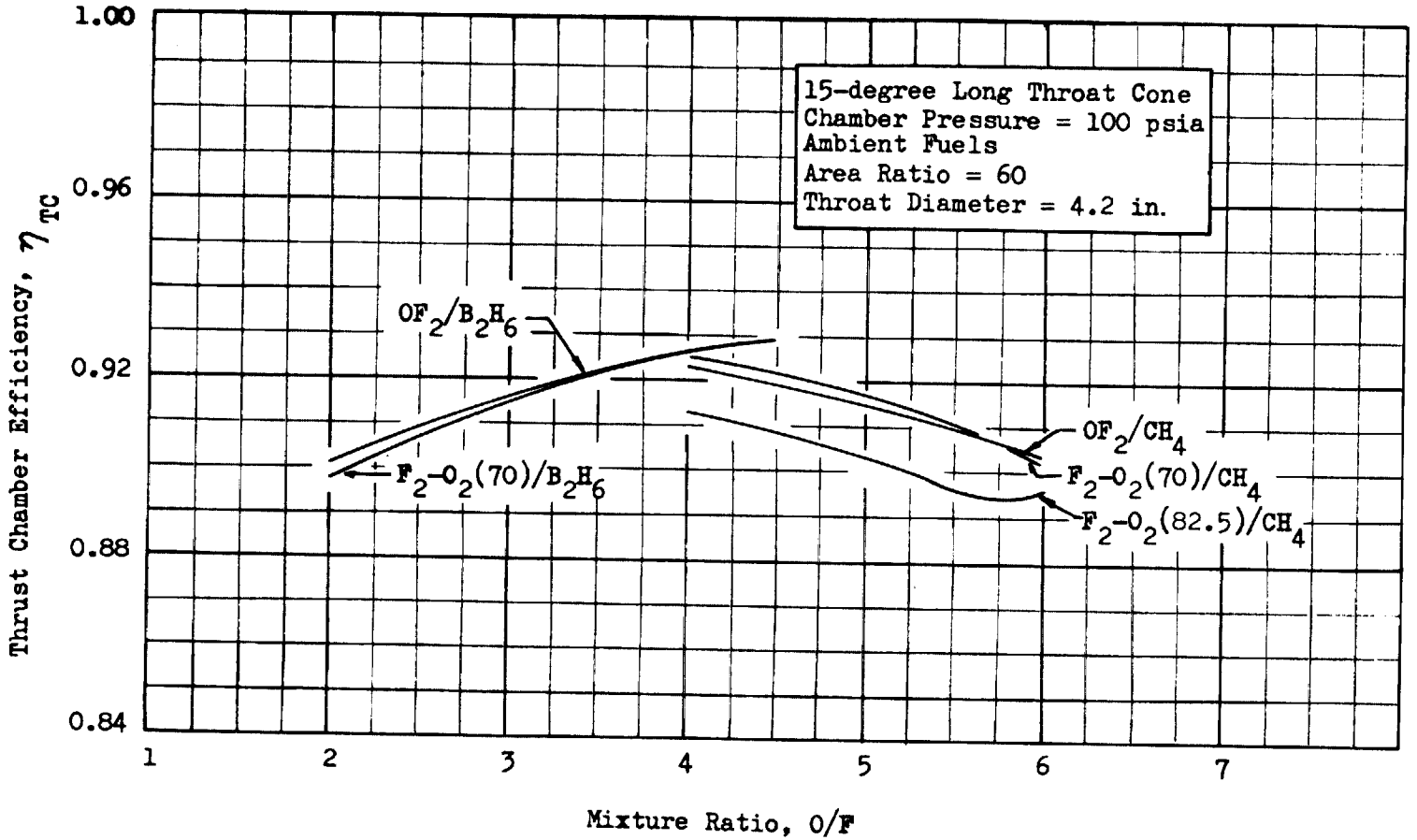

Figure E-2. Thrust Chamber Efficiency, η_{TC}, for 15-degree Long Throat Cone for 100 psia Chamber Pressure

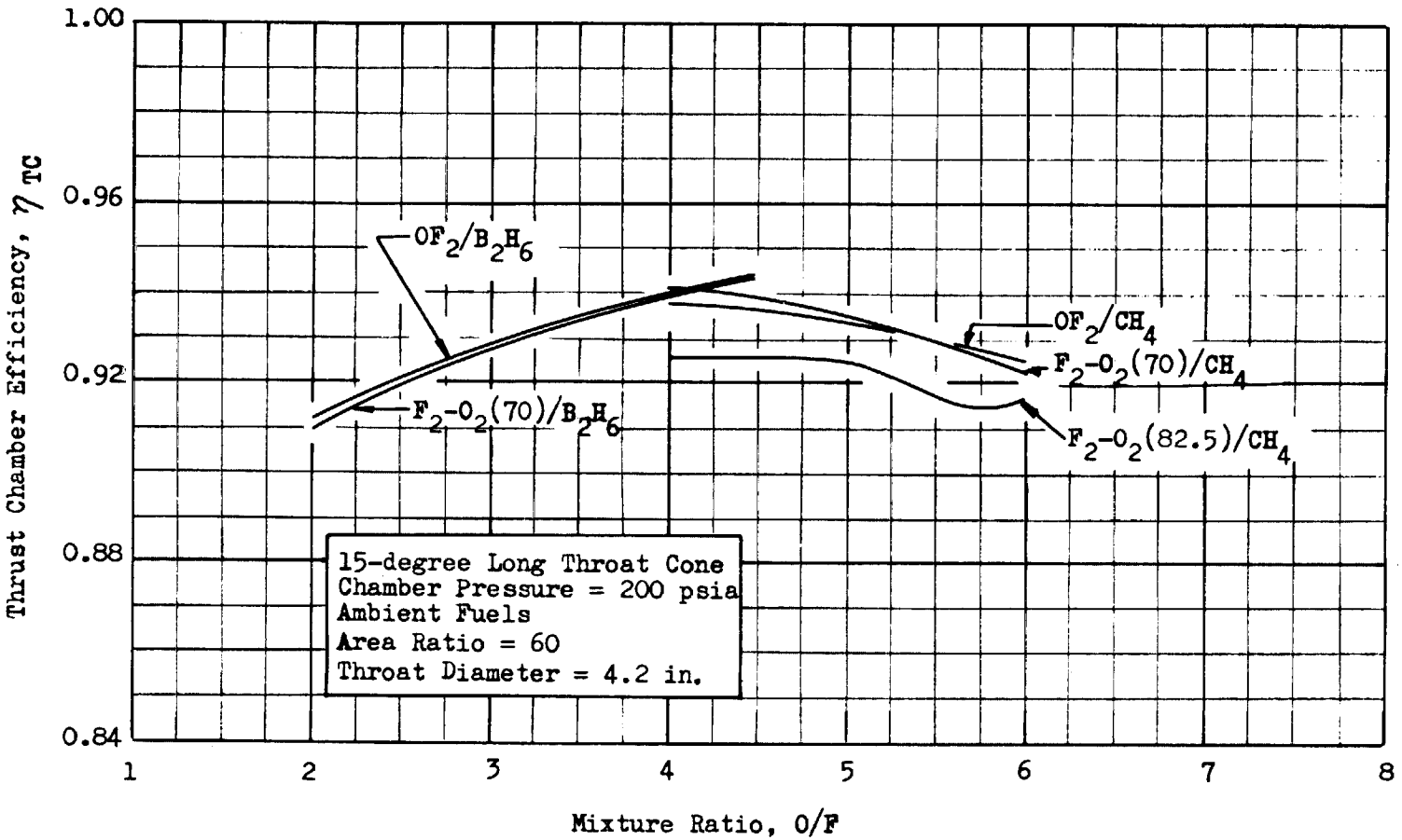

Figure E-3. Thrust Chamber Efficiency, η_{TC} for 15-degree Long Throat Cone for 200 psia Chamber Pressure

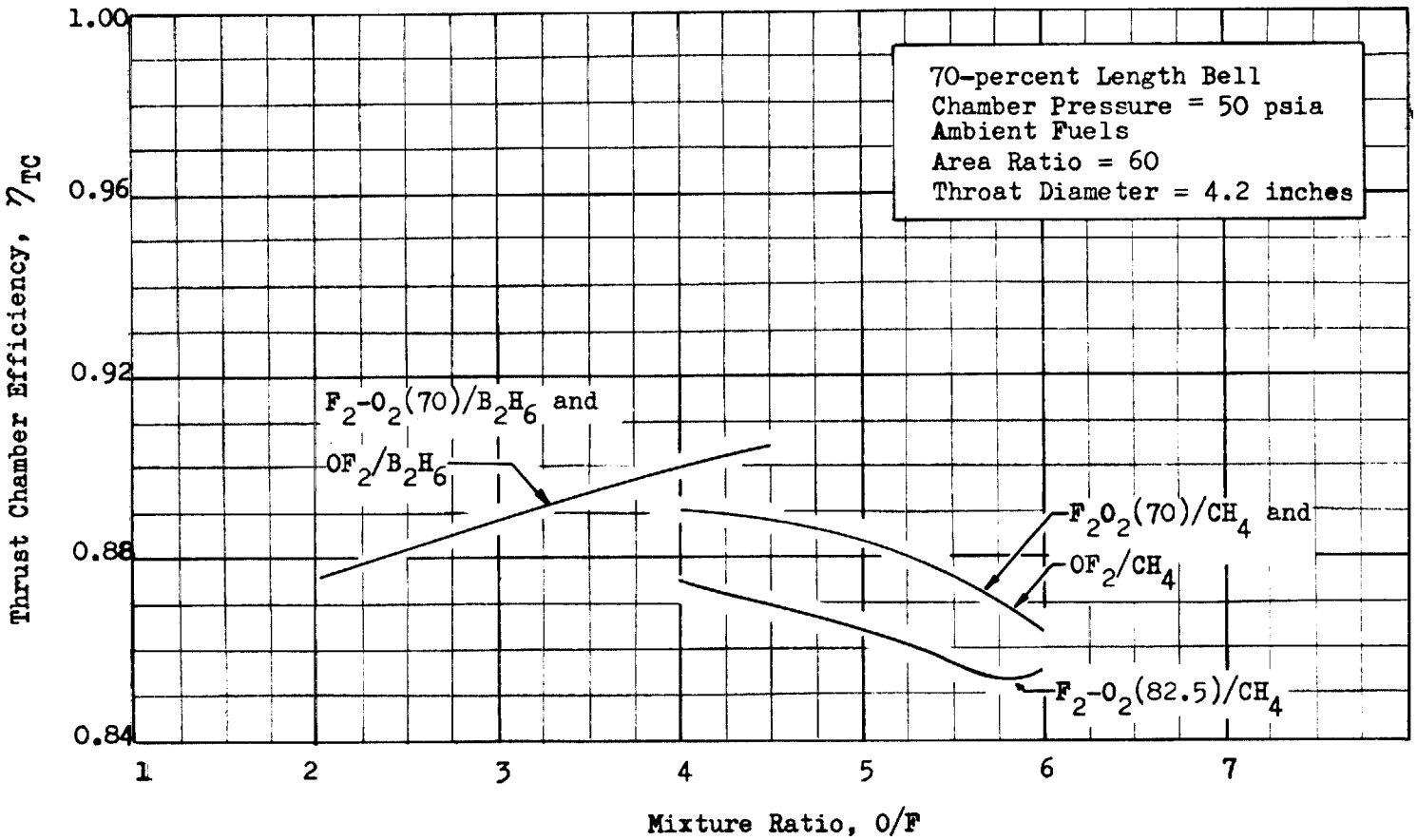

Figure E-4. Thrust Chamber Efficiency, η_{TC}, for 70-percent Bell for 50 psia Chamber Pressure

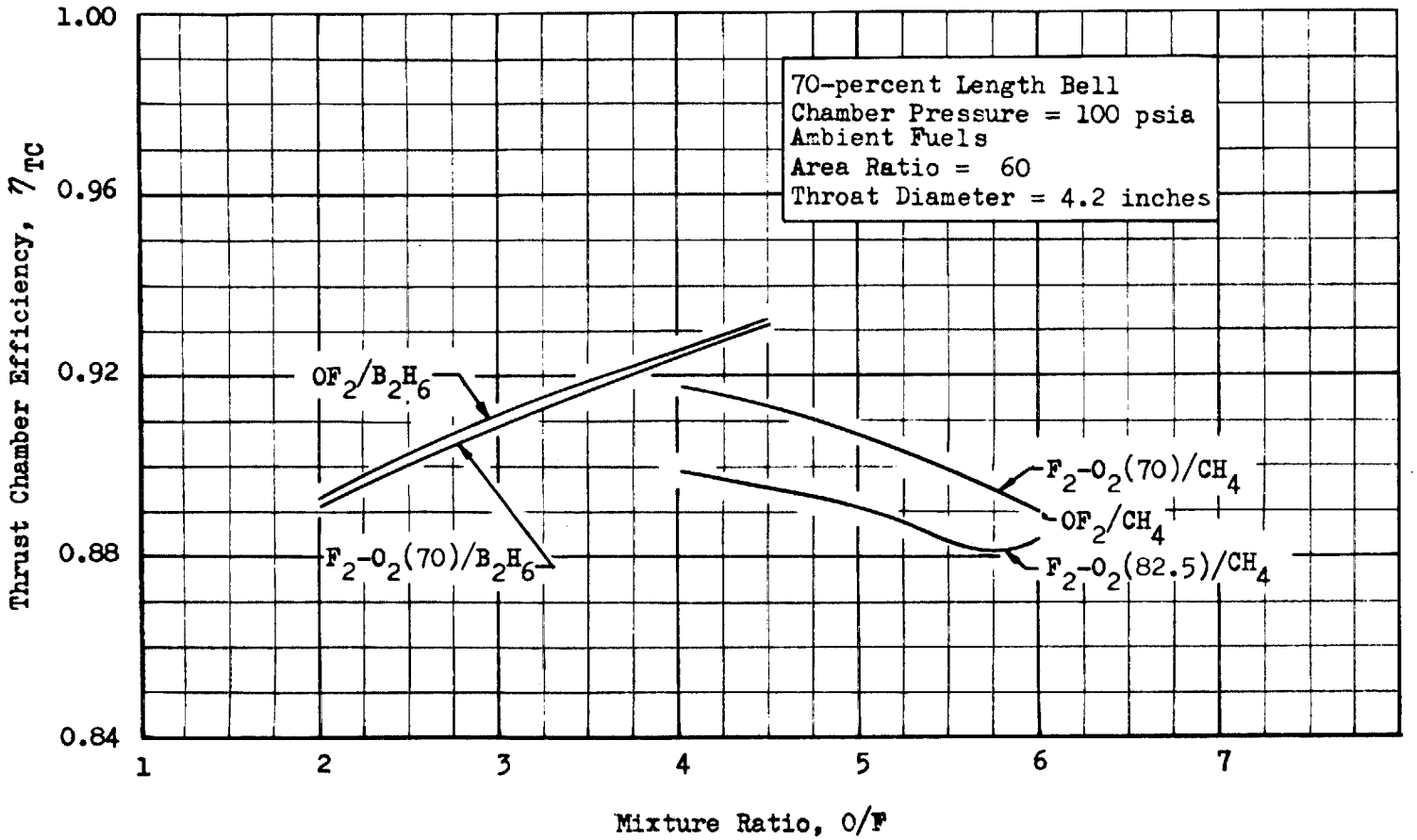

Figure E-5. Thrust Chamber Efficiency, η_{TC}, for 70-percent Bell for 100 psia Chamber Pressure

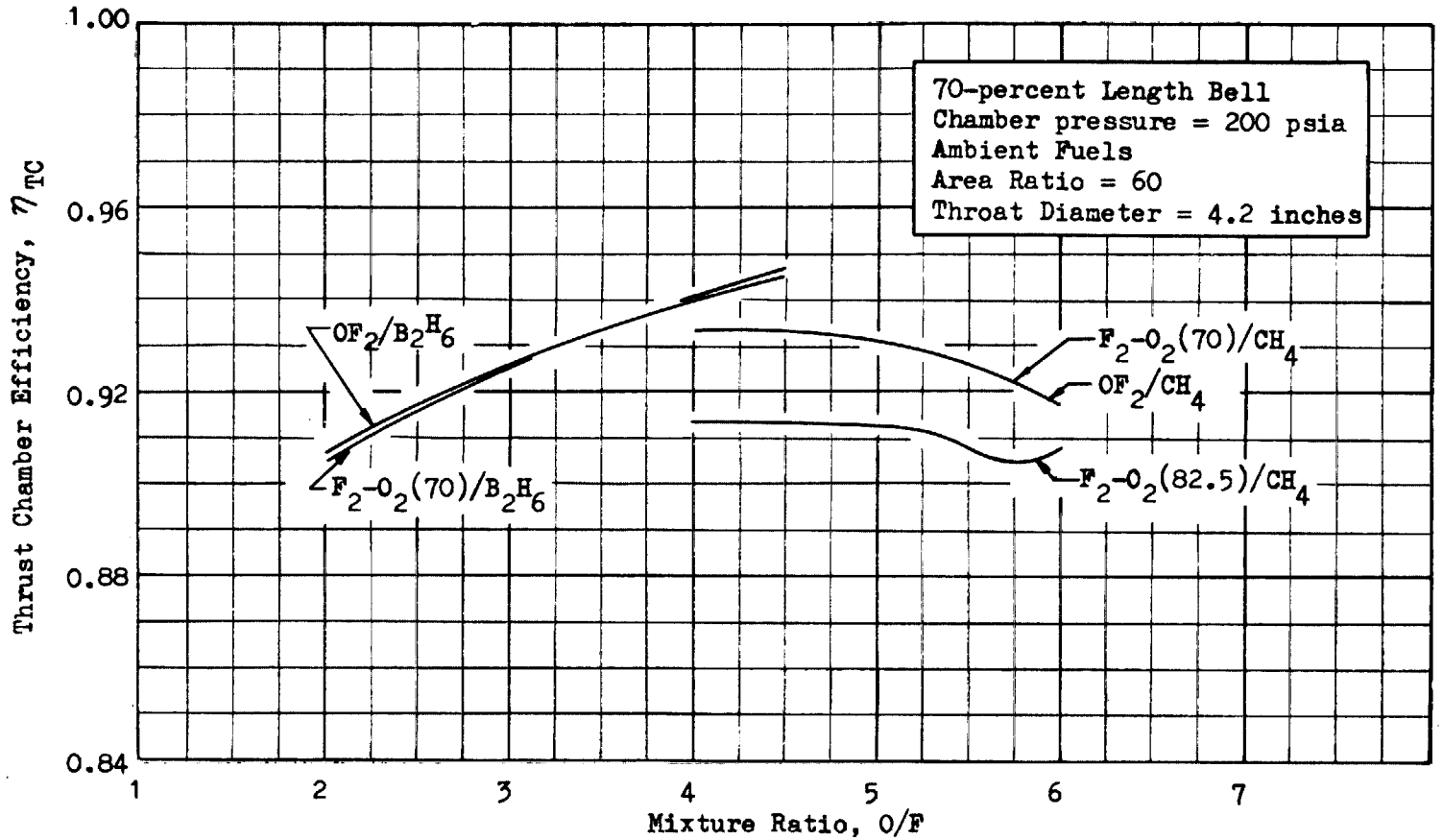

Figure E-6. Thrust Chamber Efficiency, η_{TC}, for 70-percent Bell for 200 psia Chamber Pressure

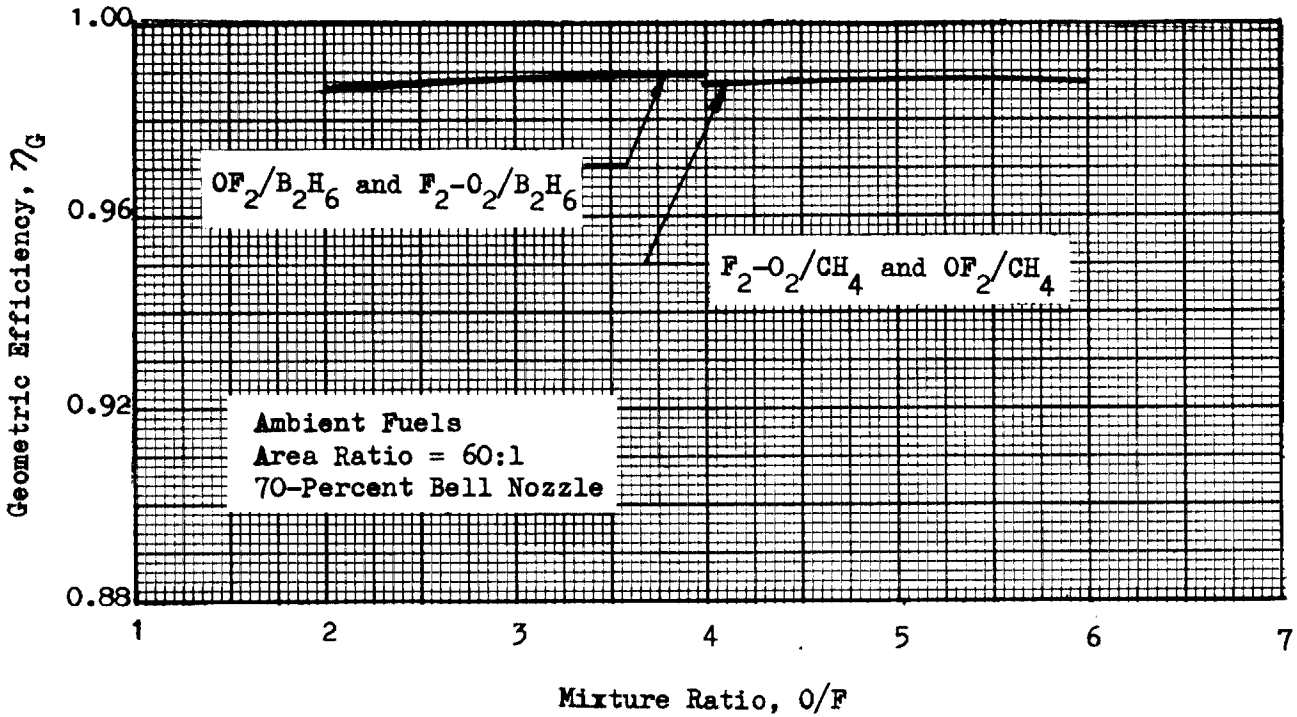

Figure E-7. Effect of Mixture Ratio on Geometric Efficiency for 70-Percent Bell Nozzle

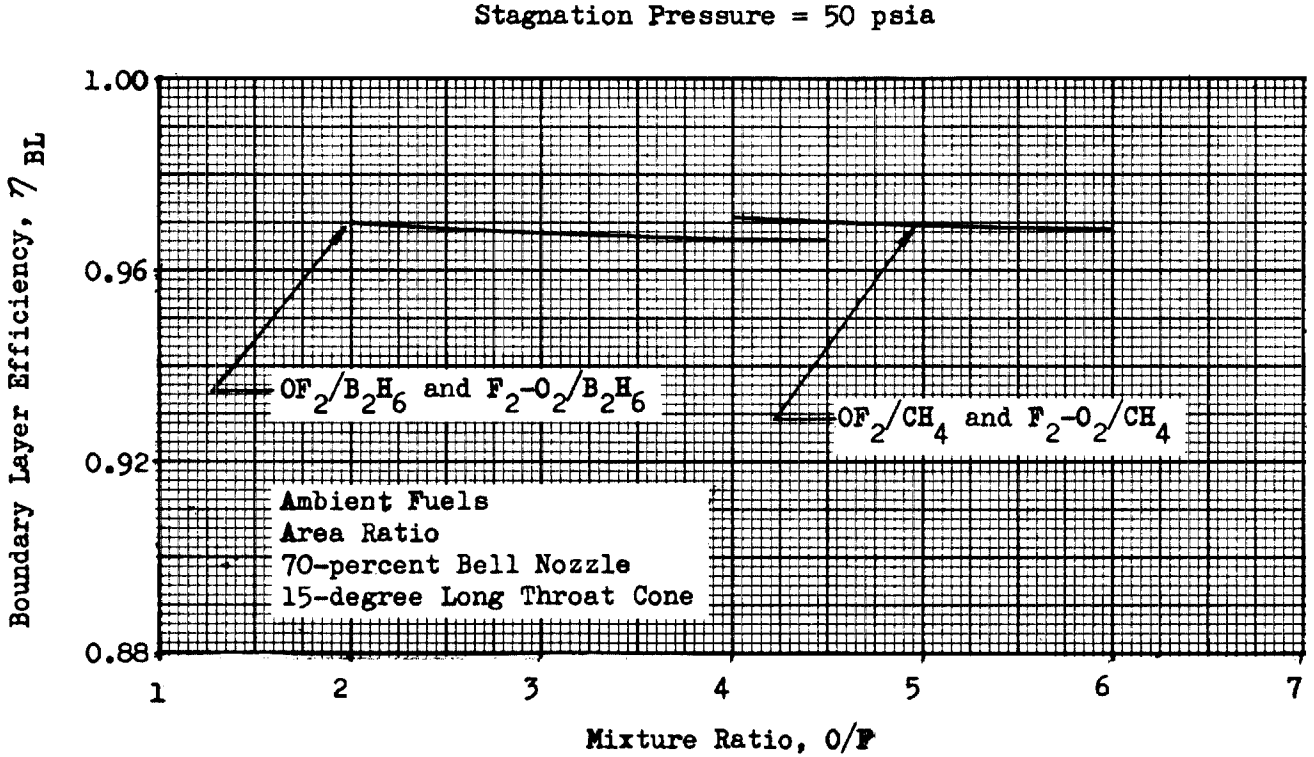

Figure E-8. Effect of Mixture Ratio on Boundary Layer Efficiency for 50 psia Chamber Pressure

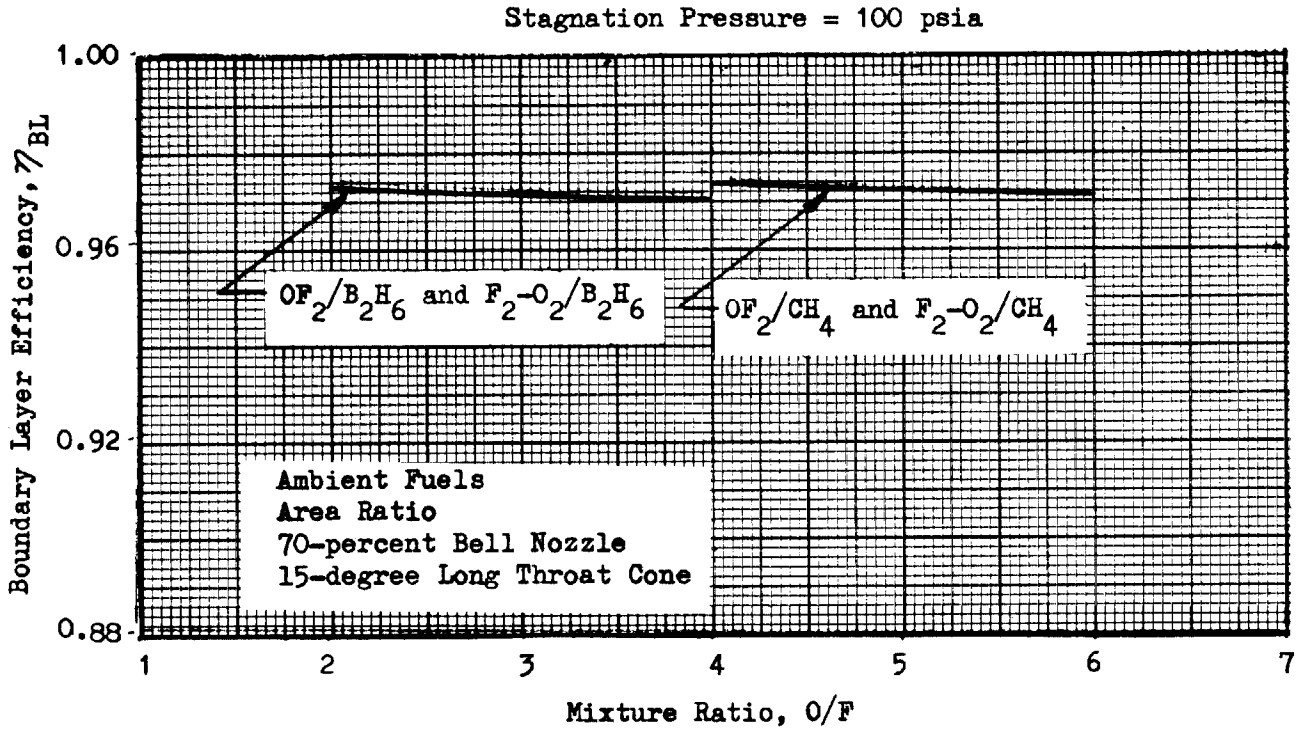

Figure E-9. Effect of Mixture Ratio on Boundary Layer Efficiency for 100 psia Chamber Pressure

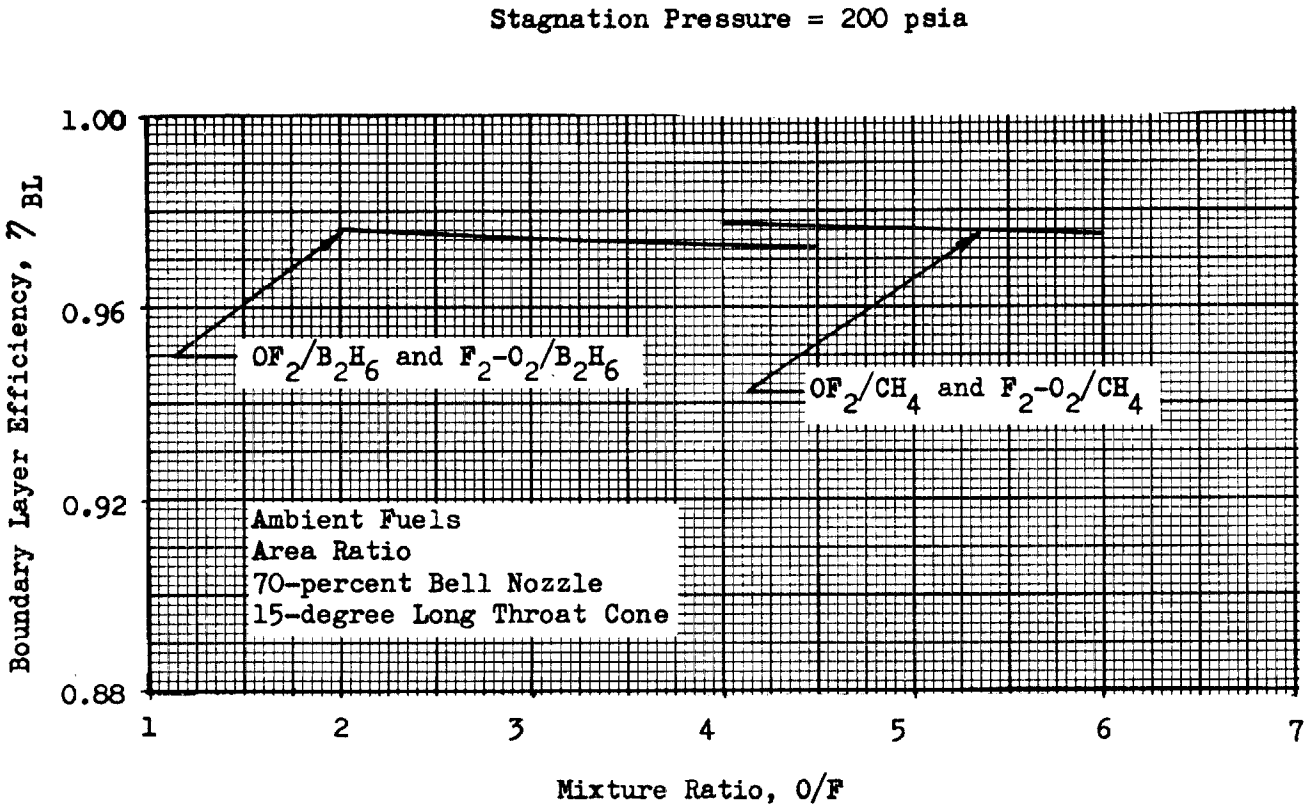

Figure E-10. Effect of Mixture Ratio on Boundary Layer Efficiency for 200 psia Chamber Pressure

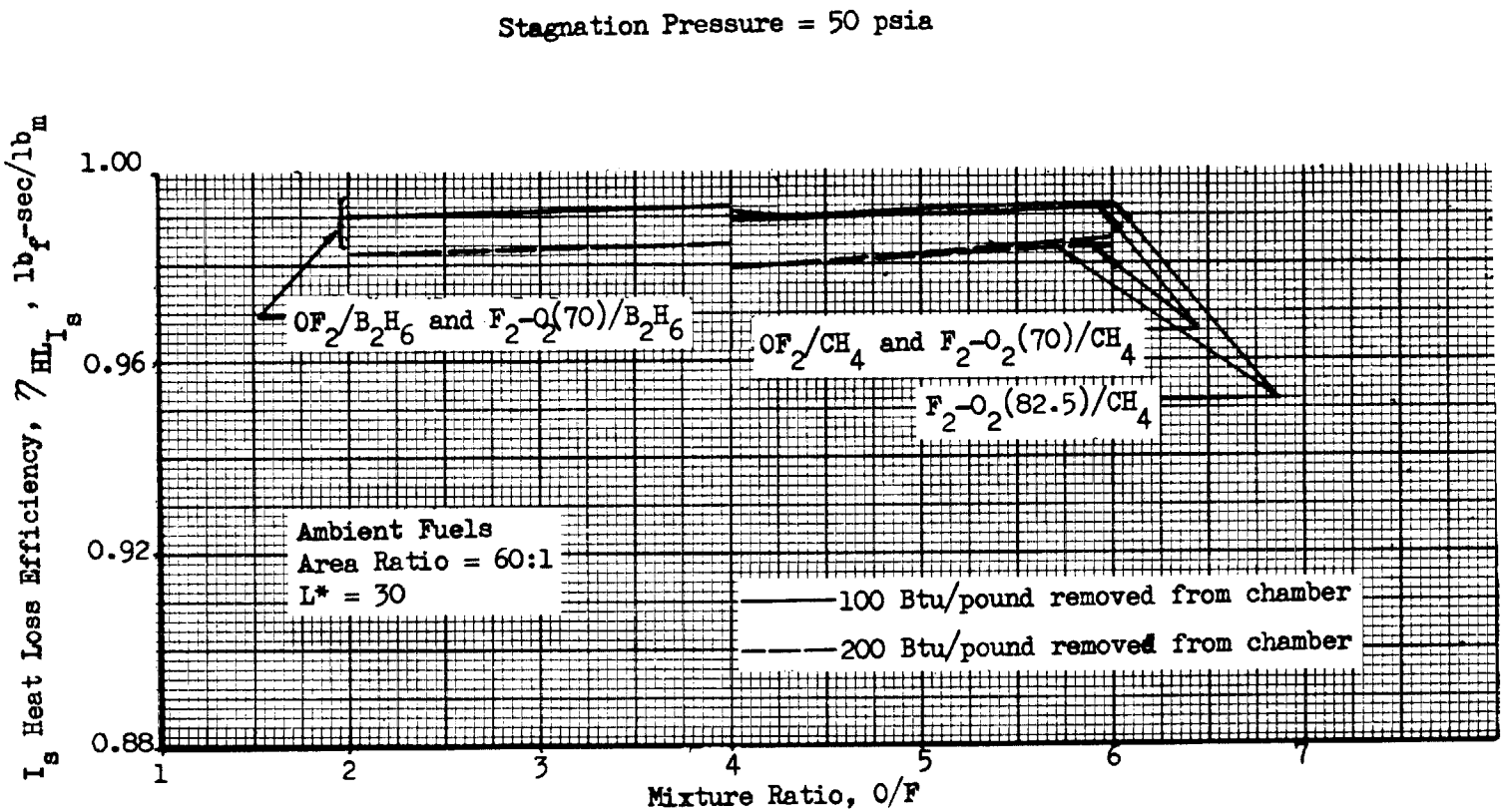

Figure E-11. Specific Impulse Heat Loss Efficiency vs Mixture Ratio for 50 psia Chamber Pressure.

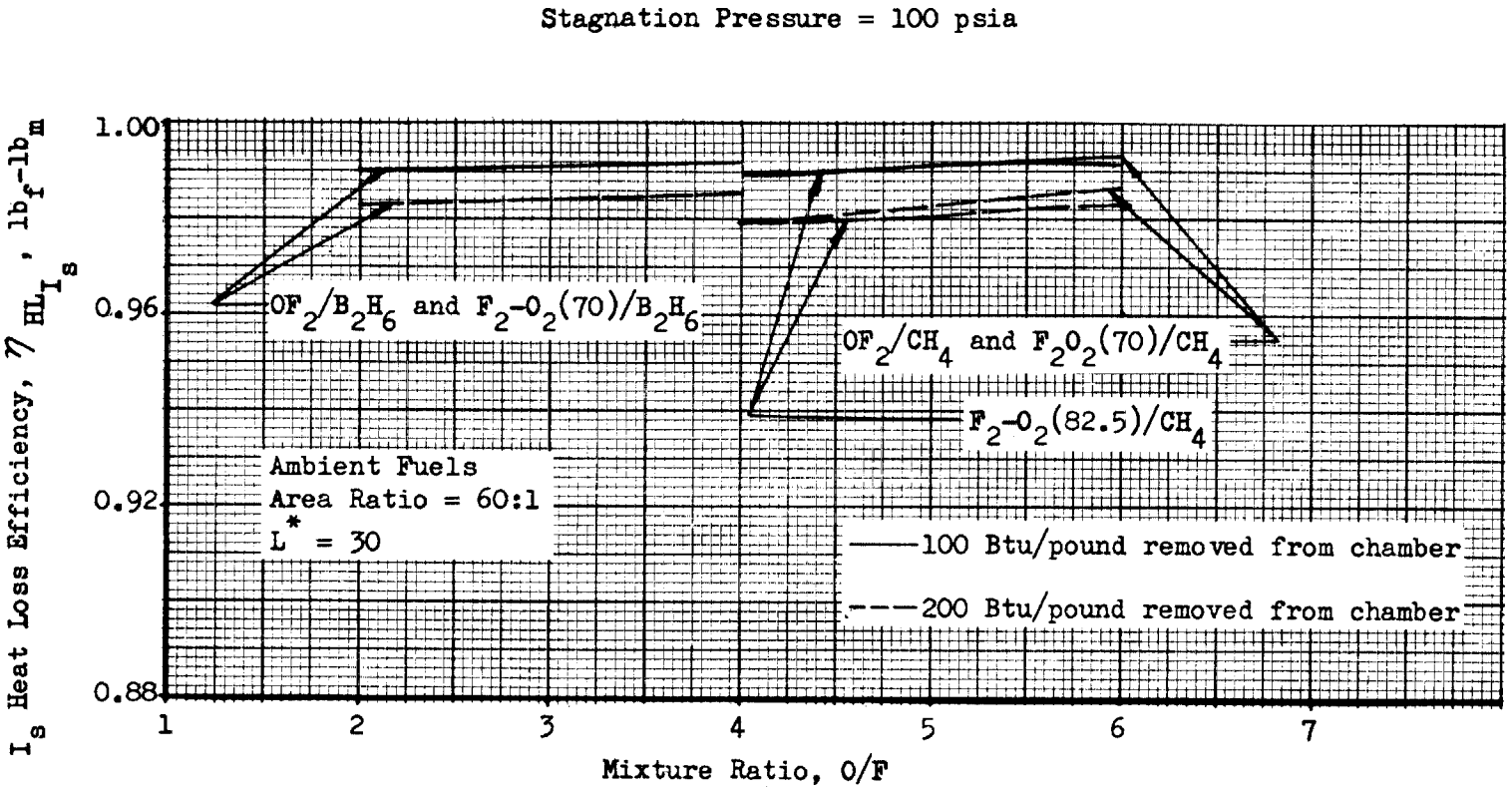

Figure E-12. Specific Impulse Heat Loss Efficiency vs Mixture Ratio for 100 psia Chamber Pressure.

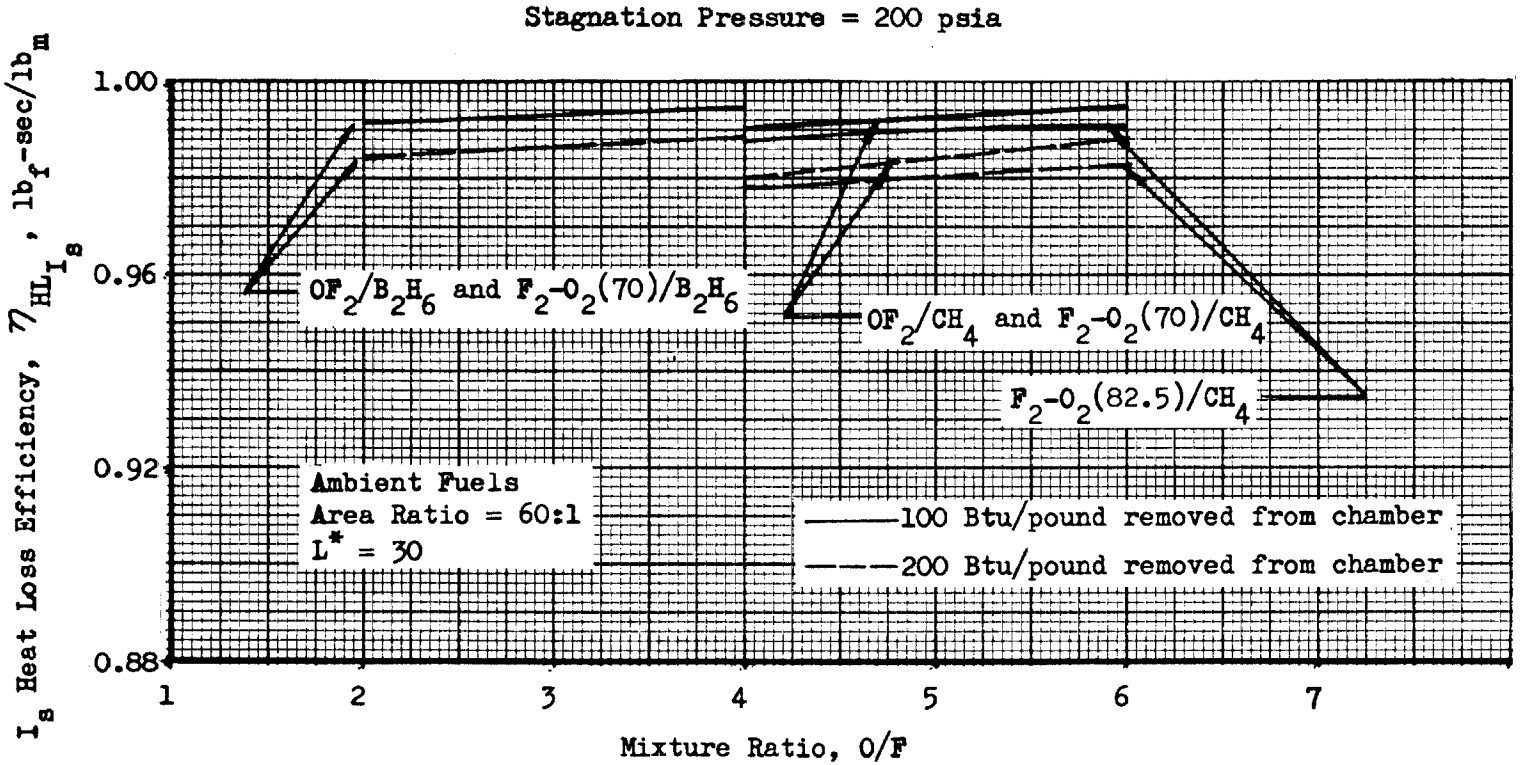

Figure E-13. Specific Impulse Heat Loss Efficiency vs Mixture Ratio for 200 psia Chamber Pressure.

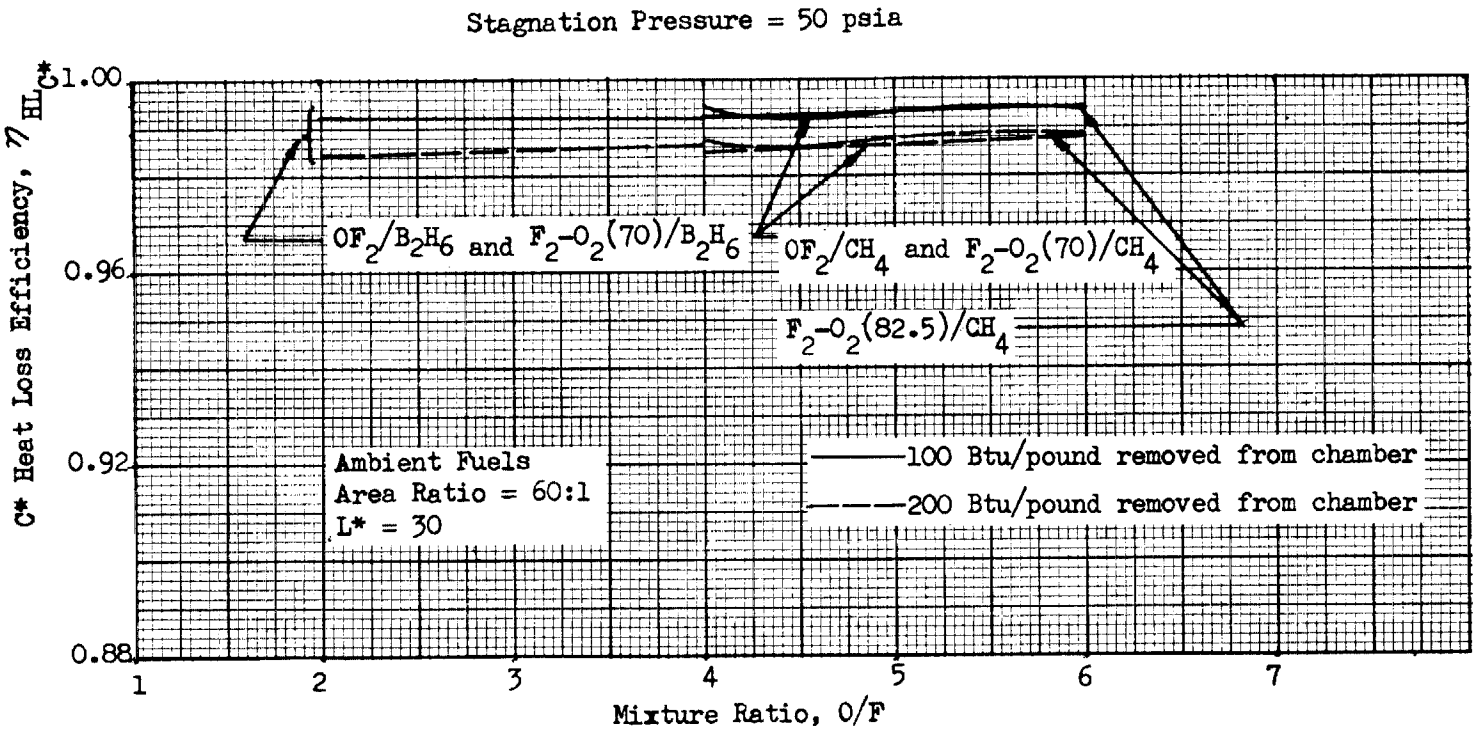

Figure E-14. Characteristic Velocity Heat Loss Efficiency vs Mixture Ratio for 50 psia Chamber Pressure

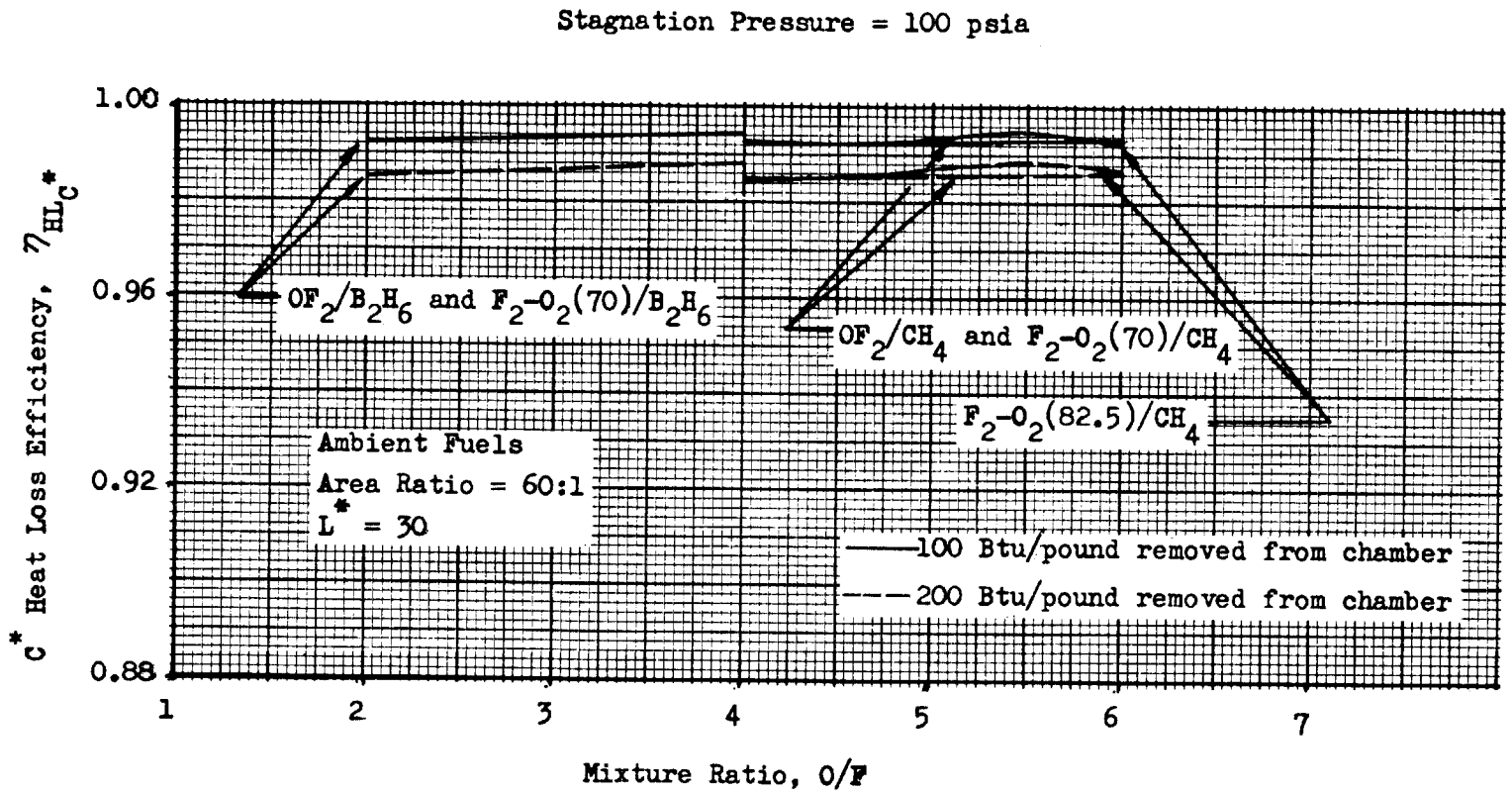

Figure E-15. Characteristic Velocity Heat Loss Efficiency vs Mixture Ratio for 100 psia Chamber Pressure

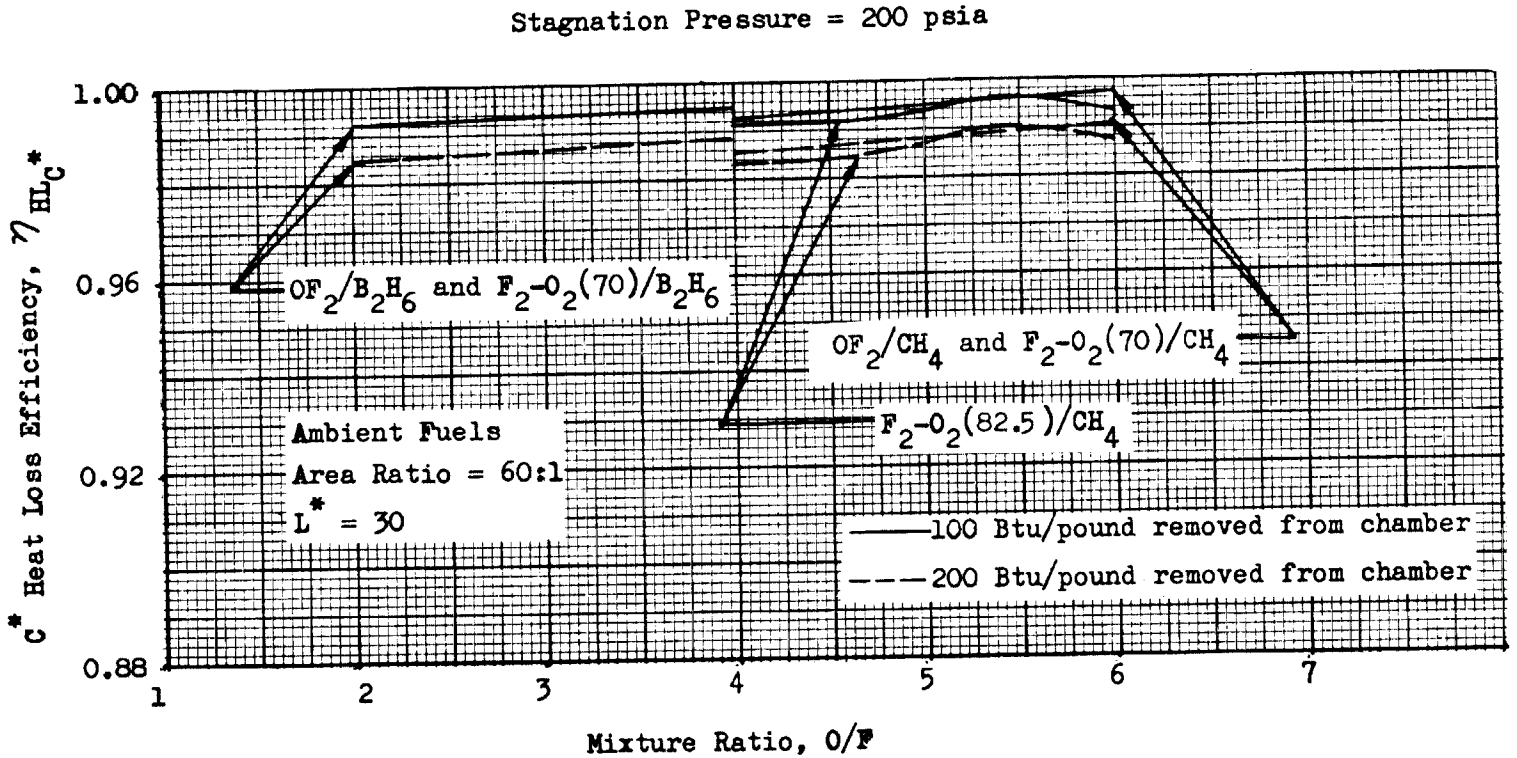

Figure E-16. Characteristic Velocity Heat Loss Efficiency vs Mixture Ratio for 200 psia Chamber Pressure.

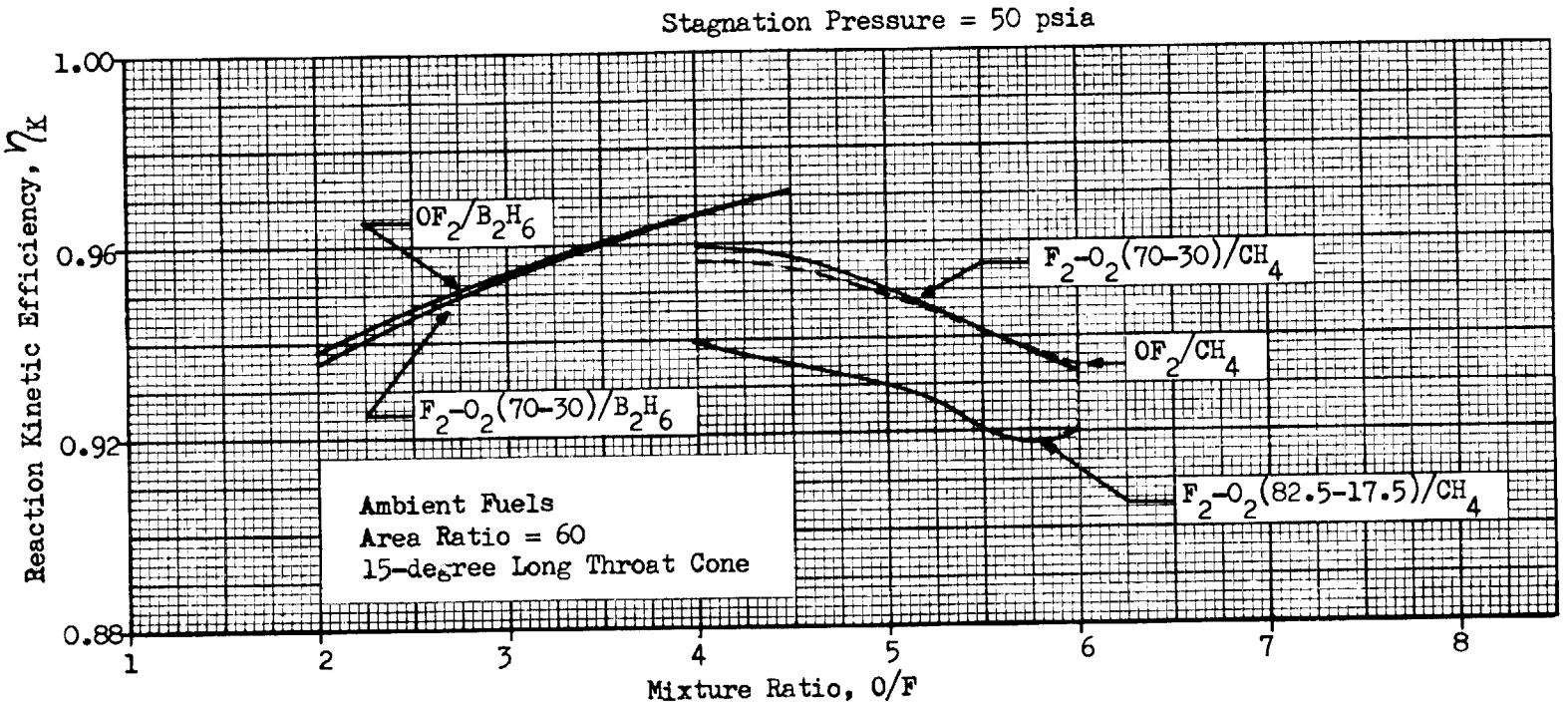

Figure E-17. Effect of Mixture Ratio on Reaction Kinetic Efficiency for 15-degree Long Throat Cone for 50 psia Chamber Pressure

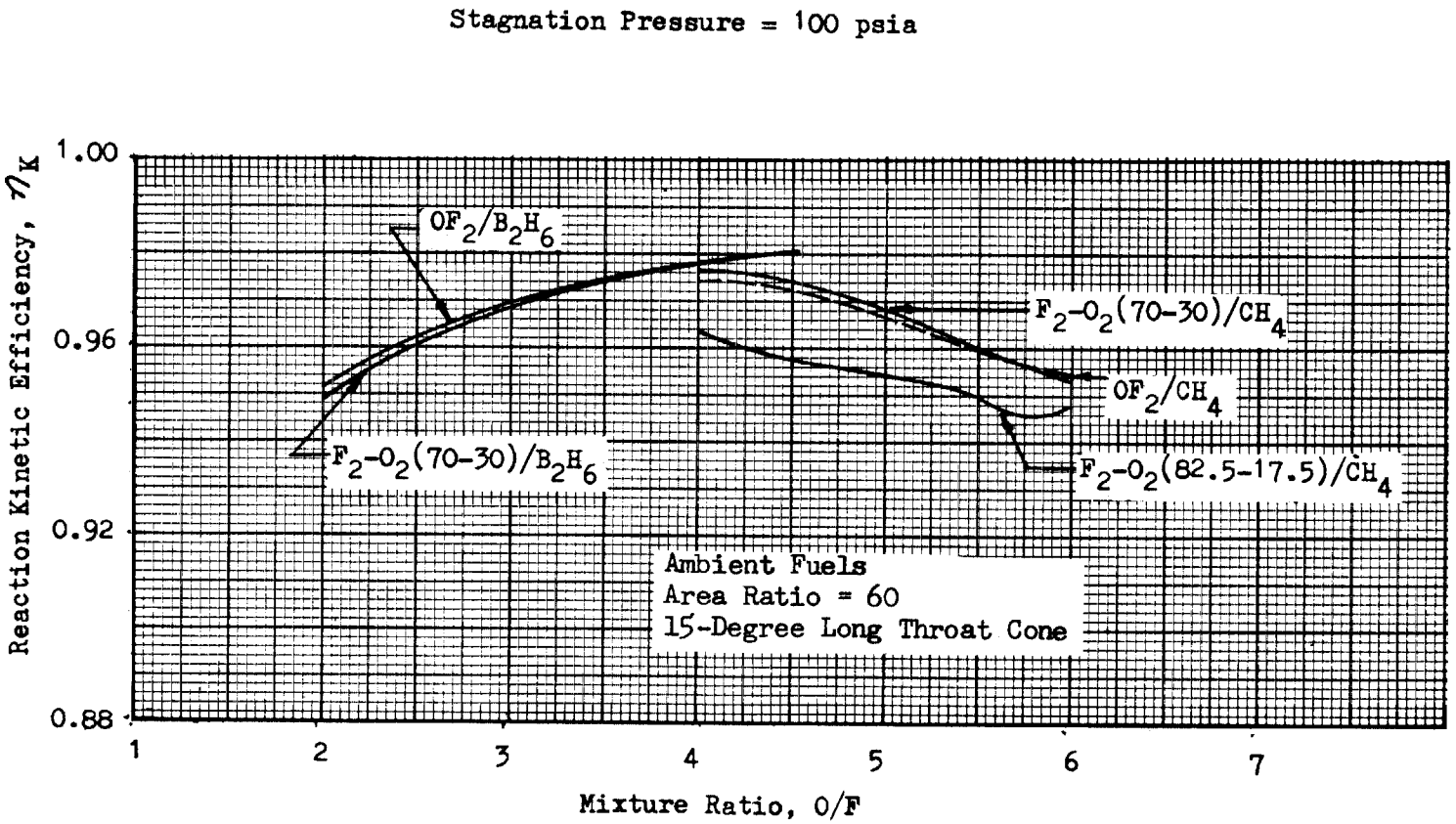

Figure E-18 Effect of Mixture Ratio on Reaction Kinetic Efficiency for 15-Degree Long Throat Cone for 100 psia Chamber Pressure

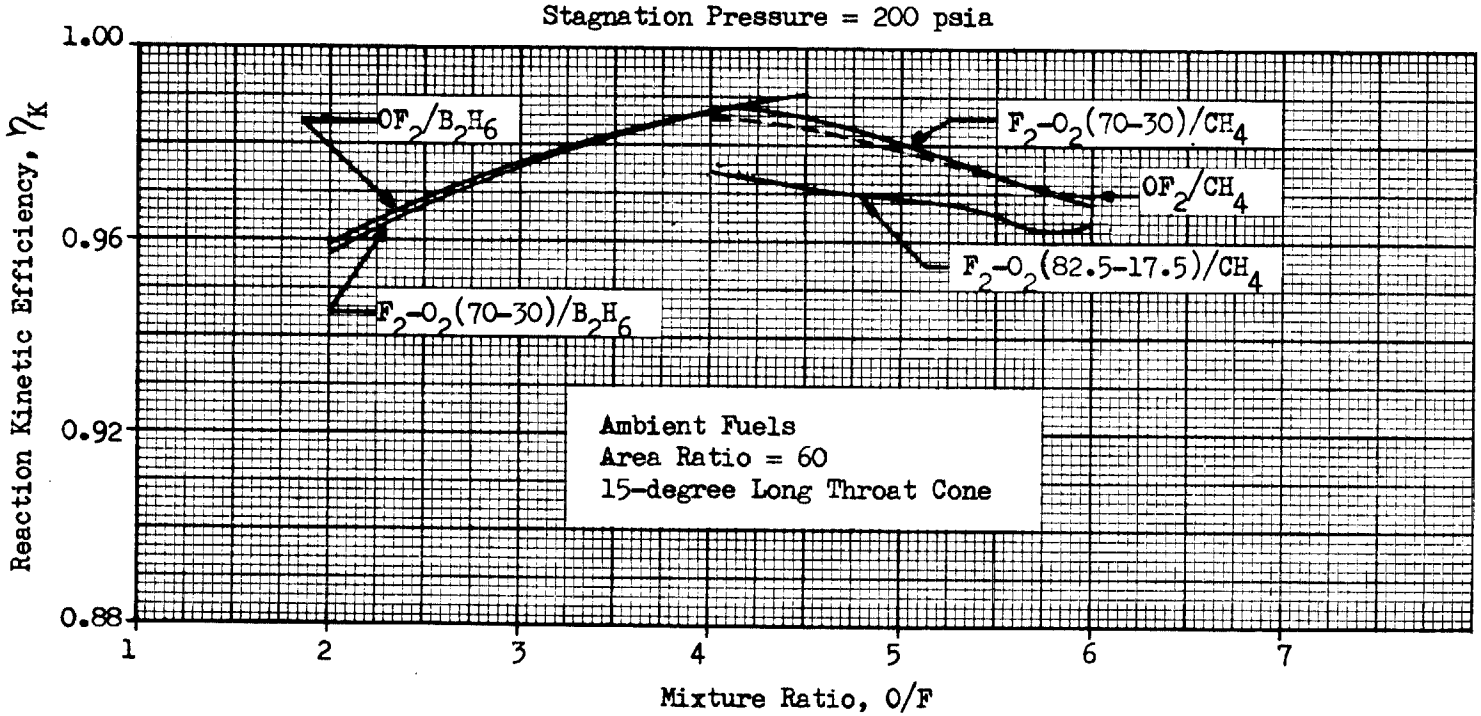

Figure E19. Effect of Mixture Ratio on Reaction Kinetic Efficiency for 15-Degree Long Throat Cone for 200 psia Chamber Pressure

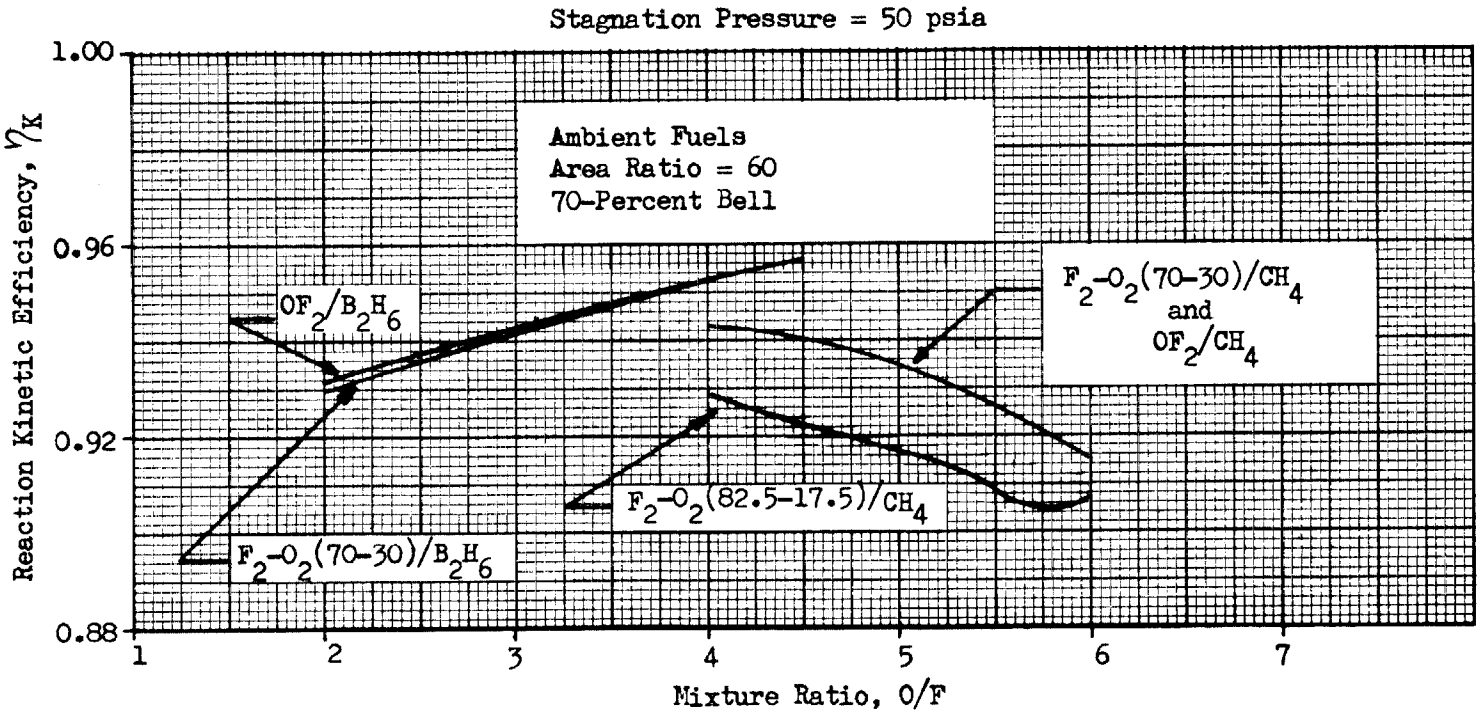

Figure E20. Effect of Mixture Ratio on Reaction Kinetic Efficiency for 70-Percent Bell for 50 psia Chamber Pressure

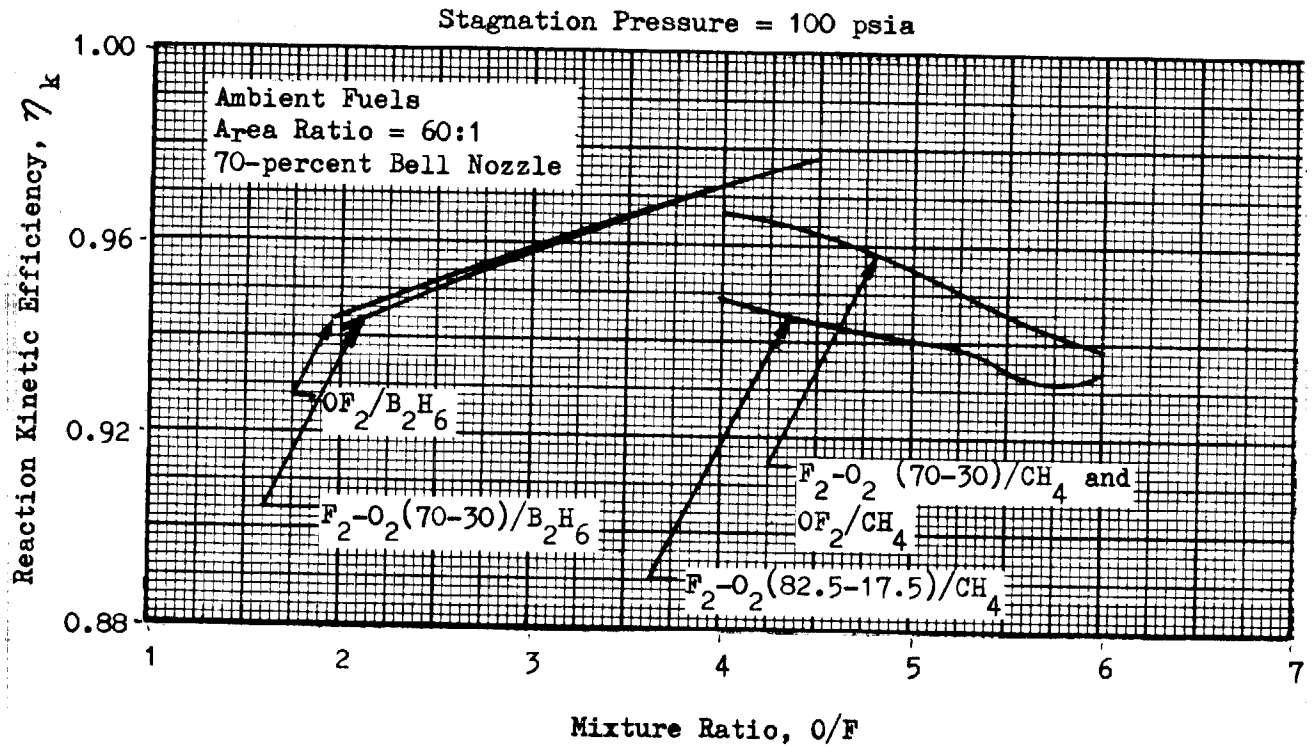

Figure E-21. Effect of Mixture Ratio on Reaction Kinetic Efficiency for 70-Percent Bell for 100 psia Chamber Pressure

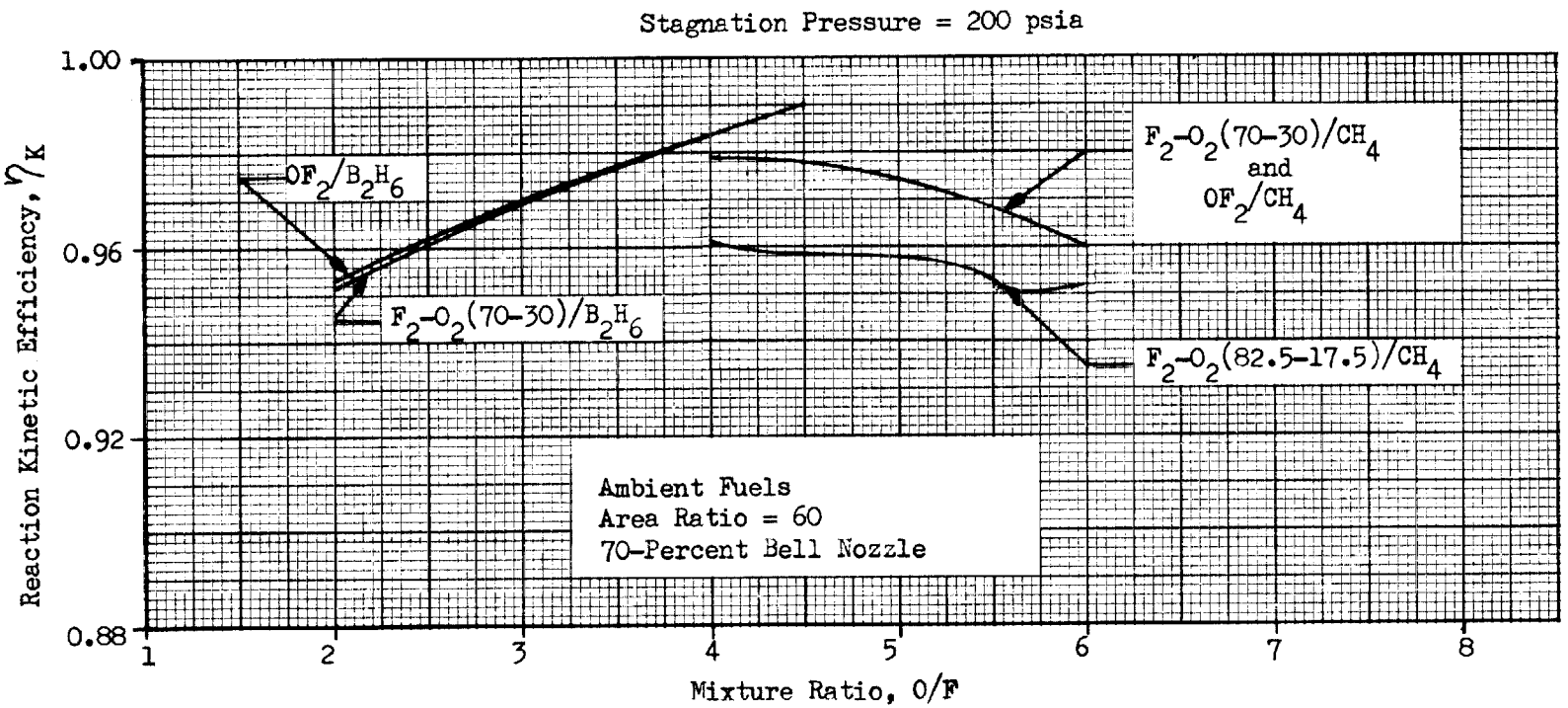

Figure E22. Effect of Mixture Ratio on Reaction Kinetic Efficiency for 70-Percent Bell for 200 psia Chamber Pressure